INSTITUTE

FOR

AEROSPACE STUDIES

UNIVERSITY OF TORONTO

TP 4916E

A THEORETICAL AND EXPERIMENTAL INVESTIGATION OF THE COMPLIANT AIR BEARING CHARACTERISTICS OF THE SAILRAIL TRANSPORTATION SYSTEM

Project Team

P. A. Sullivan, M. J. Hinchey, T. A. Graham,
M. Simard and L.-Z. Yong

Prepared for

Transportation Development Centre
Transport Canada

January 1985

CA1
DTC 820
85
T32
c.2

TP 4916E

A THEORETICAL AND EXPERIMENTAL INVESTIGATION OF THE COMPLIANT AIR BEARING CHARACTERISTICS OF THE SAILRAIL TRANSPORTATION SYSTEM

Project Team

P. A. Sullivan, M. J. Hinchey, T. A. Graham,
M. Simard and L.-Z. Yong

Prepared for

Transportation Development Centre
Transport Canada

January 1985

Library and Information Centre
Centre de Documentation (GSL)
RECEIVED – REÇU LE
OCT 8 1985
Government Publication Officielle
Transport Canada / Transports Canada

"When I was directing the research work of students in my days at Princeton University, I always used to tell them that if the result of a thesis problem could be foreseen at its beginning it was not worth looking at."

Karl Taylor Compton, 1887-1954

The contents of this report reflect the views of the contractor and not necessarily the official views or policies of the Transportation Development Centre.

REPORT DOCUMENTATION FORM

1. Transport Canada Report No. TP 4916 E	2. TDC Project No 4426	3. Recipient's Catalogue No.
4. Title and Subtitle A THEORETICAL AND EXPERIMENTAL INVESTIGATION OF THE COMPLIANT AIR BEARING CHARACTERISTICS OF THE SAILRAIL TRANSPORTATION SYSTEM		5. Report Date January 1985
		6. Performing Organization Report No.
7. Author(s) P.A. Sullivan, M.J. Hinchey, T.A. Graham, M. Simard and L. -Z. Yong		8. Transport Canada File No D 1465-310-2
9. Performing Organization Name and Address University of Toronto, Institute for Aerospace Studies (UTIAS) 4925 Dufferin Street Downsview, Ontario M3H 5T6		10. DSS File No. T8200-1-1512
		11. DSS or Transport Canada Contract No OSD81-00040
12. Sponsoring Agency Name and Address Transportation Development Centre (TDC) 1000 Sherbrooke Street West, Suite 2421 Montreal, Quebec H3A 2R3		13. Type of Report and Period Covered
		14. Sponsoring Agency Code 4426
15. Supplementary Notes		16. TDC Project Officer J.E. Laframboise

17. Abstract

A second phase investigation of the air bearing properties of a palletized goods handling system is described. The system uses cellulose shoes of elliptic cross section sliding on concave rails, and air under pressure is injected between shoe and rail through small holes drilled in the rail surface. The report describes results of tests undertaken to determine the significance to system performance of certain unconventional features. These include the shallow inclination of the feed holes relative to the track surface, and an optimum thickness of the polymer sheet used to enclose the shoe. Evidence supporting the claims of the developer is obtained, but system performance is found to be very sensitive to the viscoelastic or creep properties of the cellulose.

Experimental measurements on a large scale model of the immediate neighbourhood of the air feed holes provide a satisfactory explanation of the effect of feed hold geometry in terms of head losses in fluid flows. Experiments also indicate that the bending stiffness of the shoe cover and not its thickness is the important factor governing improved performance, but a satisfactory explanation of the mechanism involved is not forthcoming. Measurements of the minimum gap between shoe and track agree qualitatively with predictions made from an analysis of the fluid mechanics involved. Some results of preliminary investigations of the shoe structural properties are described, and a simplified analysis that couples structural properties of the shoe to the fluid mechanics is presented. Results of an exploratory analysis of the pneumatic hammer type dynamic instability suggest that the damping properties of the cellulose may play a key role in delaying its onset. Finally, an analysis of cover flutter is included.

18. Key Words Freight storage, compliant air bearing, air cushion handling of pallets, multimodal goods handling		19. Distribution Statement Limited number of copies available at TDC.	
20. Security Classification (of this report) NIL	21. Security Classification (of this page) NIL	22. No. of Pages 260	23. Price ---

TDC/CDT 79-005

FORMULE DE DOCUMENTATION POUR RAPPORT

1. **Nº du rapport Transports Canada** TP 4916 E

2. **Nº de l'étude — CDT** 4426

3. **Nº de catalogue du destinataire**

4. **Titre et sous-titre**
A THEORETICAL AND EXPERIMENTAL INVESTIGATION OF THE COMPLIANT AIR BEARING CHARACTERISTICS OF THE SAILRAIL TRANSPORTATION SYSTEM

5. **Date du rapport** Janvier 1985

6. **Nº du rapport de l'organisme exécutant**

7. **Auteur(s)**
P.A. Sullivan, M.J. Hinchey, T.A. Graham, M. Simard and L. -Z. Yong

8. **Nº de dossier Transports Canada** D 1465-310-2

9. **Nom et adresse de l'organisme exécutant**
University of Toronto, Institute for Aerospace Studies (UTIAS)
4925 Dufferin Street
Downsview, Ontario
M3H 5T6

10. **Nº de dossier — ASC** T8200-1-1512

11. **Nº de contrat — ASC ou Transports Canada** 0DS81-00040

12. **Nom et adresse de l'organisme parrain**
Centre de développement des transports (CDT)
1000 ouest rue Sherbrooke, Suite 2421
Montréal, Québec
H3A 2R3

13. **Genre de rapport et période visée**

14. **Code de l'organisme parrain** 4426

15. **Remarques additionnelles**

16. **Agent de projet — CDT** J.E. Laframboise

17. **Résumé**

Ce rapport constitue la seconde partie de la recherche concernant un palier aérostatique servant à la manutention de marchandises sur palettes.

Le système utilise des sabots en cellulose de section elliptique glissant sur des rails concaves, et l'air sous pression est injecté entre le sabot et le rail par des petits orifices dans la surface du rail. Les résultats de tests concernant l'importance de certaines innovations sur les performances sont également inclus. Celles-ci comprennent la faible inclinaison des orifices d'alimentation par rapport à la surface du rail et une épaisseur optimale de la feuille de polymère enveloppant le sabot. Des résultats supportant les assertions du manufacturier sont obtenus, mais les performances sont très sensibles aux propriétés viscoélastiques de la cellulose.

Des résultats expérimentaux obtenus d'un modèle à l'échelle agrandie de la région immédiate des orifices d'alimentation fournissent une explication satisfaisante des pertes de pression en fonction de la géométrie. La rigidité en flexion de l'enveloppe de polyéthylène, et non pas son épaisseur, semble être un paramtre important influençant les performances, mais une explication satisfaisante de ce phénomène n'est pas encore disponible. Des mesures de l'espacement minimum entre le sabot et le rail sont en accord qualitatif avec les prédictions théoriques de la mécanique des fluides. Quelques résultats préliminaires des propriétés structurales du sabot sont inclus et une analyse simplifiée des propriétés structurales couplées avec la mécanique des fluides est présentée. Une brève analyse suggère que les propriétés d'amortissement de la cellulose peuvent jouer un rôle important en retardant l'initiation d'instabilité dynamique. Finalement, une analyse du flottement de l'enveloppe est incluse.

18. **Mots-clés**
Palier résiliant pneumatique, mouvement de palettes sur coussin d'air, manutention multimodale de marchandises, entreposage

19. **Diffusion**
Un nombre limité de copies disponibles au CDT.

20. **Classification de sécurité (de ce rapport)** néant

21. **Classification de sécurité (de cette page)** néant

22. **Nombre de pages** 260

23. **Prix** ---

TABLE OF CONTENTS

Page

1. INTRODUCTION 1
   - 1.1 Overall Purpose 1
   - 1.2 A Brief Description of the SailRail System 1
   - 1.3 Controversial Features 3
   - 1.4 Discussion of Research Strategy 8
   - 1.5 Main Results of the First Research Contract 8
   - 1.6 Detailed Objectives of the Present Contract 9
   - 1.7 General Comment on Progress 11

2. RESULTS FROM PROTOTYPE TESTING 12
   - 2.1 Apparatus 12
   - 2.2 Factors Influencing Results 13
   - 2.3 Main Results Obtained from Test-Bed 13
   - 2.4 Principal Results from Pressure Measurement Apparatus 15

3. FLUID MECHANICAL ASPECTS 15
   - 3.1 Overall Classification 15
   - 3.2 Entry Region 16
   - 3.2.1 General Approach 16
   - 3.2.2 Results from Scaled-Up Models 17
   - 3.2.3 Compressibility Effects in the Entry Region 18
   - 3.3 Seal Region 20

4. STRUCTURAL ASPECTS 20
   - 4.1 Properties of Tissue 20
   - 4.2 Effect of Cover Thickness 21
   - 4.3 Modelling of the Shoe for Air Bearing Calculations 22

5. MODELLING OF THE OVERALL SYSTEM 24
   - 5.1 Air Bearing Calculations 24
   - 5.2 Dynamic Stability Calculations 25
   - 5.3 Cover Flutter Analysis 25

6. CONCLUSIONS 25
   - 6.1 General Status 25
   - 6.2 Recommendations for Future Work 26

APPENDIX A. ANALYSIS OF THE FLUID MECHANICS OF THE SEAL REGION 29
   - A.1 Introduction 29
   - A.2 Analysis of Fluid Mechanics 29
   - A.3 Relationship to Analysis of Appendix K 32
   - A.4 Solution with Gap Shape Given 32
   - A.5 Determination of Minimum Gap Height h_s 33
   - A.6 Future Work 36

APPENDIX B. SCALED UP MODEL OF ENTRY REGION 41
- B.1 Introduction 41
- B.2 Geometry and Terminology 41
- B.3 Scaling Requirements 41
- B.4 Model of Cavity-Entry Region 43
- B.5 Results for Cavity Inlet Model 46
- B.6 Effect of Nozzle Inclination Angle 54
- B.7 Computed Radial Nozzle Flow Patterns 54
- B.8 Measured Pressure Distributions for Radial and Inclined Nozzles 61
- B.9 Flow Visualization 66
- B.10 Discussion and Conclusion 66

APPENDIX C. PROTOTYPE TEST BED RESULTS 75
- C.1 Introduction 75
- C.2 A Result from Preliminary Testing of the First Aluminium Rail Section 78
- C.3 The Problem of Repeatability of Test Bed Results 81
- C.4 Effects of Feed Hole Layout and Geometry 88
- C.5 Effect of Lateral Forces 92
- C.6 Effect of Shoe Cover Thickness 92
- C.7 Effect of Pallet Weight 99
- C.8 Asymmetric Loading Effect 99
- C.9 Peformance of a Simplified Shoe Geometry 103
- C.10 Effect of Rail Width 103
- C.11 Air Consumption and Power 107
- C.12 Conclusion 107

APPENDIX D. PRESSURE MEASUREMENT APPARATUS RESULTS 111
- D.1 Introduction 111
- D.2 Concept of Ideal Bearing Cavity Pressure 111
- D.3 Typical Results 117
- D.4 Conditioning Effects 118
- D.5 Effect of Thickness of the Shoe Cover 118
- D.6 Effect of Shoe Alignment and Support 122
- D.7 Measurements of Gap in Seal Region 129
- D.8 A Concluding Note 135

APPENDIX E. REVIEW OF POLYMER FRICTION 137
- E.1 Introduction 137
- E.2 The Molecular Nature of Polymers 137
- E.3 Friction Mechanisms 139
- E.4 Properties of PTFE and HDPE 141
- E.5 Implications for the Present Work 141

APPENDIX F. SLIDING FRICTION MEASUREMENTS AND THEIR RELATION TO PROTOTYPE TEST BED RESULTS 143
- F.1 Introduction 143
- F.2 Analysis 143
- F.3 Sliding Friction Measurements 144
- F.4 Relationship to Test Bed Results 148

APPENDIX G. PRELIMINARY RESULTS OF A DYNAMIC STABILITY INVESTIGATION 153
G.1 Introduction 153
G.2 Simplified Model Assumptions 153
G.3 Governing Equations 153
G.4 Stability for the Rigid Shoe Approximation 157
G.5 Discussion and Conclusions 159

APPENDIX H. STRUCTURAL PROPERTIES OF THE SHOE TISSUE 161
H.1 Introduction 161
H.2 Test Programme and Results 161
H.3 Discussion 172

APPENDIX I. ANALYSIS OF SHOE COVER FLUTTER 173
I.1 Introduction 173
I.2 Cover Futter Analysis 175
I.3 Results and Discussion 179
I.4 Conclusion 185

APPENDIX J. VISUALIZATION OF THE FLOW BETWEEN TRACK AND SHOE 187
J.1 Introduction 187
J.2 Flow Visualization Refinement 187
J.3 Effect of Changes in Nozzle Layout 187

APPENDIX K. FINITE ELEMENT ANALYSIS OF FLOW BETWEEN SHOE AND RAIL 191
K.1 Introduction 191
K.2 A Property of Flows Obeying the Reynolds Equation 191
K.3 Local Spring Shoe Model 192
K.4 Orifice Flow Model of Nozzles 192
K.5 Results 194

APPENDIX L. FINITE DIFFERENCE SIMULATION OF RADIAL NOZZLE FLOW 201
L.1 Introduction 201
L.2 Governing Equations 201
L.3 Finite Difference Code 204
L.4 Boundary Conditions 206
L.5 Computer Program Outline 207

APPENDIX M. DEVELOPMENT OF RAIL SECTION PROFILE 209

APPENDIX N. HEAD LOSSES IN SHARP EDGED RADIAL NOZZLES 215
N.1 Introduction 215
N.2 Simplified Model 215

APPENDIX O. COMPRESSIBILITY EFFECTS IN THE NOZZLE REGION 219
O.1 Introduction 219
O.2 Measurements of Air Flow for Covered and Uncovered Nozzles 221
O.3 Discussion and Conclusions 224

APPENDIX P. COMPUTER LISTING FOR PROGRAMME USED IN APPENDIX K 229

REFERENCES 239

BIBLIOGRAPHY OF PAPERS AND BOOKS ON FRICTION AND WEAR OF POLYMERS CAUSED BY SLIDING 241

LIST OF FIGURES

Figure 1	SailRail Trailer Loading and Unloading System. In the top picture two sets of rails are mounted with their top surface flush with the trailer floor. In the bottom photograph a single fork lift truck unloads an entire load of 22 pallets.	2
Figure 2	SailRail warehouse racking system as currently produced.	4
Figure 3	Early development prototype of low speed passenger transporter. The tops of the linear induction motor primaries can be seen. The motors and the air supply are automatically activated for short sections when the presence of the vehicle is detected by a photo-electric cell.	5
Figure 4	Shoe section.	6
Figure 5	Wound cellulose paper roll prior to collapse to form a shoe.	23
Figure 6	Wound cellulose paper roll after collapse.	23
Figure A1	Coordinate system used in analysis.	30
Figure A2	Two dimensional flow in seal region. The width of the minimum gap is called seal height h_s. The fluid separates at some point S in the diverging section.	30
Figure A3	Parameters in cavity shape assumed for computation of h_s.	34
Figure A4	Typical pressure distributions in seal region computed for known H and $\bar{M}$ and with various h_s. The correct value of h_s is that corresponding to p = 100 kPa at $\xi > 1.5$.	35
Figure A5	Effect of cavity height H on estimate of seal height h_s for cosine low cavity shape.	37
Figure A6	Effect of cavity half-width D on estimate of seal height h_s for cosine low cavity shape.	38
Figure A7	Computed seal height h_s as a function of mass flux $\bar{M}$.	39

Figure B1 Geometry of entry region. 42

Figure B2 Twenty times full scale model of cavity entry region. 44

Figure B3 Location of static pressure taps in the cavity-entry region model. 45

Figure B4 Nozzle geometries tested in the cavity-entry region model. 45

Figure B5 Typical rotameter calibration curve. 47

Figure B6 Typical resistance characteristics of inclined and radial nozzles. 48

Figure B7 Flow coefficient for inclined nozzle as a function of Reynolds number with $A_{r1} = \pi/4d^2$ as reference area. 50

Figure B8 Flow coefficient for sharp edged radial nozzle as a function of Reynolds number with $A_{r1} = \pi d^2/4$ as reference. 51

Figure B9 Flow coefficient for sharp edged radial nozzle as a function of Reynolds number with $A_{r2} = \pi dh$ as reference area. 52

Figure B10 Flow coefficient for inclined nozzle as a function of Reynolds number with $A_{r2} = 6.54$ dh as reference area. 53

Figure B11 Geometries used for investigation of the effect of nozzle angle on head losses at nozzle-entry and cavity-entry regions. 55

Figure B12 Effect of nozzle angle on head losses in nozzle-entry region for three Reynolds numbers. 56

Figure B13 Effect of nozzle angle on cavity-entry head losses for three values of h/d at $Re_d = 10^4$. 57

Figure B14 Effect of nozzle angle on cavity-entry head losses for three values of h/d at $Re_d = 5\times10^3$. 58

Figure B15 Velocity vector plot of flow field for a sharp edged radial nozzle and h/d = 0.5 as determined by numerical solution of equations modelling turbulent flow. The arrows locate the base lines of the velocity vector. 59

Figure B16 Velocity vector plot of computed flow field for a sharp edged radial nozzle and h/d = 0.25. The arrows locate the base lines of the velocity vectors. 60

Figure B17 Effect of Reynolds number Re_d on pressure distribution on bottom disc for sharp edged radial nozzle. 62

Figure B18 Effect of h/d on pressure distribution on bottom disc for sharp-edged radial nozzle. 63

Figure B19 Comparison of measured and predicted pressure distributions for sharp edged radial nozzle and h/d = 0.467. 64

Figure B20 Comparison of measured and predicted pressure distributions for sharp edged radial nozzles and h/d = 0.229. 65

Figure B21 Measured pressure distributions on bottom disc for inclined nozzle along 0° and 180° radii defined in Figure B3. 67

Figure B22 Measured pressure distributions on bottom disc for inclined nozzle along radii defined in Figure B3. 68

Figure B23(A) Flow visualization for sharp-edged radial nozzle, top disc. 69

Figure B23(B) Flow visualization for inclined nozzle, top disc, showing extent of jet. The large accumulations of titanium dioxide such as that marked "A" are caused by surface tension effects on the liquid-solid suspension, and indicate the absence of any significant flow. The boundary of the nozzle is marked. 69

Figure B23(C) Flow visualization for inclined nozzle, top disc, showing details of flow. Indications of flow separation and reattachment as marked suggest a complex secondary flow with a vortex-like structure. 70

Figure B23(D) Flow visualization for inclined nozzle, bottom disc. 70

Figure B24 Flow visualization for inclined nozzle with 10 mm of tissue and 0.61 mm polyethylene sheet placed on bottom disc. The accumulation of titanium dioxide at the part of the nozzle periphery marked A is probably caused by a small separation bubble associated with the turning of the flow through 160°. Other than this, the flow is source-like. 72

Figure C1 Prototype test-bed apparatus. In the lower photograph a typical SailRail shoe is installed on the left side of the pallet and the simplified shoe is installed on the right side. The upper photograph shows the decelerating mechanism. 76

Figure C2 Typical transit time data obtained from the prototype test bed. 77

Figure C3 Nozzle patterns used in original and more recent development prototypes. 79

Figure C4 Transit time measurements obtained for rail section III ("single web rail"). New standard nozzle pattern was used. 80

Figure C5 Bending of the top surface of rail section III caused by the track-cavity pressure difference p_t-p_c acting over the width ℓ. The deflection δ increases the width of the seal region from d to d', and reduces the cavity width w to w'. 82

Figure C6 Comparison of transit time measurements for rail sections III and IV ("double web rail"). New standard nozzle pattern was used. 83

Figure C7 Effect of conditioning on transit time measurements at a representative track pressure. Error bars are given for repeated measurement at a given elapsed time. 84

Figure C8 Effect of conditioning on transit time measurements obtained after removal and reinstallation of shoes. 85

Figure C9 An example of a sudden change in transit time occurring after an extended period of conditioning. 86

Figure C10 Effect of cool air currents on transit time measurements. 89

Figure C11 Effect of the use of lateral alignment brackets on transit time data. For one set of data, curve 3, the second trial, the load would move only at the highest track pressure tested. 90

Figure C12 Mechanism used to rotate shoes while under load. 91

Figure C13 Effect of nozzle patterns on transit time. 93

Figure C14 Effect of radial nozzles at different diameters on transit time, together with a comparison with inclined nozzle performance. 94

Figure C15 Comparison of performance obtained for chamfered radial nozzles with that obtained using inclined nozzles. 95

Figure C16 Effect on transit time measurements of a lateral tilt towards the nozzles. 96

Figure C17 Effect on transit time measurements of a lateral tilt away from the nozzles. 97

Figure C18 Effect of shoe cover thickness on transit time measurements. 98

Figure C19 Effect of cover thickness on air flow rates for a range of track pressures. 100

Figure C20 Effect of pallet load M_p on transit time measurements. 101

Figure C21 Effect of asymmetrical pallet loading on transit time measurements. 102

Figure C22 The simplified shoe geometry used in exploratory tests. 104

Figure C23 Transit time measurements obtained by using simplified shoe geometry. 105

Figure C24 Effect of three different rail sections on transit time measurements. 106

Figure C25 Air flow power measurements for various nozzle configurations. 108

Figure D1 Photograph of pressure measurement apparatus; rail (1); shoe (2); cover (3); load support beam (4); linear ball bushings (5); test weights (6); air lift bags (7). 112

Figure D2 Outline diagram of pressure measurement apparatus showing attachments for measuring air gap. 113

Figure D3 Location of probes used to obtain pressure measurements. 114

Figure D4 Fixture used to align the shoe relative to the rail. 115

Figure D5 Geometry for definition of ideal cavity pressure. 116

Figure D6 Example of a conditioning effect on pressure distributions. Shoe alignment mechanism was not used. 119

Figure D7 Effect of use of shoe alignment mechanism on conditioning of the shoe. 120

Figure D8 Effect of cutting the shoe cover along the sides of the shoe on the pressure distribution between shoe and rail. 121

Figure D9 Effect of bending 0.15 mm polyethylene cover on pressure distribution between shoe and rail. 123

Figure D10 Effect of bending 1.52 mm high density polyethylene cover on pressure distribution between shoe and rail. 124

Figure D11 Effect of bending 0.20 mm steel shim stock cover on pressure distribution between shoe and rail. 125

Figure D12a Comparison of pressure distributions as obtained for three covers and with covers bent to channel. 126

Figure D12b Comparison of pressure distributions obtained for three covers left free at the edges. 127

Figure D13 Effect of a lateral misalignment on pressure distributions. 128

Figure D14 Effect of disturbance placed between shoe and load on pressure distributions. 130

Figure D15 Effect of track pressure on pressure distributions after lift-off has occurred. 132

Figure D16 Effect of track pressure on vertical displacement of load. 133

Figure D17 Vertical displacement of the shoe as a function of air flow rate. The mass flow is quoted for a unit length of seal region. For the 0.8m shoe used in the tests, an allowance of 0.1 metre for the seal at each end is included to give a total equivalent seal length of 1.8m. 134

Figure E1 Polyethylene chain. 138

Figure E2 Chain branch in polyethylene. 138

Figure E3 Effect of sliding speed on friction of polymers. 138

Figure E4 Mechanism of friction caused by deformation or ploughing, for a regular hard asperity pressed into a viscoelastic material. 140

Figure F1 Apparatus used to measure coefficients of friction. 145

Figure F2 Friction coefficient K_f for 1.27 mm extruded medium density polyethylene sheet sliding on various surfaces of extruded aluminium. The static value, K_{fs} is also given. 146

Figure F3 Friction coefficient for 0.762 mm extruded polyethylene sheet sliding on various surfaces. 147

Figure F4 Sliding friction coefficient for steel shim stock compared with that for 1.27 mm extruded polyethylene. 149

Figure F5 Measurements of sliding friction over an extended period of time. 150

Figure F6 Comparison of measured transit time data with values computed by assuming various values of k_f. 151

Figure G1 Conceptual model used in dynamic stability investigation. 154

Figure H1 Load-deflection characteristics of a sample of tissue 100 mm thick and having a cross-sectional area of 0.114 m^2. 162

Figure H2 Stress relaxation results for tissue sample of Figure H1. 164

Figure H3 Load-deflection characteristics of a 580 mm long sample of SailRail log (shoe without cover). 165

Figure H4 Effect of partial compression of shoe S5B. 166

Figure H5 Stress relaxation results for log sample of Figure H3. 167

Figure H6 Load-deflection characteristics of various logs supplied by the manufacturer, along with qualitative descriptions of performance. Note that the sample described as having the "best" performance has a stiffness intermediate between that of samples described as "poor" and "adequate". 168

Figure H7 Load-deflection characteristics of logs used in the early stages of development compared with that of sample 6. 169

Figure H8 Comparison of load-deflection characteristics of a highly flattened log, the "Clark shoe", with that of a sample designated as "hard" by the manufacturer. 170

Figure I.1 Load-deflection characteristics of shoe used to obtain data for flutter analysis. 174

Figure I.2 Simplified geometry usede in cover flutter analysis. 176

Figure I.3 Typical flutter stability boundaries. 178

Figure I.4 Typical divergence stability boundaries. 180

Figure I.5 Flutter and divergence stability boundary for 1.27 mm shoe cover. 181

Figure I.6 Frequency at flutter stability boundary as a function of wavelength. The frequency at the wavelength correspondingf to the lowest U_f at which flutter occurs is 565 Hz. 182

Figure I.7 Flutter and divergence stability boundary for 0.125 mm shoe cover. 183

Figure I.8 Frequency at the flutter stability boundary as a function of wavelength. The frequency corresponding to the lowest U_f at which flutter occurs is 1410 Hz. 184

Figure J1 Visualization of the flow between rail and shoe for original standard nozzle pattern, nozzles at -15° and +5° with 304.8 mm (12 in) spacing 188

Figure J2 Visualization of the flow between rail and shoe obtained by the metered ammonia method for a single row of nozzles at the +5° location and 152.4 mm (6 in) spacing for two nozzle orientations as indicated by the marked arrows. The left hand visualization corresponds to the new standard nozzle geometry and in the right hand visualization the nozzles point to alternate sides of the rail 189

Figure J3 Details of flow in one of the cells of Figure J2 showing streamlines 190

Figure K1 Shoe stiffness distributions assumed for finite element lubrication analysis. 193

Figure K2	Computed pressure and gap distributions for a shoe having uniform stiffness. The nozzle locations are marked by the cross-hatched circles.	195
Figure K3	Computed pressure and gap distributions for a shoe which is soft in the centre and stiff on the periphery.	196
Figure K4	Computed pressure and gap distributions for a shoe which is stiff in the centre and soft on the periphery.	197
Figure K5	Computed pressure and gap distributions for analysis including nozzle head losses.	198
Figure K6	Typical velocity vectors for flow between shoe and rail determined using equation K9.	199
Figure L1	Geometry used in turbulent flow calculations for sharp edged radial nozzle.	202
Figure L2	Staggered grid used in finite difference computations.	205
Figure L3	Flow chart for computer program.	208
Figure M1	Rail section I, used in early experiments	210
Figure M2	Rail section II, used in first pre-production prototypes. This was the only rail extruded from a plastic.	210
Figure M3	First extruded aluminium rail section (III), known as the single web rail.	211
Figure M4	Rail section IV, "double web" rail, used in the trailer loading and unloading demonstration system at E. B. Eddy Forest Products, Hull.	211
Figure M5	Rail section V, "single port" rail, used in first commercial application.	211
Figure M6	Modified double web rail used to explore the freasibility of reducing the rail width.	212
Figure M7	Extended single port rail, section VI.	212
Figure M8	Section VII, "four port" rail used in current production.	212
Figure N1	Conceptual model used to calculate head losses for sharp-edged radial nozzle.	216

Figure 0.1 Concept of gasdynamic choking as applied to SailRail nozzles. 220

Figure 0.2 Effect of track pressure on air flow through a standard 0.66 mm inclined nozzle when uncovered and when covered by a shoe. 222

Figure 0.3 Effect of track pressure on air flow through radial nozzles when covered by a shoe, and comparison with inclined nozzle data. 223

Figure 0.4 Effect of track pressure on reduced volume flows for radial nozzles covered by a shoe. 225

Figure 0.5 Comparison of covered and uncovered flow rates for radial nozzles, and with inclined nozzle data of Figure 0.2. 226

Figure 0.6 Possible shock wave patterns for supersonic flow in radial and inclined nozzles. 232

LIST OF TABLES

Table C1 Typical variation of SailRail performance over an extended period of time 87

Table H1 Composition analysis of various tissues used in prototype test bed. Analysis performed and supplied by E. B. Eddy Forest Products. 171

NOTATION

APPENDIX A

Roman

h	Gap between shoe and rail
h_s	Minimum gap or seal height
M	Mass flux per unit length of seal region
N	$12\ \mu RT$
p	Pressure
R	Gas constant = 286.8 kg/J°K for air
T	Gas temperature
u, v, w	Velocity components in x, y, z directions respectively
x, y, z	Spatial coordinates defined in Figure A1

Greek

μ	Viscosity

APPENDIX B

Roman

A_{r1}, A_{r2}	Reference areas for flow coefficient C_Q, $A_{r1} = \pi d^2/4$; $A_{r2} = \pi dh$ for sharp-edged radial nozzles and $A_{r2} = 6.54\ dh$ for 20° inclined nozzles
C_{Qi}	Flow coefficient based on reference area A_{ri}, $C_{Qi} = Q/(V_r A_{ri})$
d	Nozzle diameter
h	Shoe-rail gap
K_i, K_o	Nozzle inlet and outlet head loss coefficients
L	Length of nozzle
$\dot{m}$	Mass flux through nozzle
p_c	Pressure in cavity under the shoe, i.e., at point (4) in Figure B1
p_d	$\rho\bar{U}^2/2$

p_s	Static pressure measured at location shown in Figure B11
p_t	Air supply pressure in rail manifold
Q	Volume flux through nozzle in scaled-up model
Re_d	Reynolds number of flow through nozzle, $Re_d = 4\dot{m}/(d\mu)$
$\bar{U}$	Mean velocity in nozzle of scaled-up model, $\bar{U} = Q/A_{r1}$
V_r	Reference velocity, defined by equation B4

Greek

θ	Angle of inclination of nozzle to surface of rail
μ	Air viscosity
ρ	Air density

Subscripts

m	Scaled-up model
p	Prototype

APPENDIX C

Roman

d	Diameter of nozzle
M_p	Total mass of loaded pallet
M_d	Mass of driving weight
h	Shoe-rail gap
p_a	Atmospheric pressure
P_f	Flow power = $Q_t(p_t - p_a)$
P_i	Installed power
p_t	Air supply pressure in rail manifold
Q_t	Volume flux at pressure p_t
t	Transit time
t_c	Thickness of shoe cover

APPENDIX D

Roman

B_r	Rail width
h_s	Seal region gap
L	Shoe length
p_c	Cavity pressure
p_{cI}	Ideal cavity pressure
p_s	Pressure distribution under the shoe
p_t	Rail manifold pressure
R	Radius of curvature of track bearing surface
T	Lift force
W	Weight of load
y	Lateral distance from centreline of rail

Greek

θ	Angle from radius through track centreline

APPENDIX E

Roman

A	Apparent area of contact
A_r	True area of contact
F	Force due to friction
n	Index of elastic deformation, $A_r \propto W^n$
p_m	Flow pressure of softer material
S	Shear strength of weaker material
V	Velocity of sliding
W	Load

Greek

μ	Coefficient of sliding friction

Abbreviations

CF_3	Perfluoromethyl group
FEP	Commercial Teflon
HDPE	High density polyethylene
LDPE	Low density polyethylene
PMMA	Polymethylmelthacyclate
PP	Polypropylene
PS	Polystyrene
PTFE	Polytetrafluoroethylene
PVC	Polyvinylchloride
RH	Relative humidity

APPENDIX F

Roman

c	Fraction of pallet weight supported by direct contact
g	Gravitational constant
k	Coefficient of sliding friction
m_D	Mass of driving weight
m_p	Mass of pallet
N	Weight supported by shoe-track contact
t	Time
x	Pallet position

Greek

Δ	Interval
μ_D	Dynamic or sliding friction coefficient

Subscripts

0	Initial
1	Final

Superscript

$^{\circ}$	Time differentiation

APPENDIX G

Roman

C_s	Damping of secondary suspension connecting shoe to load mass
h	Shoe-rail gap
h_c	Average height of cavity region
h_s	Minimum shoe-rail gap, the "seal-height"
j	Choking location parameter, $j = 0$ for choking in nozzle entrance, and $j = 1$ for choking at exit
$K_{ip}K_{ih}$, K_{op}	Coefficients in linearized versions of nozzle inlet flow law and air escape or outlet law
K_s	Stiffness of secondary suspension connecting shoe to load mass
L	Effective width of shoe cavity
M	Load mass
m	Lumped equivalent shoe mass
$\dot{m}$	Mass flux
p_c	Absolute pressure in cavity
p_a	Atmospheric pressure
R	Gas constant
s	Laplace variable, $s = \sigma + i\omega$
t	Time
T_a	Ambient temperature
z	Vertical displacement of load mass

Greek

μ	Viscosity of air at temperature T_a
ρ_c	Density of air in cavity

Subscripts

e	Equilibrium
i	Inlet flow (nozzle region)
o	Outlet flow (seal region)

APPENDIX H

Greek

ε	Strain
σ	Stress

Abbreviation

LVDT	Linear variable displacement transducer

APPENDIX I

Roman

a	Speed of sound
C_s	Distributed viscous damping coefficient for the shoe
D	Bending stiffness
E	Young's modulus
f	Frequency (Hz)
h	Shoe-rail gap displacement from its equilibrium position
i	$\sqrt{-1}$
k	Wave number
K_s	Distributed shoe spring stiffness coefficient
Δp_c	Perturbation in shoe cavity pressure
Q_e	Equilibrium volumetric flow
s	Laplace variable
t	Time
t_c	Thickness of cover

T	Cover tension
U	Mean air flow speed
U_D	Flow limitation speed
U_f	Critical flow speed as a function of wave number k
U_s	Critical flow speed for onset of instability

Greek

γ	Isentropic exponent
λ	Wavelength
η	Heave displacement of the cover from its reference position
ν	Poisson's ratio
ω	Oscillation frequency (rad/sec)
ϕ	Velocity potential
ρ	Density

Subscripts

a	Atmospheric air
c	Cover

APPENDIX K

Roman

h	Gap between shoe and rail
k	Effective stiffness of shoe material
$\dot{m}$	Mass flux
p	Pressure between shoe and rail
p_s	Effective source pressure
p_t	Air supply or rail manifold pressure
u, v, w	Components of fluid velocity along x, y, z axes defined in Figure A1
v_x	Fluid velocity in x-direction averaged over shoe-rail gap

v_y	Fluid velocity in y-direction averaged over shoe-rail gap

Greek

ρ	Air density
μ	Air viscosity

APPENDIX L

Roman

C_1, C_3, C_D, C_μ	Model constants determined by dimensional arguments and geometrically simple experiments
d	Nozzle diameter
h	Gap
i	Intensity factor
k	Kinetic energy of turbulence
ℓ_m	Mixing length
p	Pressure
r	Radial coordinate
u, v	Velocities
x	Axial coordinate

Greek

δ	Correction
ϵ	Dissipation rate of turbulence
μ	Viscosity
σ_k, σ_μ	Universal constants

Subscripts

eff	Effective
ℓ	Length
pu, pv	u, v staggered velocity position respectively

Superscripts

	"Old" field

Abbreviations

N, S, E, W	Grid points north, south, east or west of either the staggered point "pu" or "pv"

APPENDIX N

Roman

C_t	Coefficient of contraction (defined in Figure N1)
d	Nozzle diameter
h	Gap between plates
p	Static pressure
q	Fluid speed
Q	Volume flux
r	Radial distance from nozzle axis
$\bar{U}$	Mean fluid velocity in nozzle

Subscripts

a	Atmospheric conditions
t	Throat defined in Figure N1

APPENDIX O

Roman

A_t	Area of nozzle at choke point
C_m	Discharge coefficient
d	Nozzle diameter
K	constant defined in Equation 0.2
$\dot{m}$	Mass flux
n	Index of compression in polytrope law
p_a	Atmospheric pressure
p_c	Pressure in cavity region (gauge)
P_c	Compression power
P_f	Flow power

p_t	Air manifold supply pressure (gauge)
Q_t	Volume flux at pressure p_t
R	Gas constant
T_t	Temperature of air in manifold
V_{ref}	Air reference velocity used in Appendix B
Greek	
γ	Specific heat ratio
ξ	Absolute pressure ratio = $(p_{tg} + p_a)/p_a$

1) INTRODUCTION

1.1) Overall Purpose

This report describes the results of a second research programme on the SailRail air bearing system, which is designed for moving loads over smooth surfaces on shallow guideways. The system is being developed by a Canadian company, SailRail Enterprises, a Division of E. B. Eddy Forest Products of Ottawa, and is based largely on the ideas of SailRail's General Manager, Mr. H. E. Gladish. The first research programme at the authors' Institute (UTIAS), undertaken during the period December 1979 to January 1981, involved a level of effort of about 1-1/2 years of professional engineers' time and obtained results which were only preliminary in nature [1]. The present Contract called for a similar level of effort, and covered the period June 1981 to September 1982. Many important insights have been obtained and these have allowed SailRail to make significant improvements in the design. However, it will also become clear to the reader that much has yet to be learned about the concept.

The overall purpose of the work remained that of the previous Contract, and was essentially as follows. Prior to support by the Transportation Development Centre (TDC), development proceeded on a largely ad hoc basis and without any theoretical foundation. Furthermore the concept also includes a number of controversial features which are considered by the developer to significantly improve the performance of the system; however no reliable data documenting the importance of these features was available, and the way in which they are caused was not initially known. They are described briefly in Section 1.3. Hence the objectives of the UTIAS work have been to provide an explanation of the functioning of SailRail in terms of the current ideas of engineering science, with particular reference to the controversial features. It was expected that this would lay a rational foundation for product improvement.

1.2) A Brief Description of the SailRail System

The concept is best introduced by description of one type of application, which is to the transportation and storage of goods handled on 1.22 m × 1.22 m pallets. The first of this type is to the loading and unloading of highway trailers at a warehouse dockside. The current method is laborious and expensive: fork-lift trucks move them, one by one. The trailer in Figure 1 is equipped with two sets of "rails" which appear as shallow grooves or guideways in the trailer floor. The elements attached to the underside of the pallet and which move along the rails are called "shoes" or "runners"; they have an 155×75 mm oval cross-section, are about 1.2m long, and are made from a combination of materials which gives them a high degree of compliance and tolerance to track misalignment. The rails also serve as air supply manifolds, and feed compressed air to a row of 0.66 mm holes or "nozzles" located near the centre of the rail and about 15 cm apart. The air supply requirements to obtain an air bearing or air cushion action are very modest. Typically a 1000 kg pallet load requires an installed air power of about 0.25 kW. The trailer's air bag springs permit vertical alignment with the warehouse dock and the flexibility of the rails on the dock allows horizontal alignment. An entire trailer load of 22 pallets weighing a total of 20 tonnes can be removed by a winch in 30

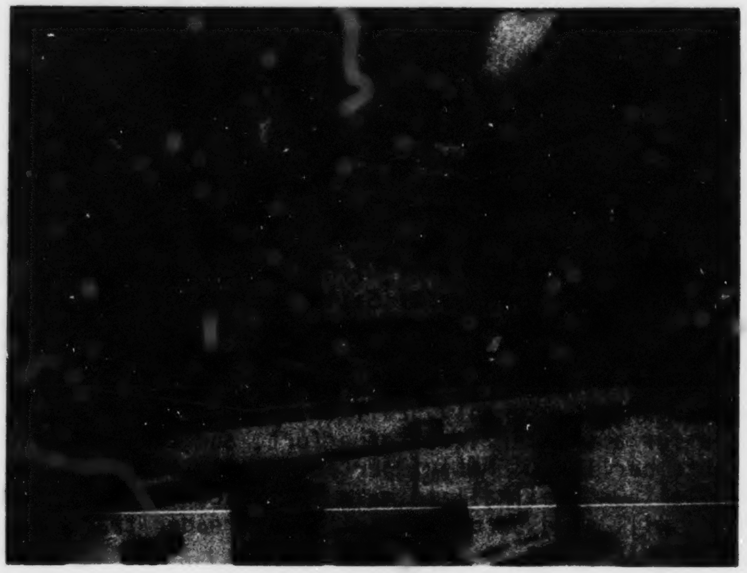

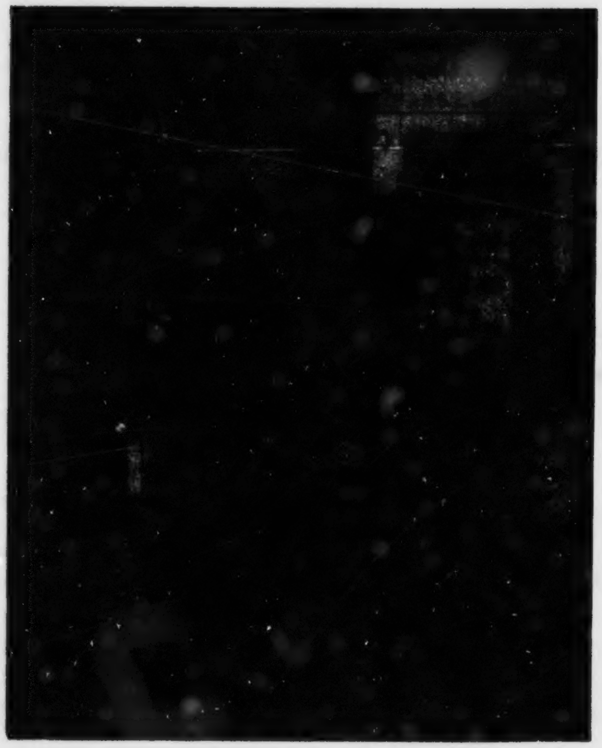

Figure 1 SailRail Trailer Loading and Unloading System. In the top picture two sets of rails are mounted with their top surface flush with the trailer floor. In the bottom photograph a single fork lift truck unloads an entire load of 22 pallets.

seconds; this contrasts with 25 to 30 minutes required by the conventional method.

Two other applications are currently undergoing intensive development. One is to warehouse systems. Figure 2 is an example. Sets of tracks are inclined at about 2° to the horizontal, are set up in closely spaced rows, and may be stacked as many as four vertically. Pallets are loaded at the high end, and removed at the low end. Timed pulses of air are periodically supplied to the tracks and the pallets move automatically down, so that there is always one ready for removal. The system makes many savings when compared with conventional approaches; for example, it automatically ensures proper stock rotation, and requires much less space. At the time of writing 30 installations having various sizes up to 4000 pallet-spaces have been sold.

The third application, currently being developed by the Urban Transportation Development Corporation of Canada (UTDC) is to low speed passenger transporters. These might, for example, be used to connect terminals at large airports. Figure 3 is a photograph of an early development prototype. Its planform dimensions are about 1.22m × 2.44m, and, to facilitate movement along curved guideways, as many as eight shoes are used, each being about 0.6m long and connected to the vehicle by an elastomer pivot which enables them to rotate through small angles both horizontally and vertically. Propulsion is provided by linear induction motors, with the primary coils being spaced at suitable intervals along the guideway, and with the extruded aluminium secondary reaction rail attached to the vehicle. Its principal advantage, when compared with such competitors as moving sidewalks, is the elimination of virtually all moving parts, thus greatly reducing mechanical complexity and thereby reducing both first and maintenance costs.

1.3 Controversial Features

The concept is not easily characterized in terms of existing air bearing or air cushion ideas, but its nearest conventional relative is probably an externally pressurized, orifice-stabilized compliant surface air bearing. However, it resembles an air cushion in some respects. The controversial features occur in two groups: those related to the construction of the shoe, and those related to the geometry and layout of the air nozzles. Consider these in turn.

Firstly, as shown in Figure 4, the shoe is comprised of three components: a flat cardboard "core" having cross-sectional dimensions of 60 mm × 3 mm, a "filler" material which is currently creped cellulose fibre tissue, and a "cover" made from a plastic such as polyethylene. It is constructed by winding the tissue onto a 39 mm diameter cardboard tube out to a diameter of about 120 mm. Both the filler material and the tube are collapsed to the characteristic oval shape and then enclosed by the cover. In early designs the cover was made in the form of an extruded tube and only loosely fitted over the oval filler, but more recently it has been made from flat sheet wrapped tightly around the filler. Both the geometry and the materials contrast with the more conventional compliant air bearing which would consist of a block of elastomer such as a vulcanized rubber. Hence the unusual features are: (i) use of a creped cellulose material wound

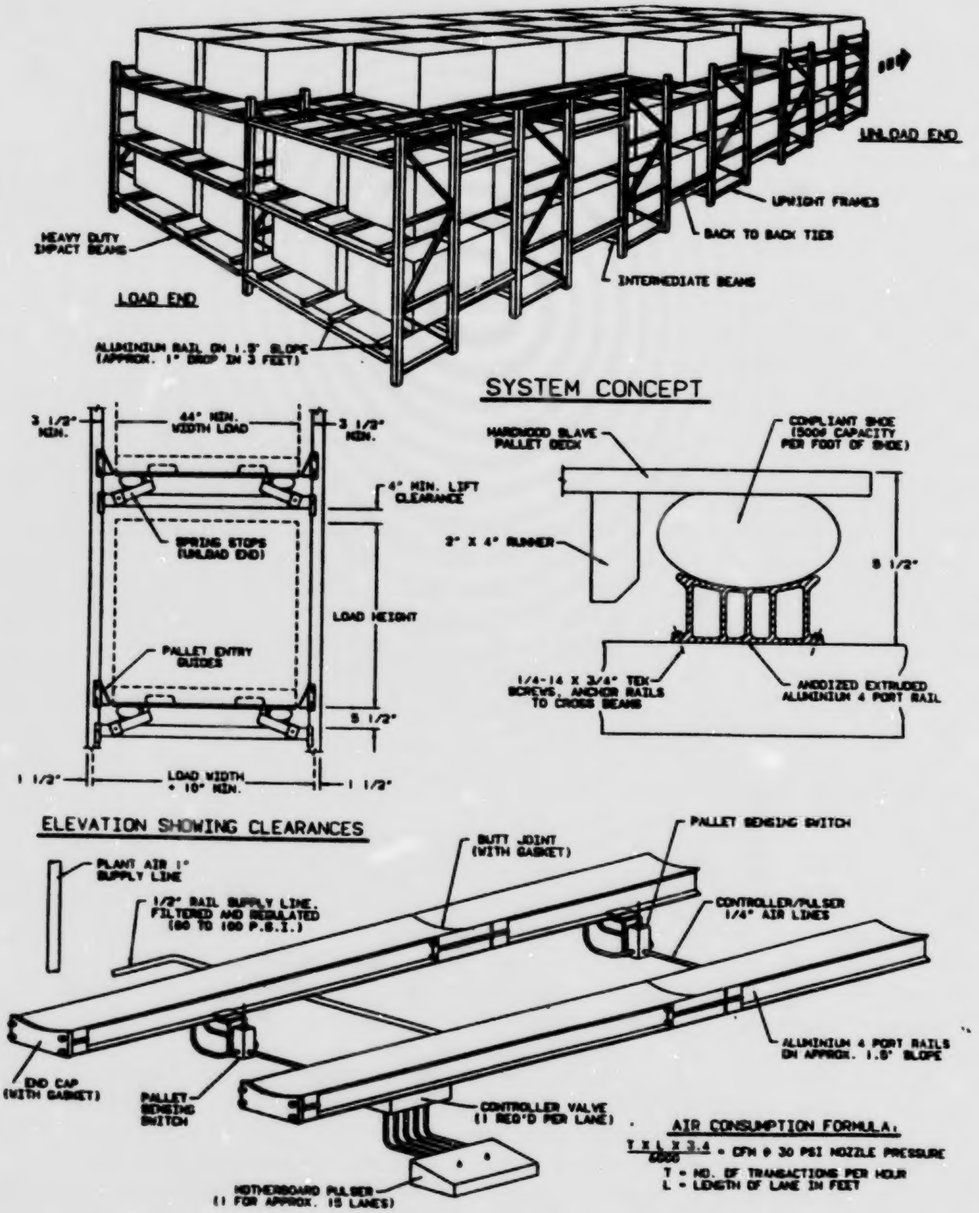
UNLOAD END
UPRIGHT FRAMES
BACK TO BACK TIES
HEAVY DUTY IMPACT BEAMS
INTERMEDIATE BEAMS
LOAD END
ALUMINIUM RAIL ON 1.5° SLOPE (APPROX. 1" DROP IN 3 FEET)
SYSTEM CONCEPT
3 1/2" MIN.
44" MIN. WIDTH LOAD
3 1/2" MIN.
4" MIN. LIFT CLEARANCE
SPRING STOPS (UNLOAD END)
LOAD HEIGHT
PALLET ENTRY GUIDES
5 1/2"
1 1/2"
LOAD WIDTH + 10" MIN.
1 1/2"
ELEVATION SHOWING CLEARANCES
HARDWOOD SLAVE PALLET DECK
COMPLIANT SHOE (500# CAPACITY PER FOOT OF SHOE)
2" X 4" RUNNER
8 1/2"
1/4-14 X 3/4" TEK SCREWS, ANCHOR RAILS TO CROSS BEAMS
ANODIZED EXTRUDED ALUMINIUM 4 PORT RAIL
PALLET SENSING SWITCH
BUTT JOINT (WITH GASKET)
PLANT AIR 1" SUPPLY LINE
1/2" RAIL SUPPLY LINE, FILTERED AND REGULATED (80 TO 100 P.S.I.)
CONTROLLER/PULSER 1/4" AIR LINES
ALUMINIUM 4 PORT RAILS ON APPROX. 1.5° SLOPE
END CAP (WITH GASKET)
PALLET SENSING SWITCH
CONTROLLER VALVE (1 REQ'D PER LANE)
MOTHERBOARD PULSER (1 FOR APPROX. 15 LANES)
AIR CONSUMPTION FORMULA:
$\frac{T \times L \times 3.4}{6000}$ = CFM @ 30 PSI NOZZLE PRESSURE
T = NO. OF TRANSACTIONS PER HOUR
L = LENGTH OF LANE IN FEET

Figure 2. Diagram of warehouse racking system as currently conceived.

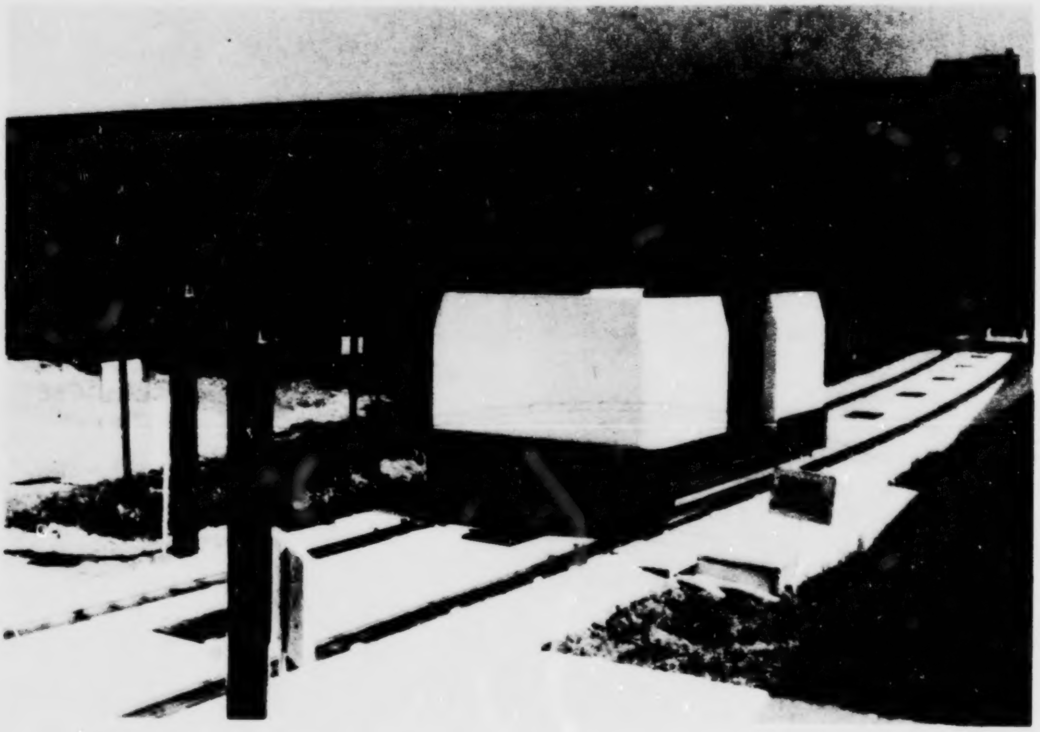

Figure 3 Early development prototype of low speed passenger transporter. The tops of the linear induction motor primaries can be seen. The motors and the air supply are automatically activated for short sections when the presence of the vehicle is detected by a photo-electric cell.

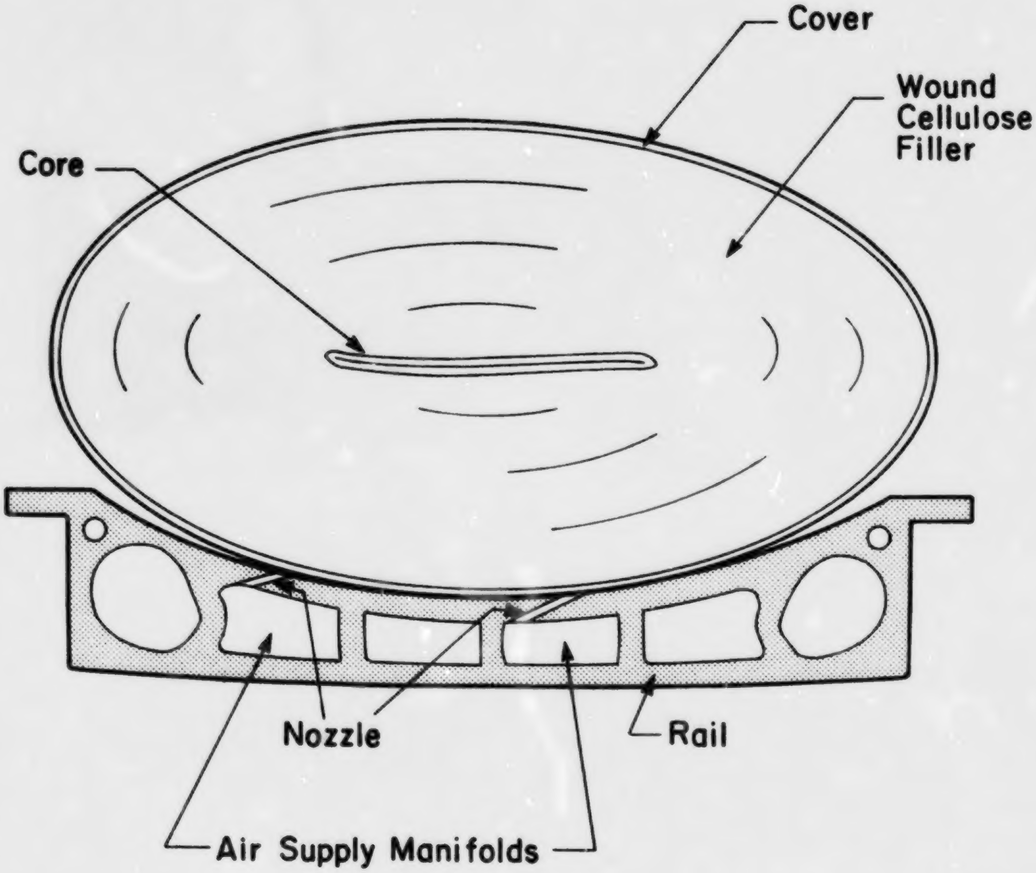
Cover
Wound Cellulose Filler
Core
Nozzle
Rail
Air Supply Manifolds

Figure 4. Cross section of SailRail shoe, or runner, and rail. The rail section is an early development prototype extruded from plastic.

under tension to provide comformability, resilience and vibration isolation, (ii) the core, which is believed to affect overall structural integrity, and (iii) the use of relatively thick covers to improve bearing action.

Consider now the second group of controversial features. The location of the nozzles as originally proposed by SailRail is shown in Figure C3 (p. 79). The concave or working surface of the rail has a radius of 6 ins or 152.4 mm, and was originally 152.4 mm wide. The nozzles were located in two rows at angular distances of +5° and -15° from the rail centreline, and spaced at 12 in (304.8 mm) intervals along the rail. The 0.026 in (0.66 mm) diameter nozzles were inclined at 20° to the tangent to the rail surface and were aligned at 45° to the rail axis. The 15° nozzles were pointed towards the centre of the rail, and their axes were aligned along those of the nozzles at the +5° location. This nozzle layout and geometry had originally been chosen to suppress a dynamic instability observed in an early development prototype, which used a single row of radially drilled nozzles located at the rail centreline. However, other than this, no clear rationale for the choice existed. The nozzle layout currently in use is also shown in Figure C3.

The design has other features which are either controversial or the way in which they function is unclear. For example, in all transportation devices, provision must be made for guidance and static stability. That is to say, when such a device is disturbed from its desired path of motion in any of the three axes of translation (surge, heave and sway) or of the three axes of rotation (roll, pitch and yaw), the suspension system must supply appropriate restoring forces or moments. In SailRail's case it seems clear that heave forces and rolling moments can be supplied by air bearing action, and that restoration forces in surge must, when required, be supplied by the propulsion and braking system. However in the original design, no explicit provision was made for air bearing action in sway, pitch or yaw. Hence a question of fundamental interest is the extent to which these restoring forces are supplied by direct shoe-rail contact as opposed to redistribution of the air pressure forces acting between shoe and rail.

An intriguing feature of the SailRail concept is its freedom from the phenomenon known in the air bearing literature as "pneumatic hammer". This is a dynamic instability which leads to potentially destructive self-excited oscillations, and compliant air bearings are especially prone to this problem; indeed it has been cited as a major obstacle to their use [21]. Only once in the entire development that has taken place since 1974 has it been observed. It took the form of a vertical oscillation of shoe and load at a frequency of the order of 2-5 Hz. Significantly, it occurred at a very high load, and when the shoe was an aluminium circular cylindrical segment onto which a 1.5 cm layer of tissue was held by the cover. It has been speculated that the damping properties of the large quantities of the tissue in the full oval shoe play a crucial role in suppressing the phenomenon.

Finally it has been observed by the developer that, on occasion acoustical tones of the order of 1 kHz were emitted by the shoes, and that when this occurred system performance improved significantly. This observation led to the speculation that the flow between shoe and rail could induce self-excited oscillations in the cover, which if it occurred in regions of contact between shoe and rail might reduce the effective coefficient of sliding friction.

1.4) Discussion of Research Strategy

Although the SailRail system appears to be very simple this appearance is in fact illusory. To obtain an understanding of the system sufficient to provide a good basis for product improvement one has to consider the fluid mechanics of the air flow processes between shoe and rail, the structural aspects of the shoe, the dynamics of the system, together with the interaction of all three. This is a formidable task. Indeed, although it is expected that SailRail will ultimately be described in terms of well established engineering principles, its complexity is such that one cannot expect to approach the task by simply writing down a set of equations for the entire system, solving them, and then comparing the results with data obtained from a prototype. The availability of modern digital computation methods notwithstanding, in our opinion such an approach is not likely to be feasible in the foreseeable future, so that development of a mathematical model appropriate for design improvement will require considerable simplification, which in turn must be based on good physical insights. For example, it is probably unnecessary to include all the details of the shoe structure when considering its interaction with the fluid mechanics. Thus an important part of the initial work is to provide insights leading to conceptual simplifications both for analysis purposes, and for development of research priorities.

Hence, as currently conceived, the research strategy involves three distinct phases. The first is the testing of a representative complete prototype to document the claims made by the developer. The second is, in parallel with this phase, to undertake a series of short preliminary investigations to provide an overall picture of the way in which SailRail functions, and to identify areas where detailed investigations are required. The final phase consists of these detailed analyical and experimental investigations. The end product is expected to be mathematical models that can be used as aids to design.

The progress described in this report is confined mainly to the first two phases, indeed the first is not yet complete.

1.5) Main Results of the First Research Contract

Prior to the commencement of the first Contract virtually nothing was known about the way in which SailRail functioned; typically the thickness of the air film between shoe and rail was unknown. Furthermore although, in conjunction with the first author of this report, the manufacturer had undertaken some developmental testing, no reliable data was available to document the significance of the unconventional features of the concept. Consequently, the first priority was the construction of a model of the complete system and the development of test techniques to obtain this information. The second priority was to obtain measurements of the gap and pressure distribution between shoe and rail, in order to guide development of an analysis. A complete model or prototype test-bed was built, and some progress on developing test techniques was made. However, only a limited amount of data was obtained, so that it was not possible to draw any clear-cut conclusions about the controversial features of the concept.

The measurements of the gap "h" between shoe and rail showed that this quantity was usually less than about 0.3 mm and, at the edges of the air pressure footprint, less than 0.05 mm, which contrasts with the standard nozzle diameter d = 0.66 mm (0.026 in). The pressure measurements showed substantial regions of constant pressure, and this implied that the velocity of the air should be small in these regions. However, they also showed that the width of the pressure footprint was substantially less than that of the shoe or rail, thus indicating that the geometry of either shoe or rail was not optimum.

The data on measured flow rates and gaps was used to obtain estimates of the reduced Reynolds number of the flow [Ref. 2, p. 109]. This indicated that, except in the immediate neighbourhood of the nozzles, the flow should be inertialess. Consequently pressure distributions between rail and shoe were computed using the compressible Reynolds equation for hydrodynamic lubrication ([1], and see Appendix K for a derivation) and assumed fixed gap distributions similar to those actually measured. Owing to the geometric complexity a numerical technique was used to obtain the solutions.

These calculations suggested that the fluid mechanics of the SailRail system might be divided into three distinct phases, each occurring in a separate region under the shoe [1]. The first encompasses the flow from the rail manifold through the nozzles and in the region under the shoe which is immediately downstream. This was designated the "entry region", and the flow processes involved are turbulent, compressible and, at high enough air supply (or "track" pressure, p_t), gasdynamically choked. As the air spreads out between shoe and rail, in a short distance the fluid speed becomes very small, and becomes effectively at rest. The pressure is constant in this region, so that it was designated the "cavity region" at air pressure p_c. It was thought that most of the lift force was generated by the pressure of the air in the cavity region. Finally, it was suggested that the air escapes to atmosphere from the cavity region through a narrow strip around the periphery of the cavity region. The gap between shoe and rail in this strip was thought to be much smaller than that in the cavity region so that it was designated the "seal region". However, this suggested classification was only tentative and one of the main aims of the present work was to establish its usefulness.

The question of static stability in pitch was explored briefly. Pressure measurements were obtained for a shoe to which a pitching moment had been applied, and these indicated that the system responded by redistributing the pressure, with the higher pressures occurring at the pitched-down end of the shoe. Some approximate calculations suggested that the redistributed pressure accounted for almost all of the applied moment.

1.6) Detailed Objectives of the Present Contract

The major tasks to be addressed under the present Contract were:

(A) Completion of fact-gathering research on the prototype test bed,

(B) Analysis of the fluid mechanics of the seal region,

(C) Investigation of the fluid mechanics of the entry region,

(D) Measurements of the structural properties of the shoe,

(E) Development of an overall mathematical model of the system in which the fluid flow processes are coupled to the structural aspects,

(F) Investigation of the pneumatic hammer and cover flutter aspects of the device.

Item (A) required continued use of the prototype test bed to provide empirical data on the effect of various parameters reported by the developer to have a significant effect on the system performance. The tests were to include:

(i) determination of the effect of nozzle location and spacing on system performance,

(ii) effect of nozzle geometry on system performance; this relates especially to comparisons between radial and inclined holes, but other geometries, such as contoured and chamfered inlets were to be considered,

(iii) a limited investigation of the sensitivity of the system performance to track misalignment and irregularities,

(iv) effect of shoe construction on system performance, especially in relation to the thickness and bending stiffness of the cover, size of core and stiffness and damping characteristics of the tissue,

(v) assessing the sensitivity of the system performance to applied lateral forces together with the effect that nozzle location may have on this sensitivity,

(vi) measurement of air flow under the shoe for various p_t required to obtain a given level of performance, so that power indices for different configurations can be computed,

(vii) determine the scale effects on system performance for pallet loads M_p ranging from 500 kg to 2500 kg,

(viii) obtain representative shoe footprint pressure distributions at two track locations only for an optimum geometry and pallet weights from 500 kg to 2500 kg, these results to include possible effects of shoe construction on width of the footprint,

(ix) development of a simplified shoe geometry which retains most of the performance characteristics of the currently used shoes, but which is amenable to analysis,

(x) measurement of system performance for shoes having steel shimstock covers of a thickness which has about the same bending stiffness modulus as the present high density polyethylene covers,

(xi) development of a simplified shoe configuration which gives a performance comparable to that of the full SailRail geometry, and which is more amenable to simple analysis.

Appendices C, D and J describe the results of this work. Also the data obtained to fulfill objective (vi) led to important insights into compressibility effects of basic significance. This data and its implications are described in Appendix O. An overview of the test-bed data and related work is given in Section 2.

The aim of item (B) was to develop an analysis of the air escape process in the seal region for smooth shoe covers in terms of assumed gap distribution profiles. This was to provide data on flow rates as related to cavity pressures and thereby, in conjunction with data obtained for the shim-stock covered shoes give an indirect estimate of minimum gaps. The work is described in Appendix A and Section 3.3.

For item (C) the overall aim was to use a scaled-up model of the entry region to provide data on such basic properties as pressure loss coefficients, and the effect of the nozzle inclination angles and other parameters on these basic properties. This work is described in Appendix B and Section 3.2.

The investigations undertaken for item (D) were limited in scope; they are described in Appendix H and Section 3.5. Data on the stiffness properties of the tissue and overall shoe was obtained. Particular emphasis was placed on the effect of repeated loading, and some data on stress-relaxation effects was also obtained. Part of the objective was to provide data for the calculations planned for item (E), but the repeated loading and stress relaxation tests were also intended to give insights into the data obtained for item (A). Also the manufacturer has used for the filler material several types of tissue, each having a different composition. He has reported significant differences in performance, which he attributed to the differences in tissue composition. Consequently the stiffness properties of samples of these tissues were measured in an attempt to relate this property to performance differences.

For item (F) two analyses were planned. The first was a linear dynamic analysis of the system similar to those carried out for air cushions or air bearings to predict the onset of dynamic instability; the analysis is given in Appendix G. For the cover flutter analysis, an approach similar to that used to explore aerodynamic panel flutter was used. This exploratory analysis is given in Appendix I.

1.7) General Comment on Progress

It was initially envisaged that the "fact-gathering" testing of the prototype would occupy only a limited period of time, perhaps three months. However, owing to difficulties in repeatability that were encountered, this aspect required much more work, indeed it was never satisfactorily resolved in the Contract period. However, some reliable data was obtained. Needless to say this had an adverse effect on progress in other areas. For example, in the absence of reliable data from the test-bed it was decided nevertheless to proceed with item (C), scaling only Reynolds number effects and not compressibility effects. The full significance of the compressibility effects in the nozzle region was not discovered until the end of the Contract Period, and the analysis and interpretation of the data given in Appendix D not undertaken until relatively recently.

These and other difficulties notwithstanding, considerable progress has been made, and a coherent overall picture of the way in which SailRail functions is now beginning to emerge.

2) RESULTS FROM PROTOTYPE TESTING

2.1) Apparatus

The prototype test bed built during the previous contract was used for this work [1]. Basically this test bed is just a 3.05m long section of SailRail track on which a standard pallet of known total mass M_p can move under the action of a driving weight whose mass M_D was usually between 1% to 2% of M_p. To obtain a high level of rigidity the rails were mounted on 0.25m × 0.25m I-beams. Air flow rates were measured with accurately calibrated industrial rotameters [1]. This test bed was also used to obtain the visualization of the air flow between shoe and rail described in Appendix J. Also, owing to the repeatability problem noted above, instead of installing pressure taps in the test bed, a separate apparatus was built. This apparatus, which used only a single shoe and included some simple alignment devices, is described in Appendix D, along with the results.

During the first contract the performance criterion used to evaluate SailRail was the track pressure p_t required to initiate motion under the action of a known driving weight [1, Fig. 29]. For the present work the criterion was changed to the time required to travel over a known distance. It was envisaged that this would average out the effects of irregularities in the surface geometry of the rail and in coefficients of sliding friction for any combination of rail and shoe cover. This criterion also provides results of direct interest to the designer, since the data can be used to estimate an equivalent coefficient of sliding friction, or possibly the fraction of the load carried by air pressure.

In this connection, it should be noted that when p_t is just high enough to initiate motion, a significant fraction of the load, perhaps as much as 10%, is still carried by direct shoe-rail contact. Indeed the test data in Appendix C suggests that p_t has to be increased by as much as threefold before contact between shoe and rail is virtually eliminated. This implies that, unlike some air bearing or air cushion concepts, under normal operating conditions there is always partial contact between shoe and rail. Some applications of SailRail rely on this partial contact to provide braking. For the present work it implies that the test bed results are very sensitive to the coefficient of sliding friction between shoe cover and rail. Therefore to assist in the interpretation of test bed and other data, the relevant literature on the sliding friction of polymers was surveyed, and a short review is given in Appendix E. Also some measurements of sliding friction coefficient for various shoe-rail combinations were made, and these are described in Appendix F.

2.2) Factors Influencing Results

In development work undertaken by SailRail prior to the UTIAS research efforts, test results obtained from prototypes had generally suffered from a lack of repeatability. It was originally thought that this was mainly caused by flexure of the rails under load. Consequently the test-bed built during the previous Contract was designed to eliminate this effect as far as possible. However it was soon found that, in addition to flexure of the rail support system, other unidentified factors had a major effect on results. Over a period of time a clear pattern emerged suggesting three major causes:

(i) Variations in the coefficient of sliding friction between shoe and rail associated with the use of a variety of shoe and rail materials and with variations in ambient temperature,

(ii) Viscoelastic or stress-relaxation effects in the shoe filler material which caused the system performance to substantially improve over a period of days or weeks,

(iii) A much higher sensitivity of the system to alignment of the shoes during installation under the pallet than had been originally supposed.

The first problem is to be anticipated for different material combinations. However, both the viscoelastic effects and alignment problems made the task of obtaining meaningful comparisons between certain properties that required change of shoe filler or cover extremely difficult.

2.3) Main Results Obtained from Test-Bed

In spite of these difficulties, some reliable results were obtained. Perhaps the most reliable were those relating to nozzle geometry and layout, since it was possible to change these features without disturbing the shoe in any way, and to take the measurements over a relatively short period of time. Two basic nozzle patterns were tested, that originally specified by the manufacturer, and known as the "original standard", shown in Figure C3 (p. 79), and a second, which used only one row of nozzles at the 5° location, but with the same number density per unit length of rail. The latter layout, shown also in Figure C3, was investigated as a direct result of the flow visualizations described in Appendix J, which suggested that the 15° row of nozzles was contributing little to the air lift process (Fig. J3, p. 190). The basic test results are plotted in Figure C13, p. 93. They show that the single row gives superior performance. This pattern was adopted by the manufacturer and is now designated "new standard". It has allowed alteration of the geometry of the rail section to simplify problems of air distribution and to improve other aspects of the design. It played a role in the evolution of Section VII (Figure M8, p. 216) and its successor, Section VIII.

Data on the effect of using radial nozzles was obtained, and the comparison is given in Figure C14 (p. 94). It suggests that nozzle diameter has to be increased from 0.66 mm to about 1.02 mm (0.040 ins) to obtain comparable transit times. This has important consequences which are discussed in Section 3.2.3 and Appendix O.

Reliable data was also obtained for the effect of an applied lateral force, cover thickness, pallet weight, and load magnitude and distribution. For the lateral force tests the new standard nozzle pattern was used and, as shown in Figure C16 (p. 96), for both rails, the nozzles were located on the same side of the rail centreline with their axes oriented away from the centreline. The lateral force was obtained by inclining the test-bed at a series of angles up to 0.924°, corresponding to a maximum force of 1.61% of the load, with a positive inclination corresponding to the force acting towards the side of the rails on which the nozzles were located. The data is given in Figures C16 and C17 (pp. 96 and 97). It showed little change when the load was forced towards the nozzles, but in marked contrast, a systematic deterioration occurred as the force was increased in the opposite direction. This suggests that when it acted towards the nozzles, the applied force was counterbalanced almost entirely by a redistribution of air pressure forces with little or no increase in shoe-rail contact forces, whereas a lateral force acting in the opposite direction caused a marked increase in contact forces. Unfortunately, since in these tests the nozzles were oriented in the direction of positive applied force one cannot, on the basis of these results alone, ascertain the relative importance of nozzle orientation and location in creating this effect. However other results, such as the flow visualization in Appendix J, suggest that orientation has only a local effect. Nevertheless this important result indicates that, in a well designed system, sway and yaw forces for guidance and stability can probably be provided by air pressure rather than by direct contact between shoe and rail.

The data on cover thickness effects is given in Figure C18, p. 98. The repeatability problem made this data the most difficult to obtain, but in spite of this a sufficient number of observations was accumulated to allow demonstration of an effect. It shows that as cover thickness was increased in steps from 0.15 mm (0.006 in) to 1.52 mm (0.060 in) systematic reductions in transit time occurred. Now it is expected that an optimum cover thickness exists since beyond a certain value, the rapidly increasing bending stiffness must inhibit bearing action. However this was not found.[1]

The effect of total pallet weight and asymmetric loading was also explored briefly, and the data obtained is given in Figures C20 and C21. (pages 101 and 102). When pallet load was increased in steps from 401 kg to 1302 kg it was found that at any given p_t above 100 kPa no reductions in transit time occurred. In Section C7 is is suggested that this behaviour might be caused by gasdynamic choking. The tests on asymmetric loading showed that side loading, corresponding to application of a rolling moment, caused no appreciable deterioration in performance, whereas front or back loading, corresponding to application of a pitching moment, did. This suggests that, as anticipated in section 1.2, rolling moments were accommodated by bearing action, whereas pitching moments can cause some increased shoe-rail contact.

---

[1] Tests performed after the contract period indicate that for thicknesses in excess of 1.65 mm, performance rapidly deteriorates.

Data on air consumption and power were also obtained; these are discussed in Appendix O and Section 3.3.

2.4) Principal Results from Pressure Measurement Apparatus

The apparatus used for measuring pressure distributions is described in Section D1. Rail section V and the new standard nozzle pattern was used for these tests. The layout of the pressure taps (Figure D3, p. 114) consisted of a single transverse row located midway between two nozzles. Generally the results obtained supported the observations made from the prototype test-bed, and provided some useful insights.

There was clear evidence of a conditioning process in which pressure distributions would become more uniform with the passage of time (see Figure D6, p. 119). Furthermore, use of a simple shoe alignment bracket could reduce this time. Since the apparatus applied a constant load during the conditioning process, the data in Figure D6 implies that the fraction of the load carried by direct air pressure increases with time; this explains the improvement in performance observed on the test bed (Figure C8, p. 85). The data on the properties of the tissue filler discussed in Appendix H suggest that creep or stress-relaxation phenomena in the tissue cause the shoe to slowly flow into improved conformity with the rail geometry. If this is the case, it suggests that the shoe geometry is not quite optimum, because if it were, there would be a reduced tendency to flow, and thus a shorter conditioning time. The pressure measurements also confirmed the existence of a cover thickness effect and gave a basic insight into a possible mechanism. They showed that it was related to the bending stiffness of the cover, and not to an improved match of shoe and rail geometry. The implications are discussed in Section 4.2.

Finally some pressure distributions were obtained with the shoe displaced laterally, first towards the side of the rail on which the nozzles were located, and then away. The displacement was 4 mm, or about 3.4% of the width of the curved part of the rail. In the first case the load carried by air pressure decreased to 82%, whereas in the second it decreased to 68%. This result is again consistent with the observations obtained on the test bed.

3) FLUID MECHANICAL ASPECTS

3.1) Overall Classification

The evidence accumulated during the present Contract shows that the classification of the flow processes under the shoe into the three regions suggested in Ref. 1 provides a useful global picture of the fluid mechanics.

For example, the pressure profile measurements described in Appendix D all show substantial regions of constant pressure, thus strongly supporting the idea of a cavity region in which the air is effectively at rest. For properly aligned and conditioned shoes the cavity region may occupy a large fraction of the width of the rail. Typically, in the profiles in Figure D15 (p. 132) the constant pressure region occupies a width of 85 mm or 72% of the available track width. In Figure D13, p. 128, for the centrally aligned shoe, this width is about 82 mm. Also one of the most striking features of the flow visualization in Figure J4 (p. 191) is the behaviour of the streamlines near the edges of the flow pattern; no matter what orientation they have in the interior, they leave the cavity region at right angles to the sides of the shoe. This implies that, before entering the seal region, the speed of individual fluid particles must be very low.

When a nozzle is under a shoe, a typical Reynolds number for the flow through it is 10^4, so that in the entry region the flow is initially turbulent. Furthermore, since a typical cavity pressure p_c is 50 kPa and the rail manifold pressure p_t is usually about 150 kPa the absolute pressure ratio across the entry region is about 0.6. Hence the flow is compressible and, for very high p_t may even be gasdynamically choked. However, the extent of the nozzle region may be very small; the pressure measurements on the scaled up model described in Appendix B suggest that it extends no more than 4 nozzle diameters or 3 mm away from the nozzle.

3.2) Entry Region

3.2.1) General Approach

The main results of the studies of the entry region are described in Appendices B and O, and additional supporting work is described in Appendices L and N. As discussed in Section B5, complete reproduction in a large-scale model of the dynamics of the cavity region requires scaling of both viscous and compressibility properties of the fluid flow processes, and of the elastic and other structural properties of the shoe cover and filler. However it appears to be impossible to simultaneously reproduce both Reynolds number and compressibility effects in a model which is much larger than the original. Now the Reynolds number of the flow in the nozzles was estimated to be in the range 0.5×10^4 to 3×10^4. Hence, since the flow in the cavity and seal regions is believed to be inertialess (see Section A2), a reverse transition from turbulent to laminar flow must occur at the downstream boundary of the entry region. It was therefore felt that in our first attempts the Reynolds number should be scaled, and detailed investigation of compressibility effects should be delayed until suitable data was obtained from the prototype test-bed. This decision was reinforced by the fact that SailRail systems had been observed to operate at very low values of track-cavity pressure difference.

A key objective of the work was to investigate the effect of nozzle inclination angle since the manufacturer has indicated that practical considerations continue to make the use of inclined nozzles desirable. Currently 0.026 in (0.66 mm) diameter mechanical twist drills are used to make the nozzles, and the work is difficult and time consuming. Even a moderate increase in inclination angle, perhaps to 30°, would considerably alleviate the problem.

3.2.2) Results from Scaled-Up Models

Two models were used to obtain the data described in Appendix B. The first was used to obtain head losses and pressure distributions for both 20° inclined and radial nozzles. The second was used to examine the effect of nozzle inclination angle on head losses, both at the entrance from the rail manifold to the nozzle, the so called "nozzle entry" region, and from the nozzle to the cavity, or "cavity entry" region (see Section B2). In these results the basic geometric parameters are the nozzle inclination angle θ and the ratio h/d of the local shoe-rail gap to nozzle diameter. In the cavity region, $0.1 < h/d < 0.5$ approximately, whereas in the seal region, $h/d \approx 0.025$ or less. It was originally suggested that, for $h/d \ll 1$, the area controlling the flow processes in the entry region was not the nozzle cross-sectional area $A_{r1} = \pi d^2/4$, but the area A_{r2} of the cylindrical surface of height h generated by the nozzle periphery. For a 20° nozzle, $A_{r2} = 6.54$ dh, or about twice that of a sharp-edged radial nozzle, which is $A_{r2} = \pi dh$. Hence it was speculated that one explanation of the superior performance of the inclined nozzle might be that, when compared with sharp-edged radial nozzles, they offer less resistance to the flow. Typical data is given in Figure B6 (p. 48), which compares the head losses of inclined and radial configurations at $h/d = 0.109$. It shows that at any given volume flux the inclined nozzles incur about one third of the pressure drop of the radial nozzles. However, if the sharp edge of the radial nozzle is removed as shown in Figure B3 (p. 45) to produce the contoured or diffuser radial nozzle, the resistance of the radial nozzle becomes very small indeed.

Figures B7 to B10 (pp. 50-53) give the head loss data for the radial and inclined nozzles expressed in nondimensional form, in order to permit scaling to the prototype size. A flow coefficient C_Q is defined, $C_Q \underline{\Delta} Q/V_rA_r$ where the reference velocity V_r is that corresponding to the total head of the flow in the nozzle. When $A_r = A_{r1}$, then $C_Q = C_{Q1}$, and when $A_r = A_{r2}$, then $C_Q = C_{Q2}$. Note that an increase in either C_Q corresponds to a reduction in head loss, and C_{Q1} is related to the usual loss coefficient K_o used in presenting data on head losses in pipes through the formula $K_o = 1/C_{Q1}{}^2 - 1$. Dimensional analysis considerations described in Section B5 indicate that, with compressibility effects omitted, the flow coefficients should be a function only of Re_d, h/d and θ, with the effect of nozzle size occurring only indirectly through the definitions of C_Q, Re_d, and the ratio h/d.

The data for C_{Q1} is given in Figures B7 and B8 for 20° inclined nozzles and sharp-edged radial nozzles respectively; it is presented as a function of Re_d and for three representative values of h/d. This data is essentially independent of Re_d. Now it is well known that head losses in such pipe fittings as valves or abrupt turns are Reynolds-number independent if the flow is turbulent; this fact suggests that for SailRail nozzles almost all of the head losses occur in the turbulent part of the flow. This in turn implies that in future model tests of the entry region, Reynolds number need not be scaled.

Table B1 (p. 54) gives a comparison of the flow coefficients for inclined and sharp-edged radial nozzles at a representative Re_d. It shows that, at $h/d = 0.109$, the inclined nozzle is substantially more efficient, but as h/d increased towards 0.5 the advantage all but disappears. The data obtained on the effect of nozzle inclination angle, given in Figures B12 to B14 (pp. 56-58) is consistent with this. It shows that, for nozzles located well inside the cavity region, increasing θ from 10° to 90° has a negligible effect on head losses, whereas at $h/d = 0.11$, corresponding to the edge of a cavity region, the losses are very sensitive to θ, typically the losses increase by a factor of 7 to 8 as inclination angle increases from 10° to 90°. Thus there is a clear advantage for nozzles in this region.

A computer programme for the numerical solution of incompressible turbulent flows, developed for another project, was used to compute flow patterns for the sharp-edged radial nozzles. (The inclined nozzle geometry is beyond the scope of presently available methods.) The results, for $h/d = 0.5$ and 0.25 are given in Figures B15 (p. 59) and B16 (p. 60) respectively. The main feature of the flow is the separation at the nozzle edge leading to the formation of a toroidal eddy downstream. The fluid not recirculating in this eddy is forced to accelerate through a nozzle formed by the separation bubble and the opposite wall. The subsequent deceleration of the flow as it spreads out to fill the space between the upper and lower discs of the model is associated with considerable turbulence and viscous dissipation, and with a significant pressure rise. An approximate analysis of the head losses for this configuration, applicable in the limit $h/d \to 0$ is given in Appendix N. It is based on the assumption that all of the head losses occur in the decelerating turbulent flow just downstream of the eddy. It gives estimates of C_{Q1} and C_{Q2} which are independent of Re_d and in reasonable quantitative agreement with the measured data for $h/d = 0.109$. This confirms the suggestion made above that the subsequent transition to inertialess flow that must occur as the flow spreads out into the cavity region plays no significant role in the fluid mechanics.

Measured pressure distributions for the sharp-edged radial nozzle are given in Figures B17 to B20 (pp. 62-65), and those for the inclined nozzles are given in Figures B21 and B22 (pp. 67 and 68). Figures B19 and B20 also include predicted pressure distributions. They show Reynolds number independence and regions where the pressure is substantially below that further downstream, as predicted by the theory. Figure B18 shows that the magnitude of this low pressure (or "suction" relative to cavity pressure) increases rapidly as h/d decreases. The pressure distributions for the inclined nozzles have a more complex structure, but they also exhibit smaller regions of suction. It is thought that these suction forces may play a role in the cover thickness phenomenon, which is discussed in Section 4.2.

3.2.3) Compressibility effects in the Entry Region

The compressible flow phenomenon of main interest is gasdynamic choking in a nozzle whereby, once a certain critical pressure ratio across the nozzle is reached, any further reduction in downstream pressure cannot cause an increase in mass flux through the nozzle. Data obtained towards the end of the contract period and shown in Figure C19 (p. 100) indicated that, at the values of p_t used in practise, which are about 140 kPa or 20 psi, the nozzles were, or very close to being, choked. However the full implications of this, which are described in Appendix O, were not investigated until after the end of the contract period.

The question of major practical interest is: Where does the choking occur? Generally this must be at the point of minimum flow area, and consideration of the SailRail geometry suggests two likely sites: the vena contracta formed at the nozzle entrance (point 1 in Figure B1, p. 42), and in the nozzle exit region (between points 2 and 3 in Figure B1). The latter is expected to occur for sufficiently small h/d. If it occurs at the first point then, according the inviscid fluid theory, when nozzles become uncovered owing to passage of a pallet or vehicle along the track, there will be no increase in mass flux through the nozzles.

The data comparing mass flow for covered and uncovered nozzles is given in Figure O.5 (p. 230). Included in this comparison are measurements for sharp-edged radial nozzles of 0.508 mm (0.020 cm), 0.711 nmm (0.028 cm) and 1.016 mm (0.040 cm) diameter. It shows that at p_t = 140 kPa (200 psi) the 0.66 mm inclined nozzles are close to choking when covered by a pallet having a typical load. This implies that, when uncovered their flow increases by only 9%. In contrast, the 1.016 mm radial nozzles, which have 130% more cross-secional area, deliver only 7% more mass flow at 140 kPa, yet when uncovered their mass flow increases by a factor of 2.4. This and other aspects of the data, discussed in detail in Appendix O, clearly show that the inclined nozzles choke at the nozzle entrance, whereas the 0.711 mm and 1.016 mm radial nozzles choke at the exit when covered.

These results and those described in Appendix B have certain important implications. First it should be observed that, owing to the work required to compress air, transmission of air at pressures substantially higher than that required to levitate the load involves a significant power penalty. Calculations given in Appendix O suggest that, for a typical cavity pressure p_c of about 50 kPa, delivery of air at p_t = 140 kPa requires an installed power of about 11.2 Watts/nozzle. If the air is delivered at p_t = 60 kPa, or 10 kPa above p_c, the data in Appendix B can be used to show that a nozzle diameter of 1.23 mm is required. However owing to the reduced work of compression, the power is only 5.75 W/nozzle. Of course when this nozzle is uncovered, since it is not choked, the power per nozzle increases significantly, but only to 11.9 W/nozzle.

Now the air power requirements for SailRail are already so low that for systems in which the air is compressed centrally at one or a few locations, the economics of the system may dictate air transmission at relatively high p_t, simply in order to cut capital costs. Hence in such cases inclined nozzles should continue to be used to minimize air losses from uncovered nozzles, especially if significant fractions of the track are uncovered at any given time. However, it is envisaged that some applications may involve compression of the air on board the moving element and transmission through the shoe. Such systems will not normally operate with any nozzles uncovered so that, to minimize power and compressor weight penalties, large diameter contoured radial nozzles of the type discussed in Appendix B should be used.

3.3) Seal Region

The analysis of the flow through the seal region in Appendix A assumes that the flow is inertialess, that the surface roughnesses of shoe and rail are much smaller than the minimum gap, and that the streamlines pass through the seal region at right angles to the line of minimum gap, or sides of the shoe. The last assumption was suggested by the analysis of Appendix K (see Figure K6, p. 201). With this simplification the flow becomes two-dimensional and the resultant equations can be integrated analytically.

One of the most difficult quantities to measure is the minimum gap h_s between shoe and rail that occurs in the seal region, and thus far no direct measurements have been obtained. Hence a major objective of this work was to use measured flow rates and such data on gap distribution as was available to infer this quantity. The data suggested that typical values of h_s were of 0.017 ;mm (0.67×10^{-3} ins). Attempts to validate this computation by measuring the effect of flow rate on displacement of a loaded shoe, described in Section D.7 (p. 129), were complicated by shoe deformation effects and alignment difficulties. Nevertheless, allowing for these difficulties, the agreement between theory and experiment shown in Figure D.17 is reasonable.

The theory in Appendix A also suggested a simplified form of the dependence of flow on minimum gap and cavity pressure, which was used in the stability analysis of Appendix G.

The theory has one major limitation. In Section A6 it is observed that over 50% of the computed pressure drop from shoe cavity to atmosphere occurs downstream of the point of minimum gap, and thus where the air passage is diverging. At some point in this divergent passage flow separation from the cover must occur, and beyond this point no further pressure drop could occur (see Fig. A2, p. 30). Since flow separation involves fluid inertia, the present inertialess analysis is incapable of predicting it. It has been simply assumed that the separation occurs well downstream of the point where significant pressure decay occurs. In view of the relevance of this theory to the stability calculations, and to the possibility of simplifying the overall bearing calculations described in Appendix K, its validity should be checked.

4) STRUCTURAL ASPECTS

4.1) Properties of Tissue

Measurements of the stiffness properties of samples of tissue and complete shoes were obtained from compression tests in the UTIAS Tinius-Olson test machine, and the results are described in Appendix H. The samples of tissue were subjected to repeated loading and unloading, and they showed permanent deformation, nonlinearity, static hysteresis and stress relaxation. Almost all of the permanent deformation occured during the first cycle of loading and unloading, so that the hysteresis was largest for this cycle. In a typical test the stiffness varied from about 170 kPa near zero load to about 205 kPa at a working load and 250 kPa at the highest value tested. In the first loading-unloading cycle, over 50% of the total work done can be absorbed by hysteresis, but this drops rapidly to 30% and less for subsequent cycles. The permanent deformation in the first cycle was to about 30% of the total initial compression. In the stress-relaxation tests, the samples were subject to a known fixed amount of compression, and the load decreased by about 10% in ten minutes. Presumably this effect would manifest itself as creep in the constant load case, which is the typical SailRail application. Collapsed rolls taken from shoes which had been in use were also compressed and showed similar overall characeristics, typically the work absorbed by hysteresis was about 30%.

The presence of creep would explain the improvement in performance with time, or conditioning, observed in the prototype testing. Measurements of shoe deformation over an extended period by E. B. Eddy Forest Products indicated that creep could take place for several days and longer [23]. Also the hysteretic damping could play a key role in explaining the large discrepancy between prediction and observation of the dynamic stability properties of the system. This point is discussed in Section 5.2 and Appendix O.

Now sigificant variations in the performance of systems operating in the field have been observed by the developer, and he attributed these to differences in composition of the tissue used in these applications. Samples of some of the tissues were subject to compression tests in an attempt to relate stiffness properties to observed behaviour. No consistent pattern was found, indeed the data demonstrated the difficulty of using largely subjective field observations. For example some samples, designed as "hard" in field observations, when tested at UTIAS, were found to be relatively soft. The literature on the structural properties of wound paper rolls was examined, and we concluded that other factors such as the tension of winding, which were not controlled in the experiments, could be very important.

4.2) Effect of Cover Thickness

One of the intriguing features of the SailRail concept is the effect of cover thickness on system performance, and the mechanism or mechanisms by which this occurs. One possibility, suggested by the data in Appendix B, is the so called "suck-down" effect. The pressure measurements obtained for the sharp-edged radial nozzles show that, relative to the force exerted on the shoe by the cavity pressure, fluid mechanical effects can generate a significant suction force (Section B10). For materials such as tissue, which have very small bending stiffness, this suction force might decrease h locally, thus increasing hydrodynamic losses. This effect could conceivably be very large since the data in Figure B18 (p. 63) shows that any reduction in h substantially increases the suction pressures. Hence it was speculated that the presence of a relatively stiff barrier between the tissue and the air flow might impede the "suck-down" effect. It was also speculated that one benefit of the use of inclined nozzles is a reduction of this suction force. The data in Figure B22 p. 68) was not integrated to check this, however some exploratory flow visualizations shown in Figure B24 (p. 72) suggested that, at least for the scaled up model, suck-down in the presence of inclined nozzles could occur.

One test of the hypothesis is to compare air flow rates as a function of track pressure for different cover thicknesses. If the thicker covers can significantly reduce hydrodynamic losses, then at a given p_t and pallet load the flow rate through the nozzles should increase as cover thickness increases. Data obtained from the prototype test bed (see Figure C19, p. 100) for cover thicknesses in the range 0.61 mm (0.024 in) to 1.321 cm (0.052 in) shows no increase in air flow rates as thickness increases. Unfortunately no data was obtained for very thin covers or even in the absence of a cover. Thus the effect cannot be ruled out, however since the test bed data given in Figure C18 (p. 98) shows that performance continues to improve as cover thickness increases from 0.15 mm (.006 ins) to 1.52 mm (.060 ins), another mechanism must be present.

The data in Appendix D suggests this second mechanism. In tests in the pressure measurement apparatus described in Section D5 a cover was placed between a collapsed tissue roll and rail but not wrapped around the shoe. With the shoe loaded, pressure measurements were taken. Then the cover was bent downwards to partially simulate the wrapping process. For the 1.52 mm (0.060 in) cover it was found that the width of the cushion pressure footprint increased significantly, thus increasing the fraction of load carried by air pressure (see Figure D10, p. 124). Similar results were obtained when an 0.020 mm (0.008 in) steel shim-stock cover was used. The latter test confirmed that the crucial quantity was the bending stiffness of the cover, and not simply an improvement in shoe-rail radius match.

Hence it is concluded that the bending stiffness of the cover modifie the response of the shoe in such a way as to increase the width of the cushion footprint However, the details of the way in which this occurs are not understood.

4.3) Modelling of the Shoe for Air Bearing Calculations

One of the ultimate objectives of the structural testing is to provide a model for the compliant air bearing analyses described in Appendix K. Ideally, one would expect to use data obtained in uniaxial compression tess on samples of tissue and tension tests on cover material to predict the overall load-deformation characteristics of the shoe. The structural analysis would have to include consideration of properties of the tautly wound tissue roll before it is collapsed to form the oval shoe, the effect of the collapse process, and the presence of the flattened core and bent cover on the stress distribution in the finally formed shoe. Figures 5 and 6 give a visualization of the compression that the tissue undergoes when a roll is collapsed to form the shoe. It is evident that the amount of compression varies widely throughout the shoe, indeed in some places, such as adjacent to the middle of the core, the tissue may be partially unloaded. It has been concluded that, in view of the complex properties of the tissue and of the geometry of the final shape, a computation of stiffness properties of the shoe from first principles is beyond the scope of the present programme. Consequently, an alternative solution was sought.

This alternative approach was to choose a geometry which would be more amenable to analysis, but which would retain the features essential to the iar bearing phenomena involved. The geometry finally chosen is shown in Figure C22 (p. 104). It consists of a rigid block of width equal to that of the rail, with the lower portion a circular segment having a radius slightly less than that of the rail. The tissue was to be modelled by a layer of

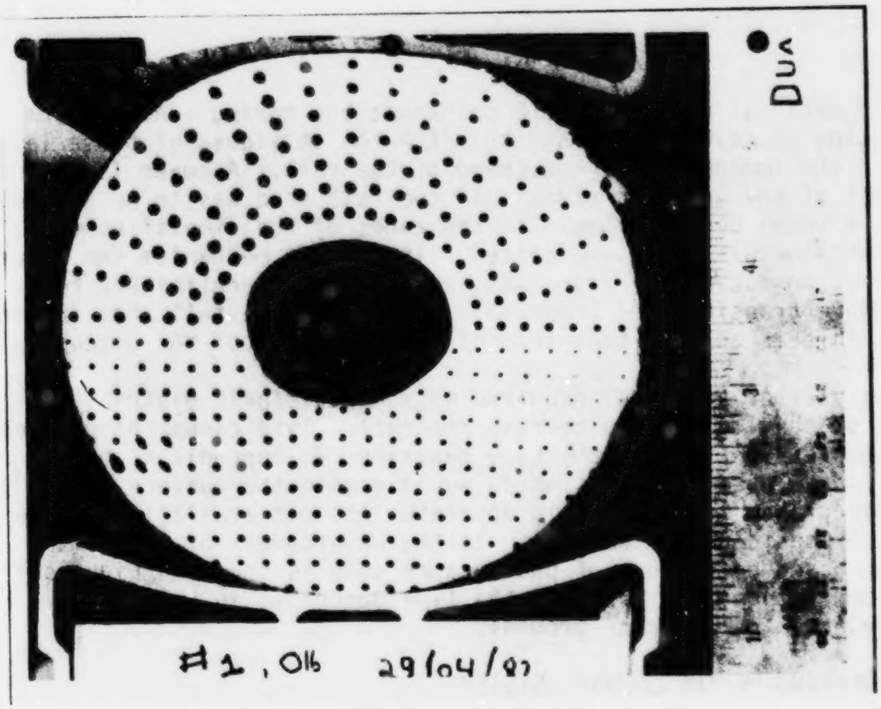
DUA
#1 , 0lb
29/04/8

Figure 5 Wound cellulose paper roll prior to collapse to form a shoe.

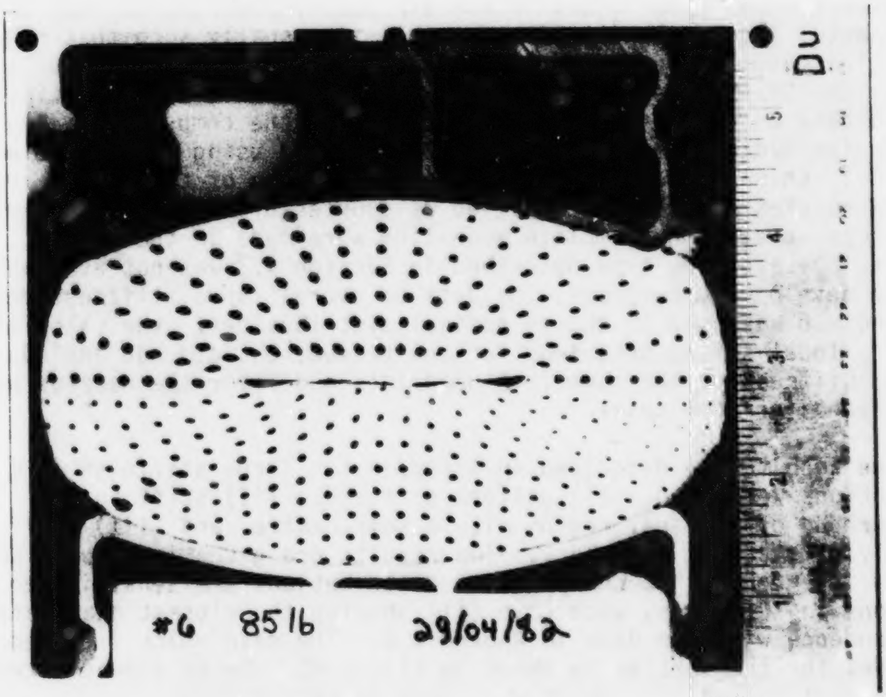
Du
#6 85lb
29/04/82

Figure 6 Wound cellulose paper roll after collapse.

compliant material having uniform thickness but having a nonuniform distribution of stiffness chosen to match the stiffness of those layers of tissue in the immediate neighbourhood of the rail. A cover is included, and the effect of the wrapping process in the full shoe was to be simulated by applying a known bending moment to the edges of the simplified shoe. A simplified shoe was built and tested, although no mechanism for adjusting the bending moment at the edges was included. The preliminary tests showed that it gave transit times comparable to that of the full shoe (Figure C23, p.105). This is an important test of the viability of the concept.

Analyses of the model requires data on stiffness distribution across the face of the loaded shoe nearest the rail. This cannot be obtained in a single compression test of the type described in Appendix H, but requires a specially developed apparatus which would enable the surface of the loaded shoe to be probed locally. This apparatus was not available for the present Contract. Consideration was given to the development of an optical technique based on the use of photographs such as those in Figures 5 and 6, and uniform compression tests of the type described in Appendix H. However, it was rejected on accuracy grounds.

5) MODELLING OF THE OVERALL SYSTEM

5.1) Air Bearing Calculations

In a complete compliant air bearing analysis, the pressure and gap distributions have to be determined by simultaneous solution of two sets of equations, the first set describing the structural properties of the compliant element and the second, the fluid mechanics. The model also has to account for pressure losses in the air supply passages if they are significant. The complexity of the problem is usually such that numerical computation must be used, especially if the geometries are complex as is the case for the SailRail system. For the first Contract, as a starting point, measured data on gap distribution was used, and the compressible Reynolds equation for hydrodynamic lubrication were solved using a finite element technique; this allowed a realistic representation of the nozzle locations. Also the nozzles were simply modelled as sources of known constant pressure air. Steps towards the complete modelling were made in the present Contract. Data of the type described in Section 4.3 was not available, so that for development purposes, the data on overall shoe stiffness described in Appendix H was used to choose nominal distributions. the calculations assumed a local spring behaviour for the tissue, but did not include the bending stiffness of the cover. A head loss model for the nozzles was also incorporated for some cases.

The results are described in Appendix K. Three stiffness distributions were used: (i) uniform stiffness, (ii) stiff in the neighbourhood of the seal region with a soft centre, and (iii) stiff centrally with a soft periphery. The results are given in Figures K2-K5 (pp 197-200); they show that the pressure distributions are sensitive to variations in stiffness, with case (ii) showing the closest qualitative correspondence with the data in Appendix D. The case which included a head loss model for the nozzles is shown in Figure K5. These showed a tendency computational instability which will have to be resolved.

5.2) Dynamic Stability Calculations

The dynamic stability investigation is described in Appendix G. It used a simplified model for the air escape process through the seal region suggested by the analysis in Appendix A, assumed that a rigid shoe connected to the load through a secondary suspension having known stiffness and damping, and that nozzles are gasdynaically choked either at the nozzle entrance in the rail or the exit. Results were obtained only for the rigid shoe case; in this instance a simple formula was obtained for the stability criterion.

Now it is characteristic of this type of instability that it can usually be triggered by increasing sufficiently the load and hence the cavity pressure p_c. The formula for the rigid shoe case suggested that, for the typical SailRail geometry, instability would be encountered for p_c as low as 2.8 kPa. Yet SailRail has been known to operate free of pneumatic hammer at p_c = 50 kPa and higher. This result has led us to speculate that the structural properties of the shoe, and especially the damping properties of the tissue, must play a key role in suppressing the instability.

5.3) Cover Flutter Analysis

The cover flutter analysis, given in Appendix I, was exploratory in nature and followed closely the ideas and simplifications traditionally used in such analyses. It used a two-dimensional model and assumed that the wavelength of the oscillations is much smaller than the width of the shoe, and included the inertia and bending stiffness of the cover, and the compressive stiffness of the damping of the tissue. The flow was assumed incompressible, unsteady and irrotational, and the equilibrium gap was taken to be constant. With these simplifications, explicit formulae were obtained for the mean velocity of the flow between shoe and rail above which flutter would occur.

The results suggested that flutter could occur for representative values of the parameters involved, and would have oscillation fequencies in the range expected. Typically, for 1.27 mm (0.050 in) and 0.127 mm (0.005 in) covers the predicted frequencies are 565 and 1410 Hz respectively. This compares with measured values of the order of 750 Hz.

It must be noted that the simplifications used in the analysis were made to allow quick adaptation of existing work. There are a number of aspects which need to be improved before this analysis could be assumed to have reasonably close correspondence with the physical situation. However, unlike the other unconventional features of SailRail, the practical significance of cover flutter remains unclear. Hence no further development of this analysis is recommended at this time.

6) CONCLUSIONS

6.1) General Status

A coherent overall picture of the way in which the SailRail compliant air bearing functions has now emerged, and the role of several of its unconventional features in achieving its current level of performance have been documented. The fluid mechanics involved has been broadly sketched out, and some insights into the structural aspects have been obtained. The research described in this report has already led to significant changes by the developer in the design of the rail section and nozzle layout pattern which in turn have enabled him to make major improvements in his product (see Appendix M, p. 213). However, it is also very clear that much remains to be learned. Much of this information will be particularly important for such demanding applications as passenger transporters.

The role of nozzle inclination in limiting the flow through uncovered nozzles has been documented and the mechanism - gasdynamic choking - identified. The effect of bending stiffness of the shoe cover in improving performance has been demonstrated but the mechanism by which this occurs is not yet completely identified. It has been shown that one of the two rows of nozzles in the original standard nozzle pattern was not contributing significantly to the air bearing action, and as a result this has been removed from current designs. Certain early rail profiles were shown to have inadequate bending stiffness in the curved upper surface, and this caused serious degradation in performance. As a direct result the rail section has been modified considerably. The preliminary work on dynamic stability suggests that the damping property of the tissue plays a key role in suppressing the dynamic instability known as pneumatic hammer.

We have made much less progress in understanding the structural properties of the shoe and in identifying the factors essential to the functioning of SailRail.

6.2) Recommendations for Future Work

(i) Prototype Testing: Even at this stage much remains to be obtained from testing of the prototype. To give just two examples, the effect of nozzle orientation and location on system response to lateral forces needs to be explored carefully, and the role of covers in preventing possible tissue suck-down the neighbourhood of nozzles needs to be documented. Improvements in both test procedure and data analysis are required. One suggestion is to use a monorail in which the load is suspended underneath. This removes the difficulty of having to align two shoes with respect to each other. At the time of writing such an apparatus has been set up and is giving promising results. Also it has been found that preconditioning of the shoes can be used to speed up the data acquisition process.

Ultimately, the test data should be presented in a form that is independent of the coefficient of sliding friction of the particular cover-rail combination being tested. One possible approach is to measure the friction coefficient in the monorail apparatus at the beginning and end of each transit time measurement, and then use this data and the analyses in Appendix F to compute the fraction of the load carried by air pressure, that is the air bearing load.

The quantity that is simple to measure and perhaps most useful in interpreting SailRail performance is the air pressure distribution between rail and shoe. This gives direct information on the fluid mechanics and, in principle at least, pressure profiles can be integrated to give the air bearing load. However, as currently set up, this is a time-consuming process. Owing to the very small shoe-rail gaps the time required for pressure tap measurements to stabiize can be as long as twenty minutes. Currently, the pressure sensing device is a laboratory grade Bourdon tube gauge. It is believed that, by replacing this with a pressure transducer having very small volume in the sensing element, and by keeping the length of all pressure tapping lines to a minimum, this time can be greatly reduced. Furthermore, we have recently acquired a microprocessor and a digital data acquisition system. With the use of a computer-controlled pressure tap switching device, the experiment can be fully automated. This would allow acquisition of large amounts of pressure data both for insight purposes and direct calculation of air bearing performance.

(ii) Fluid Mechanical Aspects: The work required falls into two parts, the first relates to the entry region, and the second to the seal region. For the work on the entry region, large scale models should be used to investigate compressibility and shoe flexibility phenomena. As noted above, Reynolds number effects need not be scaled. The two main objectives would be to ascertain the effects of nozzle inclination and other geometrical features on the location of choking, and the significance of tissue flexibility and cover stiffness for the "suck-down" phenomenon. The work in the seal region is mainly analytical; it would consider the effect of flow separation in the divergent portion of the seal region passage discussed in Section 3.3 on the accuracy of the calculations in Appendices A and K.

(iii) Structural Aspects: The required work on the shoe also falls into two parts; the first is continued prototype testing to identify the factors in the shoe construction that play a key role in the performance of SailRail. The second part is the determination of stiffness and damping data for the air bearing and dynamic stability calculations. The prototype testing would include investigation of the effect of using tissue of different composition and winding tension on performance and the role of the collapsed core. For the latter we envisage the development of techniques to remove the core from the collapsed shoe. In the second group of tests special apparatus will have to be developed to obtain the shoe stiffness distribution while under load. The damping properties in the frequency range of interest can be measured in the UTIAS servohydraulically driven heave table.

(iv) Air Bearing Calculations: These would use actual tissue stiffness data obtained as described above, and a model for the bending stiffness of the cover. In the first instance the calculations would be developed for the simplified shoe and a purely two-dimensional model. In spite of the simplifcations suggested by the analysis of Appendix A, it is envisaged that numerical techniques will be required. Ultimately the analysis would be extended to the case in which pitching moments are applied to the shoe.

(v) Dynamic Stability Investigations: This is perhaps the most intriguing unresolved aspect of the SailRail system. Both experimental and analytical work is required, and particular emphasis should be placed on the role of the damping properties of the tissue in the phenomenon. It is envisaged that the analysis and experiment will use simplified models, for example, even the "rigid shoe" analysis of Appendix G should be checked. However a key first step would be detailed review and assessment of the existing literature on pneumatic hammer.

APPENDIX A. ANALYSIS OF THE FLUID MECHANICS OF THE SEAL REGION

(P. A. Sullivan)

A.1 Introduction

One of the most striking features of the flow visualization in Figure J3 (p. 190) is the behaviour of the streamlines near the edges of the flow pattern; no matter what orientation they have in the interior, they leave the pattern at right angles to the sides of the shoe. That is, in terms of the coordinate system shown in Figure A1, fluid velocities at the edges of the pattern have no significant component in the x-direction. This behaviour is one of the most important indications of the existence of a cavity region, in which the pressurized air is effectively at rest, but it also suggests that the analysis of the air escape process can be greatly simplified. If the surface roughness of the rail and shoe cover is a small fraction of the minimum gap h_s between the two, the flow in the seal region can be assumed two-dimensional and through a smooth, narrow channel having a slowly varying cross section. The idea is depicted in Figure A2. The surface roughness of samples of new shoe covers and rails were measured and found to be less than 35 μin or 9×10^{-4} mm. Since h_s is believed to be greater than 10^{-2} mm, for the present purposes the smooth channel assumption appears reasonable. Finally, estimates of the relative magnitude of inertia and viscous forces on a typical fluid particle in the seal region, discussed below, show that the flow is inertialess, so that further simplification is possible; it becomes, in effect, one dimensional.

During the first Contract, some measurements of gap between shoe and rail and thus of the cavity shape were obtained, but the measurement technique did not have sufficient resolution to permit a reliable measurement of h_s [1]. The primary purpose of this Appendix is to use the available data on cavity shape together with measured flow rates to obtain an estimate of h_s. The work is exploratory in nature, but it affords an interesting comparison with the measurements described in Appendix D.

A.2 Analysis of Fluid Mechanics

In texts on hydrodynamic lubrication it is shown that, for flow in a long, narrow channel in which the width is changing slowly along its length, the correct Reynolds number for estimating the relative magnitude of viscous and inertia forces on a fluid particle is not based on either the passage length L in Figure A2 or even the minimum width h_s, but on the so-called reduced Reynolds number Re* [2, p. 109]:

$$Re^* \triangleq \frac{UL}{\nu}\left(\frac{h_s}{L}\right)^2 = Re_L\left(\frac{h_s}{L}\right)^2 \tag{A1}$$

Here ν is the kinematic viscosity, and U is a reference velocity, such as the average value of velocity at the point of minimum gap. This form of Reynolds number must be used because the dominant viscous shear terms are scaled by h_s whereas the dominant acceleration terms are scaled by L. Estimates of Re* for the seal region from data obtained under the previous

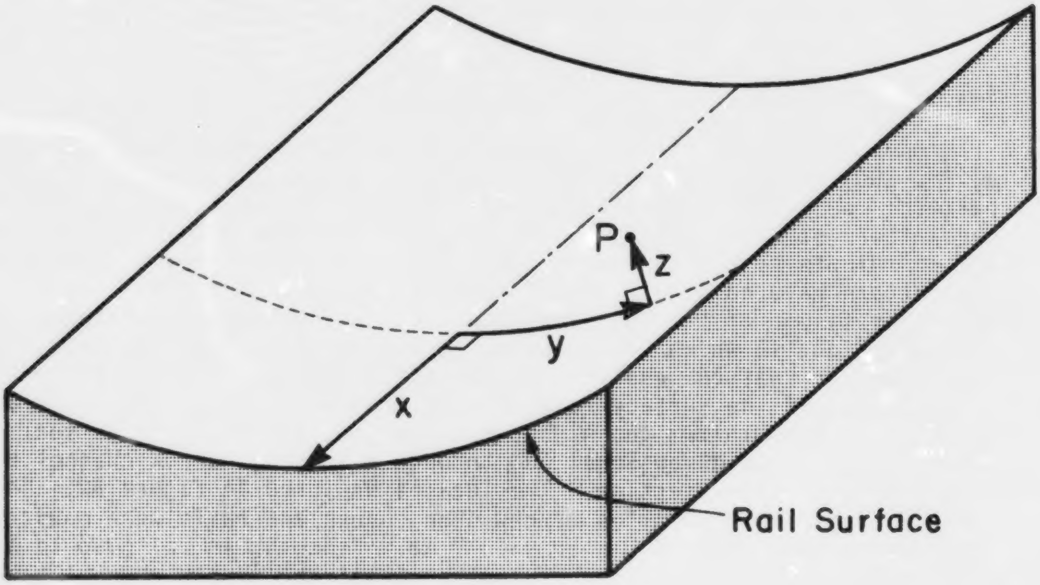
P
z
y
x
Rail Surface

Figure A1. Co-ordinate system used in analysis of flow between shoe and rail.

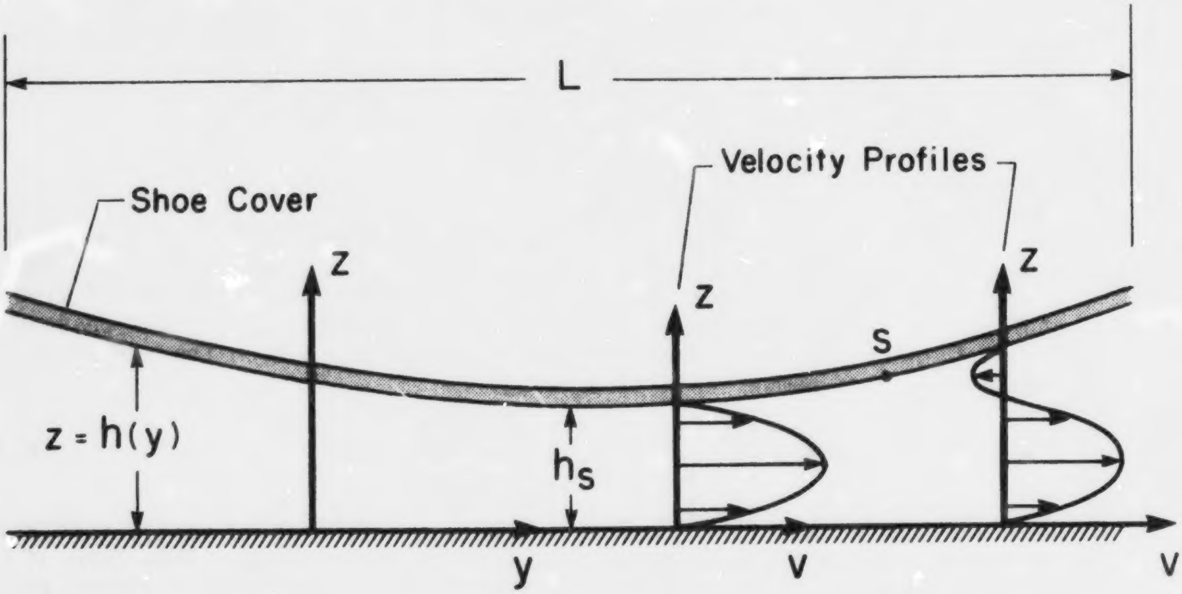
L
Velocity Profiles
Shoe Cover
Z
Z
Z
S
z = h(y)
h_s
y
V
V

Figure A2. Two dimensional flow in seal region. The width of the minimum gap is called seal height h_s. The fluid separates at some point S in the diverging section.

Contract suggested that Re* ≅ 0.05. This implies that the flow is effectively inertialess and that on each fluid particle there is a direct balance of viscous shear and pressure forces.

For the geometry depicted in Figure A2 the passage is so narrow that pressure gradients in the z-direction are negligible, and viscous shear forces generated by velocity gradients in the y-direction are also extremely small, in which case the momentum equations reduce to

$$\frac{dp}{dy} = \frac{\partial \tau}{\partial z} \tag{A2}$$

where p is the local hydrostatic pressure and τ is the shear stress on planes perpendicular to the z-direction. For a Newtonian fluid $\tau = \mu(\partial v/\partial z)$ so that equation (A2) becomes

$$\frac{dp}{dy} = \frac{\partial}{\partial z} \left(\mu \frac{\partial v}{\partial z}\right) \tag{A3}$$

Equation (A3) applies to compressible flows. Here, following the usual approach in the analysis of air bearings, it is assumed that the passage width is so small that heat conduction from the surrounding bearing structure keeps the gas temperature T constant and equal to that of the structure. Since for gases μ is a function of temperature and not of density, equation (A3) becomes

$$\frac{dp}{dy} = \mu(T) \frac{\partial^2 v}{\partial z^2} \tag{A4}$$

This equation can then be integrated twice in the z-direction to give the parabolic velocity profile characteristic of incompressible flows:

$$v(y, z) = \frac{1}{2\mu} \left(\frac{dp}{dy}\right) z^2 + C_1(y)z + C_2(y) \tag{A5}$$

Application of the no-slip condition v = 0 at z = 0 and z = h(y) determines the functions of integration, and equation (A5) then becomes

$$v(y, z) = -\frac{1}{2\mu} \frac{dp}{dy} z\left[h(y) - z\right] \tag{A6}$$

Note that $dp/dy < 0$ implies flow in the positive y-direction, as is to be expected.

The next step in the analysis is to use the continuity principle which requires the mass flux to be the same at all values of y; that is

$$M(y) \triangleq \int_0^{h(y)} \rho v dz = \text{constant} \tag{A7}$$

where M is the mass flux per unit length in the x-direction. Here, from the ideal gas law, $p/\rho = RT$, where R is the gas constant, = 287J kg^{-1}K^{-1} for air. Since T is assumed constant, equation (A7) then becomes

$$M = \frac{1}{RT} \int_o^{h(y)} p(y)v(y,\ z)dz \qquad \text{(A8)}$$

or, on using equation (A6) for the velocity profile

$$M = -\frac{1}{2\mu RT}\, p\, \frac{dp}{dy} \int_o^{h(y)} z(h-z)dz \qquad \text{(A9)}$$

Carrying through the integration gives

$$M = -\frac{1}{12\mu RT}\, p\, \frac{dp}{dy}\, h^3 \qquad \text{(A10)}$$

A.3 Relationship to Analysis of Appendix K

Now since dM/dy = 0, equation (A10) can also be written

$$\frac{d}{dy}\ (ph^3\, \frac{dp}{dy}) = 0 \qquad \text{(A11)}$$

This is simply the compressible Reynolds equation for hydrodynamic lubrication used in Appendix K, simplified to the case when the local flow is along one of the coordinate axes. That is, writing out explicitly the vector field operations of equation (K1) one has, since $\nabla p = (\partial p/\partial x)e_x + (\partial p/\partial y)e_y$,

$$\nabla_o\ [ph^3\ (\frac{\partial p}{\partial x}\, \hat{e}_x + \frac{\partial p}{\partial y})\, \hat{e}_y] = 0 \qquad \text{(A12)}$$

Then, since for $\vec{V} = u_x e_x + v_y e_y$ and $\nabla_o \vec{V} = \partial u/\partial x + \partial u/\partial y$, equation (K1) becomes

$$\frac{\partial}{\partial x}\ [ph^3\ \frac{\partial p}{\partial x}\ ] + \frac{\partial}{\partial y}\ [ph^3\ \frac{\partial p}{\partial y}\ ] = 0 \qquad \text{(A13)}$$

Equation (A11) is recovered when there is no pressure gradient in the x-direction of Figure A1.

A.4 Solution with Gap Shape Given

In the general case for a compliant air bearing the gap distribution z=h(y) is dependent on the pressure distribution and the deformation properties of the shoe, and is therefore initially unknown. However, if h(y) is assumed and the mass flow M is given, then equation (A10) can be integrated; rearrange it to obtain

$$p\, \frac{dp}{dy} = -\ N/h^3 \qquad \text{(A14)}$$

where

$$N \triangleq 12\mu RTM \qquad \text{(A15)}$$

This can be integrated immediately to obtain

$$\frac{p^2}{2} + N \int \frac{dy}{h^3(y)} = C_1 \tag{A16}$$

The constant of integration is determined by specifying the pressure at a reference point. Here the natural reference pressure is the value P_c at the centre of the cavity under the shoe, which is at y=0. Hence equation (A16) becomes

$$P_c{}^2 - p(y)^2 = 2N \int_o^y \frac{dy'}{h^3(y')} \tag{A17}$$

For the present work the assumed form of the gap distribution is

$$h(y) = A_0 + A_1 \cos(\pi\xi) \tag{A18}$$

where

$$\xi \triangleq y/D$$

$$A_0 \triangleq (H+h_s)/2; \quad A_1 \triangleq (H-h_s)/2 \tag{A19}$$

The quantity H is the maximum height of the cavity, which is assumed to occur at y=0, and the minimum gap occurs at y=D or ξ=1, as shown in Figure A3. This distribution corresponds qualitatively to that measured in the previous Contract. With this distribution given, the corresponding pressure distribution p(y) is then given by

$$p(\xi) = \left\{P_c{}^2 - \frac{192\mu RTMD}{(H+h_s)^3} \int_o^{\xi} \frac{d\xi'}{[1+A_1\cos(\pi\xi')/A_0]^3}\right\}^{1/2} \tag{A20}$$

Integration is completed numerically.

A.5 Determination of Minimum Gap Height h_s

Given P_c, M, H and D, the quantity of interest, h_s, is determined by a trial and error process. That is, given a trial value of h_s, the corresponding pressure distribution p(ξ) is computed from equation (A20); typical results of this computation are shown in Figure A4. As expected, significant pressure decay occurs only in the range $0.8 < \xi < 1.2$ with essentially constant pressure regions occurring both upstream (ξ<1) and downstream (ξ>1). The required value of h_s is that corresponding to a downstream constant pressure equal to atmospheric pressure, or about 100 kPa. Pressure profiles are computed for selected values of h_s as shown in Figure A4. The value of h_s corresponding to 100 kPa is then determined by an interpolation technique. Thus for the values of the parameters used in Figure A4, h_s = 0.017 mm (0.67×10^{-3} in). Note that the downstream pressure is very sensitive to the value of h_s. Typically a reduction of h_s by 12% to 0.015 mm causes the downstream pressure to fall by 30% to 70 kPa.

One would expect that for the method to succeed, the estimate of h_s

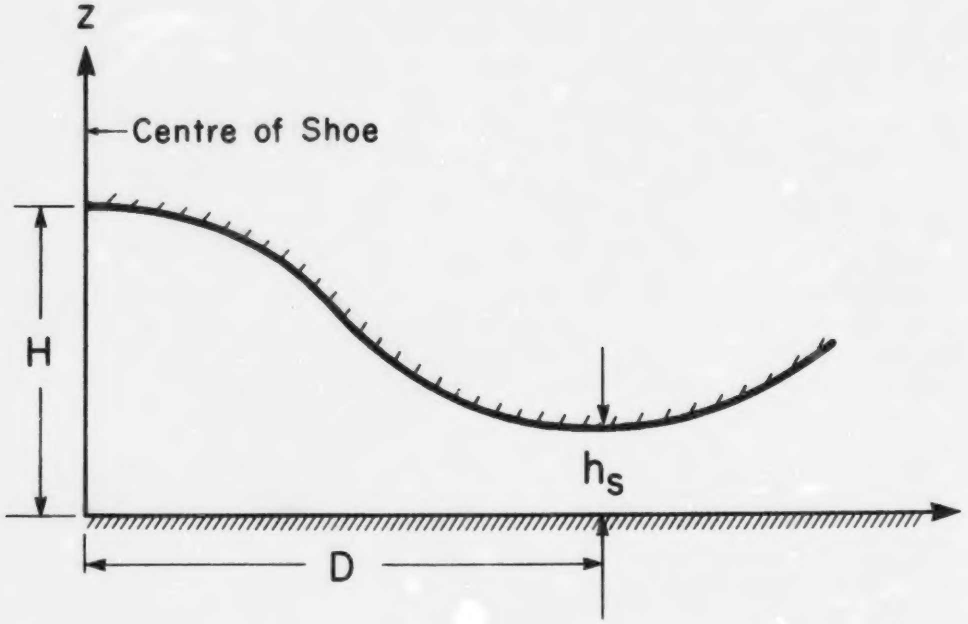
z
Centre of Shoe
H
h_s
y
D

Figure A3. Parameters in cavity shape assumed for computation of h_s.

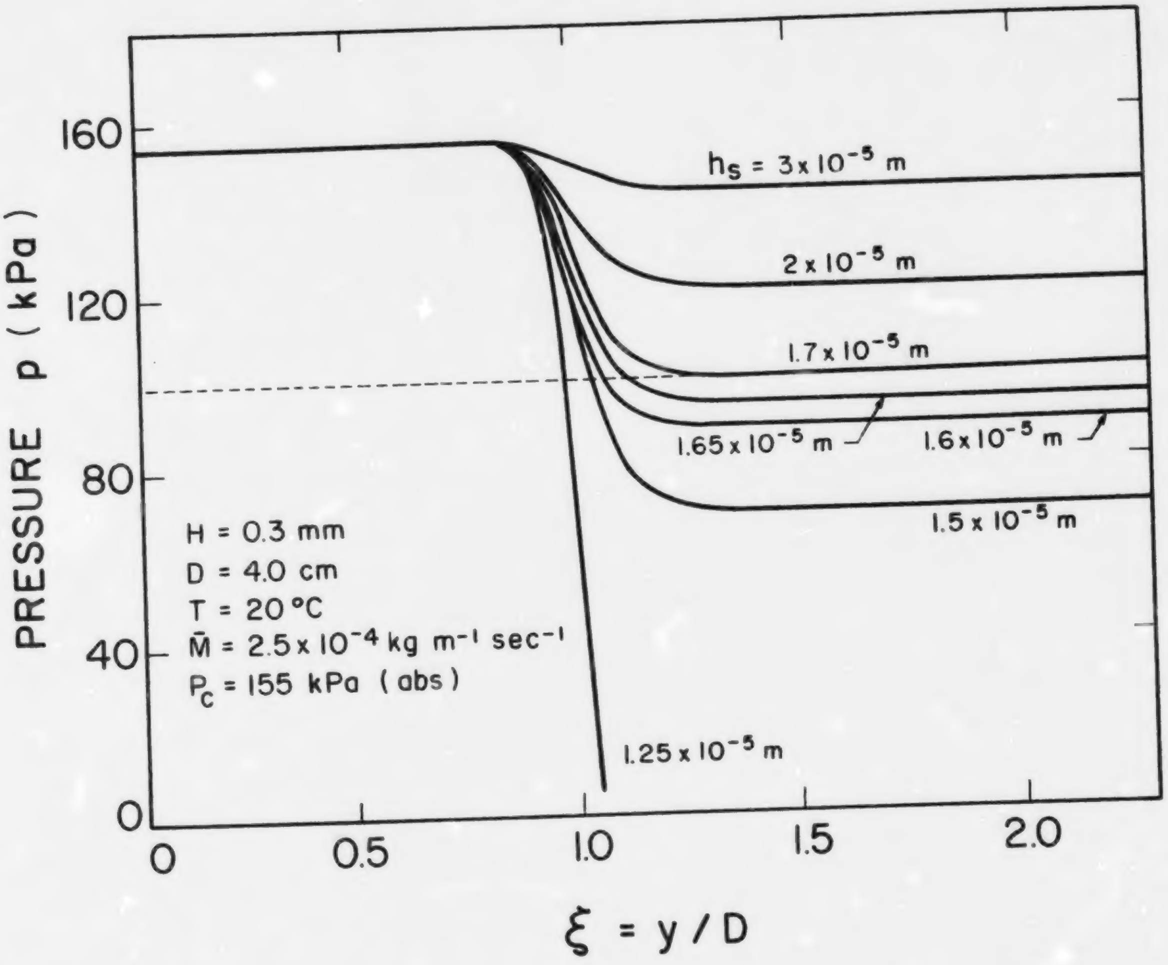

Figure A4. Typical pressure distributions in seal region computed for known H and $\bar{M}$ and with various h_s. The correct value of h_s is that corresponding to p = 100 kPa at $\xi > 1.5$.

should be only weakly dependent on the details of the geometry in those places where pressure gradients are small. Thus, for the cosine gap distribution, h_s should only depend weakly on the maximum cavity height H or the half width D. Figures A5 and A6 give predicted values of h_s for a range of H and D. They show that increasing H by a factor of two causes the estimate of h_s to decrease by 14%, whereas doubling D causes h_s to increase by 30%. Now, for the cosine gap law, changes in H and D cause some geometry changes in the neighbourhood of the seal region. Hence the results in Figures A5 and A6 suggest that, if in the integration of equation (A17) one used any measured values of h(y) for those parts of the cavity adjacent to the seal region, the estimate of h_s would probably be quite accurate.

Finally, Figure A7 shows the effect of seal height h_s on mass flux M when both cavity pressure P_c and cavity height, $(H-h_s)$, are held constant. The pressure profiles in Figure D15 (page 132) show that, once a certain critical value of air supply pressure p_c is attained, any further increase in p_t does not alter P_c significantly. Hence the prediction in Figure A7 should correspond closely to constant weight $W = 20 \int_0^\infty p(\xi)d\xi$. The values of P_c and D were chosen to permit a comparison with the measured data on the effect of mass flux on vertical displacement of the shoe. This comparison is discussed in Appendix D.

A.6 Future Work

The computed pressure profiles such as those in Figure A4 show that the amount of pressure falloff downstream of the point of minimum gap, $\xi=1$, is usually greater than that for $\xi < 1$. For example, in Figure A4 for h_s = 0.017 mm the falloff for $\xi > 1$ is about 57% of the total. But beyond $\xi = 1$ the channel is diverging, and the fluid must eventually separate from the cover at some point S shown in Figure A2. Since separation is a direct result of fluid inertia, this implies that at some point upstream of S the inertialess approximation used here becomes invalid. It has been assumed that this occurs downstream of the point at which pressure decay has effectively ceased; that is for $\xi > 1.3$ in Figure A4. This assumption should be checked by undertaking an appropriate boundary layer type analysis.

A variation of the technique is to use equation (A14) and the more easily measured pressure data such as that in Figure D14. However, this involves differentiation of numerical data and, since the pressure decrease in the seal region occurs over a relatively short distance, the method could involve large errors. A method which used both gap and pressure data might well be the most satisfactory.

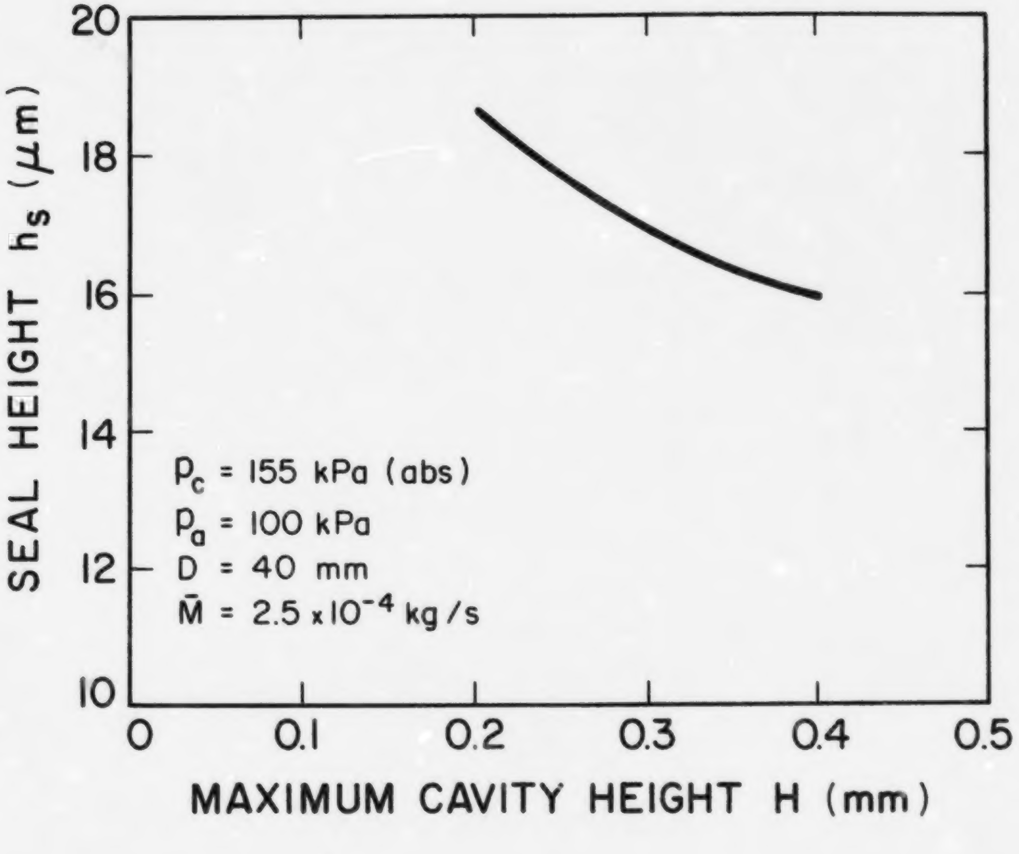

Figure A5. Effect of cavity height H on estimate of seal height h_s for cosine low cavity shape.

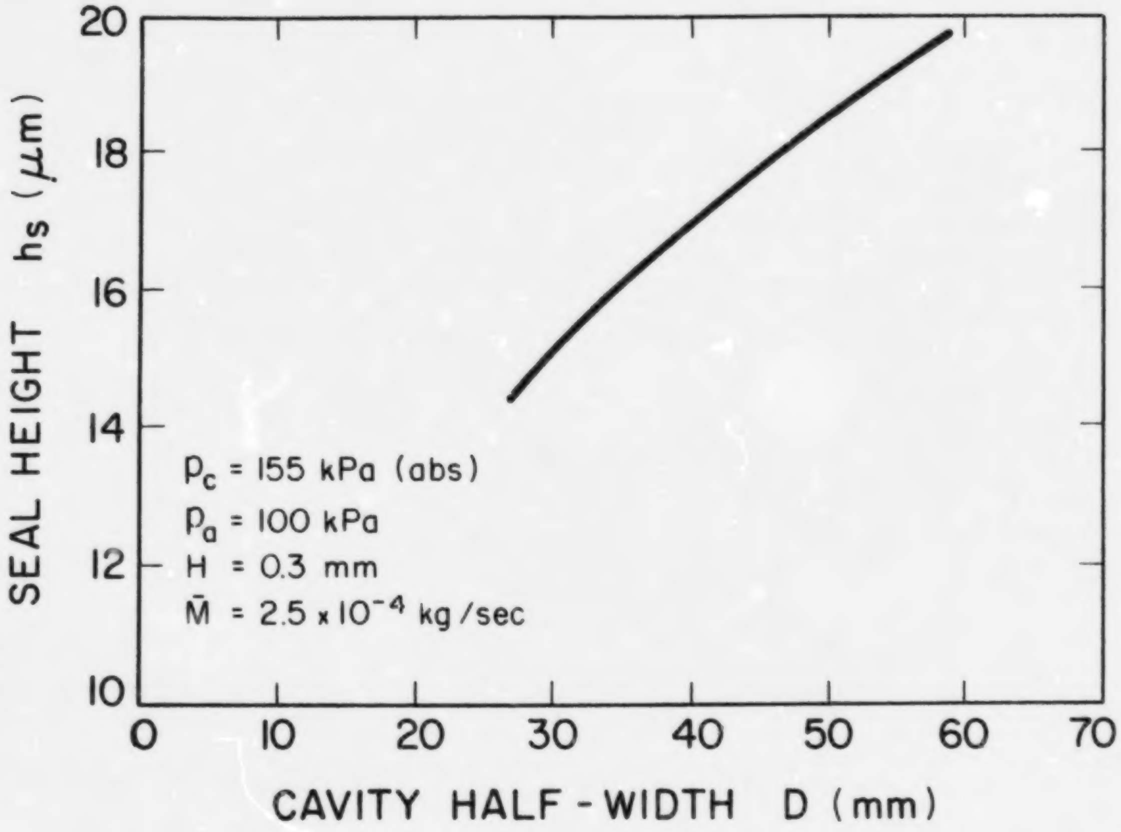

Figure A6. Effect of cavity half-width D on estimate of seal height h_s for cosine low cavity shape.

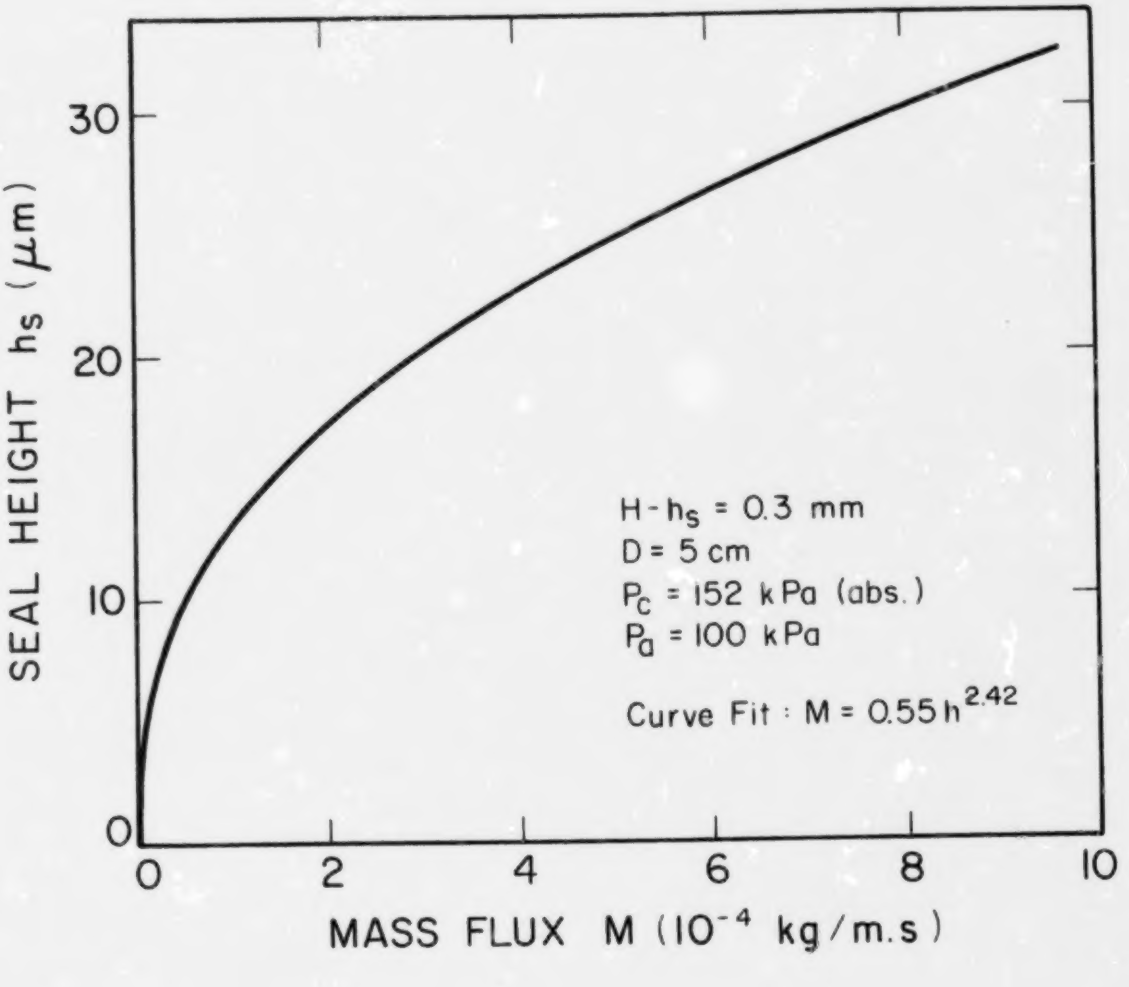

Figure A7. Computed seal height h_s as a function of mass flux $\bar{M}$.

APPENDIX B. SCALED UP MODEL OF ENTRY REGION (M. J. Hinchey and P. A. Sullivan)

B.1 Introduction

Measurements of SailRail system performance obtained during the previous Contract period showed that the air feed holes in the rail give better performance when they are drilled at an angle of 20° to the track surface instead of normal to it [1]. Since the diameter of these holes is believed to be about four to five times larger than the size of the gap between shoe cover and rail, it has been speculated that the 20° inclination reduces the hydrodynamic losses associated with delivering the air to the cavity under the shoe. To check this hypothesis, twenty times full scale models were built and tested, and this Appendix describes the apparatus and results.

B.2 Geometry and Terminology

The geometry of the air feed system from the air supply manifold in the rail to the cavity under the shoe is depicted in Figure B1. The pressure of the air supply in the rail manifold cavities is called the "track pressure" or p_t. The air feed holes, which are drilled in the top surface of the rail, supply the air to the underside of the shoe. In current practice their diameter d is 0.026 in (0.66 mm), their length L is about 14d, and they are oriented at an angle $\theta = 20^{\circ}$ to the local tangent to the rail surface. They are described as "nozzles", even though the idea of a directed momentum flux usually associated with the use of that term may not be important to the fluid mechanics. Also, holes drilled at $\theta = 90^{\circ}$ are termed "radial nozzles". The local gap is "h", and usually $h \ll d$.

The air flow processes involved are considered to occur in two stages or regions. In the "nozzle entry" region the flow accelerates from pressure p_t and is delivered to the point labelled "2" in Figure B1. The flow processes downstream of this point, which deliver the air to the cavity at pressure p_c, are said to occur in the "cavity entry" region. The pressure decrease from p_t to that at point 2 includes both that associated with accelerating the flow to point "1" and any entry and pipe friction losses from "1" to "2". For the geometry currently in use, the pipe loss from "1" to "2" is usually a very small fraction of the other pressure drops, so that p_1 is roughly equal to p_2. Thus the pressure p_2 is defined as the "nozzle" pressure.

B.3 Scaling Requirements

To obtain a dynamically scaled model of the entire "nozzle-cavity" region, three basic requirements have to be satisfied. First, Reynolds number scaling ensures that the ratio of inertia forces to viscous forces is the same in prototype and model, and it requires

$$Re_d \triangleq \frac{\rho_m U_m L_m}{\mu_m} = \frac{\rho_p U_p L_p}{\mu_p} \qquad (B1)$$

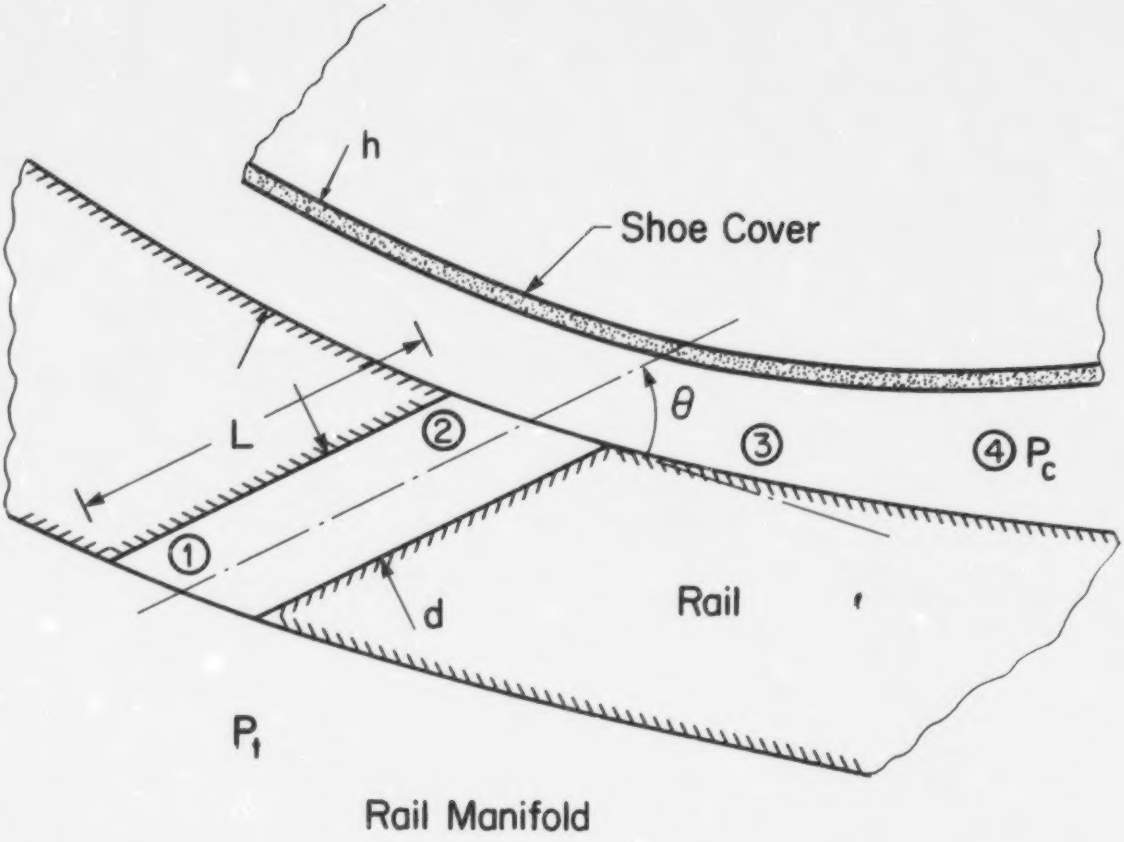
h
Shoe Cover
L
θ
②
③
④ P_c
①
d
Rail
P_t
Rail Manifold

Figure B1 Geometry of entry region.

In this equation, ρ and μ are the air density and viscosity respectively, U is a reference air speed, L is a reference length, and the subscripts "m" and "p" denote model and prototype respectively. Here U is taken to be the mean velocity U of the flow at a reference point in the nozzle, and L = d. For the present work Re is more conveniently expressed in terms of the mass flow $\dot{m}$ per nozzle, and since $\dot{m} = \pi\rho d^2\bar{U}/4$

$$Re_d = \frac{4\dot{m}}{d\mu} \tag{B2}$$

Typical Reynolds numbers are in the range 0.5×10^4 to 3×10^4. The second effect to be scaled is air compressibility. Since the air supply pressure in the rail manifold is about 130 kPa (gauge), and since a typical pressure in the cavity region is about 50 kPa (gauge), the absolute pressure ratio across the entire nozzle-cavity region is about 0.65. Hence the flow is compressible, and probably gasdynamically choked [see Appendix 0]. Compressibility scaling requires that the Mach number of the flow in the nozzle be the same for model and prototype. Finally, complete scaling would require consideration of the flexibility of both the cover and cellulose filler of the shoe.

It may be impossible to satisfy all the above scaling requirements in a single experiment. For example, to obtain Reynolds number scaling on a model which is 20 times larger than the prototype, if the air density and viscosity is about the same in both model and prototype, then the model flow velocities must be twenty times smaller than the prototype velocities. This in turn means that the model pressures would be about 400 times smaller, and would thus rule out compressibility scaling. Also, scaling of shoe tissue and cover properties might be extremely difficult.

For the present investigation it was decided to scale only Reynolds number effects. It was initially envisaged that this might be the most important of the three requirements, since it controls the transition of the flow from inertia dominated in the neighbourhood of the nozzle to viscosity dominated in the cavity. Furthermore, the SailRail system has been observed to operate at differences between p_t and p_c of less than 7 kPa; this suggests that compressibility effects are not intrinsic to the concept. Finally, data given in Appendix C shows that performance increases with increase in shoe cover thickness. Thicker covers have increased bending stiffness and are therefore expected to limit deflections locally around a nozzle. Hence it is suggested that, in the first instance, the cover can be modelled as a rigid surface.

B.4 Model of Cavity-Entry Region

The model consists of two 1.4 cm thick, 38 cm diameter steel discs machined smooth and flat and which lie horizontally on a table, one on top of the other as shown in Figure B2. The bottom disc is fitted with pressure probes along radii at angles of 0^o, 45^o, 90^o, 135^o, 180^o and 270^o to the line directly below the axis of the inclined nozzle, as shown in Figure B3. The nozzle is attached to the centre of the top disc, and it consists of a 30 cm long 13.3 mm diameter pipe as shown in Figure B4. The top disc is also fitted with some pressure probes. The gap between the disc is set by

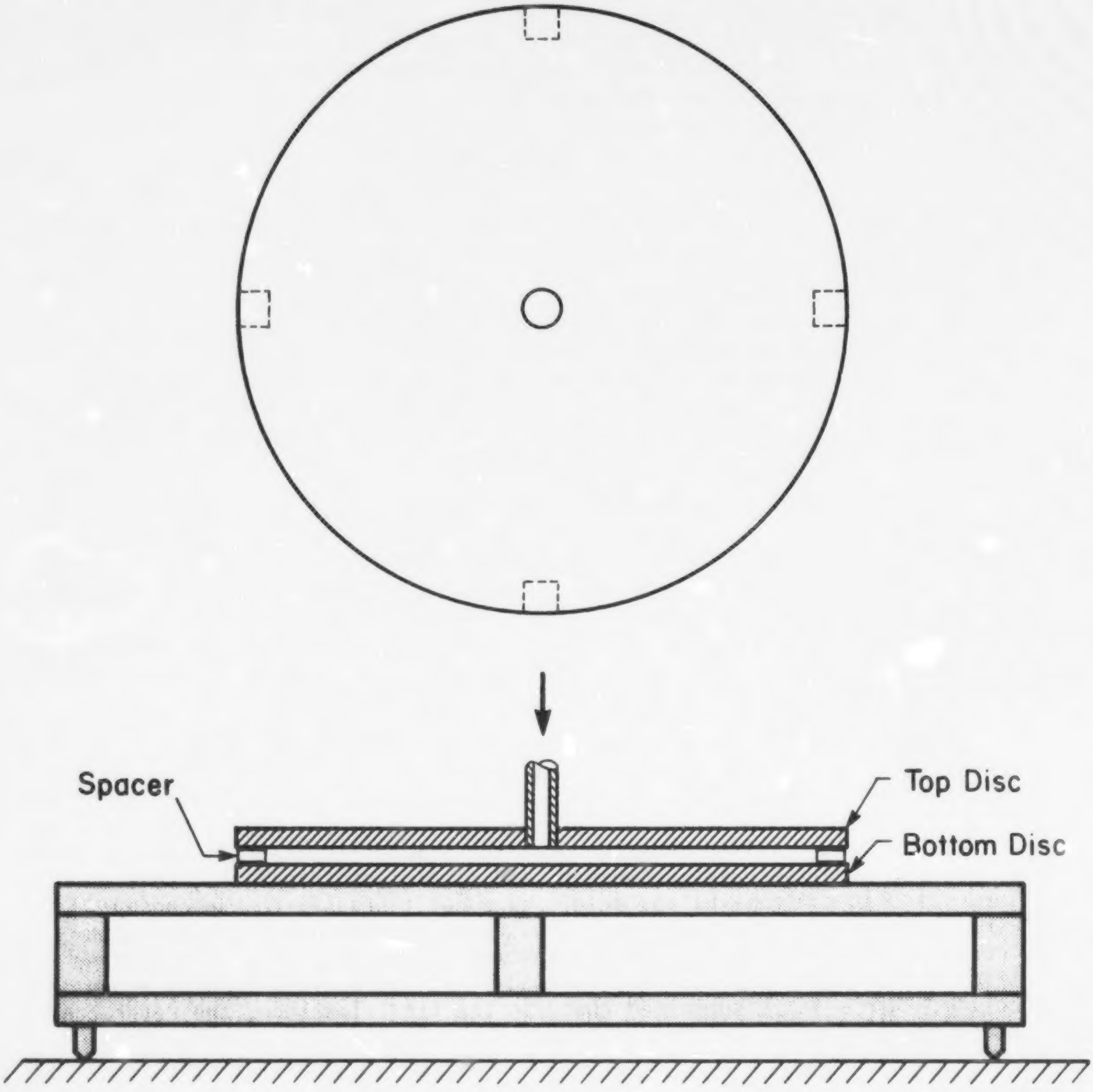
Spacer
Top Disc
Bottom Disc

Figure B2 Twenty times full scale model of cavity entry region

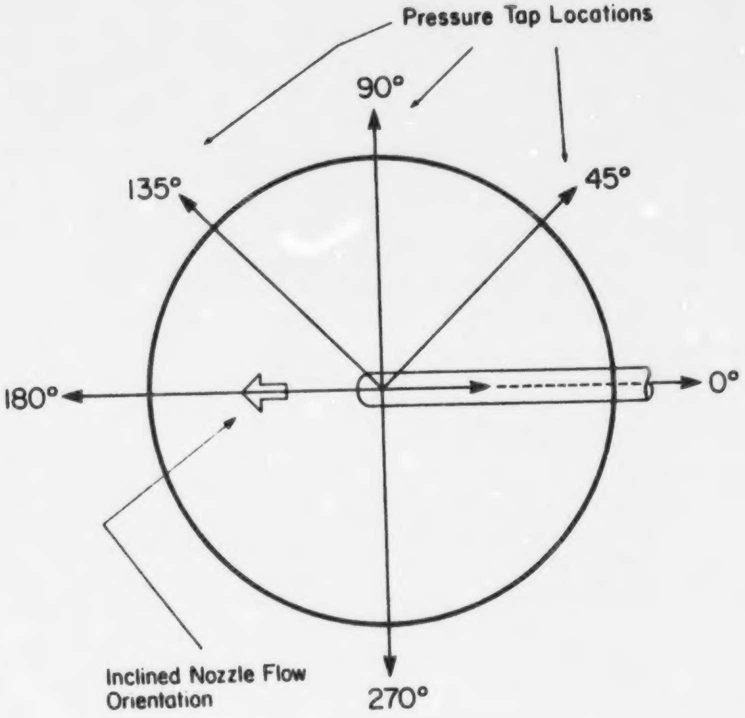
Pressure Tap Locations
90°
135°
45°
180°
0°
270°
Inclined Nozzle Flow Orientation

Figure B3 Location of static pressure taps in the cavity-entry region model

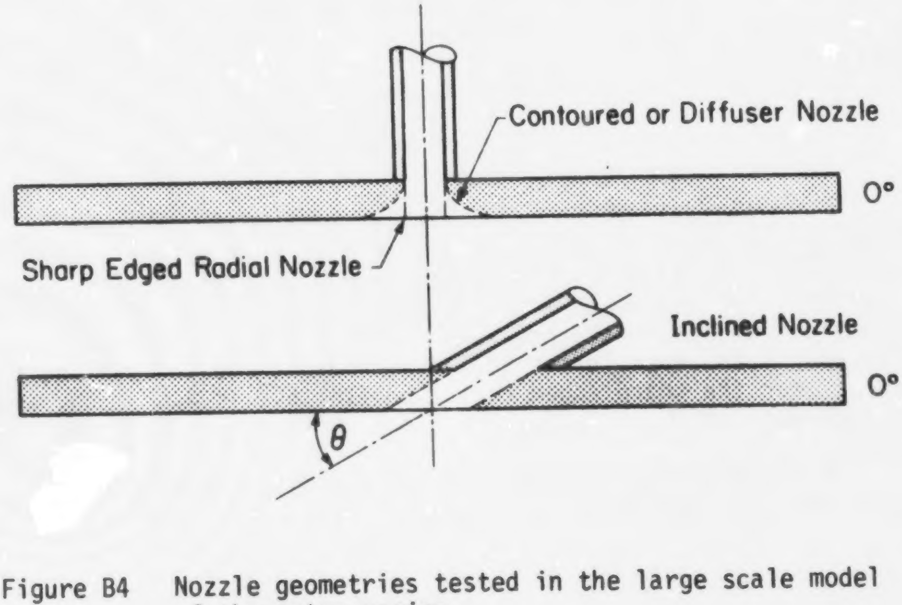
Contoured or Diffuser Nozzle
0°
Sharp Edged Radial Nozzle
Inclined Nozzle
0°
θ

Figure B4 Nozzle geometries tested in the large scale model of the entry region.

using 3 accurately machined peripherally located spacers. The air is supplied to the apparatus through a rotameter type flowmeter calibrated during the previous Contract; the calibration curve is given in Figure B5. Three nozzle geometries were used in the experiments. In addition to the sharp edged radial and inclined nozzles depicted in Figure B4, a contoured or radial diffuser nozzle was tested. The shape of this radial diffuser nozzle is shown by the dotted lines in Figure B4.

In designing this model it was assumed that the disc diameter was sufficiently large to ensure that the pressure at the periphery, which is ambient atmosphere in the model, corresponds to the shoe cavity pressure p_c. The validity of this assumption is confirmed by the pressure profile data, discussed below.

B.5 Results for Cavity Inlet Model

Figure B6 gives nozzle pressure p_2 as a function of Q for the three nozzle geometries and for a small value of h/d. This shows that, at a given Q, p_2 for a radial sharp edged nozzle is substantially higher than that for the inclined nozzle; typically at $Q = 2.0\times10^{-3}\ m^3/sec$, it is higher by a factor of 4.3. Hence the inclined nozzles are much less resistive than the radial nozzles; however, note that the resistance of the radial diffuser nozzle is much smaller than that of the inclined nozzle.

Additional insights into the results can be obained by presenting them in a suitable nondimensional form. A nondimensional flow coefficient C_Q is defined as follows:

$$C_Q \triangleq \frac{Q}{V_r A_r} \tag{B3}$$

The quantities V_r and A_r are a reference flow speed and a reference area respectively. The natural value of V_r is that corresponding to frictionless acceleration of the air from the conditions at point 2 in Figure B1 to the equivalent of p_c; according to Bernoulli's theorem this is, for the model in Figure B2,

$$V_r = [(2p_2/\rho) + \overline{U}^2]^{1/2} \tag{B4}$$

where $\overline{U} = Q/(\pi d^2/4)$ is the mean velocity of the air in the pipe. For the prototype, in which the air accelerates from rest at a pressure p_t, this velocity is that which would be obtained by lossless flow from rail manifold to cavity. The choice of a suitable A_r is not so straightforward, however. One obvious choice is the cross-sectional area of the feed pipe $A_{r1} = \pi d^2/4$. A second is the area formed by the gap height and the periphery of the nozzle; for the sharp edged radial nozzle this is $A_{r2} = \pi dh$, and for the 20^0 inclined nozzle it is $A_{r2} = 6.54dh$. Both reference areas are used below.

For the geometry in Figure B2, if the disc diameter is large enough to ensure that its periphery corresponds to the cavity under the shoe, then

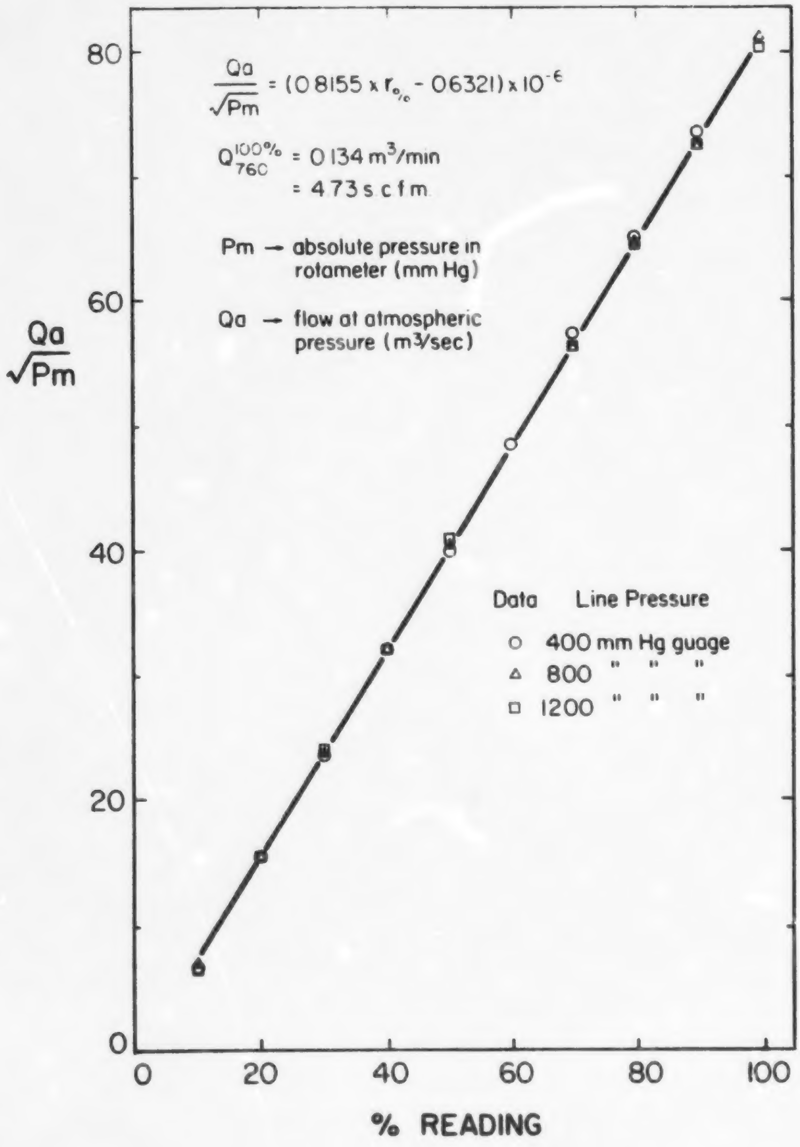

Figure B5 Typical rotameter calibration curve

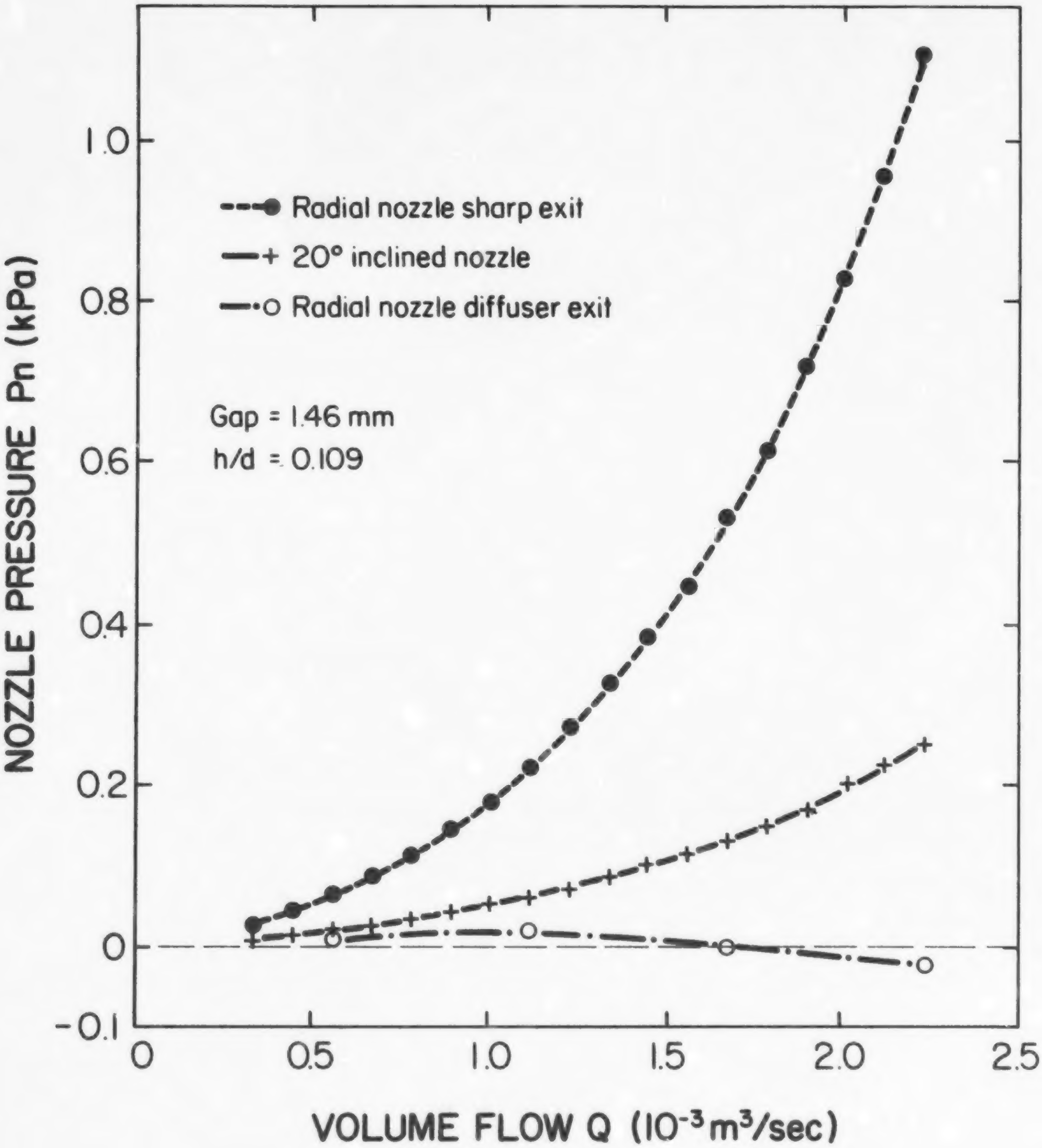

Figure B6 Typical resistance characteristics of inclined and radial nozzles

$$Q = f(d,\ h,\ \mu\ \rho,\ p_2,\ \theta) \qquad \text{(B5)}$$

According to the Π-theorem of dimensional analysis, since the seven variables in equation B5 contain between them only three dimensions, this equation can be replaced by one involving only four dimensionless groups. Two possible choices are

$$C_{Q1} = f_1\left[Re_d,\ \frac{h}{d},\ \theta\right] \qquad \text{(B6a)}$$

$$C_{Q2} = f_2\left[Re_d,\ \frac{h}{d},\ \theta\right] \qquad \text{(B6b)}$$

where C_{Q1} and C_{Q2} are the flow coefficients computed by using A_{r1} and A_{r2} as reference areas. Note that an increase in either C_Q corresponds to a reduction in hydrodynamic losses, and that $C_{Q1} = 1$ corresponds to completely frictionless acceleration by the available pressure drop. Also if $p_d \triangleq \rho\bar{U}^2/2$ is the dynamic head of the flow inside the nozzle, then C_{Q1} is related to the pipe loss coefficient K_0 through the expression

$$K_0 \triangleq p_2/p_d = (1/C_{Q1}^2) - 1 \qquad \text{(B7)}$$

so that $K_0 \rightarrow 0$ as $C_{Q1} \rightarrow 1$. In the limit $h/d \rightarrow 0$ the nozzle becomes a plenum chamber or reservoir, and the flow should be similar to that through a slot orifice of height h. In this case the flow is proportional to A_{r2} and one would expect that $C_{Q2} = f(Re_d, \theta)$ only. Appendix N describes a simplified analysis of the flow through the sharp edged radial nozzle. This analysis, which uses the assumption that $h/d \ll 1$, predicts that $Q = 2.64\ dh\ V_{ref}$, and implies that $C_{Q1} \rightarrow 3.36\ (h/d)$ and $C_{Q2} \rightarrow 0.84$ as $h/d \rightarrow 0$.

Figures B7 and B8 give C_{Q1} for the inclined and radial nozzles respectively, and h/d = 0.109, 0.229, and 0.466. The calculations in Appendix A suggest that in the cavity region $0.1 < h/d < 0.5$ approximately. The results in Figures B7 and B8 show only a very small effect of Reynolds number; this suggests that most of the hydrodynamic losses occur in the immediate neighbourhood of the nozzles where the flow is turbulent. For the radial nozzle, the data agrees favourably with the analysis of Appendix N for h/d = 0.109, but the error at h/d = 0.229 is much larger. Table B1 compares the maximum values of C_{Q1} in Figures B7 and B8 for the two nozzles at the three values of h/d. They show that for h/d = 0.109 the inclined nozzle delivers about 50% more flow than does the radial nozzle, however as h/d approaches 0.5, this advantage almost disappears. Also Equation B8 shows that as h/d is reduced from 0.466 to 0.109, the head losses increase by a factor of about six for the radial nozzle, in contrast with a factor of about two for the inclined nozzle.

Figures B9 and B10 give C_{Q2} as a function of Re_d for the two nozzles, and the strong dependence on h/d shows that the flow is not equivalent to that through a slot orifice. Furthermore for all three values of h/d, C_{Q2} for the inclined nozzle is significantly less than the corresponding value for the radial nozzle. This suggests that although it is substantially more efficient than the radial nozzle, it is nevertheless not making full use of the available peripheral area.

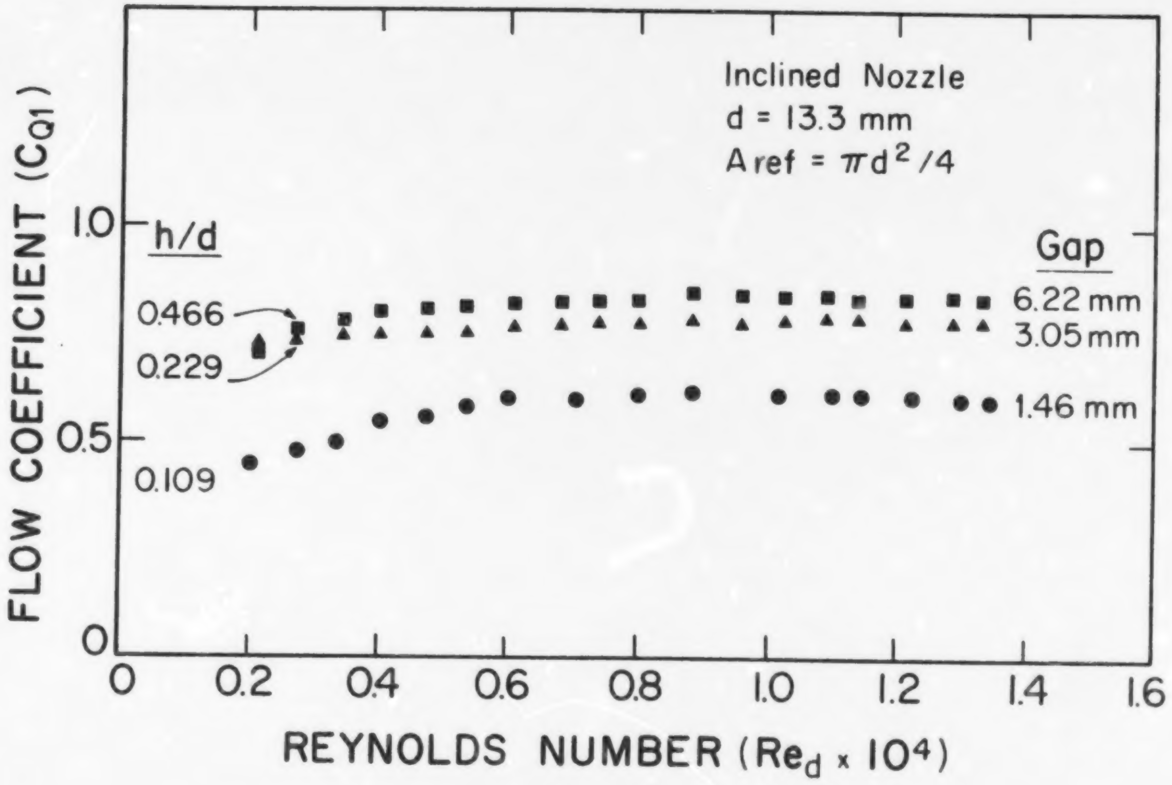

Figure B7 Flow coefficient for inclined nozzle as a function of Reynolds Number with $A_{r1} = \pi/4d^2$ as reference area

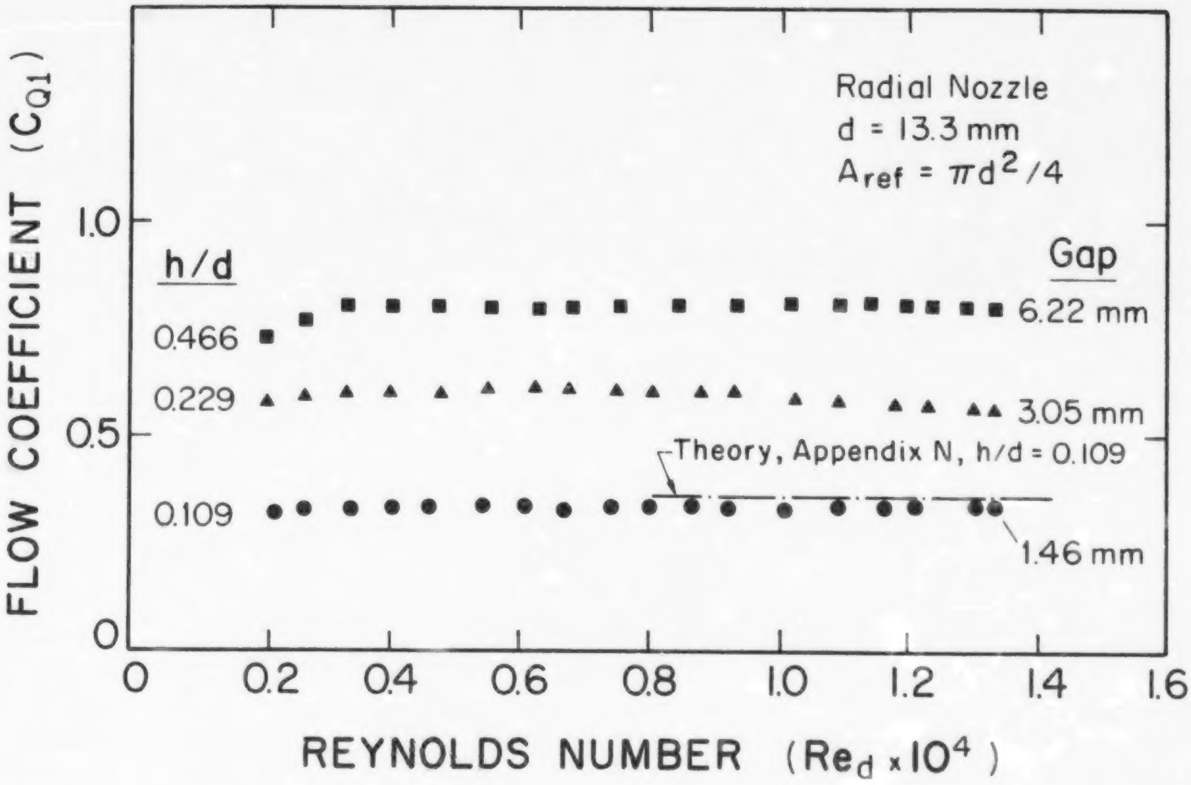

Figure B8 Flow coefficient for sharp edged radial nozzle as a function of Reynolds Number with $A_{r1} = \pi d^2/4$ as reference area

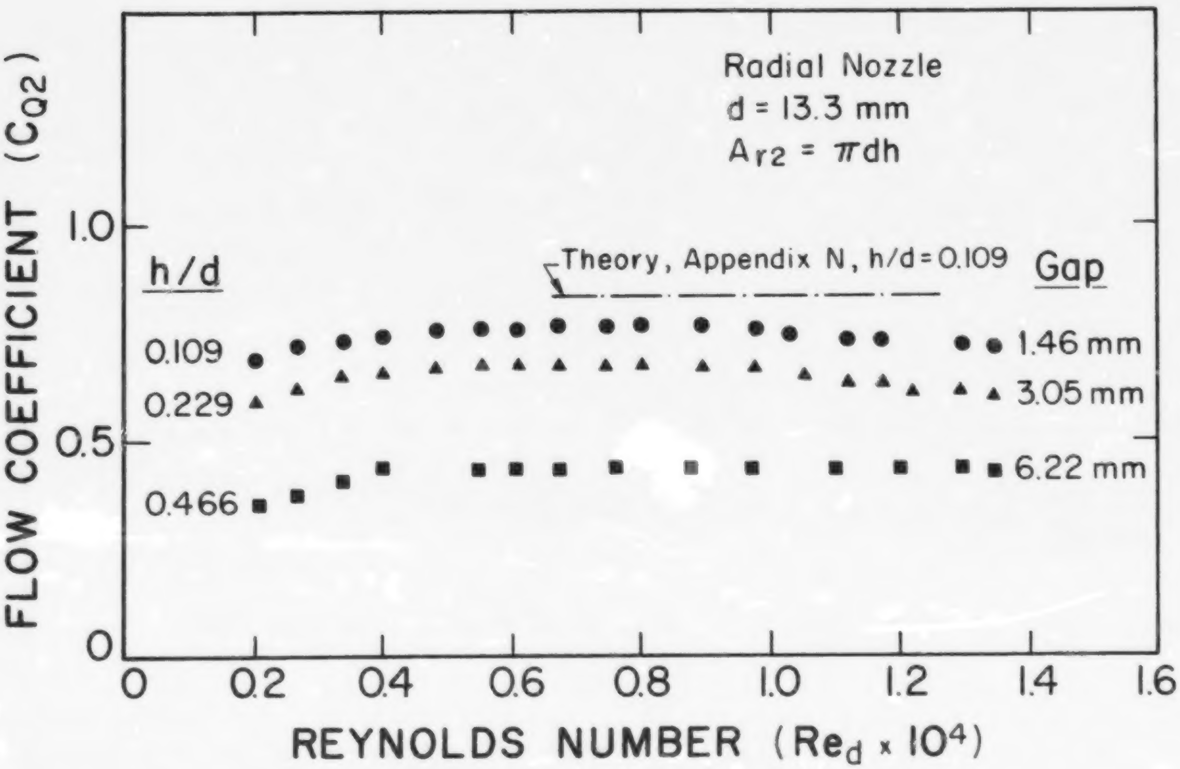

Figure B9 Flow coefficient for sharp edged radial nozzle as a function of Reynolds Number with $Ar_2 = \pi dh$ as reference area

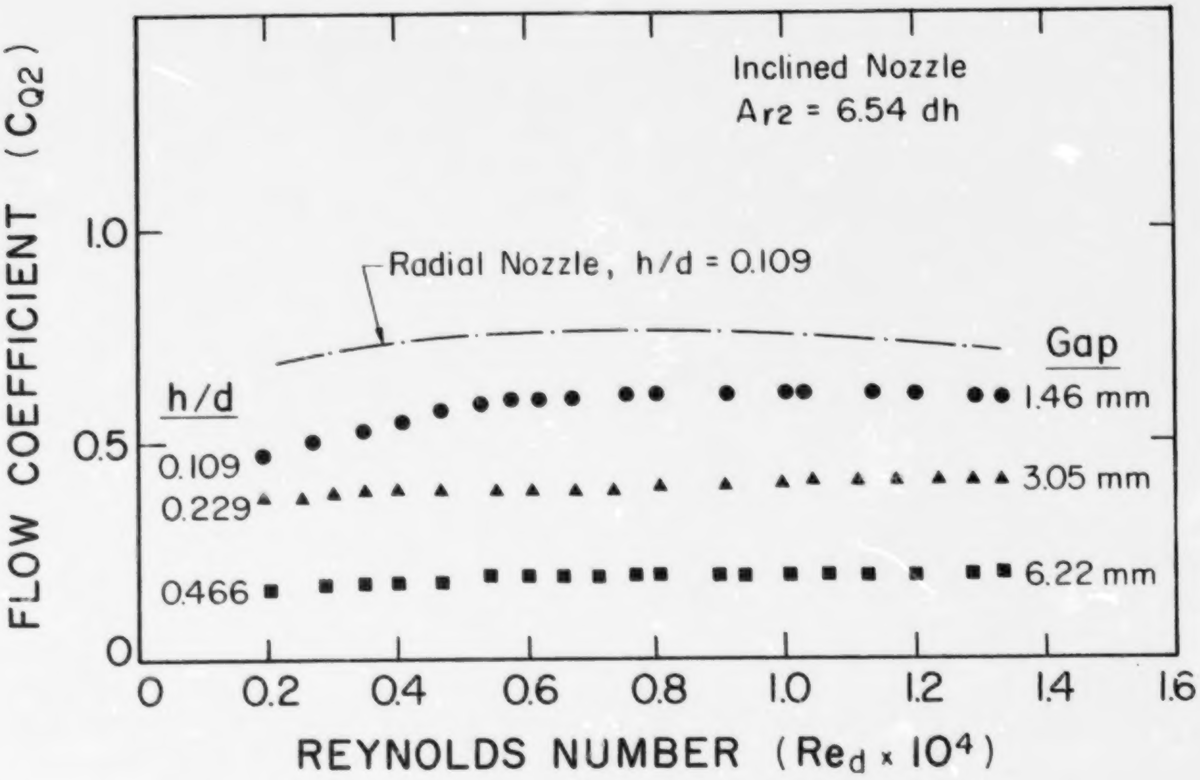

Figure B10 Flow coefficient for inclined nozzle as a function of Reynolds Number with Ar_2 = 6.54 dh as reference area

Table B1

Effect of h/d on C_{Q1} for radial and inclined nozzles

	C_{Q1}	
h/d	Radial Nozzle	Inclined Nozzle
0.109	0.370	0.565
0.229	0.560	0.692
0.466	0.700	0.712

B.6 Effect of Nozzle Inclination Angle

Six plywood plates, each containing a nozzle at a different angle θ, were used to study the effect of nozzle inclination on the resistance characteristics, both at the nozzle inlet region and at the cavity inlet region. The two configurations are depicted in Figure B11. The data is presented in terms of the loss coefficients K_i and K_o as functions of θ. That is, with p_s = static pressure measured at the point shown in Figure B11

$$K_i \triangleq \frac{(-p_s)-p_d}{p_d}, \qquad K_o = \frac{p_s}{p_d} \tag{B8}$$

Note that for the nozzle inlet, p_s is negative, and $(-p_s) > p_d$, so that K_i expresses only that fraction of the pressure drop caused by friction. For $\theta = 90^0$, corresponding to radial nozzles, as Re increases K_i should approach the theoretical limit of 0.5 [3, p. 187]. The data for K_i is given in Figure B12, and that for K_o in Figures B13 and B14. It shows that inlet losses decrease significantly with increase in θ up to a minimum at $\theta = 90^0$, and at $\theta = 90^0$, $K_o \rightarrow 0.5$ as Re increases. The data in Figure B13 also shows that for a nozzle located near the centre of the cavity, where $h/d \approx 0.5$, the nozzle angle has little or no effect. However for nozzles located near the edges of the cavity, the effect of θ is very large, although an increase in θ from 20^0 to 30^0 would probably have only a very small effect on overall system performance.

B.7 Computed Radial Nozzle Flow Patterns

Flow patterns for the radial nozzle geometry were obtained by a numerical simulation technique. A finite difference algorithm was applied to a mathematical model suitable for the investigation of recirculating turbulent flows; the details are described in Appendix L. The results for h/d = 0.5 and 0.25 are given in Figures B15 and B16 respectively, which are velocity-vector plots. The lines in these figures are oriented along the local streamline direction, and the length of each is proportional to the fluid speed at the base point from which it is drawn. The base points lie

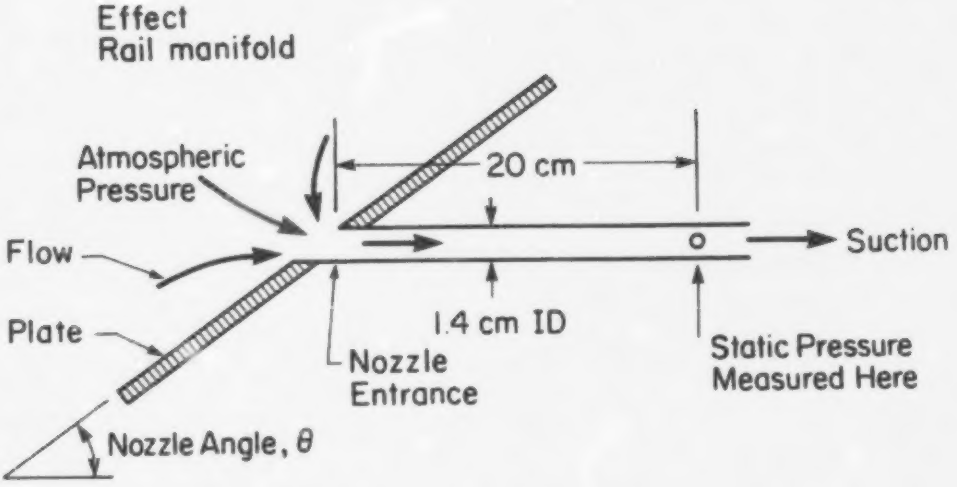
Effect
Rail manifold
Atmospheric Pressure
20 cm
Flow
Suction
Plate
1.4 cm ID
Nozzle Entrance
Static Pressure Measured Here
Nozzle Angle, θ

Nozzle Inlet Model

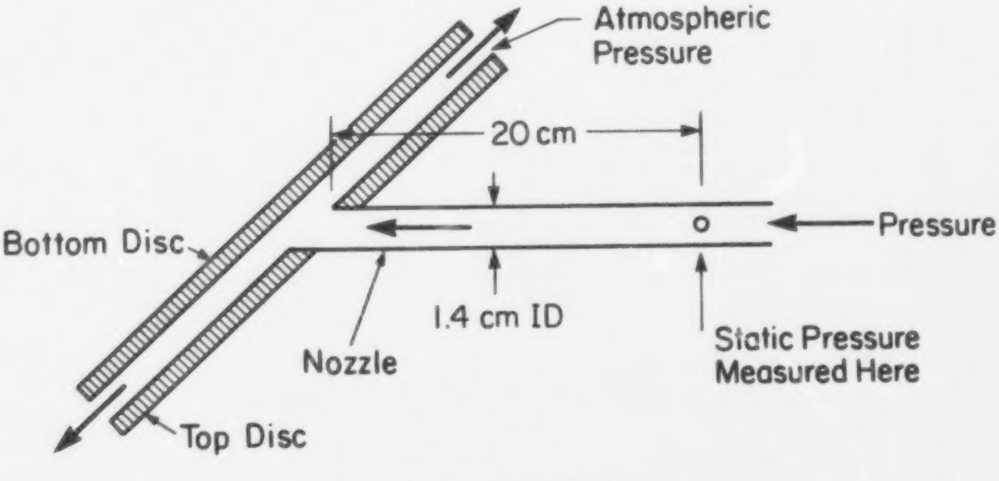
Atmospheric Pressure
20 cm
Pressure
Bottom Disc
1.4 cm ID
Static Pressure Measured Here
Nozzle
Top Disc

Cavity Inlet Model

Figure B11 Geometries used for investigation of the effect of nozzle angle on head losses at nozzle-entry and cavity-entry regions

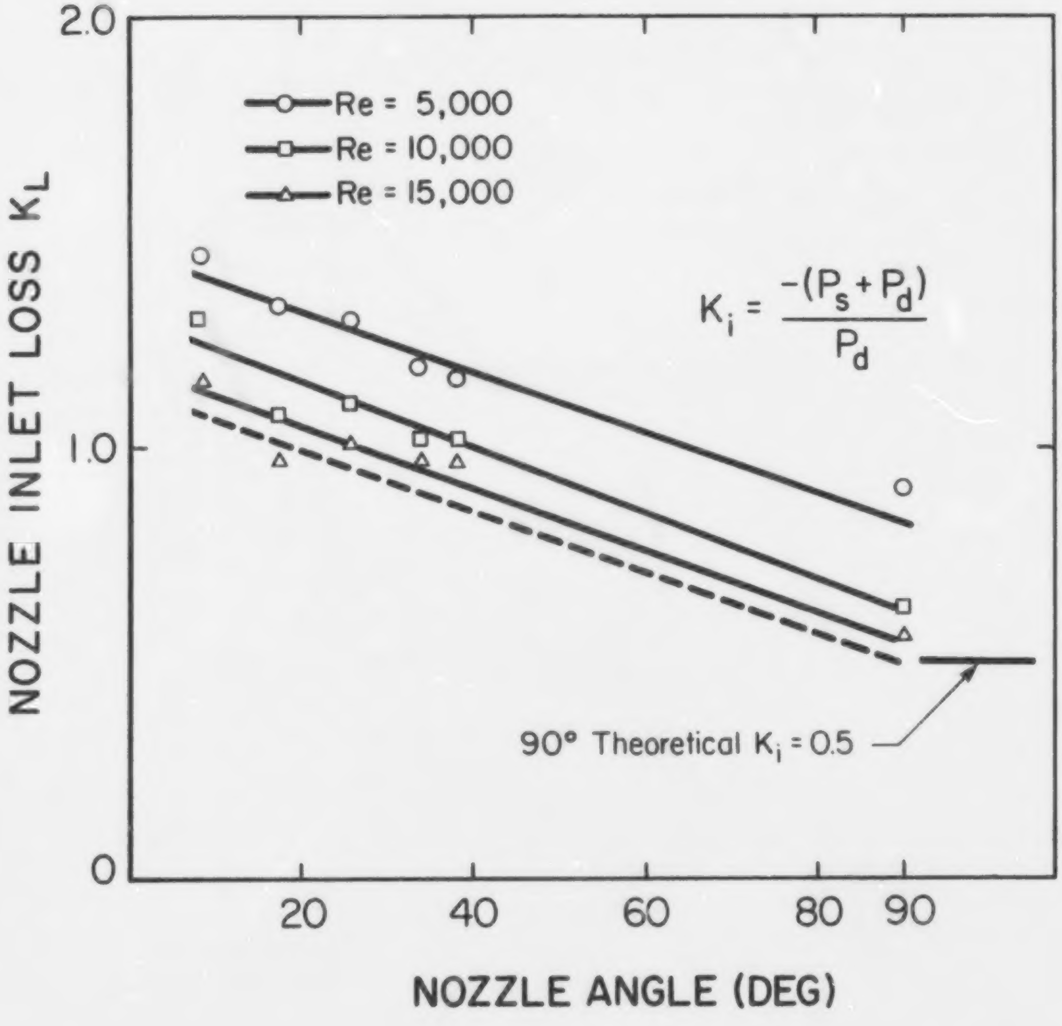

Figure B12 Effect of nozzle angle on head losses in nozzle-entry region for three Reynolds Numbers

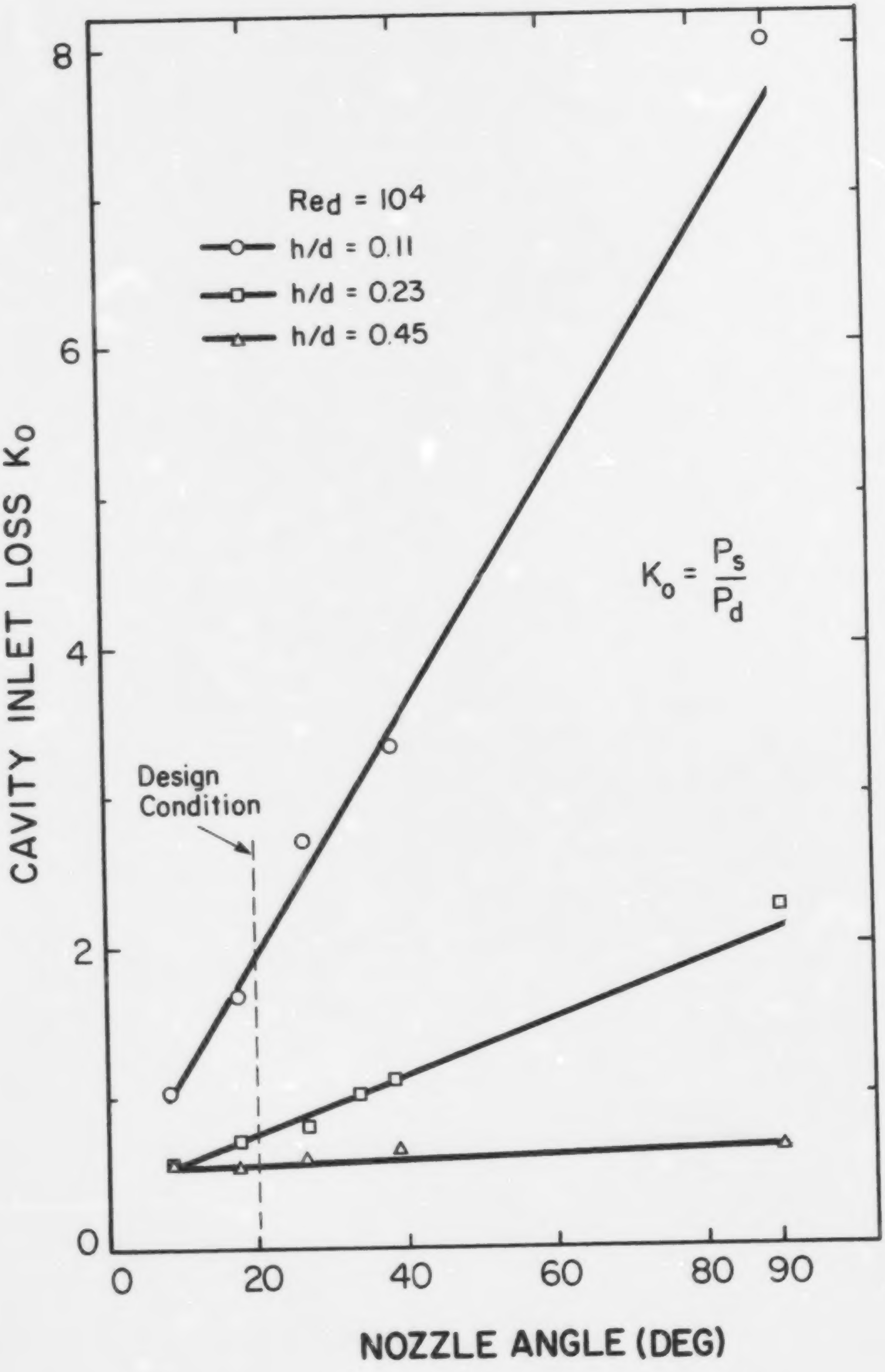

Figure B13 Effect of nozzle angle on cavity-entry head losses for three values of h/d at $Re_d = 10^4$

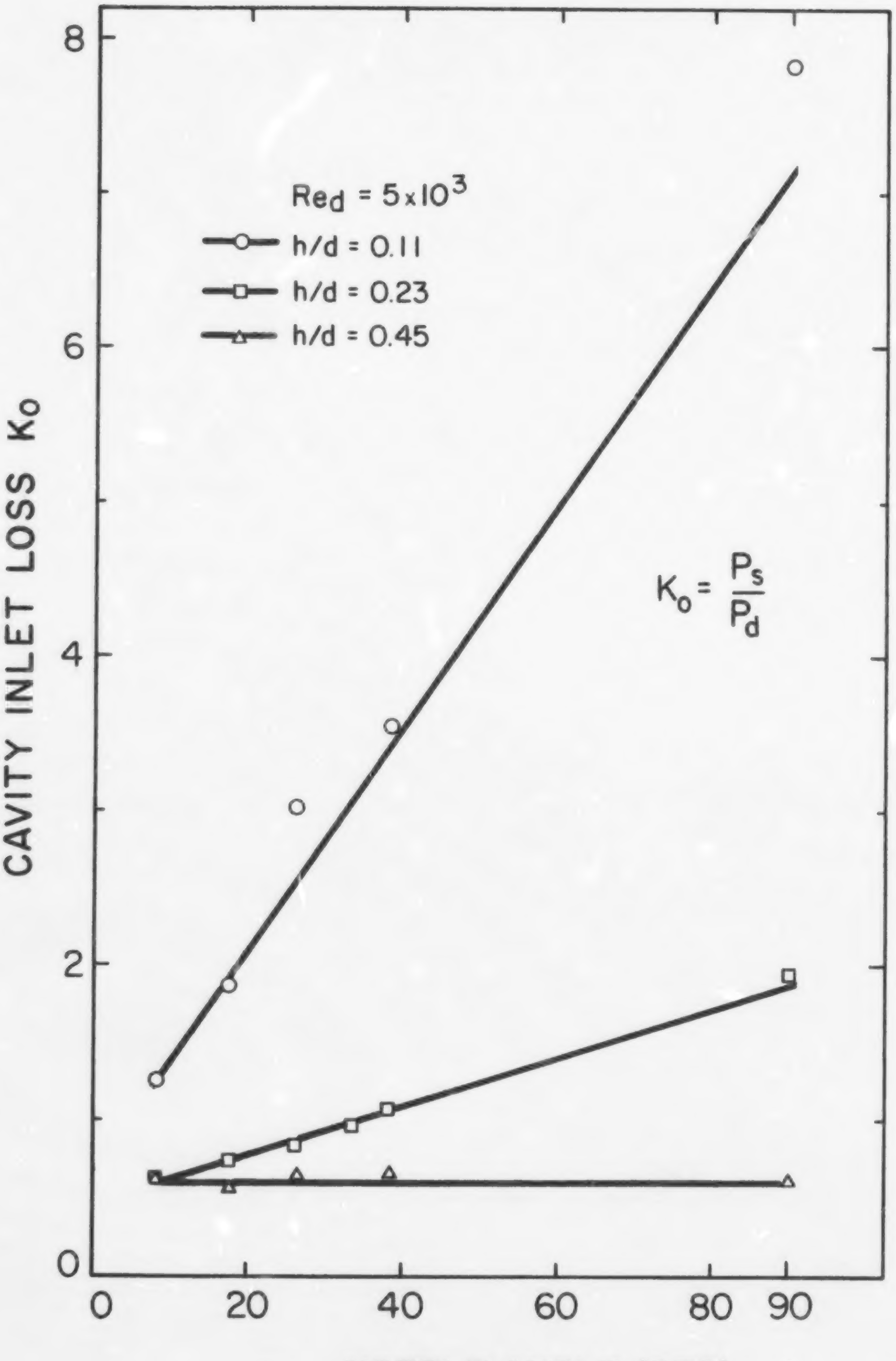

Figure B14 Effect of nozzle angle on cavity-entry head losses for three values of h/d at $Re_d = 5 \times 10^3$

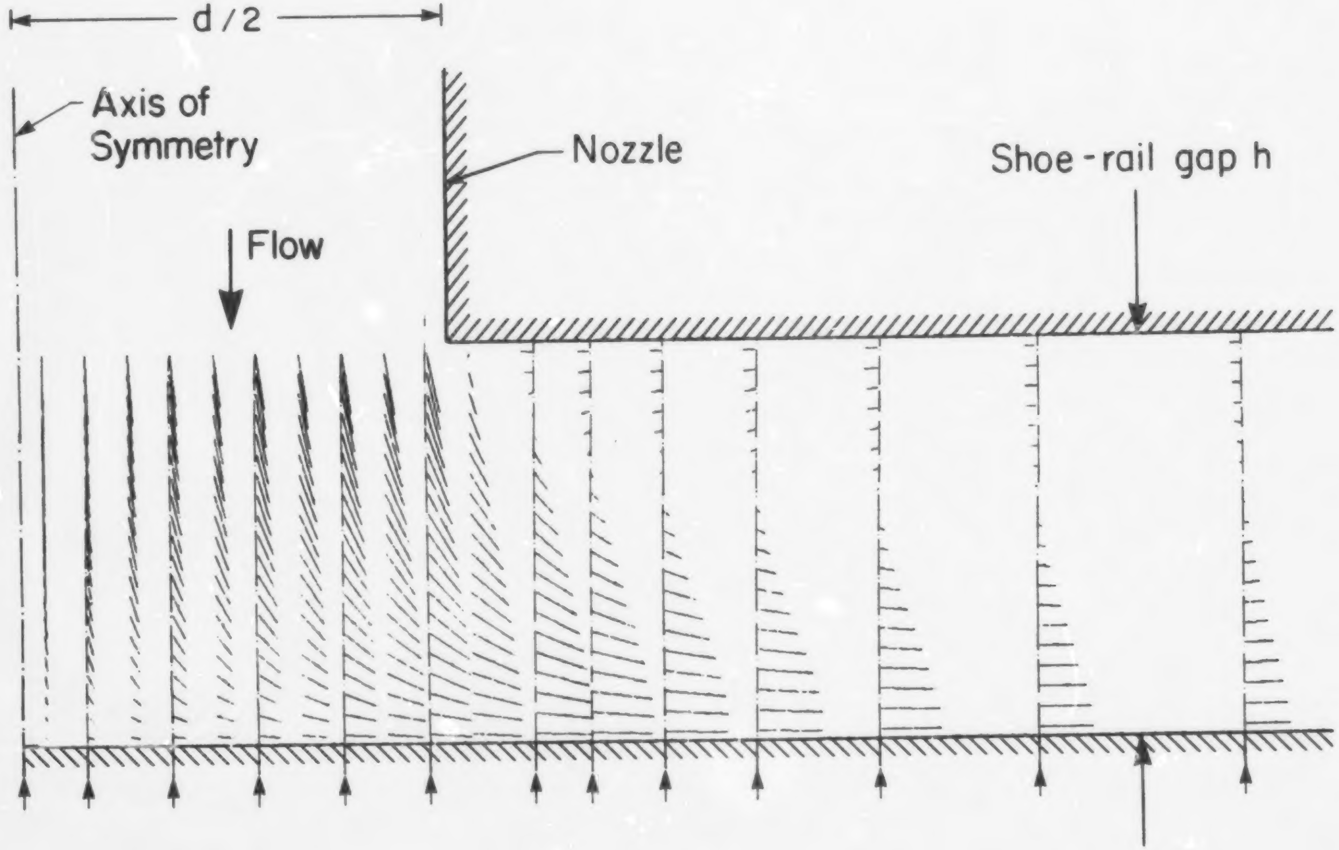

Figure B15 Velocity vector plot of flow field for a sharp edged radial nozzle and h/d = 0.5 as determined by numerical solution of equations modelling turbulent flow. The arrows locate the base lines of the velocity vector

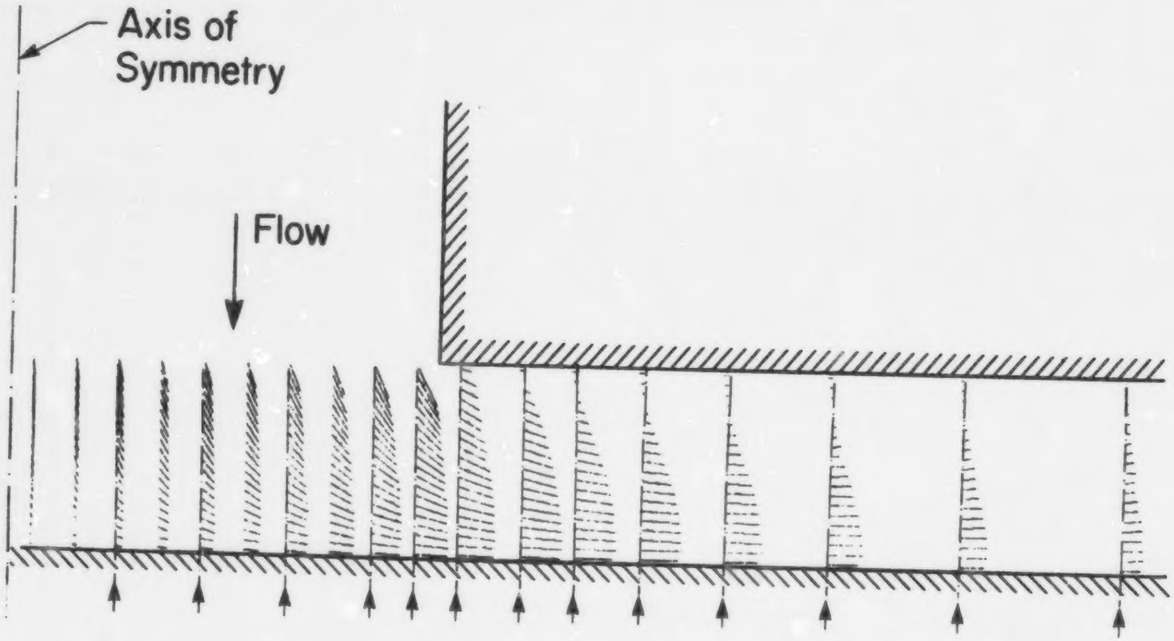

Figure B16 Velocity vector plot of computed flow field for a sharp edged radial nozzle and h/d = 0.25. The arrows locate the base lines of the velocity vectors.

along vertical lines located by the arrows at the bottom plate. Thus a line extending to the right or left of its base point indicates flow to the right or left. Also note that although some of the vectors immediately adjacent to walls are relatively large, this does not imply the existence of fluid slip there. The boundary layers are too thin to be represented.

Both plots show a stagnation point on the bottom plate at the axis of symmetry, flow separation at the nozzle edge, and a separation bubble or weak standing eddy extending downstream. For h/d = 0.25 the length of the separation bubble is about 3.5h. This bubble acts as an obstruction to the flow of the fluid that is not recirculating inside it and, in effect, forms a convergent-divergent nozzle through which the escaping fluid must pass. In passing through this "nozzle" the escaping fluid must accelerate and reach a maximum speed at the throat, and the subsequent downstream deceleration that occurs as the fluid spreads radially and vertically is probably the main source of the hydrodynamic losses. Momentum balance considerations (see Appendix N) imply that this deceleration must be accompanied by a pressure rise, so that the fluid pressure at the throat can be substantially below that far away from the nozzle. In terms of the SailRail terminology, this implies that in the neighbourhood of the radial nozzles there may be substantial "suction" relative to the shoe cavity pressure p_c.

If this picture of the fluid loss process is correct, then modification of the radial nozzle geometry to eliminate the separation bubble, or at least to greatly reduce its size, should greatly reduce the nozzle resistance. Since the sharp edge of the radial nozzle is the immediate cause of separation, then removing it by contouring, as shown in Figure B4, should achieve the desired goal. The data in Figure B6 shows that the resistance of the contoured radial nozzle is much smaller than both the sharp edged radial and the inclined nozzle, thus confirming the hypothesis about losses.

Currently available numerical methods in fluid mechanics for computing turbulent flows are not capable of solving for the complex geometry of the inclined nozzle.

B.8 Measured Pressure Distributions for Radial and Inclined Nozzles

Typical measured pressure distributions on the bottom disc for the radial nozzle are given in Figures B17 and B18. In both cases the pressures are expressed as fractions of the stagnation pressure observed on the axis of symmetry, and radial distances are referred to the nozzle diameter. Figure B17 shows the effect of Reynolds number at h/d = 0.229, and Figure B18 shows the effect of h/d. All results show the region of negative pressure or suction predicted by the theory, and the suction peak increases rapidly as h/d decreases. For h/d = 0.109 this suction is about 80% of the stagnation pressure. All cases show that pressure recovery is complete at a radial distance of 3-1/2d to 4d. Note that the results show only a modest effect of Reynolds number on the pressure profiles. Figures B19 and B20 compare the measured pressure distributions for both top and bottom discs with the theory for h/d = 0.229 and 0.466; agreement between the two is satisfactory.

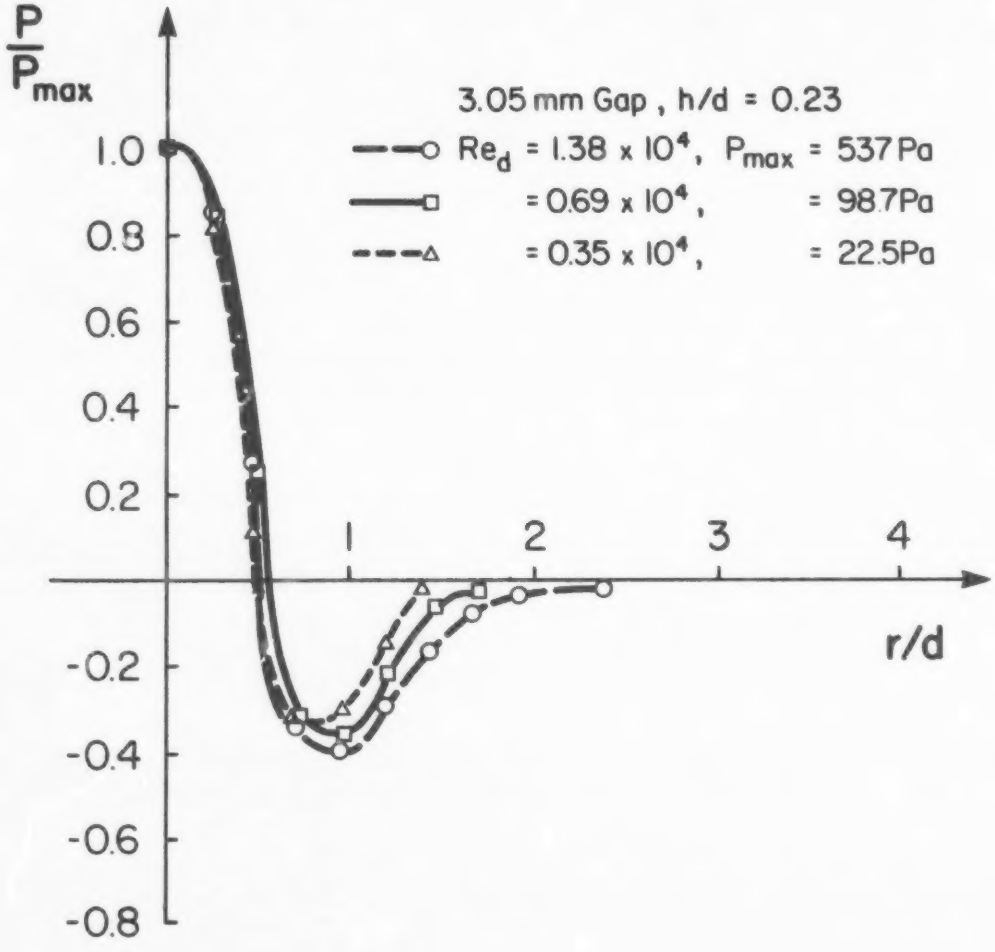

Figure B17 Effect of Reynolds Number Re_d on pressure distribution on bottom disc for sharp edged radial nozzle

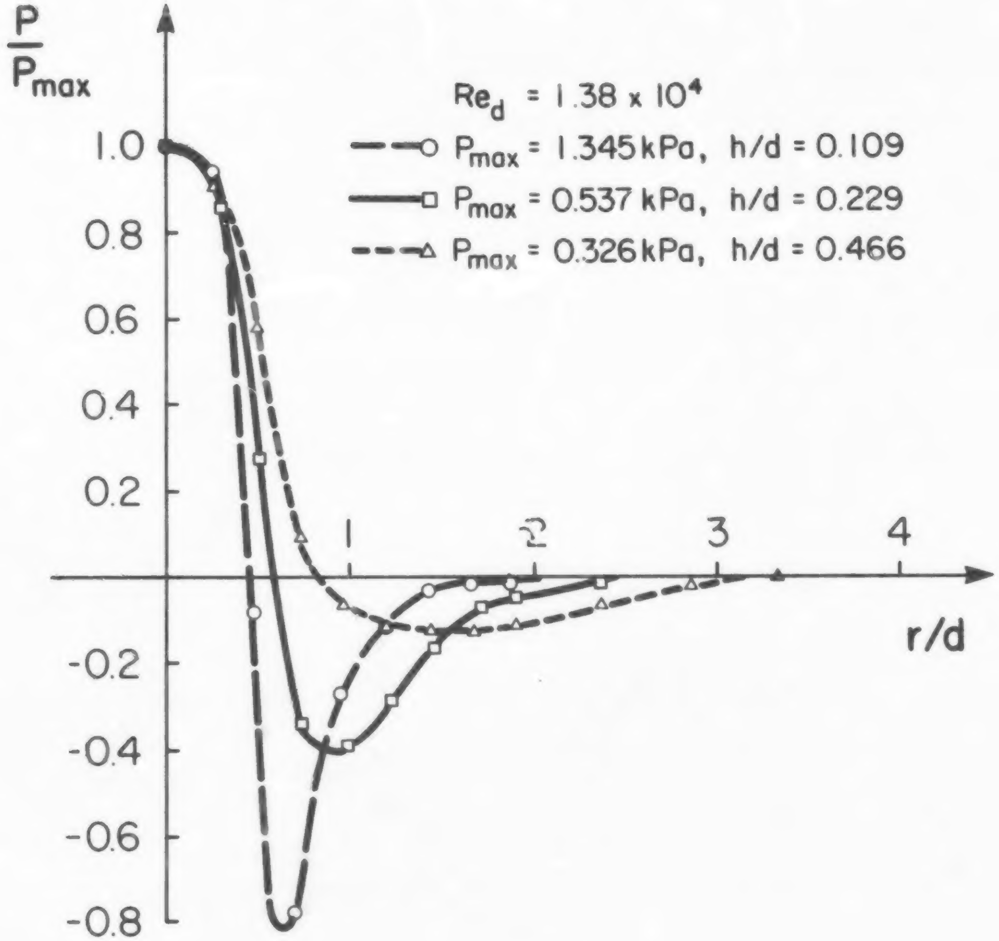

Figure B18 Effect of h/d on pressure distribution on bottom disc for sharp-edged radial nozzle

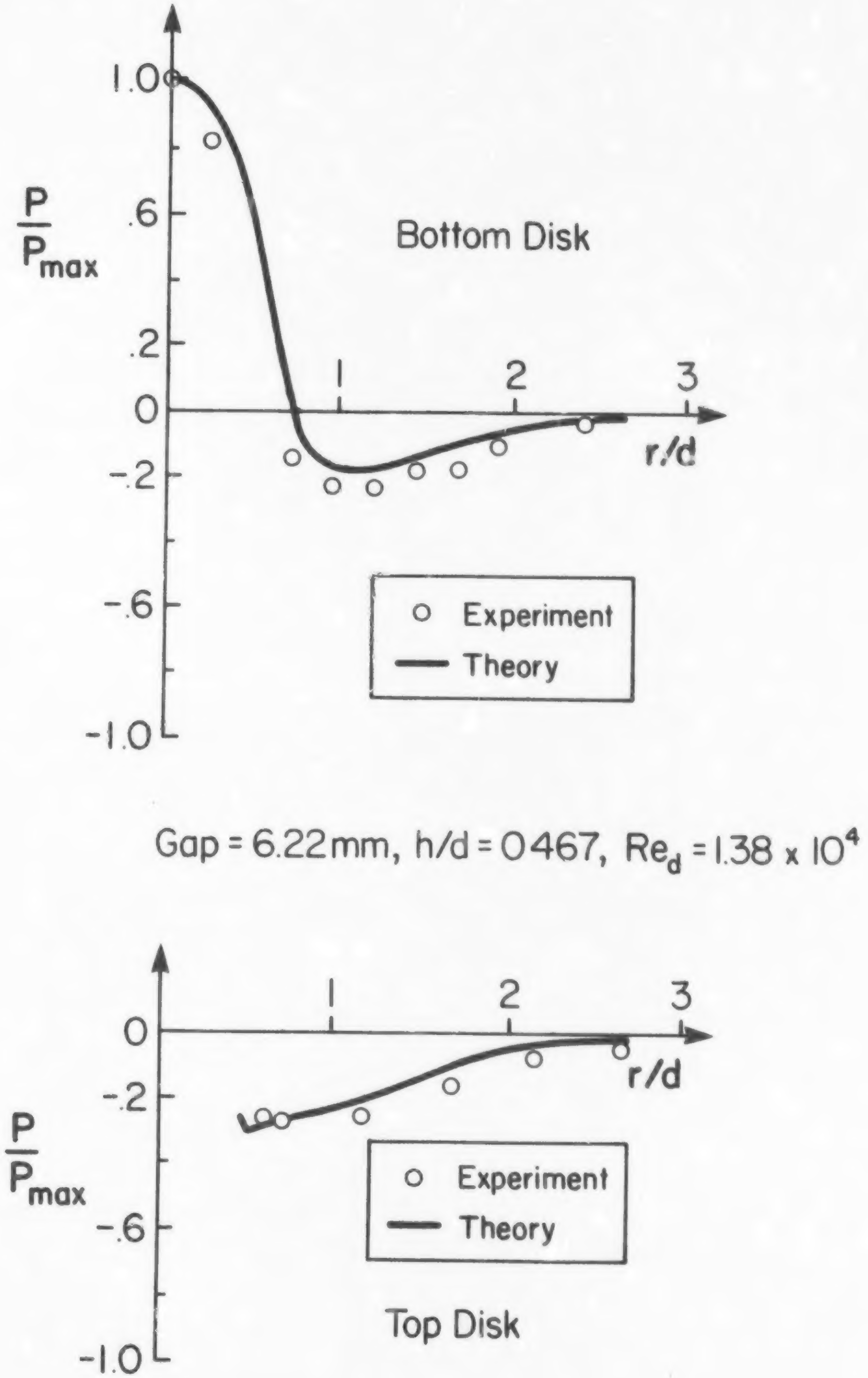

Figure B19 Comparison of measured and predicted pressure distributions for sharp edged radial nozzle and $h/d = 0.467$

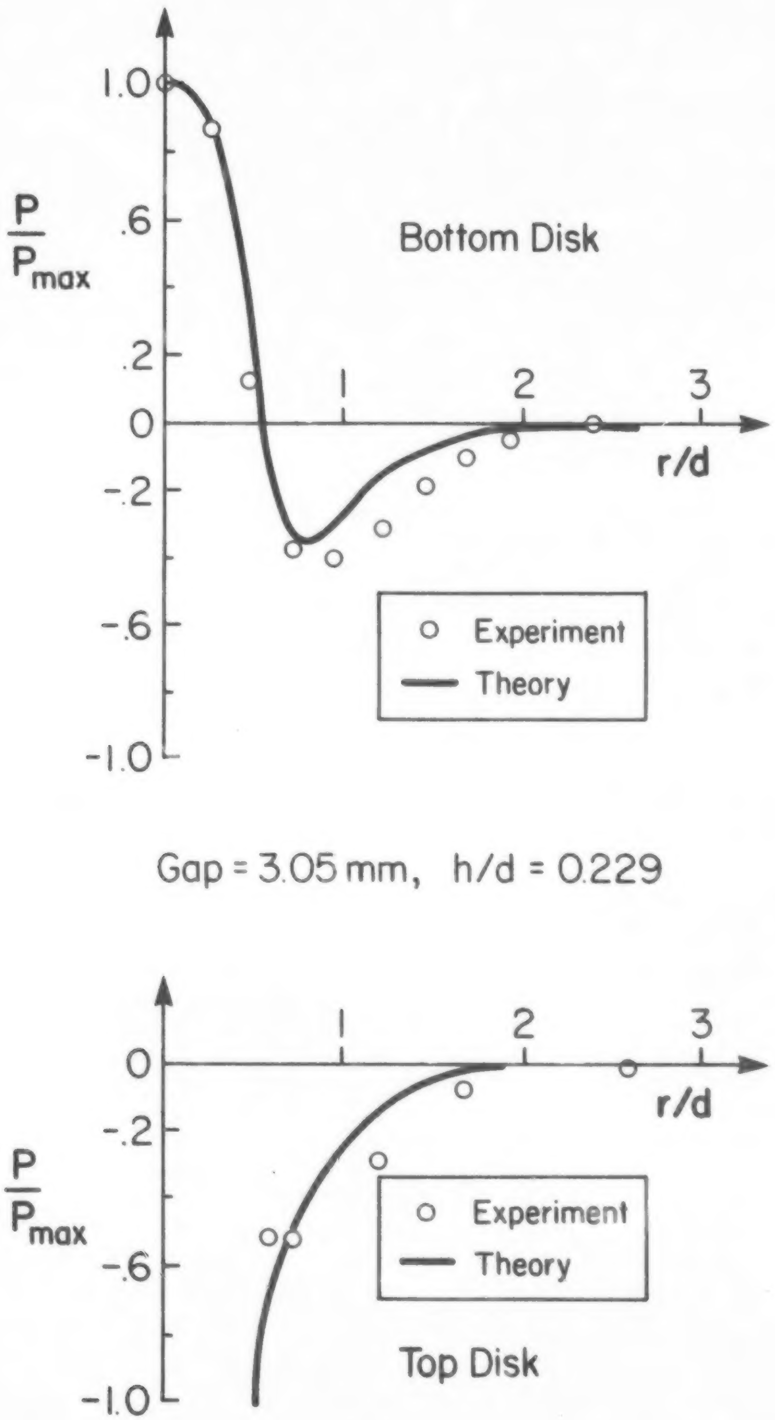

Figure B20 Comparison of measured and predicted pressure distributions for sharp edged radial nozzles and h/d = 0.229

Figure B21 gives the measured pressure distributions for the inclined nozzle along the 0^0 and 180^0 radii defined in Figure B3. These distributions reflect the asymmetry of this nozzle, but otherwise they have the same qualitative structure as those for the radial nozzle. There is a stagnation region and areas of suction adjacent to the nozzle edges. And, as one might expect, since along the 0^0 radius the fluid has to negotiate a 160^0 turn when leaving the nozzle, the suction is much greater than on the 180^0 radius. Also, as for the radial nozzle, the magnitude of the suction increases as h/d decreases. On the 0^0 radius it is greater than that of the radial nozzle; typically for $h/d = 0.23$, the peak suction is about $-0.4\ p_{max}$, for the radial nozzle, whereas it is $-0.8\ p_{max}$ for the inclined nozzle. Figure B22 gives the pressure distributions on the bottom disc along the $\theta = 45^0$, 90^0 and 135^0 radii for $h/d = 0.23$; it shows that the peak suction decreases as θ increases, and beyond $\theta = 75^0$ is less than that for the radial nozzle.

B.9 Flow Visualization

Visualization of the pattern of streamlines of the flow adjacent to the discs of the scaled up model was obtained by the following technique. The surface of the disc was painted with a mixture of titanium dioxide, silicone oil and kerosene. The model was then assembled, and air was pumped through it to evaporate the kerosene and set the pattern. Photographs of the results are given in Figure B23. For the sharp-edged radial nozzle the reattachment line of the separation bubble predicted by the numerical computations is clearly defined. The photograph of the inclined nozzle pattern shows a distinct boundary between the fluid at rest and the air escaping from the nozzle. A well-defined jet is formed and this jet appears to persist for a much greater distance downstream from the nozzle than suggested by the pressure measurements.

B.10 Discussion and Conclusion

The experimental data presented here provide one explanation of the way inclined nozzles can give better overall performance than sharp edged radial nozzles. Depending on their location in the cavity region, they may substantially reduce the hydrodynamic losses associated in delivering the air from the rail manifold. Now it has been speculated that the inclined nozzles can also act as injectors by pumping air against adverse pressure gradients into regions where it is required. The flow visualization in Fig. B23 lends support to this possibility, but based on the evidence currently available to us, we have to conclude that it is unlikely. Firstly, such an effect cannot be significant in the cavity region, since that is the region of highest pressure between shoe and rail and it is where the lift air should be delivered. Hence it could only be of value in the seal region at the periphery of the cavity. Figure J1 (p. 188) is a flow visualization obtained for the original standard feed hole pattern, which used a set of nozzles located at 15^0 from the rail centre, but oriented inwards. It is thought that this set is in or near the seal region, and it is clear that any momentum effect acts for only a short distance. All the air from this nozzle flows outward at right angles to the side of the shoe, as if under the action of the pressure gradients in the seal region, in the manner discussed in Appendix A. However, as noted in Appendix D (see Figure D13),

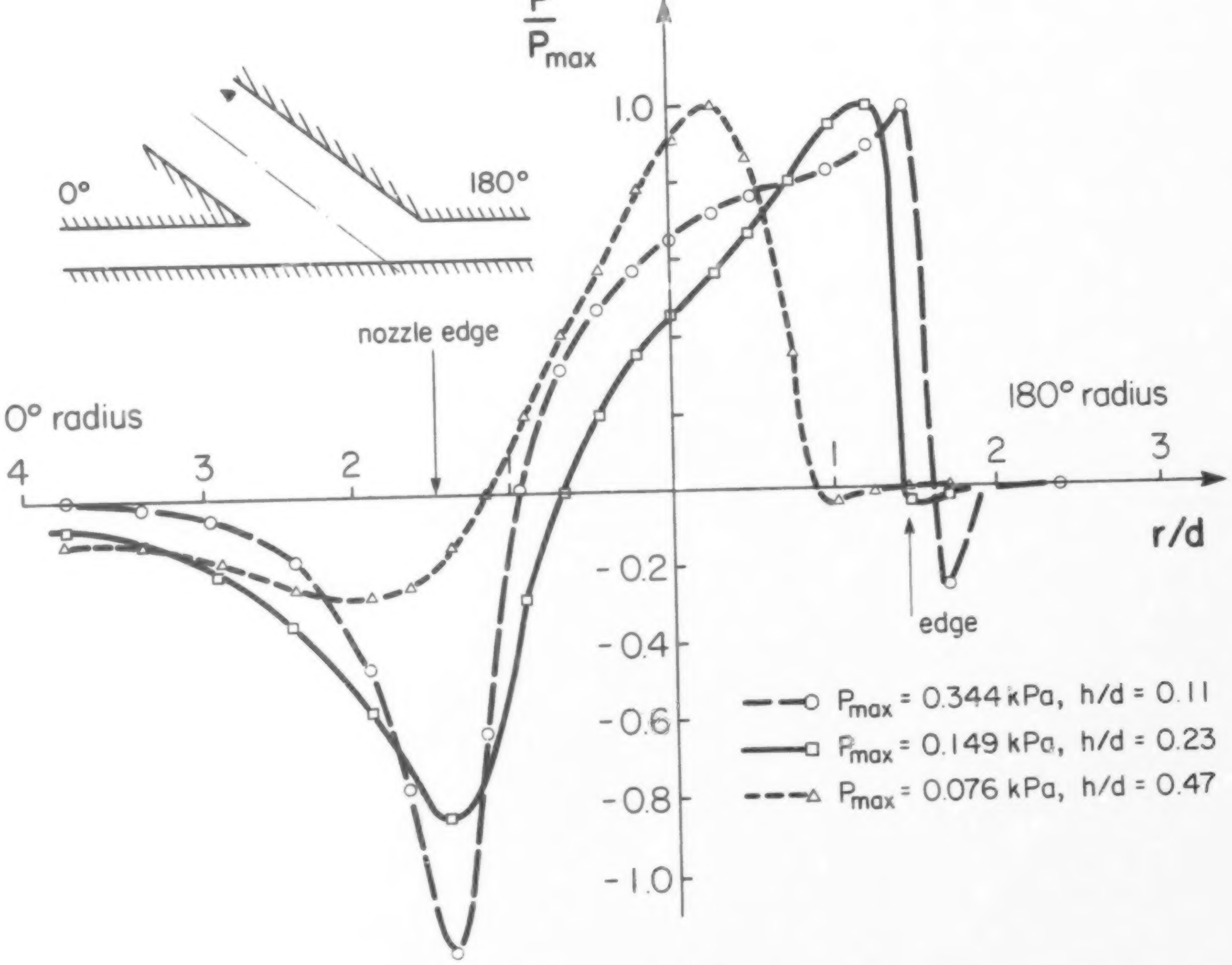

Figure B21 Measured pressure distributions on bottom disc for inclined nozzle along 0^{o} and 180^{o} radii defined in Figure B3.

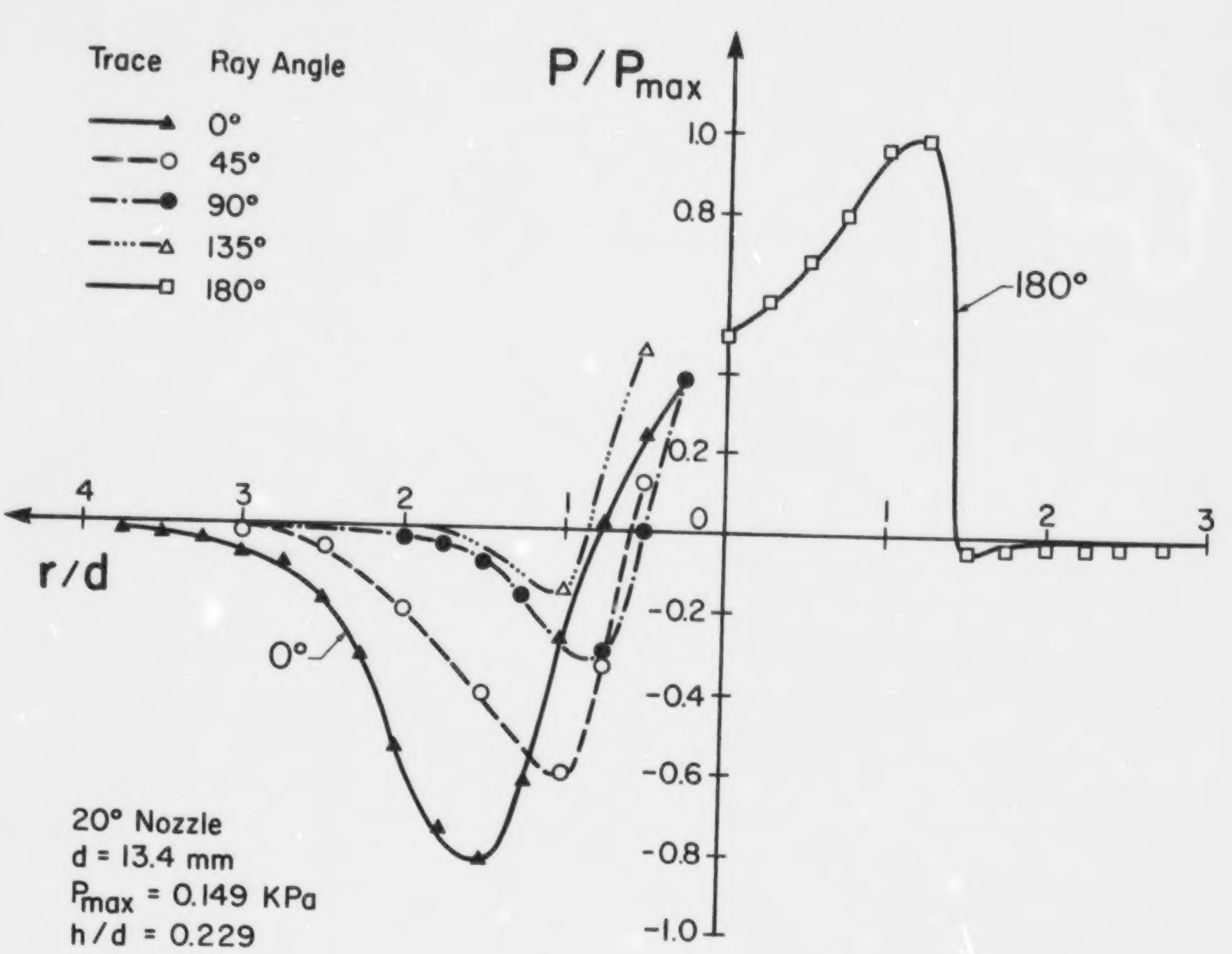

Figure B22 Measured pressure distributions on bottom disc for inclined nozzle along radii defined in Figure B3.

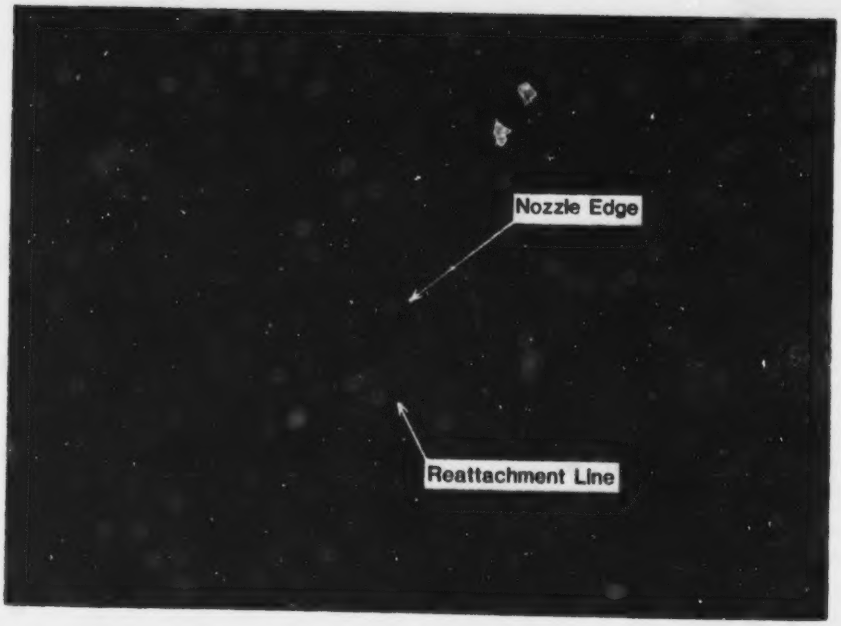
Nozzle Edge
Reattachment Line

Figure B23(A) Flow visualization for sharp-edged radial nozzle, top disc.

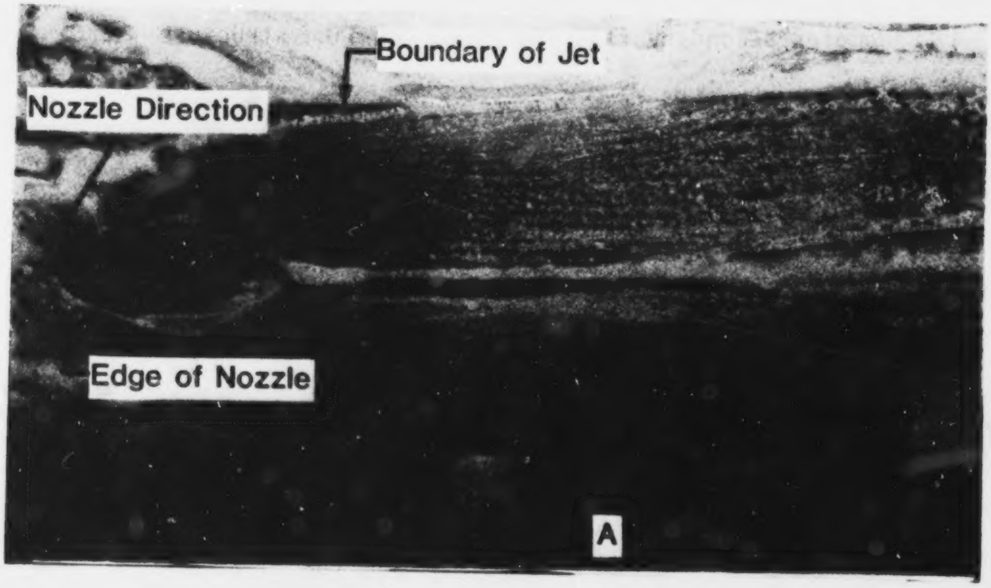
Boundary of Jet
Nozzle Direction
Edge of Nozzle
A

Figure B23(B) Flow visualization for inclined nozzle, top disc, showing extent of jet. The large accumulation of titanium dioxide such as that marked "A" are caused by surface tension effects in the liquid-solid suspension, and indicate the absence of any significant flow. The boundary of the nozzle is marked.

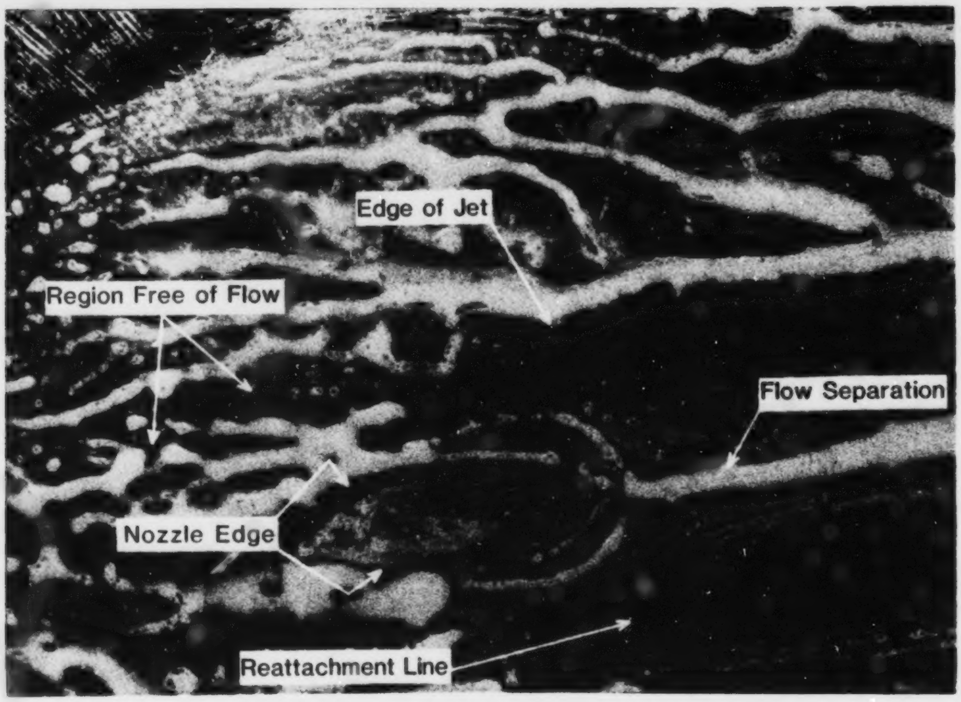
Edge of Jet
Region Free of Flow
Flow Separation
Nozzle Edge
Reattachment Line

Figure B23(C) Flow visualization for inclined nozzle, top disc, showing details of flow. Indications of flow separation and reattachment as marked suggest a complex secondary flow with a vortex-like structure

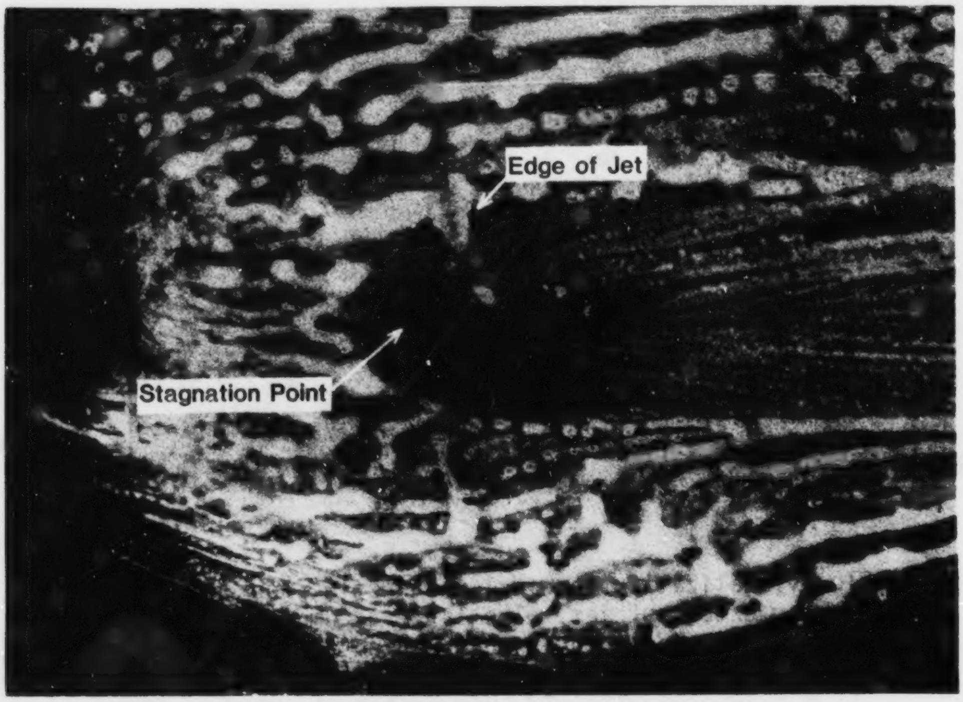
Edge of Jet
Stagnation Point

Figure B23(D) Flow visualization for inclined nozzle, bottom disc.

more evidence is required before this injection effect should be completely ruled out. If the purpose of the nozzle is to act as a pipe delivering air to a volume, the cavity region, then the present flow phenomenon is equivalent to that generated by an obstruction placed directly in front of the pipe entrance to the volume. In a well designed system this obstruction would be eliminated, if possible, to make p_2 equal to the cavity pressure p_c or $C_{Q1} = 1$ and $K_0 = 0$.

The presence of regions of negative pressure in the scaled up model tests for both the sharp edged radial and inclined nozzles has two implications. The first is the generation of hydrodynamic losses discussed above, but the second relates to a possible explanation of the importance of the bending stiffness of the cover. The pressure distributions in Figure B18 for the radial nozzle can be used to compute the resultant pressure force on the bottom disc of the scaled up model. Assuming axial symmetry the force F_p is given by

$$F_p = 2\pi \int_o^R p(r) r dr, \tag{B9}$$

or in nondimensional form

$$C_F \triangleq \frac{F_p}{p_{max} A_{r1}} = \frac{8}{d^2} \int_o^R \frac{p(r)}{p_{max}} r dr \tag{B10}$$

For $h/d = 0.109$, in spite of the presence of a stagnation region at $r = 0$, there is a resultant suction force on the bottom disc in the neighbourhood of the nozzle of 0.409N so that $C_F = -2.19$. It implies that if the disc is replaced by a layer of tissue or other highly flexible material this suction force could reduce h near the nozzle. According to the analysis in Appendix N, the head losses K_0 depend on h/d through the relation

$$K_0 = C_{Q1}^{-2} - 1 = 0.088(d/h)^2 - 1 \tag{B11}$$

so that K_0 increases very rapidly as h/d decreases. One way of preventing this additional loss would be to place between the flexible material and the air flow a sheet of material having sufficient bending stiffness to distribute the suction force over a much wider area of tissue.

For the inclined nozzle the pressure data was not integrated to determine if there was a resultant suction force, however an exploratory experiment was performed. To qualitatively simulate the shoe structure a 1 cm layer of tissue was placed on the bottom plate and covered with polyethylene sheet having a specified thickness. The top plate was painted with the flow visualization mixture, the model was assembled, and air pumped through it at a representative flow rate. Two cover thicknesses were tested, 0.15 mm (0.006 in) and 0.61 mm (0.024 in), and Figure B24 gives the results obtained for the thick cover; the results for the thin cover were very similar. The general character of the flow has changed completely from that shown in Figure B23. The streamlines emerge from the nozzle normal to its periphery; this is characteristic of the slot-orifice flow that would be expected if h/d is very small. It indicates that h has been greatly reduced.

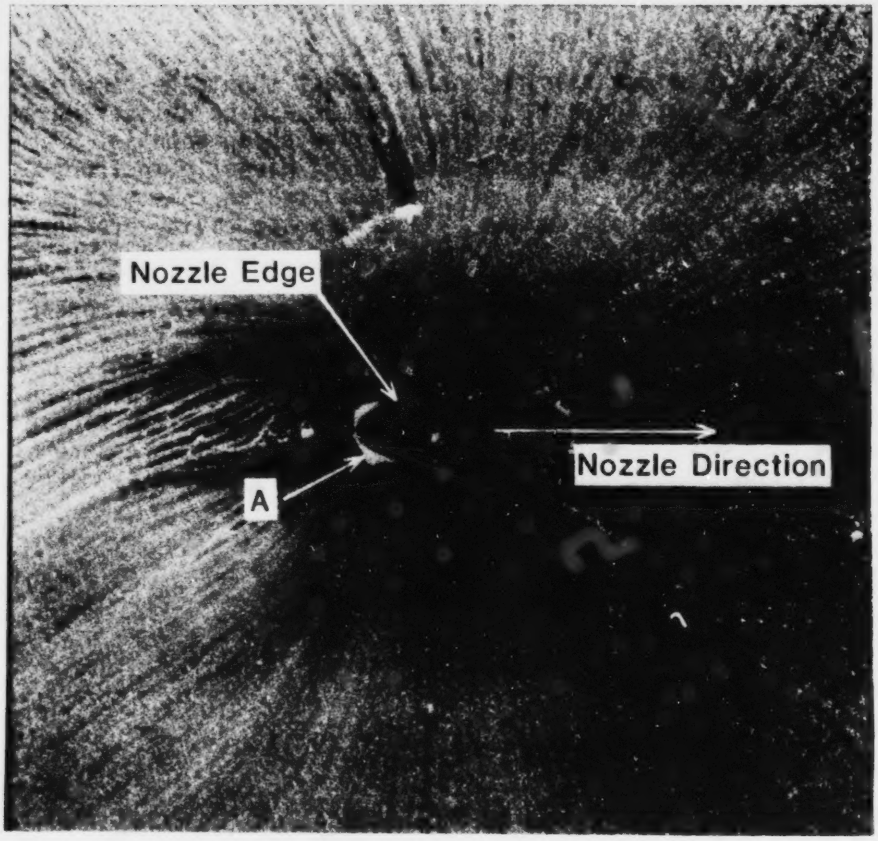

Figure B24 Flow visualization for inclined nozzle with 10mm of tissue and 0.61mm polyethylene sheet placed on bottom disc. The accumulation of titanium dioxide at the part of the nozzle periphery marked A is probably caused by a small separation bubble associated with the turning of the flow through 160^{0}. Other than this, the flow is source-like.

Since in this experiment no attempt was made to scale tissue and cover flexibility, the significance of the result is unclear. However it indicates that an important part of any follow-on work should be the construction of a large-scale model in which flexibility is correctly scaled. In this respect, many turbulent flows become independent of Reynolds number Re_d if Re_d is above a certain critical value. This applies to head losses in pipes and fittings. If the flow is dominated by separation at sharp edges, as is the case for the SailRail system, then the critical Re_d can be relatively small. The data for C_{Q1} and K_Q obtained from the scaled up model is essentially independent of Re_d. This implies that a model designed to investigate the flexibility need not satisfy Reynolds number scaling. Hence the design can be greatly simplified.

APPENDIX C. PROTOTYPE TEST BED RESULTS (P. A. Sullivan, M. Simard, and T. A. Graham)

C.1 Introduction

During the previous Contract period, to evaluate the SailRail system, a prototype test bed had been built. Its objective was to provide reliable data on the effect on system performance of a number of unconventional features of the design. This included the geometry and layout of the air feed holes in the rail, and various aspects of the shoe construction. Figure C1 is a photograph of the apparatus. However, only a very limited amount of preliminary data was obtained.

For the previous Contract, the performance criterion was the air supply pressure p_t in the rail manifold required to initiate motion under the action of known driving weight. This has been changed to the time Δt required to travel a specified distance at a given value of p_t. It was envisaged that the latter criterion would give more consistent results, since it averages out the effects of local irregularities in both the track geometry and coefficient of sliding friction. Furthermore, it gives results of direct interest to the designer, since it can be used to calculate the effective coefficient of sliding friction of the system.

The rail initially used by SailRail was extruded from a PVC plastic; it had cross section II (shown in Appendix M), and the results obtained during the previous Contract were mainly for this rail. Some results were obtained for a just introduced aluminium rail (Section III), but this rail was subject to considerable surface wear. As a result, the subsequently manufactured rails were given a hard anodization and teflon impregnation surface treatment, and when rails having this treatment were installed in the test bed, substantial reductions in transit times were obtained. This was believed to be associated with both reduction in the forces arising from sliding friction, and with closer tolerances on rail profile. However the deceleration forces caused by these reduced transit times caused severe misalignment of the rig. This problem was solved by installing a deceleration system which used shock absorbers to reduce the forces involved and which transmitted them directly into the laboratory floor. This is shown in Figure C1. A pneumatic cylinder load return system was also installed to speed up testing and to ensure a consistent return motion for the pallet. Finally, the time-consuming task of changing shoes by using manually operated hydraulic jacks to raise the pallet was eliminated by incorporating a lift system using inflatable air bags and the laboratory compressed air supply.

Figure C2 shows typical results obtained by the transit time method. The curves give transit time Δt as a function of p_t, and they show asymptotic decay at both low and high p_t. For low p_t, the limit corresponds to no pallet motion, whereas for high p_t, the limit corresponds to zero friction between shoe and rail. The latter limit, which is called the inertial time, can vary slightly from test to test owing to a variety of factors, but was about 3.5 to 3.6 seconds for most tests. Now it appears that, of the two performance criteria, the transit time method is more sensitive to design changes than the initial motion method. However, for the transit time method one has to choose a value or range of values of p_t

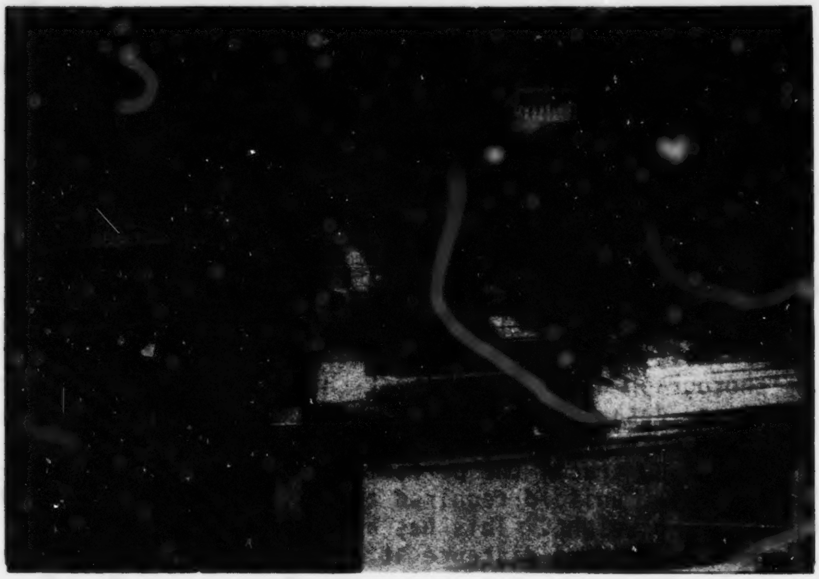

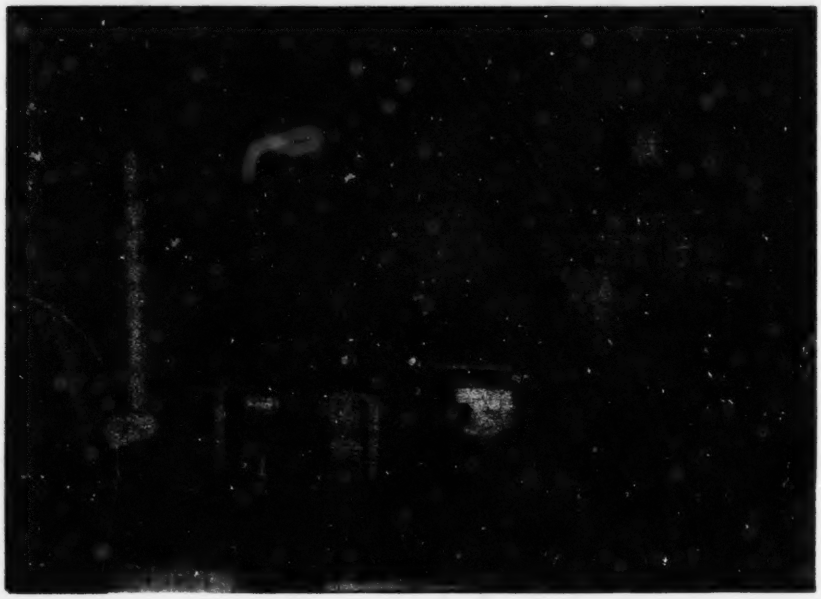

Figure C1 Prototype test-bed apparatus. In the lower photograph a typical SailRail shoe is installed on the left side of the pallet and the simplified shoe is installed in the right side. The upper photograph shows the decelerating mechanism.

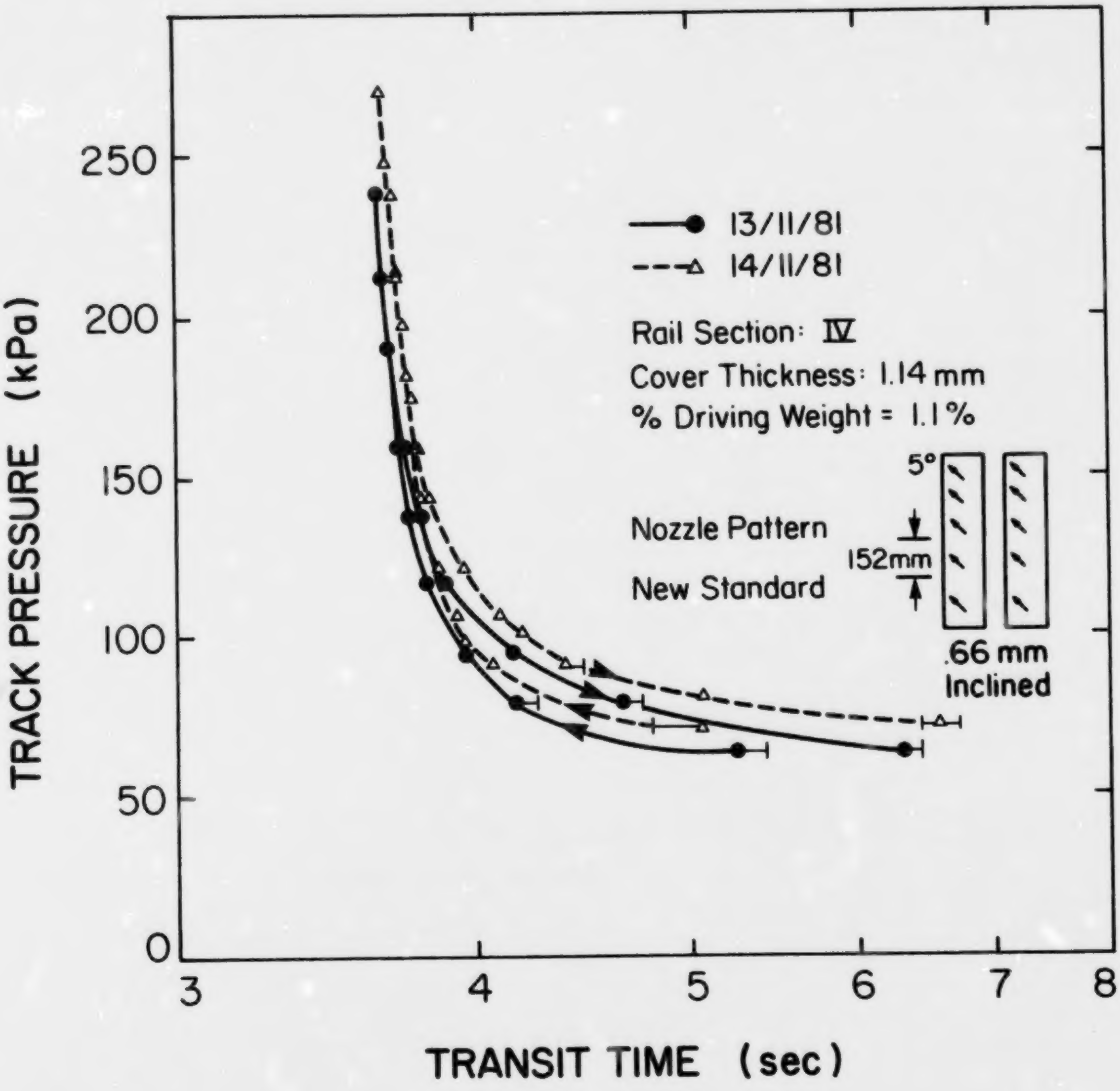

Figure C2 Typical transit time data obtained from the prototype test bed.

at which to make the comparison. One approach might be to use values of p_t equal to those used in current practice, but the design has been evolving rapidly so that these can change. Furthermore, as the value of p_t is increased, the test ultimately loses its sensitivity, since all times approach the inertial limit. Hence there is an optimum value of p_t for maximum discrimination, but in general this is not known initially, and may vary from test to test. Consequently we have adopted the practice of presenting the data in graphical form for the complete range of p_t used in the tests, even though this is, perhaps, more cumbersome than using a single number such as transit time or equivalent coefficient of friction at a nominal value of p_t. It has also been found that the sensitivity of the test depends critically on the choice of the mass M_d of the driving weight. For example, tests on aluminium rail using $M_d = 2.2\% M_p$, which corresponds to a 1.25^0 inclination in a warehouse installation, gave time differences of only a few hundredths of a second for p_t in the range used in practice, which is 130 kPa and above. Hence a value of M_d of approximately 1.1% M_p was used for most of the tests.

The data for the effect of p_t on transit time was initially taken twice in any given test, first with p_t increasing to an upper limit of about 250 kPa, and then with p_t decreasing. This is shown in Figure C2. The curves obtained in this way showed remarkably little scatter, in fact this scatter was so small that a slight but consistent tendency to longer-transit times on the decreasing p_t portion of the test cycle was observed. No explanation for this shift was obtained, and it could not be eliminated; consequently, for comparison purposes, only data for the increasing p_t portion of the cycle was used.

The layout of the nozzles used by the developer in his first designs is given in Figure C3a. During the course of the Contract this layout was changed to that shown in Figure C3b. This second pattern is here called the "new standard" layout to distinguishing it from the "original standard". Both layouts and certain variants of them were tested for the present Contract.

C.2 A Result from Preliminary Testing of the First Aluminium Rail Section

Initial testing of the first extruded aluminium rail (Section III of Appendix M) gave an unexpected result which both very effectively demonstrated the sensitivity of the system performance to the details of the geometry of the rail section, and supported the hypothesis developed in the previous contract about the lift mechanism. According to this hypothesis, a very thin cavity is formed between shoe and rail and, except in a narrow peripheral region, the air in the cavity is at rest and at constant pressure. In the peripheral region, which is called the "seal region", the air escapes to atmosphere. The incident occurred during tests originally intended to evaluate the effect of radial feed holes on system performance. Typical results are given in Figure C4; they show that, in contrast with all previous data, above p_t 100 kPa transit times increase rapidly with increase in p_t.

Now the original standard feed hole pattern was used in this rail, so that to simplify the supply of air, only one asymmetrically located web was used. It was suggested by one of us (TAG) that bending of the longer portion of the rail surface under the action of increasing p_t below it was

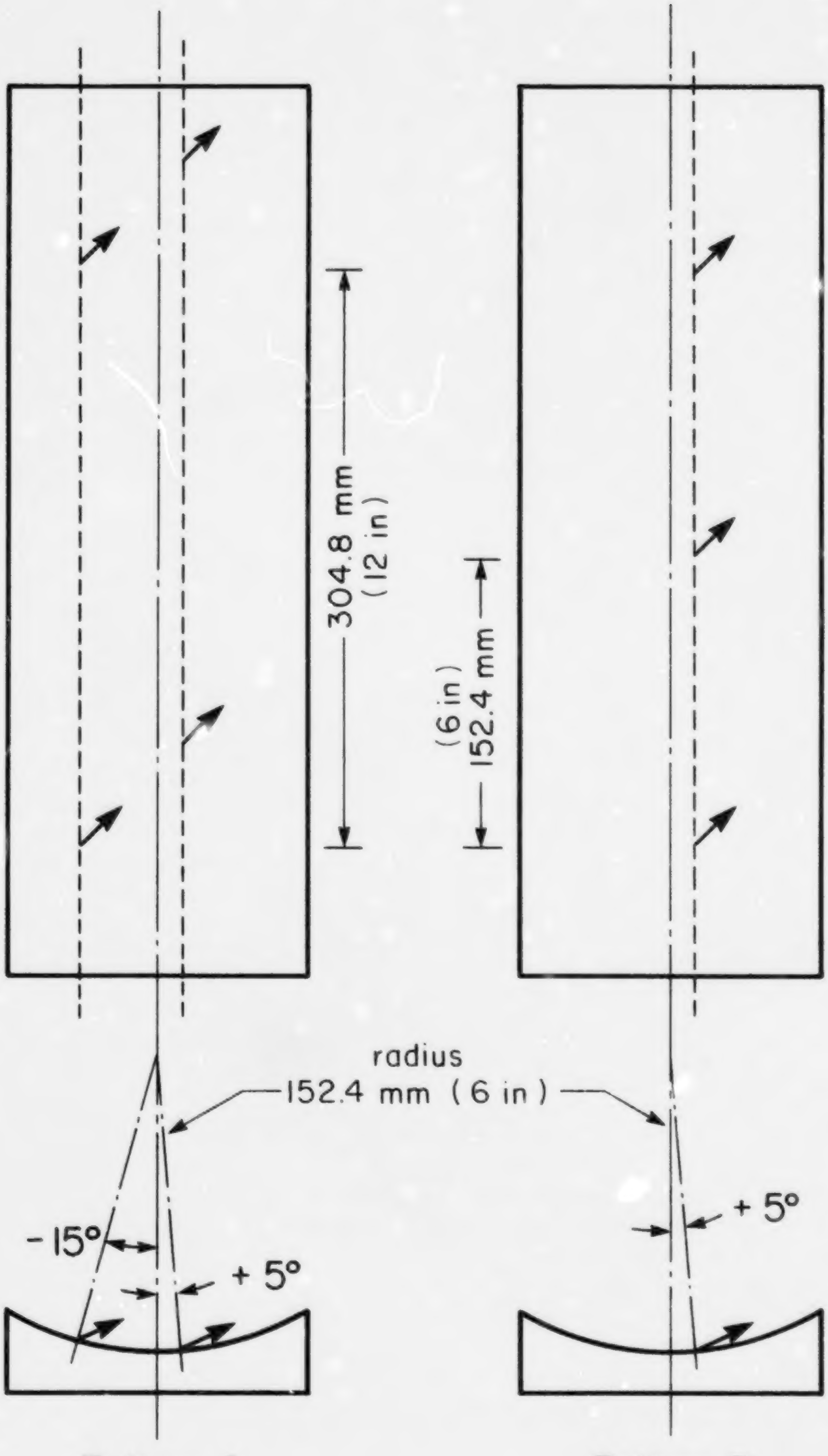
304.8 mm
(12 in)
(6 in)
152.4 mm
radius
152.4 mm (6 in)
- 15°
+ 5°
+ 5°
Pattern A
original standard
Pattern B
new standard

Figure C3 Nozzle patterns used in original and more recent development prototypes.

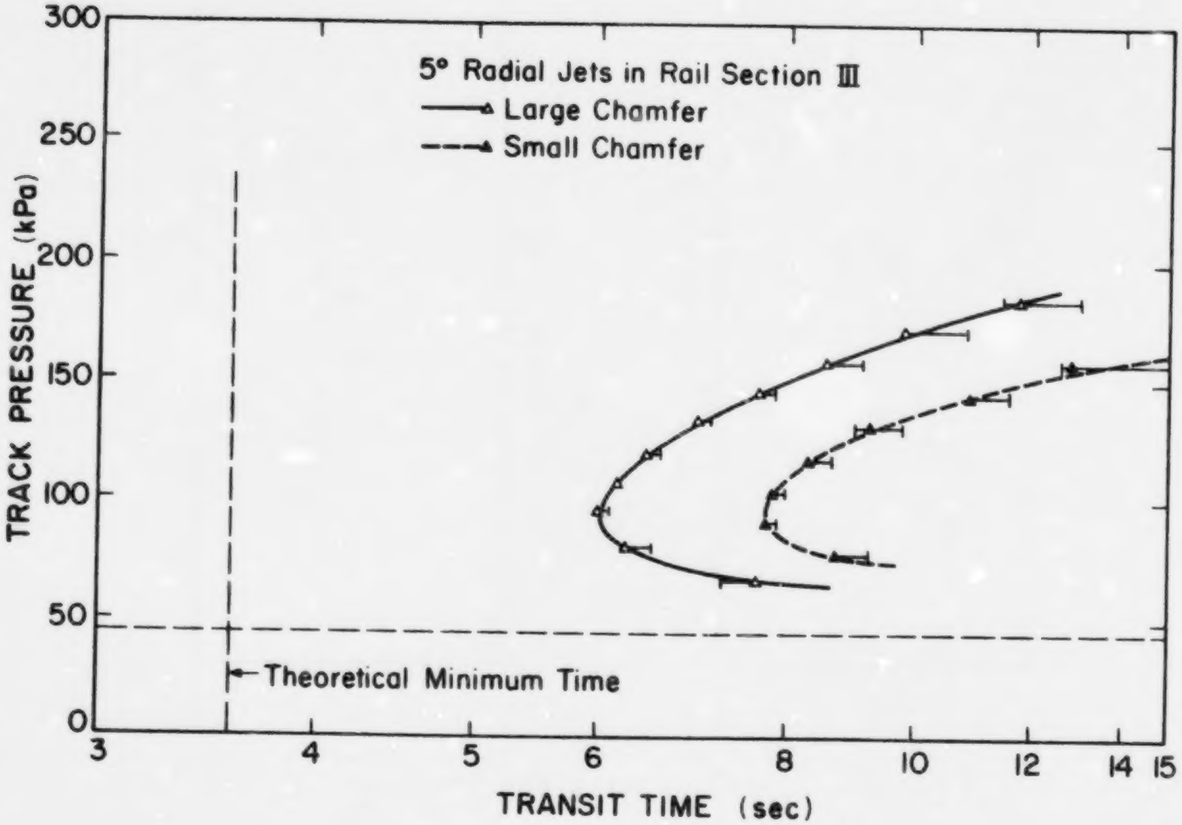

Figure C4 Transit time measurements obtained for rail section III ("single web rail"). New standard nozzle pattern was used.

forcing the seal region towards the centre of the rail, and thus reducing the width of the cavity region. This is depicted in Figure C5. Calculation of the midpoint deflection of the top surface obtained by using the formula for a clamped flat plate gave a value of 0.28 mm at p_t = 185 kPa, whereas measurement of this quantity gave a value of 0.14 mm. However, this measurement was obtained by using a dial gauge attached to the flange, and this would give a lower limit to the actual value owing to flange rotation. It compares with measurements of cavity height of 0.10 mm to 0.30 mm and estimated seal gap heights of less than 0.025 mm.

A second web was subsequently added to the rail by the manufacturer, and the new geometry became Section IV. Figure C6 compares the results of transit time measurements for the two sections. It shows that the problem has been completely eliminated.

C.3 The Problem of Repeatability of Test Bed Results

As noted in Section 2.2, data obtained on a developmental test bed prior to the commencement of the UTIAS research programme showed an unsatisfactory lack of repeatability. It was originally thought that the main cause was insufficiently rigid support of the rails, especially because plastic rail (Section II, Appendix M) was then in use. Therefore care was taken to ensure that the base of the test bed developed for the first Contract was very rigid. The preliminary data obtained using the initial movement performance criterion for driving weights M_d in the range 2% to 10% of M_p seemed to give acceptable repeatability [1, p. 14]. However, following adoption of the transit time method and the reduction in M_d it rapidly became clear that other factors were also very important. Now Figure C2 shows that the functional dependence of transit time on p_t obtained in any given test run is measured with remarkably little scatter. But this was not the case from day to day or when changes of shoe were made. In excess of 500 test runs were made in attempts to establish trends, and a pattern eventually emerged. No attempt has been made to present all the data so obtained; instead examples are given below to illustrate the main points.

The most noticeable feature is a "conditioning" effect in which the performance usually improves over a period of hours or even days. This is illustrated in Figure C7, which plots the history of transit time changes over an extended period. It was also observed that, in many cases, the conditioning process could be much more rapid, requiring hours instead of days to reach equilibrium. Figure C8 is an example of this behaviour; the set of curves 1 is the data obtained for an initial insertion and conditioning, whereas the set 2 were obtained after removal and immediate reinstallation of the shoes.

As a rule, the test results showed a tendency to stabilize after a sufficient period of time had elapsed; for example, Figure C2 presents data taken on successive days after an extended period of conditioning. However, this was not always the case, as the data given in Table C1 and Figure C9 shows. The characteristic feature is a high level of repeatability interspersed with occasional sudden changes. The developers have also encountered performance variability in their installations, and they suggested that an environmental factor, possibly humidity, might be important. The data given in Figure C9 seems to support this contention;

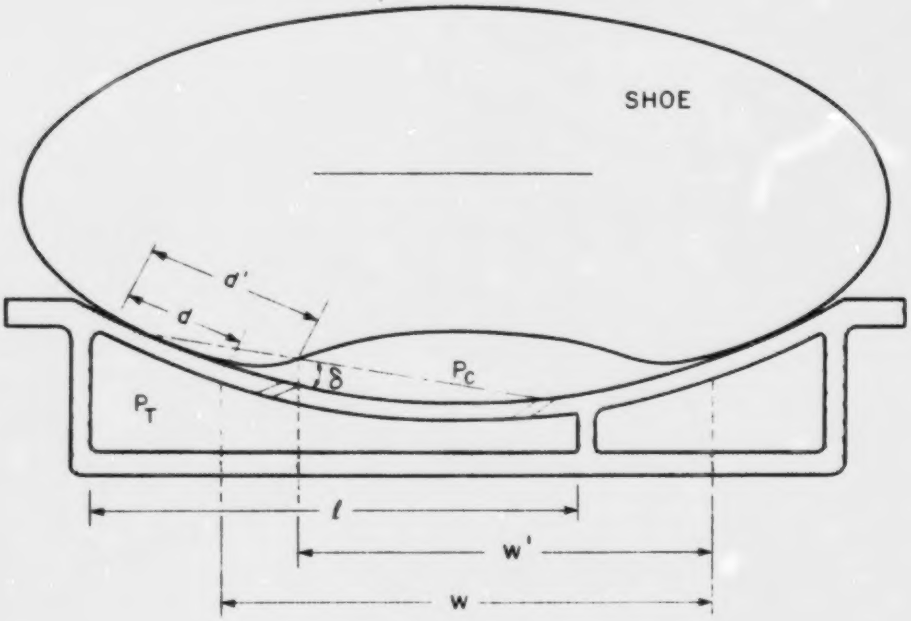

Figure C5 Bending of the top surface of rail section III caused by the track-cavity pressure difference p_t-p_c acting over the width ℓ. The deflection δ increases the width of the seal region from d to d', and reduces the cavity width w to w'.

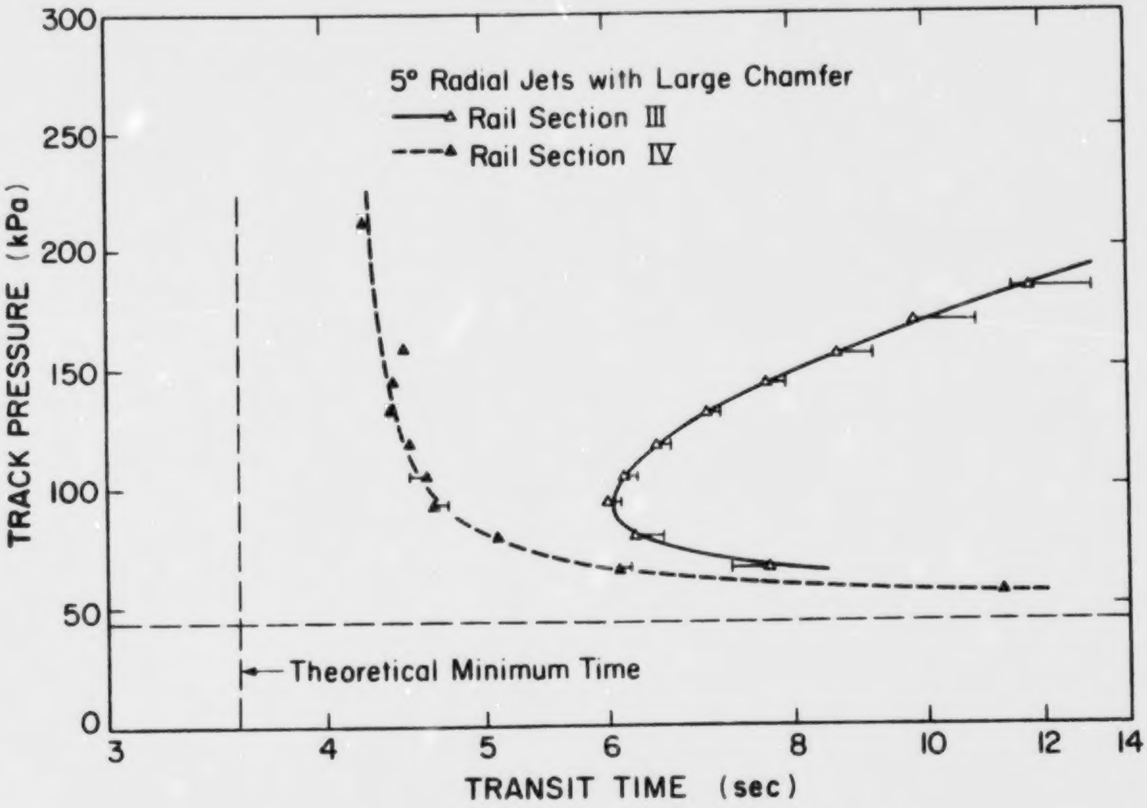

Figure C6 Comparison of transit time measurements for rail sections III and IV ("double web rail"). New standard nozzle pattern was used.

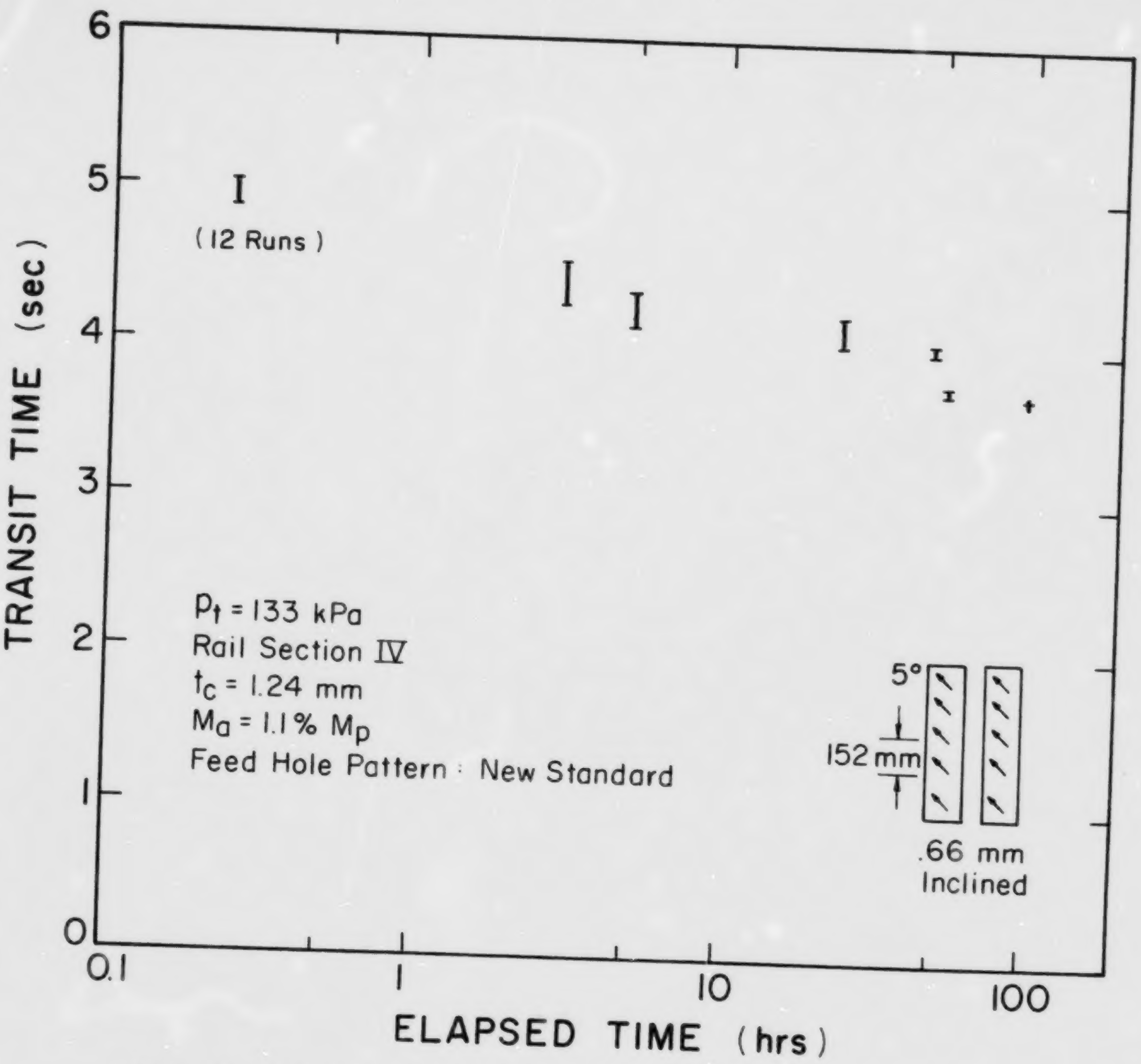

Figure C7 Effect of conditioning on transit time measurements at a representative track pressure. Error bars are given for repeated measurements at a given elapsed time.

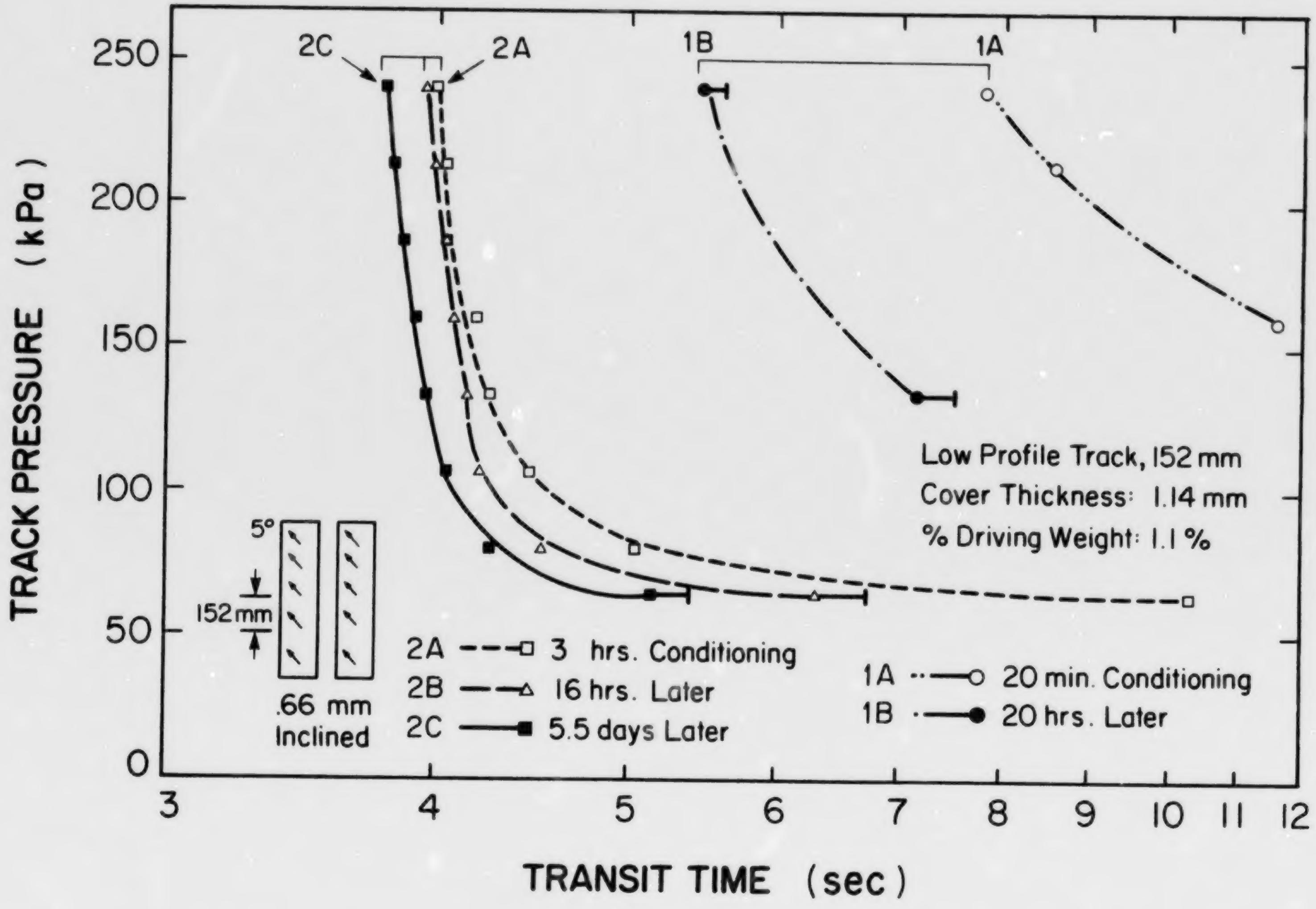

Figure C8 Effect of conditioning and removal and reinstallation of shoes on transit time measurements.

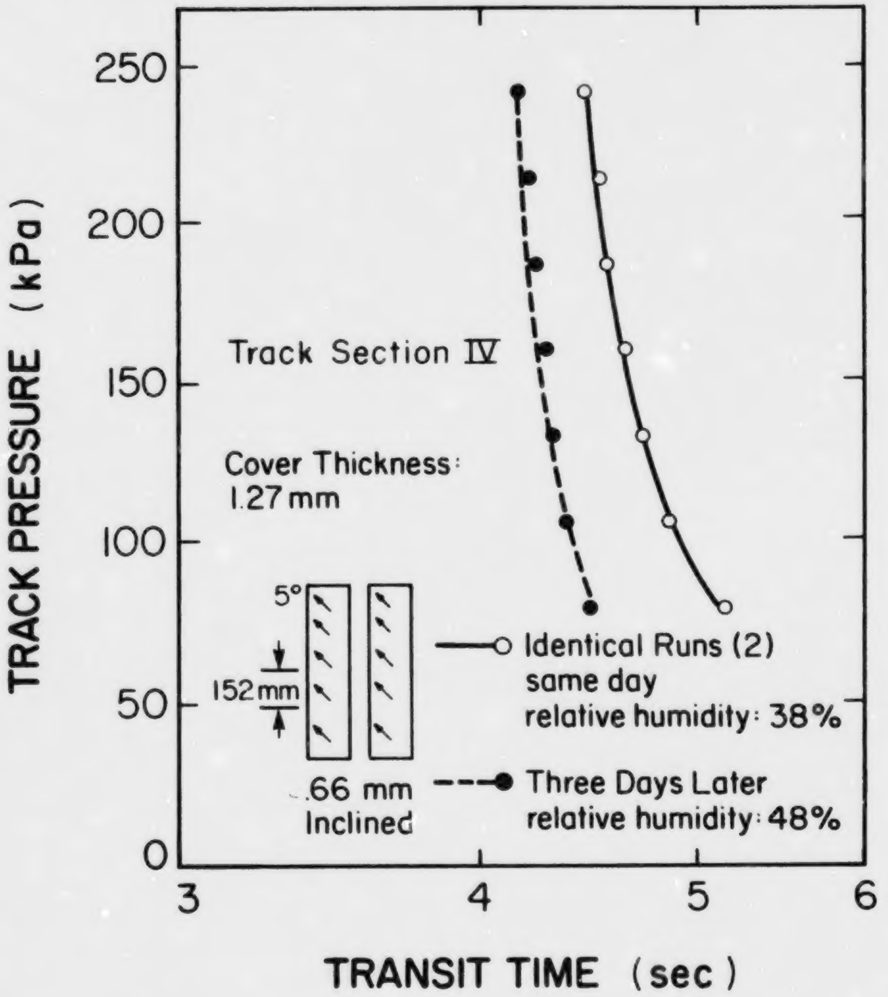

Figure C9 An example of a sudden change in transit time occurring after an extended period of conditioning.

Table C1

Typical variations in SailRail performance over an extended period of time

Date, Time	7/05/82 0900(1)	7/05/82 1500	10/05/82 1005	10/05/82 1555	11/05/82 1415	12/05/82	13/05/82 1430	18/05/82 1045
Laboratory Temperature (^{0}C)	22	22	22	22	22	22	22	22
Atmospheric Pressure (mmHg)	744	746	752		750	746	751	750
Relative (percent) Humidity	46	48	38	37	39	45	80	46
Transit Time (secs) for Track Pressure = 133 kPa	4.69	4.71	4.29	4.27	4.28	4.27	4.21	4.06
Transit Time (secs) for Track Pressure = 186 kPa	4.55	4.55	4.24	4.17	4.17	4.18	4.13	3.95

however, Table C1 suggests that there may be no meaningful correlation between humidity and performance.

Occasionally performance was found to deteriorate with time, and one environmental effect was established. The apparatus was located directly under two ducts which allowed laboratory air flow to an unheated fan room located on the roof. In very cold weather, a substantial reverse flow of cold air into the laboratory could occur, and this cooled the rails by as much as 5°C. Figure C10 shows test data obtained with the ducts opened and then closed off, with suitable time delays between each trial for equilibrium of rail temperature. One possible explanation is that the coefficient of sliding friction for the shoe-rail combination decreased with increase in temperature; however, this has to be reconciled with the observation that transit time tended to increase slightly when a run was repeated (see Fig. C2), since repeated runs might be expected to increase the temperature of the track and shoe.

Although the SailRail system has in practice proven to be remarkably tolerant of the misalignments characteristic of routine operation of most applications, the difficulties encountered in the UTIAS test programme forced consideration of this aspect. For example, the data shown in Figure C8 suggested strongly that the results were sensitive to the way in which the shoes were installed, because only about a half hour elapsed between recording results 1B and removal, reinsertion and loading of the shoes to obtain data set 2. A variety of techniques were tried in order to eliminate alignment problems, but none resulted in any significant improvement in repeatability. For example, initial practice was to lay the shoes in the rails and turn the air supply on prior to lowering the pallet. The shoes were thus floating on air while being loaded. However, it was observed that as the air bags were being deflated, the pallet would invariably load one shoe before the other, and move it laterally in the rail by a significant amount. To circumvent this problem the bracket system described in Appendix D was used to keep the shoes centred in their respective rails while being loaded. Figure C11 is an example of the data obtained when these brackets were used. Included in Figure C11 as a reference is data obtained when the shoes had been conditioned for several days, but installed without the use of the alignment brackets. For the first two trials using these brackets the shoes were conditioned overnight, while for the third, three days conditioning was allowed. For the second trial, except at the highest track pressure used, the load would not move at all!

To examine the effect on performance of the position of the shoes relative to the air feed holes, we installed the mechanism depicted in Figure C12, to allow rotation of the shoes while under load. In the experiments, the shoes were rotated about 10°, first towards the nozzles and then away from the nozzles. In both cases serious degradation in performance occurred, in fact when the shoes were moved towards the jets, the load could not be moved even at the highest available track pressure. No satisfactory resolution of the alignment problem was obtained during the present contract period.

C.4 Effects of Feed Hole Layout and Geometry

The data obtained on the effects of feed hole layout and geometry is believed to be the most reliable since it was usually taken over a

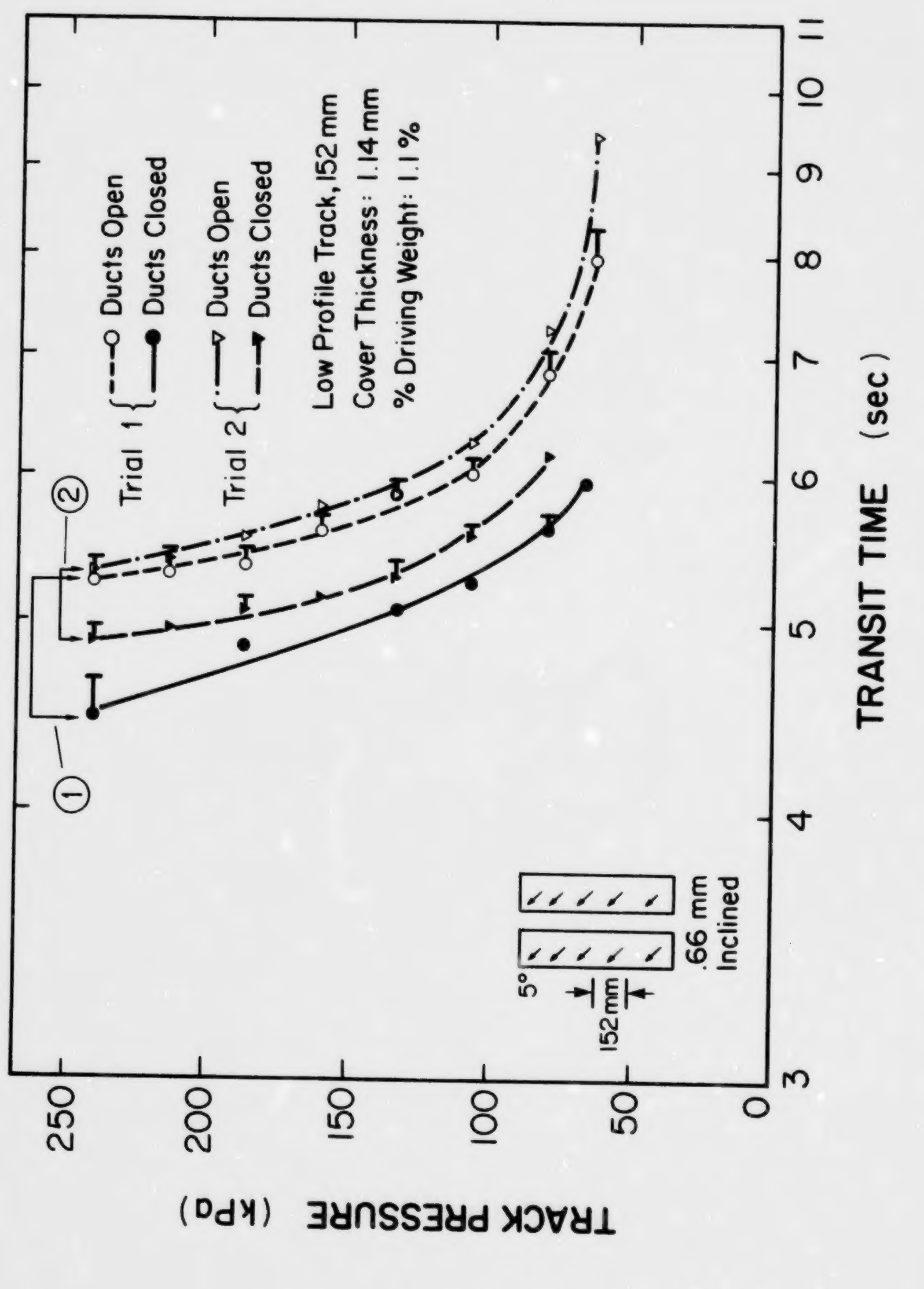

Figure C10 Effect of cool air currents on transit time measurements.

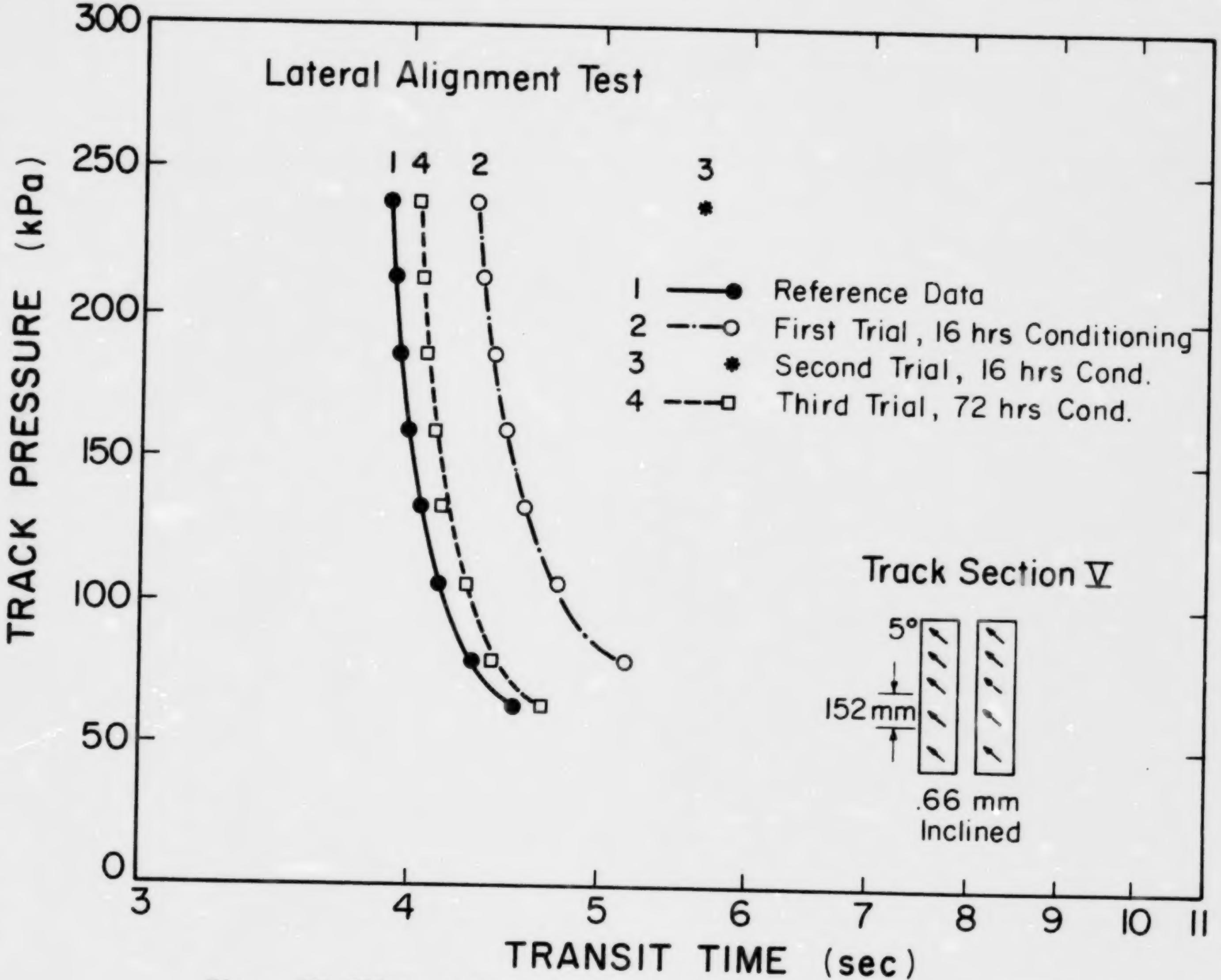

Figure C11 Effect of the use of lateral alignment brackets on transit time data. For one set of data, curve 3, the second trial, the load would move only at the highest track pressure tested.

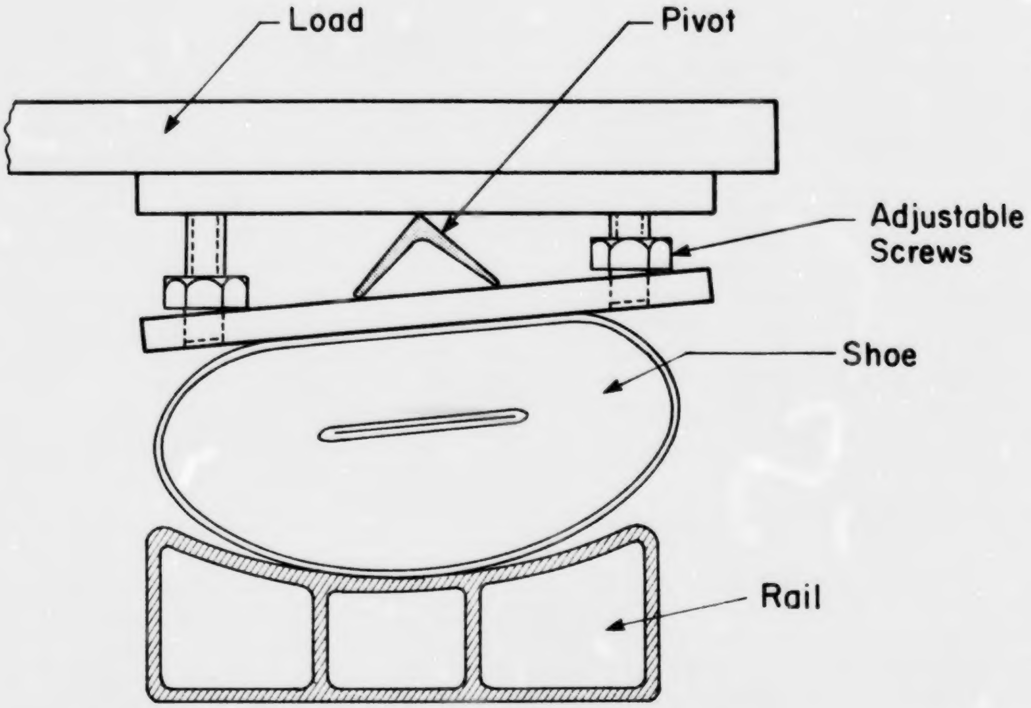
Load
Pivot
Adjustable Screws
Shoe
Rail

Figure C12 Mechanism used to rotate shoes while under load.

relatively short period without disturbing the shoes in any way. That is, all requisite patterns were drilled in the rail before installation in the test bed, and all holes but the configuration under test were sealed. A fast setting woodwork filler compound was used for this purpose, because it was found that this could seal the holes without leaving any protruberance above the rail surface and, with care, could be removed without damaging the hole.

Figure C13 compares the effects of using three hole pattern layouts, the original standard (pattern A), the new standard (pattern B), a modified original standard (pattern C). This test used rail section II, the "plastic" track and, as noted above, it required a high driving weight (2.2% M_p). It is clear that the new standard layout is superior to the original standard, at least when no significant lateral forces are involved. It also suggests that the improved uniformity of distribution of air along the rail direction given by pattern B is more beneficial to performance than the improved lateral distribution obtained with pattern A. This is consistent with inferences made from the flow visualizations described in Appendix J.

The data on the effect of using radial nozzles is given in Figures C14 and C15. Note that, for the data in Figure C14, as a control, measurements for the inclined nozzles were taken at the beginning and the end of the tests. The transit times for the 0.66 mm inclined holes fall between those of the 0.51 mm and 1.02 mm radial nozzles. Figure C15 also shows that, when radial nozzles are chamfered or countersunk to reduce the entry losses discussed in Appendix B, the performance is close to that of inclined nozzles. Indeed the data seems to suggest that, of the two factors affecting performance, nozzle geometry and layout, the latter is much more important.

C.5 Effect of Lateral Forces

The susceptibility of the system to performance degradation by applied lateral forces and its relationship to feed hole pattern was examined by inclining the test bed laterally. A series of shims was placed under one side, and then the other, to a maximum inclination angle of 0.92^0, which is equivalent to a lateral force up to 1.6% of pallet weight. Track section IV and the new standard feed hole pattern were used, and the results are given in Figures C16 and C17. They show that when the lateral force pushes the shoes to the side of the rail on which the nozzles are located, only small changes occur, whereas when the lateral force is in the opposite direction a very marked degradation occurs. These results clearly indicate that, for applications in which significant lateral forces are expected, care will have to be exercised in choosing nozzle location.

C.6 Effect of Shoe Cover Thickness

In spite of the difficulty experienced in obtaining repeatable data for anything but the tests described in Section C4, a comparison of the effect of cover thickness on performance is ventured in Figure C18. The thinnest material used in these tests was the extruded polyethylene film used as a vapour barrier in housing; all the other covers were specially manufactured for SailRail from a medium density polyethylene. The comparison was obtained by selecting from the many runs performed for each cover that run having the shortest transit time. Considering the variability obtained in

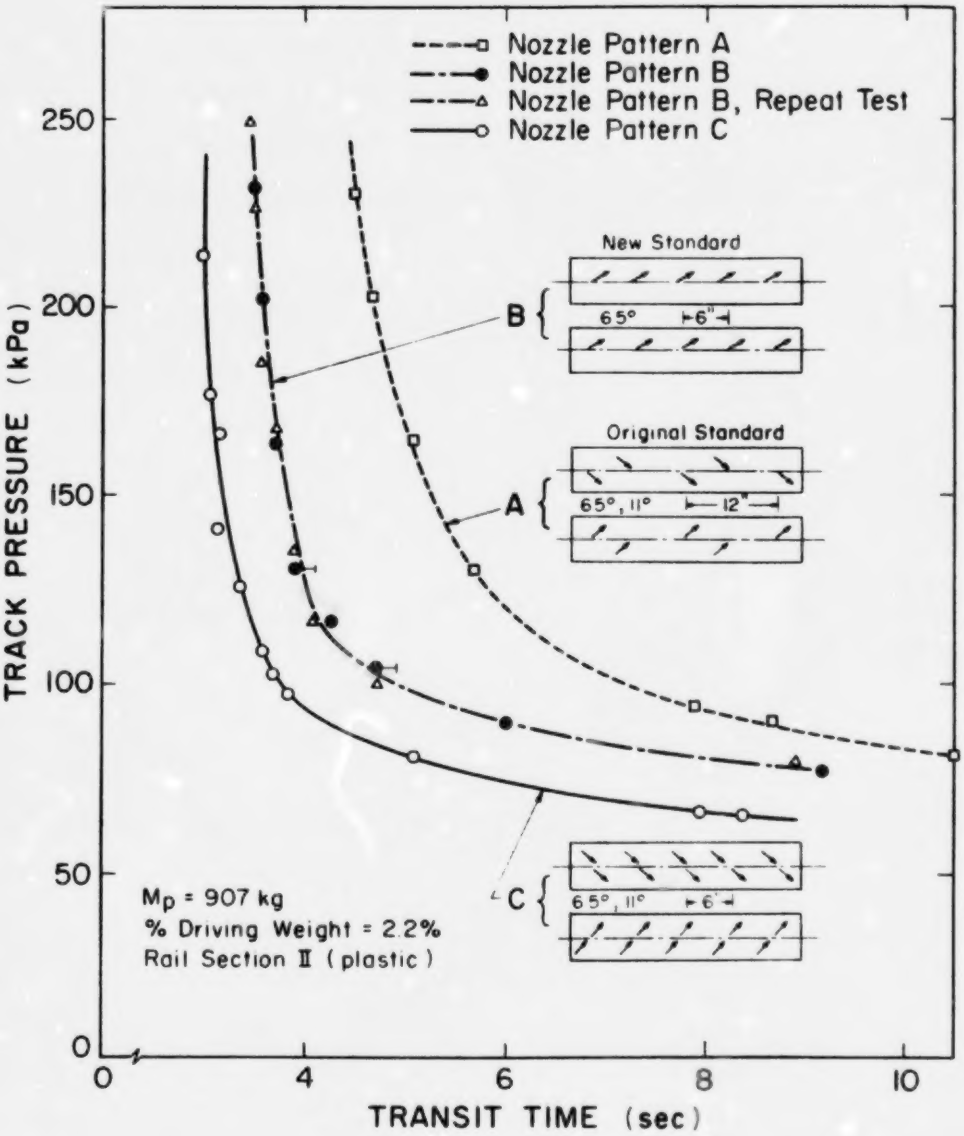

Figure C13 Effect of nozzle patterns on transit time.

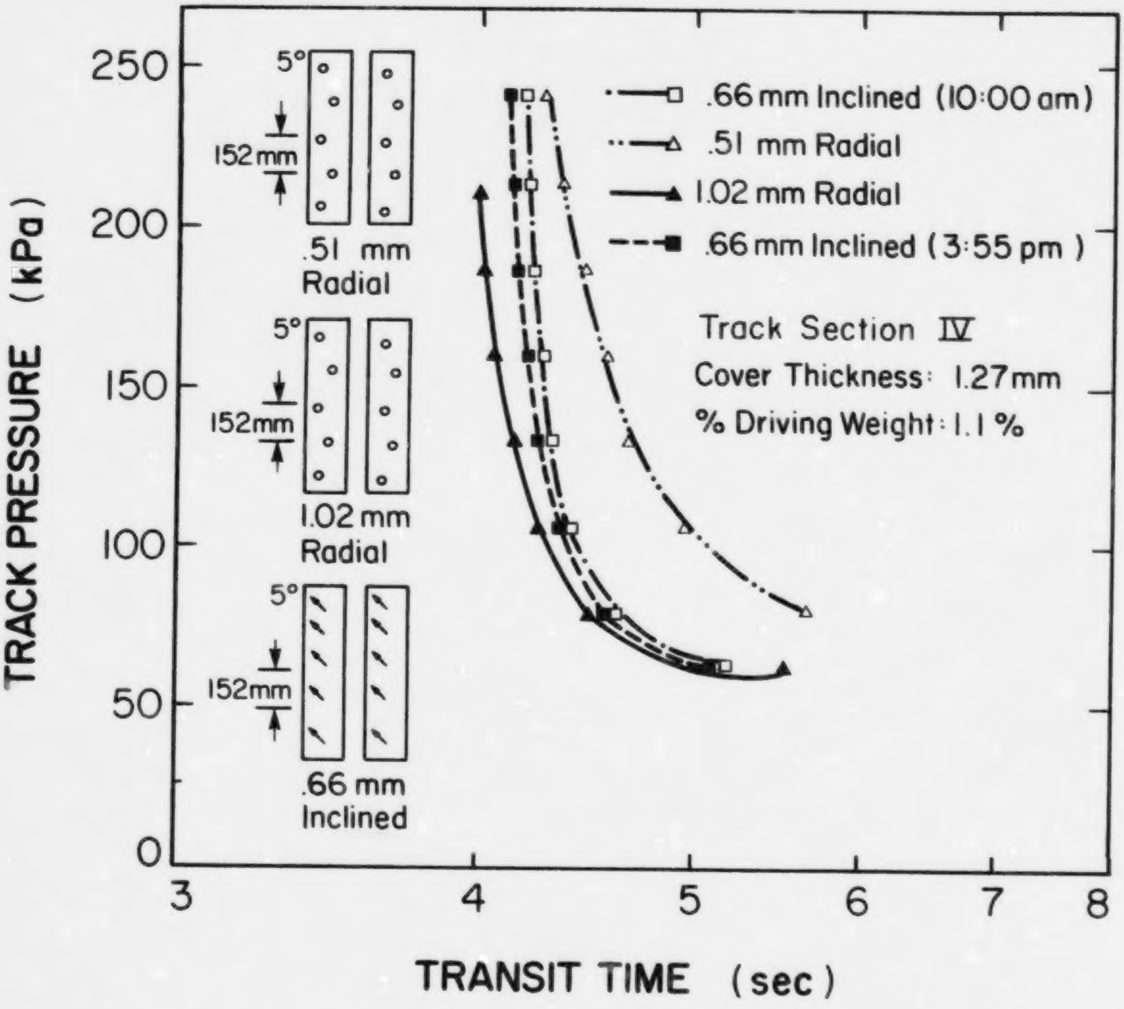

Figure C14 Effect of radial nozzles at different diameters on transit time, together with a comparison with inclined nozzle performance.

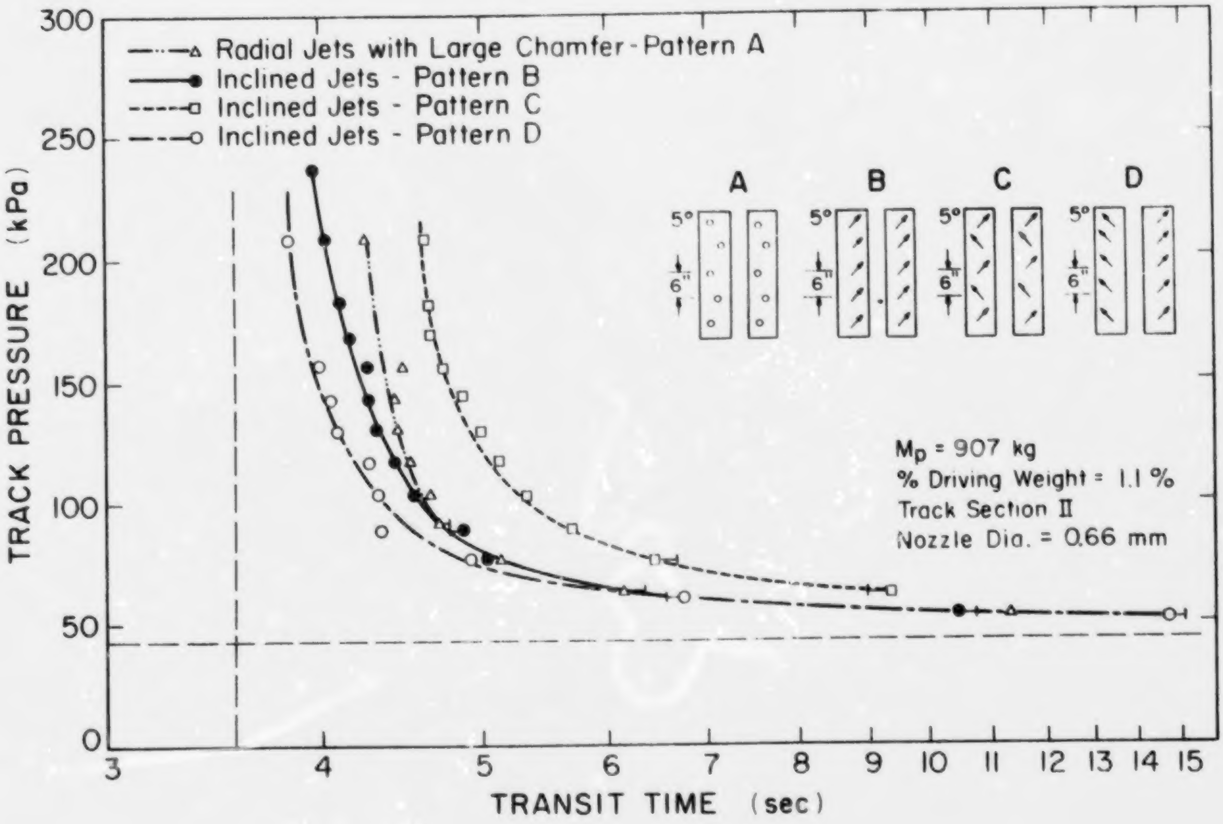

Figure C15 Comparison of performance obtained for chamfered radial nozzles with that obtained using inclined nozzles.

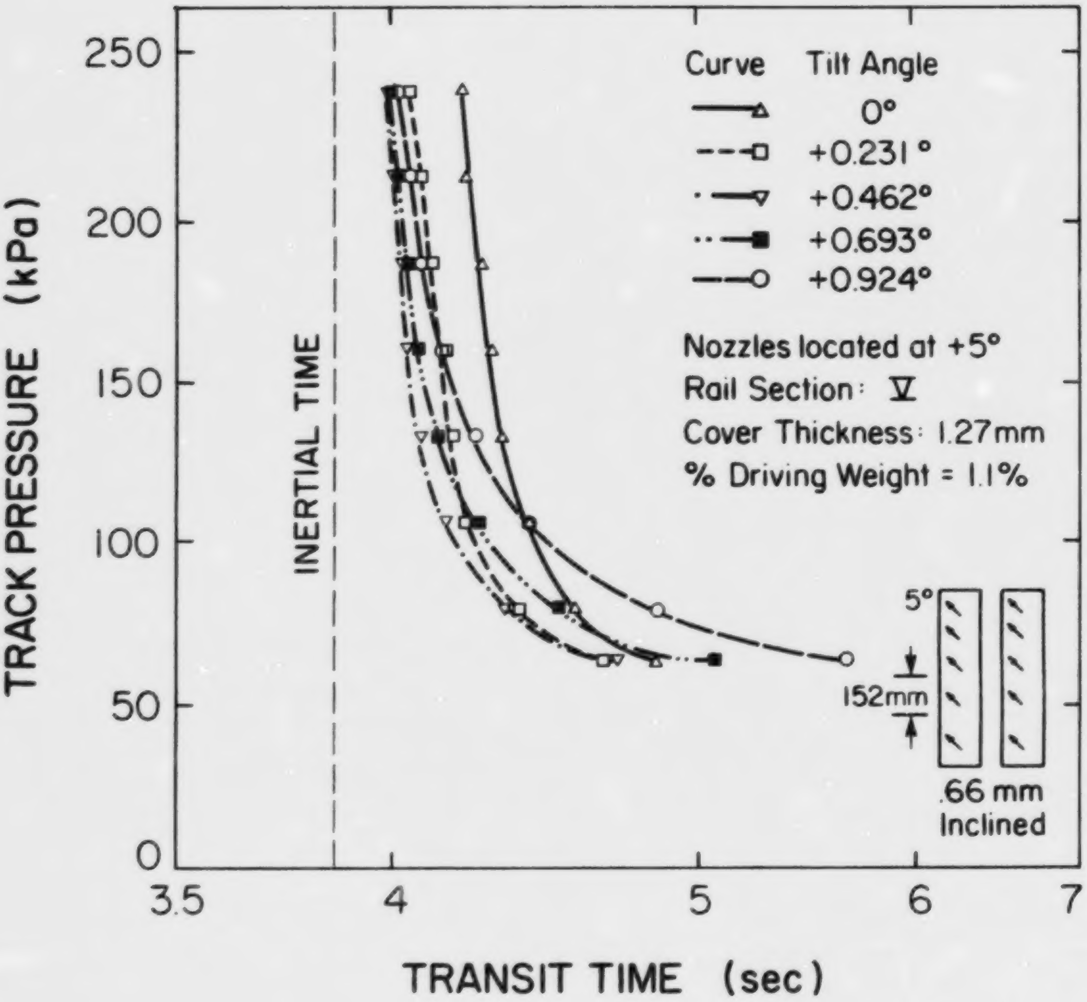

Figure C16 Effect on transit time measurements of a lateral tilt towards the nozzles.

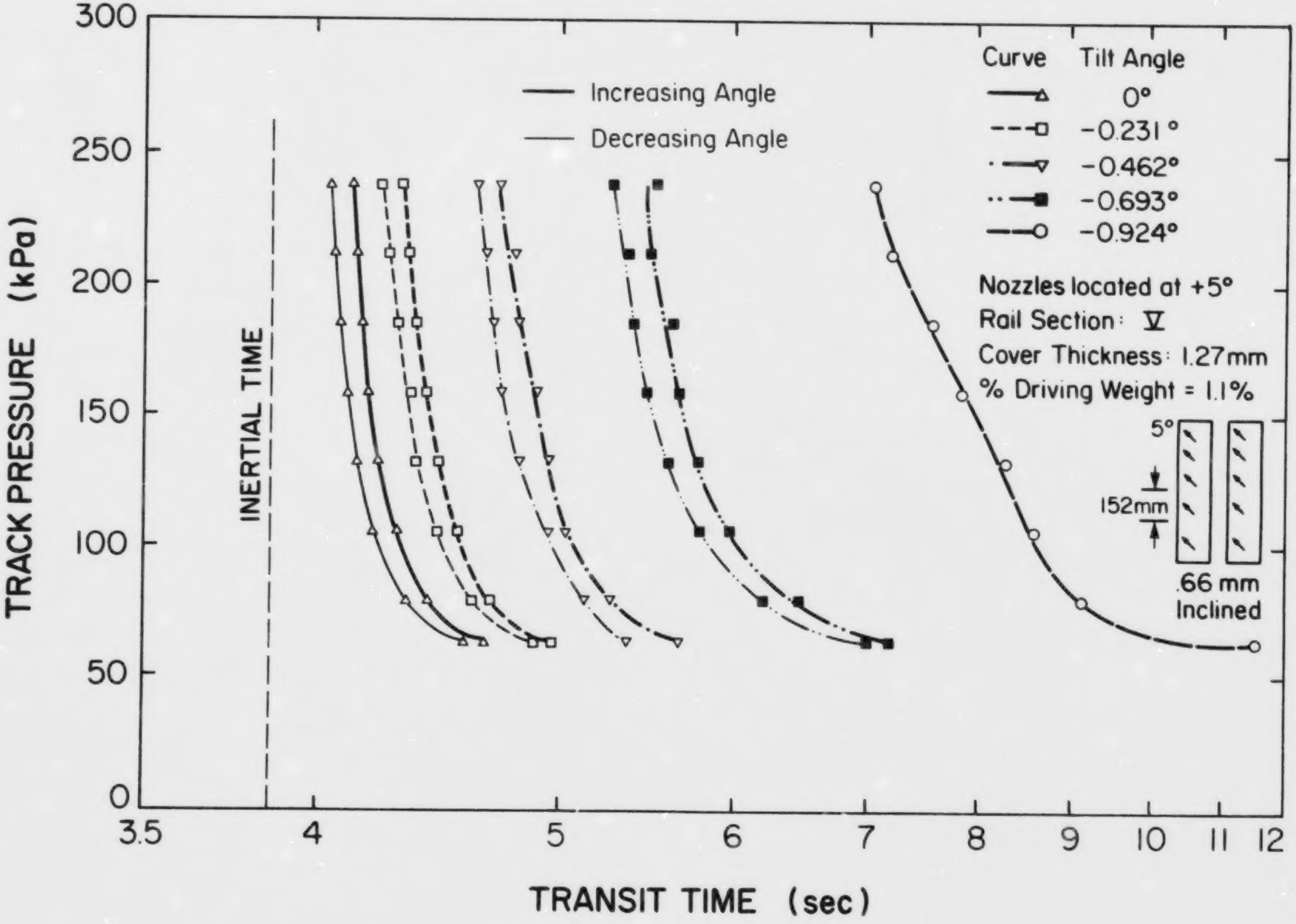

Figure C17 Effect on transit time measurements of a lateral tilt away from the nozzles.

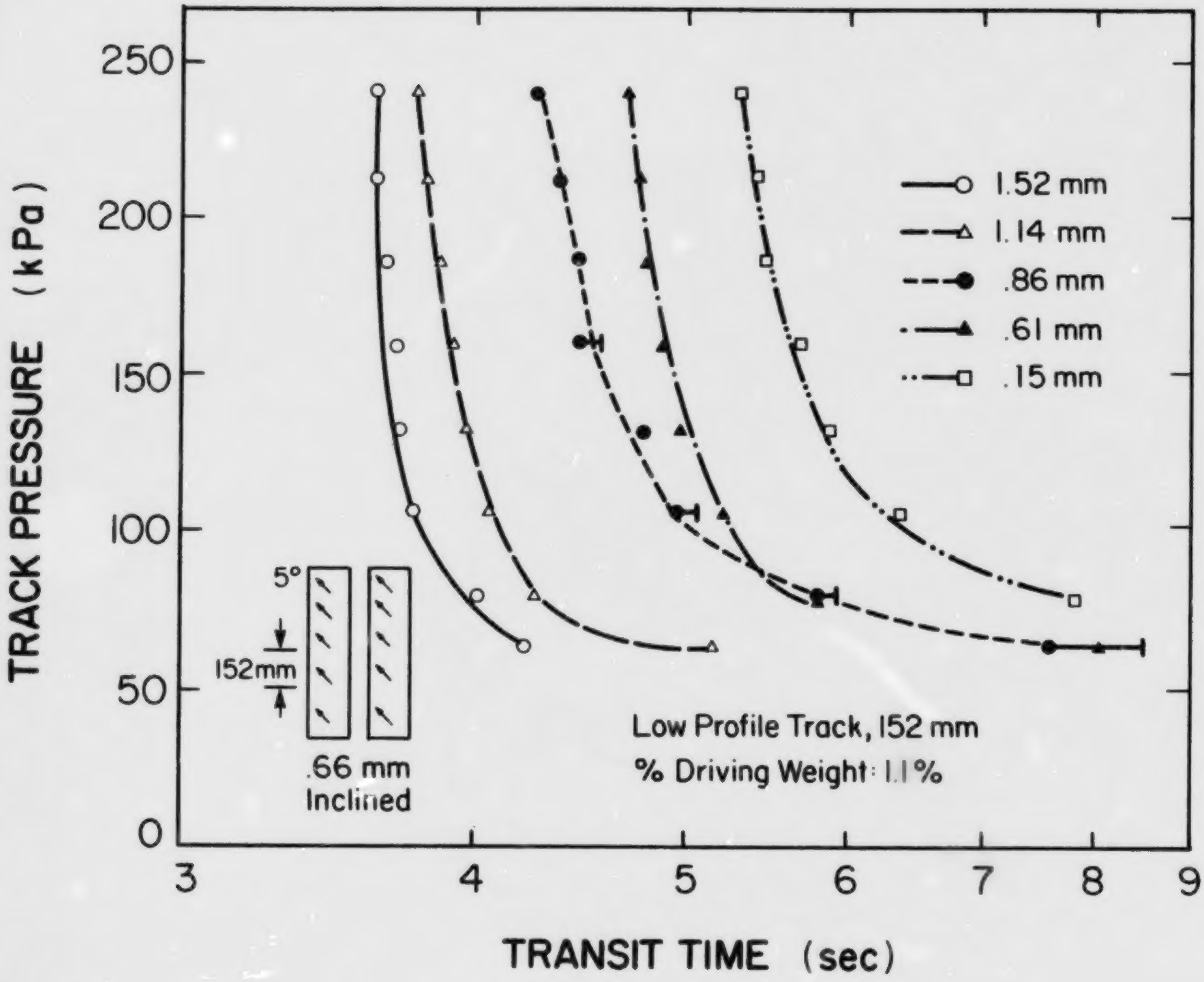

Figure C18 Effect of shoe cover thickness on transit time measurements.

the tests of any individual cover, a remarkably consistent trend exists, and one can therefore safely conclude that, within the range of thickness tested, increases in cover thickness cause significant performance improvements.

The pressure measurements on the scaled up model of the entry region described in Appendix B suggest that one possible mechanism of the cover thickness effect is the prevention of "suck-down" of the tissue by fluid mechanical effects occurring in the immediate neighbourhood of the nozzles. One way to verify this hypothesis would be to compare air flow rates as a function of track pressure for different cover thicknesses, since, as noted in Appendix B, suck-down would increase hydrodynamic losses. That is, at a given p_t, the flow should increase as cover thickness increases. The data in Appendix O taken to assess the importance of compressibility effects included covers having thickness in the range $0.610 \text{ mm} < t_c < 1.321 \text{ mm}$. The results are given in Figure C19; there is no detectable effect. Hence this evidence supports the data obtained from the pressure measurement apparatus (Appendix D), which suggests that the bending stiffness of the cover improves performance by altering the overall structural behaviour of the shoe. However, the measurements in Figure C19 do not include very thin covers or no cover at all, so that a suck-down effect cannot yet be completely ruled out, especiall;y in the light of the flow visualization in Figure B24.

C.7 Effect of Pallet Weight

In these tests we examined the effect on performance of change in pallet weight and of asymmetrical loading. For the pallet weight variation tests, four values of M_p were used: 401 kg, 702 kg, 1044 kg and 1303 kg, and the driving weight M_d was maintained at 1.1% M_p. The results, given in Figure C20, show that for $p_t < 100$ kPa, at a fixed p_t, increasing the pallet weight causes no detectable reduction in transit times. The data in Appendix O on the effect of p_t on the mass flow through covered and uncovered nozzles suggests that for inclined nozzles the flow is gasdynamically choked at the nozzle entry (point 1 in Figure B1). The behaviour shown in Figure C19 could be caused partly by this choking. As discussed in Appendix F, since when M_p was increased M_d was maintained at a constant fraction of M_p, then if the coefficient of sliding friction was independent of load, the fraction of the load supported by direct shoe-rail contact must have remained constant. This implies that the effective cavity pressure p_c must have increased in proportion to M_p. For unchoked nozzles this would reduce the mass flow, since for fixed p_t the pressure difference across the nozzle would be reduced. This reduced flow would be accompanied by a reduction in the effective seal height h_s, and thus with increased shoe-rail contact. Of course, even when the mass flow is fixed by choking, the analysis in Appendix A shows that an increase in p_c must be accompanied by a reduction in h_s, so that some increase in shoe-rail contact must occur; however it should be much less than for the unchoked case.

C.8 Asymmetric Loading Effects

The effects of asymmetrical loading is given in Figure C21. Two cases are considered: side loading, corresponding to application of a moment about an axis parallel to the direction of pallet motion; and front-back loading, corresponding to application of a moment about a horizontal axis at

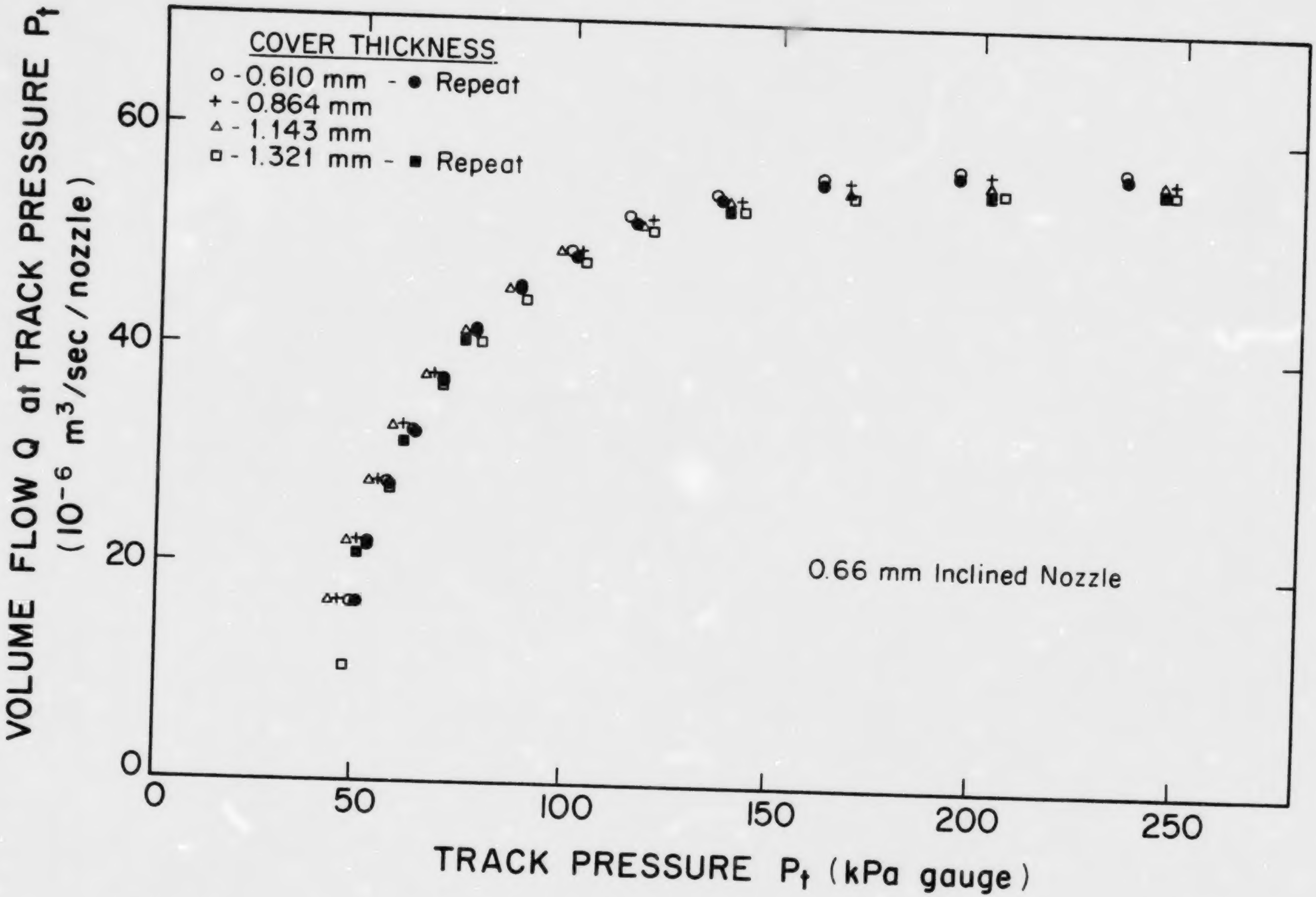

Figure C19 Effect of cover thickness on air flow rates for a range of track pressures.

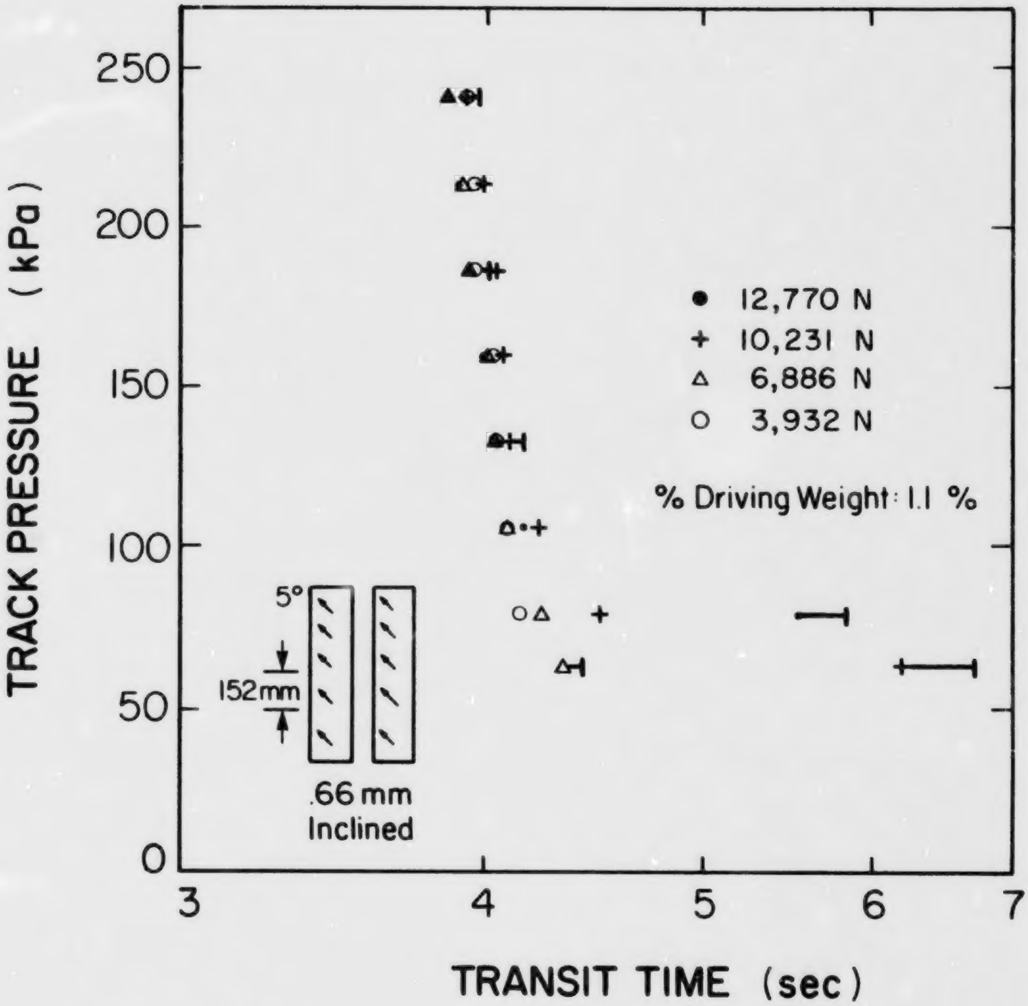

Figure C20 Effect of pallet load M_p on transit time measurements.

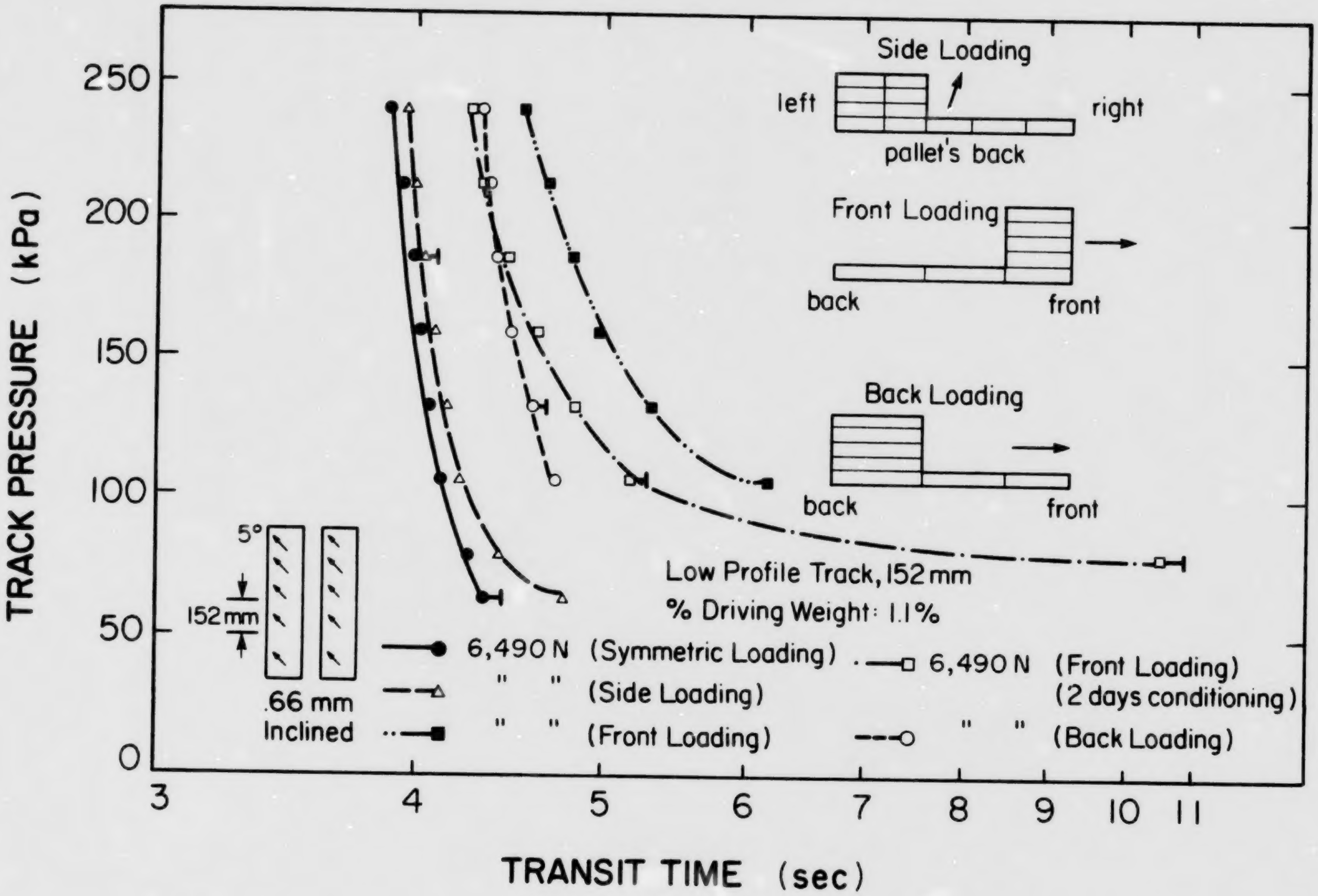

Figure C21 Effect of asymmetrical pallet loading on transit time measurements.

right angles to the pallet motion direction. The amount of asymmetry used is depicted geometrically in Figure C21. Now the results in Figure C20 suggest that side loading asymmetry should not affect performance, since it amounts to changing the loads carried by the shoe, but not the point of application. The data in Figure C21 confirms this. In contrast, front-back loading asymmetry moves the point of load application parallel to the rail and some degradation might be expected. Figure C21 shows that this does occur, although it is important to note that conditioning seems to improve it significantly. Even though experiments undertaken during the previous contract indicated that most of an applied pitching moment is counterbalanced by a redistribution of air pressure under the shoe, the present results suggest that some increase in cover-rail contact force occurs when the load is not centred over the shoe.

C.9 Performance of a Simplified Shoe Geometry

A complete analysis of the air bearing characteristics of the SailRail system requires computation of the structural deformation of the shoe under the action of the air pressure distribution; but for the shoe geometry and construction used in practice this is likely to be very difficult. Consequently, an important aim of the exploratory work described here was to find a simplified geometry which would be amenable to analysis and yet give performance comparable to that of the full SailRail shoe.

Figure C22 is a diagram of the cross-section of the first trial simplified geometry. The bulk of the SailRail shoe was replaced with a solid aluminium block having one side machined to a radius slightly less than that of the rail. Layers of cellulose filler and a sheet of cover material were added until, when loaded, the outer radius of the combination matched that of the rail. The radius of the block was initially chosen to be 146 mm (5.75 ins) or just 6.4 mm (0.25 in) less than that of the rail, but it was envisaged that this would be reduced in steps until performance comparable to that of the full shoe was attained.

Owing to the repeatability problems described here, only this first block radius and two cover thicknesses, 0.86 mm (0.033 ins) and 1.52 mm (0.060 ins), were tested. Results of the test of the 0.86 mm cover are given in Figure C23 and are compared with that for a full shoe having the same cover thickness. When the 1.52 mm cover was installed the load would not be moved by the standard 1.1% driving weight. These results are however very encouraging, since it was initially envisaged that, in order to obtain satisfactory performance, the tissue thickness would have to be much greater than was used in a first trial.

C.10 Effect of Rail Width

As a direct result of experiments undertaken for this and the previous contract, the manufacturer decided to reduce the overall width of the rail from 6 ins (152 mm) to 5 ins (127 mm). This cut the width of the curved part of the rail, the 6 in. radius top surface, from 5.54 ins (141 mm) to 4.54 ins (115 mm). The height of the rail was also increased, so that the new section (V in Appendix M) had a much greater bending stiffness. As a preliminary test, the active width of a section IV rail was reduced to 4.75 ins (121 mm) by machining off part of the top edges as shown in Appendix M. Figure C24 gives test bed data obtained for these three sections. It shows that the modified section IV gave significantly poorer results than those of

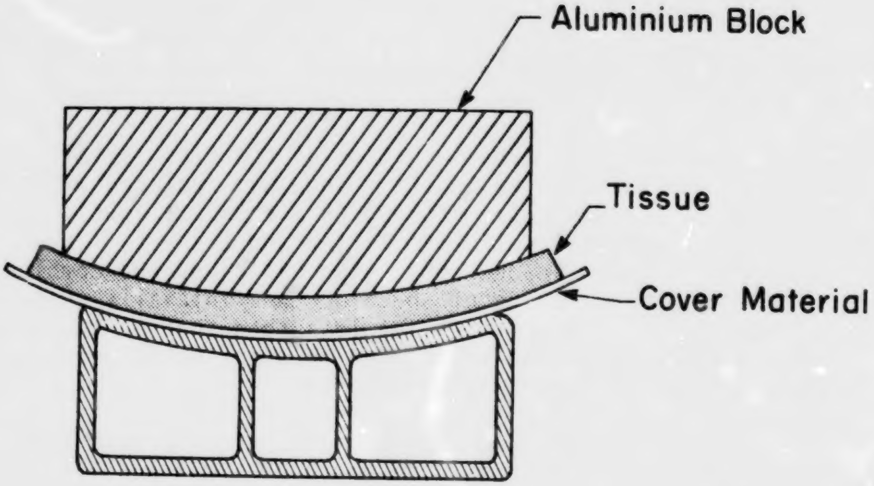
Aluminium Block
Tissue
Cover Material

Figure C22 The simplified shoe geometry used in exploratory tests.

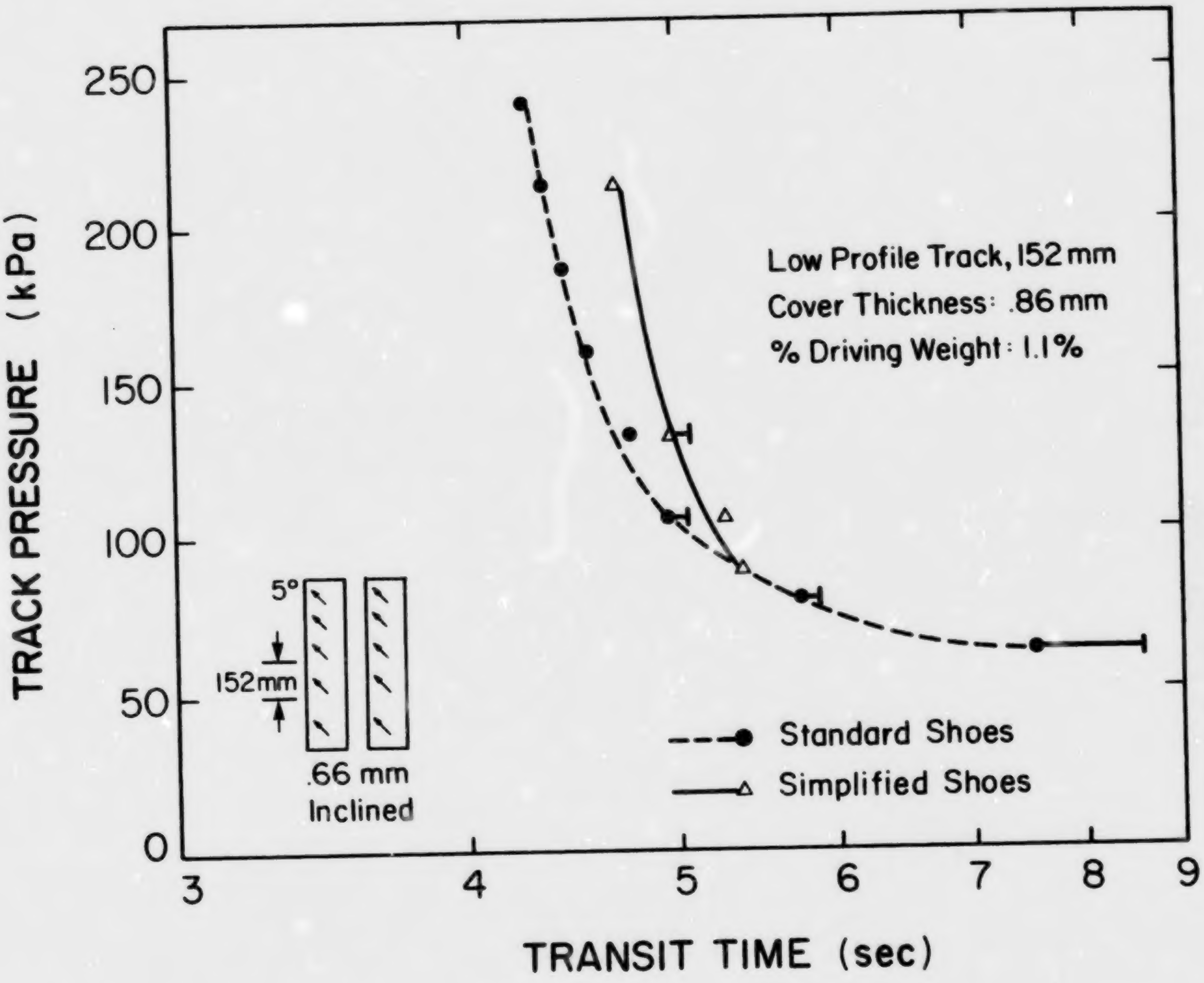

Figure C23 Transit time measurements obtained by using simplified shoe geometry.

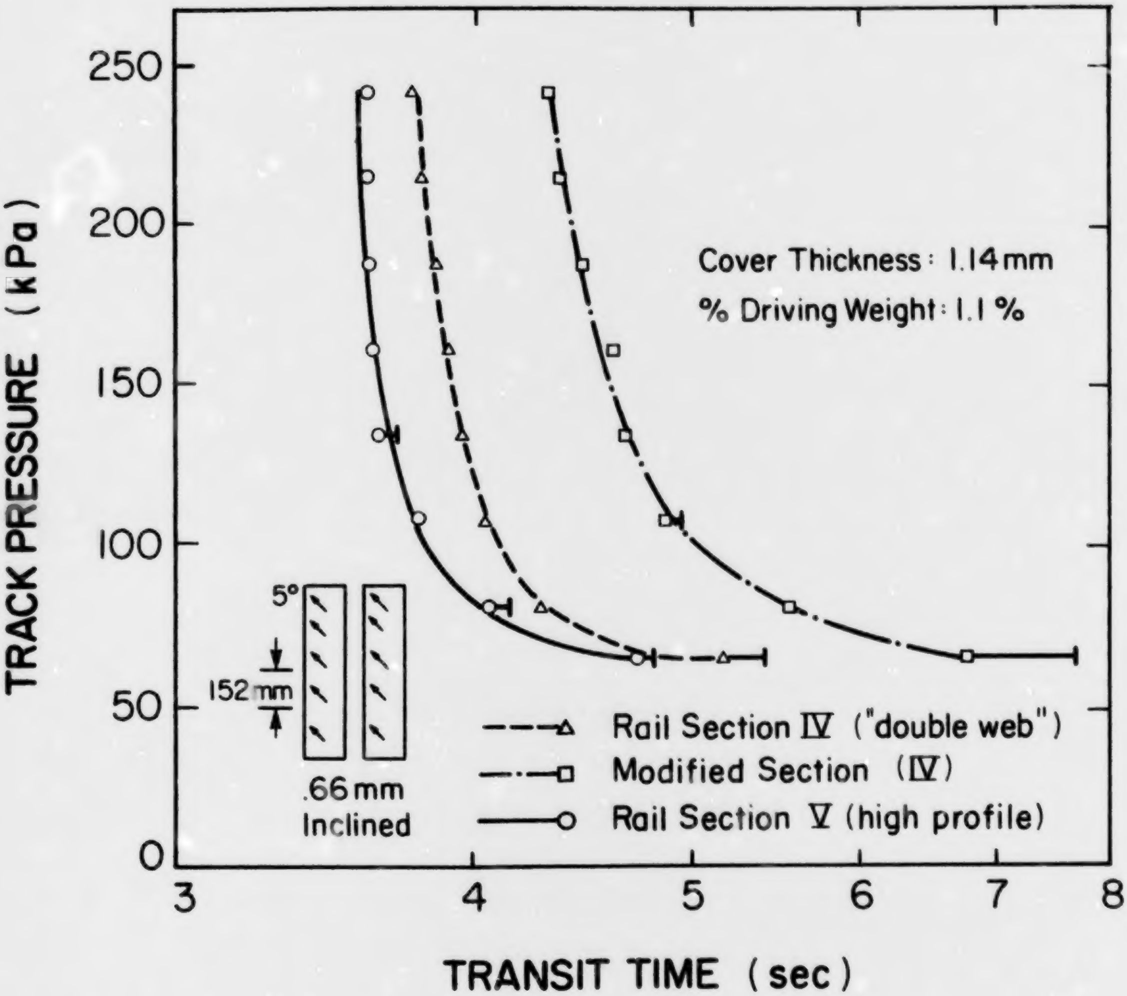

Figure C24 Effect of three different rail sections on transit time measurements.

either the original section IV on the new section V. Now the results in Section C.2 show that the system performance is very sensitive to the lateral bending stiffness of the top surface of the rail, and it is likely that the removal of material from the top edges, as shown in Appendix M, significantly reduces this stiffness. Hence it seems reasonable to attribute these results to bending stiffness effects, but whatever the reason, this data is included here to demonstrate once again the sensitivity of system performance to the details of the rail section geometry.

C.11 Air Consumption and Power

The best overall index of system performance is probably the power required to supply the necessary compressed air. Owing to the difficulties encountered in the present test programme this aspect was not explored in the detail originally envisaged. However some measurements were obtained, and these are given in Figure C25.

The quantity plotted is the flow power per pallet; it is the product $P_f = (p_t - p_a)Q_t$ where Q_t is the volume flux at p_t. To estimate the actual minimum installed motor power required for an air compressor in continuous operation, the work to compress the air, the head losses in supply piping, and frictional losses in the compressor and transmission have to be added. The actual amount depends on the details of the design of the compressor and air supply system, but a representative value has been calculated here. This assumes negligible head losses in the piping, a single stage of compression to 140 kPa (20.3 psig), an air compression law $p/\rho^n = p_a/\rho_a{}^n$ with n=1.2, 15% frictional losses in the compressor and a transmission belt efficiency of 95%. This gives a minimum installed power $P_i = 1.728\ P_f$. The data in Figure C25 suggests that for 0.66 mm inclined nozzles, a minimum installed power per pallet is about 0.22 kW or 0.30 HP at 140 kPa (20.6 psig).

C.12 Conclusion

Although the prototype tests described in this Appendix have, with a reasonable degree of confidence, documented some of the important properties of the SailRail system, the most important aspect in need of further work is the development of improved testing techniques. At the time of writing a monorail apparatus in which the load is suspended beneath the rail, has been found to eliminate some of the problems. For example, use of a single shoe greatly simplifies alignment. Also we have found that loading of the shoes prior to insertion into the apparatus can speed up testing without sacrificing repeatability.

Finally, the use of transit time as an index of performance, although it has served its purpose in the present work, has unsatisfactory aspects. It depends on such details of a particular experiment as the value of M_d and M_p, and on the coefficients of sliding friction for a given shoe-rail combination. Now since it appears that for most practical applications there is always partial contact between shoe and rail, the most basic index of the air bearing aspects of the SailRail system is probably the fraction of total weight carried by the pressure of the air in the cavity and seal regions. However, as noted in Appendix D, this is still best obtained by

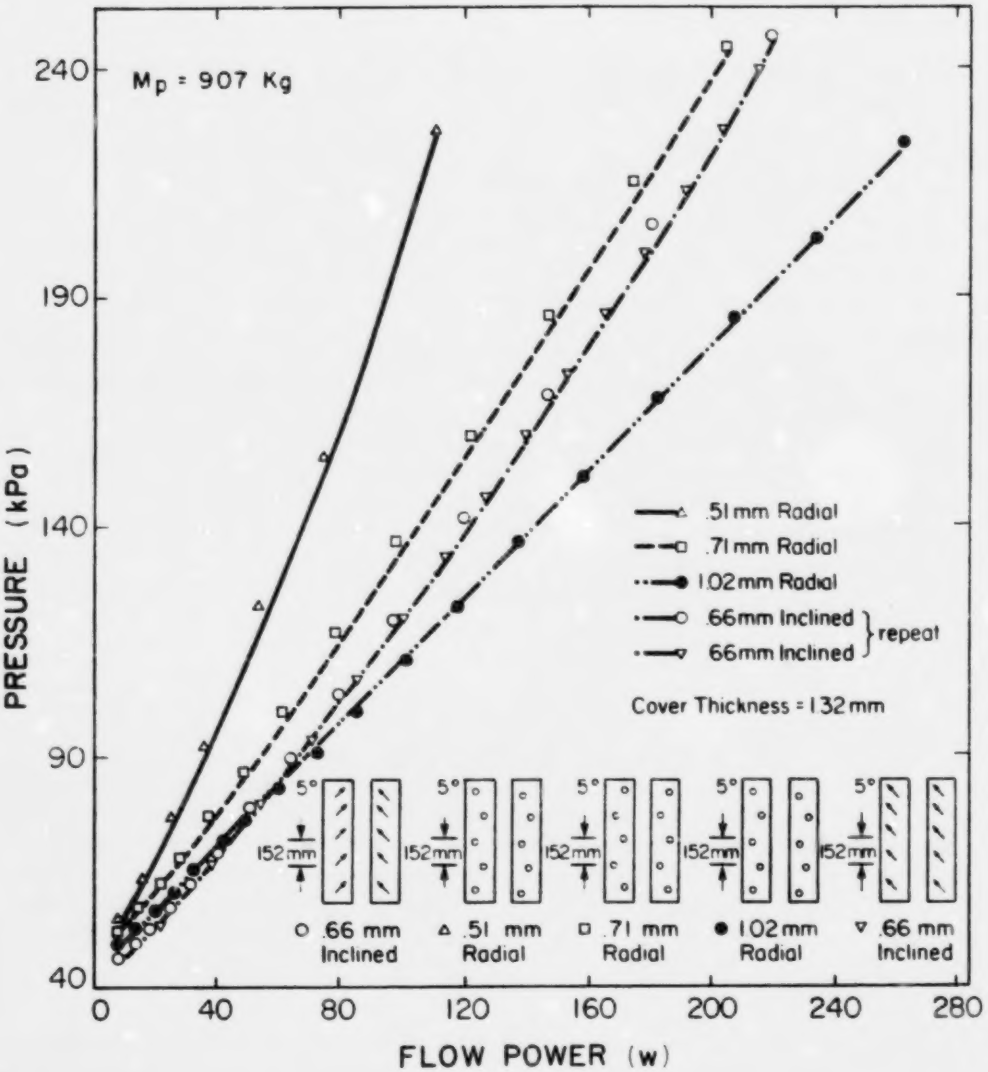

Figure C25 Air flow power measurements for various nozzle configurations.

use of transit time measurements instead of by integration of the measured pressure distributions.

APPENDIX D. PRESSURE MEASUREMENT APPARATUS RESULTS (T. A. Graham and P. A. Sullivan)

D.1 Introduction

Although the prototype test bed incorporates all aspects of the SailRail system, and thereby gives information on performance which is of direct interest to the designer, measurements of the pressure distribution between shoe and rail provide much more basic and detailed information on the air bearing aspects of the design. For example the integral of the pressure distribution gives the fraction of the load supported by air pressure. Original plans called for installation of pressure taps in one of the prototype test bed rails, however the alignment sensitivity problem described in Appendix C led to a decision to build a separate apparatus in which alignment could be more carefully controlled.

Figure D1 is a photograph of this apparatus, and Figure D2 is an outline diagram. A single rail having cross section V and the new standard feed hole pattern was mounted above the shoe, and the load was suspended on cables directly underneath. This arrangement greatly simplified the task of gaining access to the pressure taps. Vertical shafts and linear ball bushings placed at either end allow the rail section to be raised and lowered using air bags while maintaining alignment with respect to the body of the rig. Figure D3 gives the location of the pressure taps; a single transverse row was located midway between the nozzles. The pressure measurements obtained for the previous contract showed that in the central part of the rail the pressure is usually constant and rapid fall-off occurs only in narrow regions at either side [1]. Hence in the central 34 mm part of the rail, which for Section V contained the air feed manifold, pressure taps were omitted. Outside of this part probes were located at every 0.1 inch (2.54 mm) out to the edges of the rail. Also two probes were placed near the ends of the rail to detect asymmetry in the loading of the shoe.

The mechanism used to align the shoe relative to the rail is shown in Figure D4. A tab on the side of the cross piece was inserted in the slot formed by the collapsed core of the shoe, and distances relative to the rail-supporting structure were measured to determine roll, pitch and transverse position of the shoe.

D.2 Concept of Ideal Bearing Cavity Pressure

Important to the interpretation of the data is the concept of an ideal cavity pressure p_{ci}. This is defined to be that uniform pressure which has to act over the maximum available area for load support provided by the rail in order to support the load weight W. In the present case, since the surface of the rail on which the load acts is circular, support is provided by the resolved vertical components of the pressure forces acting at each point support W. The idea is depicted in Figure D5.

Figure D1. Photograph of pressure measurement apparatus; rail, (1); shoe, (2); cover, (3); load support beam (4); linear ball bushings, (5); test weights, (6); air lift bags, (7).

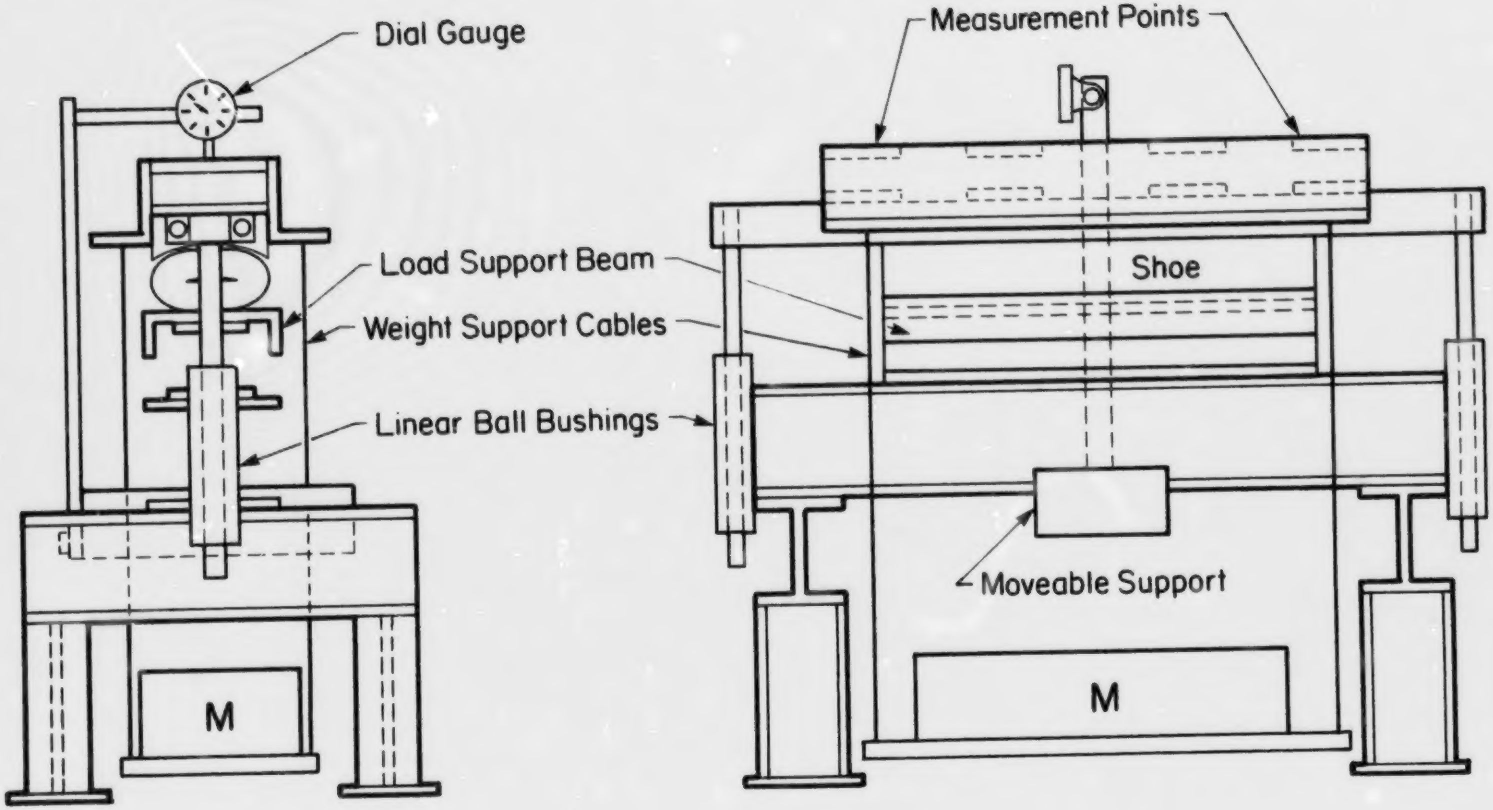
Dial Gauge
Load Support Beam
Weight Support Cables
Linear Ball Bushings
Measurement Points
Shoe
Moveable Support
M
M

Figure D2. Outline diagram of pressure measurement apparatus showing attachments for measuring air gap.

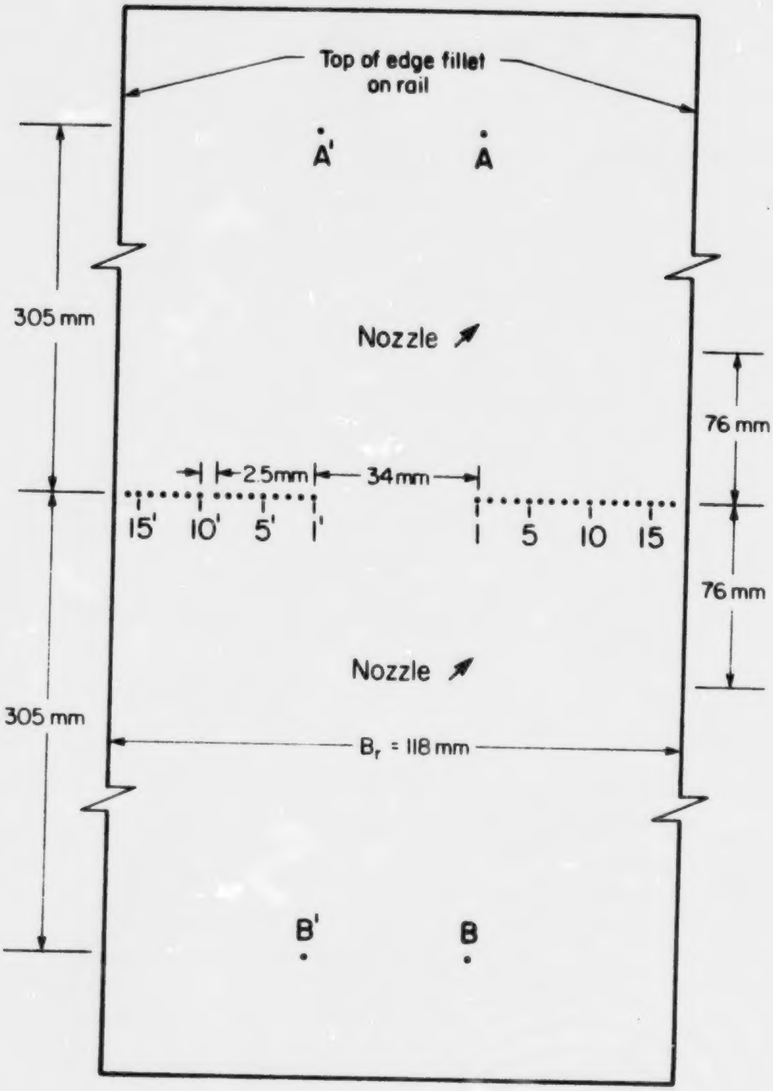
Top of edge fillet on rail
A'
A
305 mm
Nozzle
76 mm
2.5mm
34mm
15'
10'
5'
1'
1
5
10
15
76 mm
Nozzle
305 mm
B_r = 118 mm
B'
B

Figure D3. Location of probes used to obtain pressure measurements.

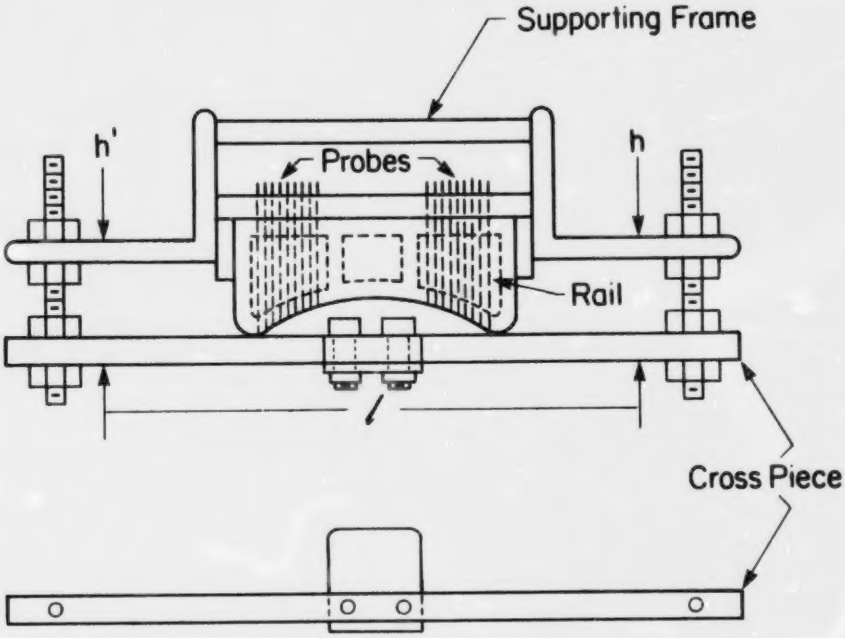
Supporting Frame
h'
Probes
h
Rail
l
Cross Piece

Figure D4. Fixture used to align the shoe relative to the rail.

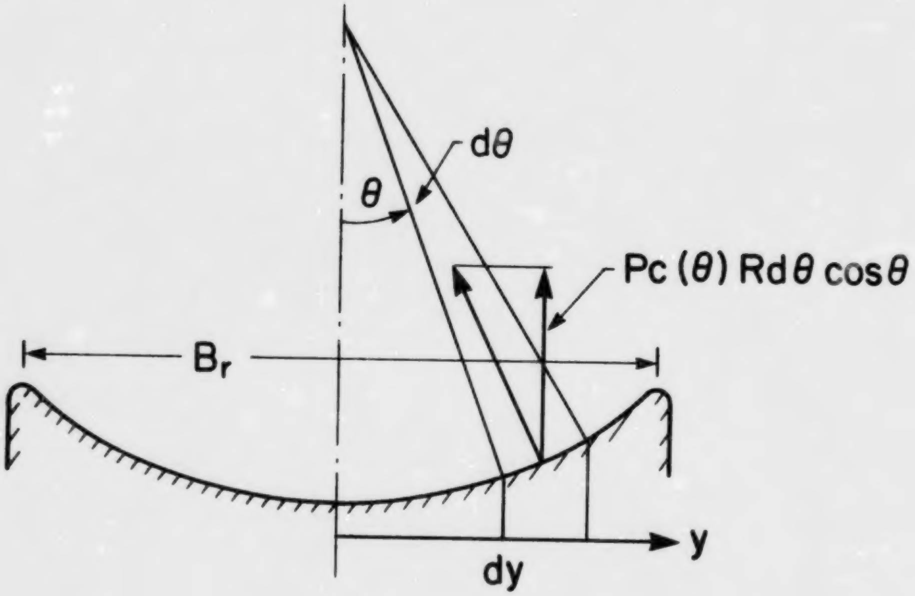
dθ
θ
Pc (θ) Rdθ cosθ
B_r
y
dy

Figure D5. Geometry for definition of ideal cavity pressure.

Consider for simplicity the pressure distribution for a very long shoe, in which case p_s is a function only of the lateral distance y from the centreline, or equivalently of the angular distance θ. The resultant vertical lift T is given by

$$T = \int_{-\theta_m}^{+\theta_m} \cos\theta \, p_s(\theta) R d\theta \qquad (D1)$$

in which θ_m is the value of θ at which p_s becomes zero. But $Rd\theta\cos\theta = dy$, so

$$T = \int_{-y_m}^{+y_m} p_s(y) dy \qquad (D2)$$

where $y_m = y(\theta_m)$. When p_s is uniform and T = W/L, where L is the length of the shoe,

$$p_s \triangleq p_c = W/(2Ly_m) \qquad (D3)$$

Now the ideal shoe should make use of the maximum available track width. Here this is defined to be the distance B_r between the highest points of the rail section. Hence with $y_m = B_r/2$ and a shoe of length L

$$p_{ci} = \frac{W}{LB_r} \qquad (D4)$$

It should be noted that for the present rail geometry the reduction of the vertical thrust arising from the rail curvature is small, about 1.6% for a uniform pressure. However, it is equally easy to plot pressure distributions as a function of y or θ, and the above result is valid for large corrections that might occur for different geometries.

D.3 Typical Results

Typical pressure profiles are given in Figures D6 to D15. All show clear evidence of a region of essentially constant pressure $p_s = p_c$, thus strongly supporting the idea of a cavity region in which the air is essentially at rest. As an example, the data in Figure D15 (see p. 132) suggests that the width of the cavity may be in excess of 80 mm (3-1/4 in) or 70% of B_r. Also for the data in Figure D15, the seal region appears to be only about 10 mm (.39 in) wide.

The ideal cavity pressure p_{ci} is generally about 80% of the measured cavity pressure p_c, thus suggesting that the shoe geometry is not far from an optimum for the current rail section. The discrepancy between p_c and p_{ci} can arise from three sources: (i) incomplete use of the available track width, (ii) pressure fall-off towards the ends of the shoe, and (iii) load supported by direct shoe-rail contact. The relative importance of the two sources can be ascertained by computing the load that the shoe could carry if the measured pressure distribution at the centre of the shoe is assumed to act over the entire length. For the data in Figure D15, at p_t = 133 kPa (20 psi), which is typical of that used in practice, integration of the profile shows that this load is 520.6 kg (1147 lbf) for each metre of shoe length. For an 0.786m (2.78 ft) shoe this corresponds to a load of 409.2 kg (902 lbs), so that end effects reduce this to the supported load of 387.2 kg (854 lbf), or by just over 5%. Hence, if one assumes a linear decay of pressure in those parts of the seal region at the end of the shoe, the effective seal width is 42 mm (1.65 in), considerably larger than that along the sides.

D.4 Conditioning Effects

One of the most significant features of the results obtained from the prototype test bed is the phenomenon of conditioning, in which system performance improves significantly with time after a set of shoes have been installed, and this improvement may take a period as long as several days in extreme cases. Some evidence of conditioning was observed in the pressure measurements. Figure D6 compares pressure distributions obtained immediately after shoe installation with a second set obtained 19 hours later. A third set, taken after 72 hours additional conditioning gave results virtually identical to the second. For these tests, the shoe was aligned only visually, whereas for the data given in Figure D7, the alignment mechanism shown in Figure D3 was used. In this case, 24 hours conditioning resulted only in a negligible change.

This is typical of a trend observed in this and other experiments, which is that conditioning effects can be minimized by careful alignment. Also this behaviour is consistent with the idea that stress relaxation and other viscoelastic phenomena in the tissue, and possibly in the cover, can cause the shoe to "flow" into a geometry which is a better match to that of the rail, if it is not accurately aligned initially.

D.5 Effect of Thickness of the Shoe Cover

Several important results concerning the effect of the cover thickness on the pressure profile were obtained. An initial profile measurement was made using the standard 1.2 mm (0.047 in) thick extruded high density polyethylene tube cover. The shoe and cover combination was loaded and allowed to condition for 24 hours. The profile obtained is marked "Elliptical Cover" and shown in Figure D8. While the shoe was still under load the cover was slit along each side without disturbing the tissue. The pressure distribution was again measured and is shown as the curve marked "Slit Cover" in Figure D8. Further conditioning resulted in only minor changes to this second profile. The slit cover curve shows a marked decrease in measured pressure towards the edge of the shoe. The right side

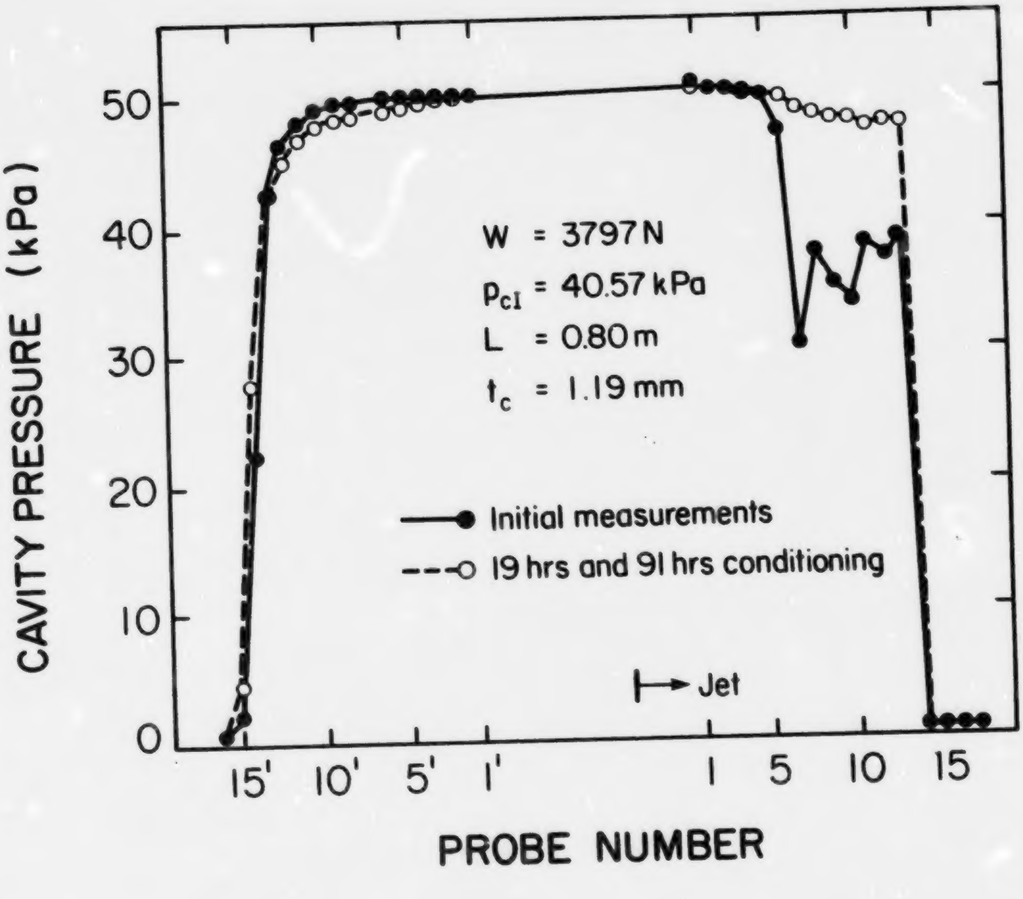

Figure D6. Example of a conditioning effect on pressure distributions. Shoe alignment mechanism was not used.

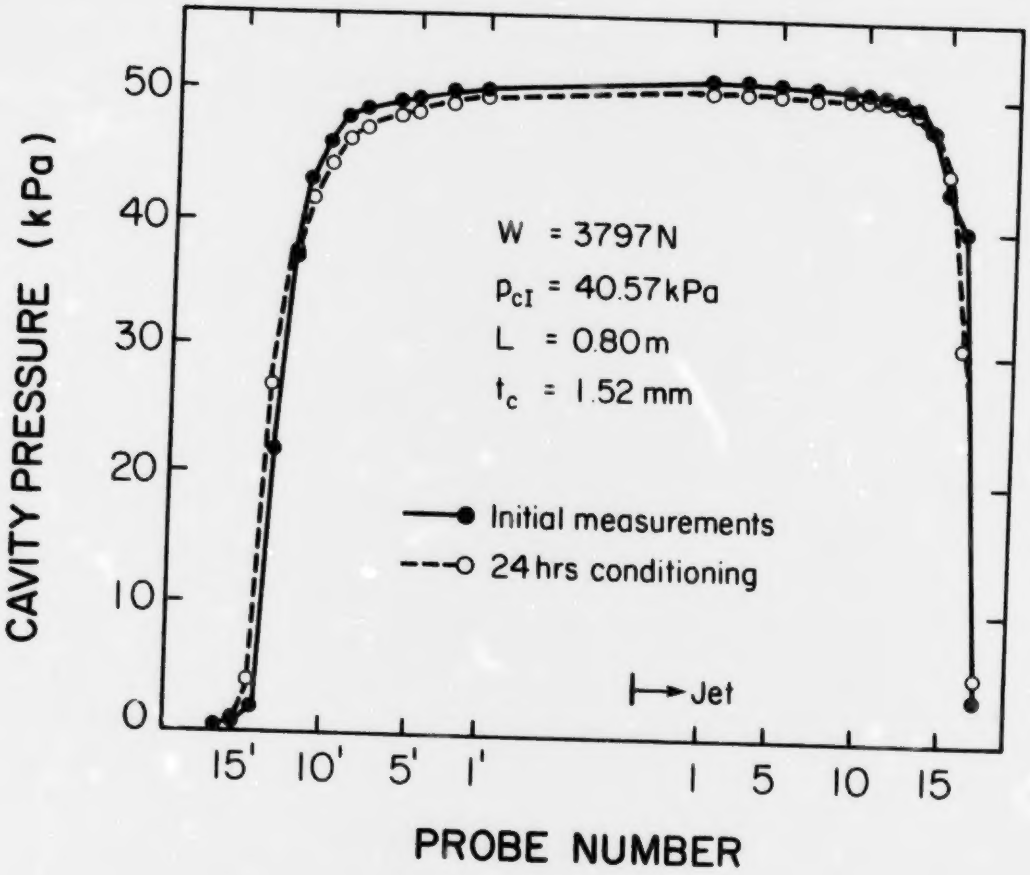

Figure D7. Effect of use of shoe alignment mechanism on conditioning of the shoe.

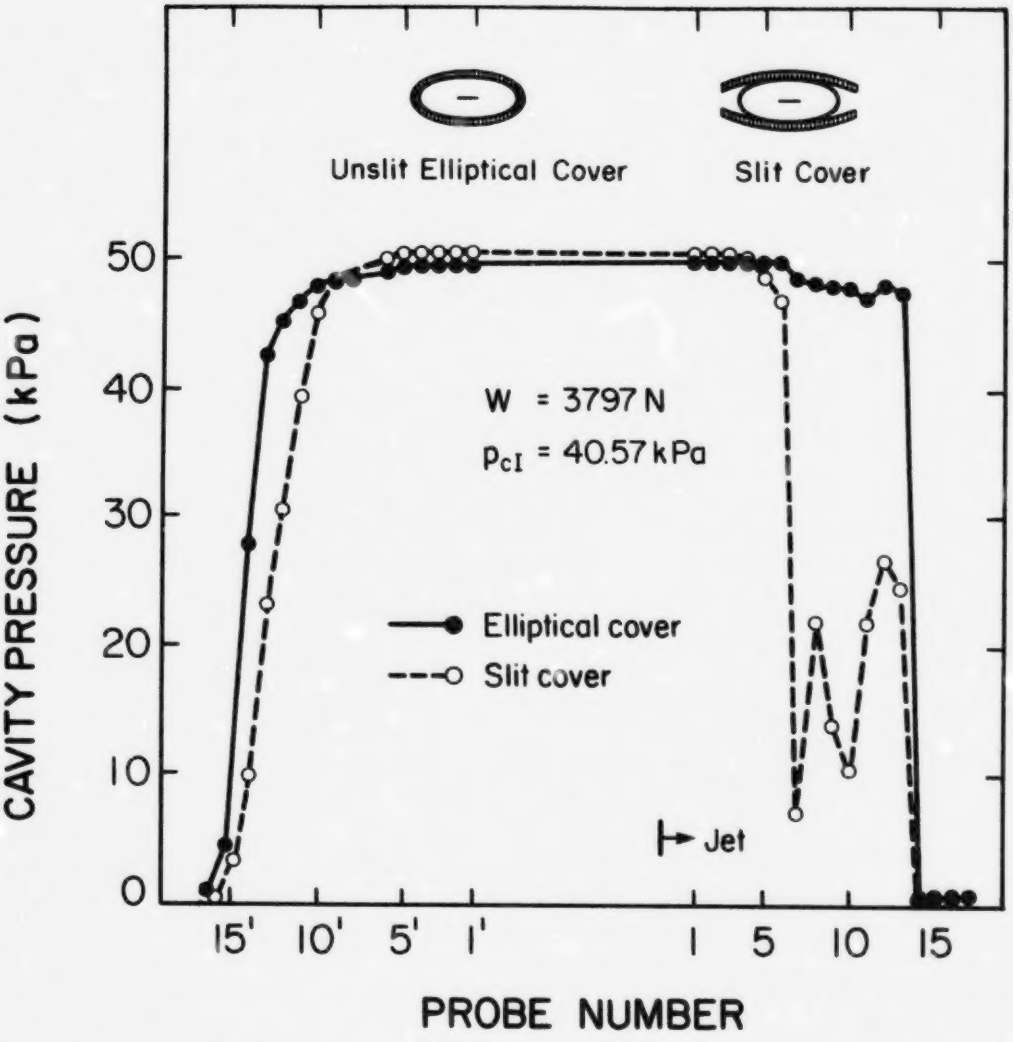

Figure D8. Effect of cutting the shoe cover along the sides of the shoe on the pressure distribution between shoe and rail.

shows a reduction of greater than 50% while the left side shows an increase in seal region width by a factor of about two. This indicated that the bending stiffness of the cover plays a significant role in determining the pressure profile.

Additional tests were performed to confirm this cover effect. The cellulose core was first covered with free-hanging 0.15 mm (0.006 in) thick polyethylene film. The cover was then bent down to the sides of the channel which supports the shoe and fastened there. Profiles measured after conditioning are shown in Figure D9, there is very little difference. The 0.15 mm (0.006 in) cover was replaced with a 1.5 mm (0.060 in) high density polyethylene cover, and identical tests were performed. Figure D10 shows the marked change in profile, with the bent cover being much closer to the ideal profile. To check that the improvement in pressure profile was not due to a radius mismatch effect caused by the tenfold increase in cover thickness, an 0.20 mm (0.008 in) steel shimstock cover was tested. Pressure profiles were again measured for the free and bent cases after the same conditioning periods, and the results are shown in Figure D11; bending this cover also improves the profile. Figures D12a and D12b compare the pressure distributions obtained for the three covers, and in the bent and unbent states respectively. The most important feature in Figure D12a is the difference in pressure gradients and size of the seal region; the 0.15 mm (0.006 in) polyethylene cover having a wider seal region and correspondingly lower pressure gradient than either the 1.52 mm (0.060 in) polyethylene cover or 0.2 mm (0.008 in) shim-stock. The data in Figure D12b shows much smaller differences.

The bending stiffness of a flat plate is proportional to Et_c^3, where E is the material modulus and t_c is the thickness. Values of Et_c^3 for the three covers are as follows: polyethylene sheeting, 8.1×10^{-4} N-m (6.0×10^{-4} lb-ft); high density polyethylene, 2.8 N-m (2.1 lb-ft); shimstock, 1.7 N-m (1.3 lb-ft). One concludes that that the bending stiffness of the shoe cover is the factor affecting performance.

D.6 Effect of Shoe Alignment and Support

The effect of lateral alignment changes was investigated. The results presented in Figure D13 were taken with the 1.5 mm (0.060 in) cover bent down and fastened to the supporting channel. Also note that the location and orientation of the air feed holes is marked in the figure. A preliminary test of the sensitivity of the pressure distribution to the way in which the shoe supports the load was made by inserting between shoe and support beam a strip having cross sectional dimensions of 1.5 mm × 15 mm and length equal to that of the shoe. No differences in pressure distribution were detected.

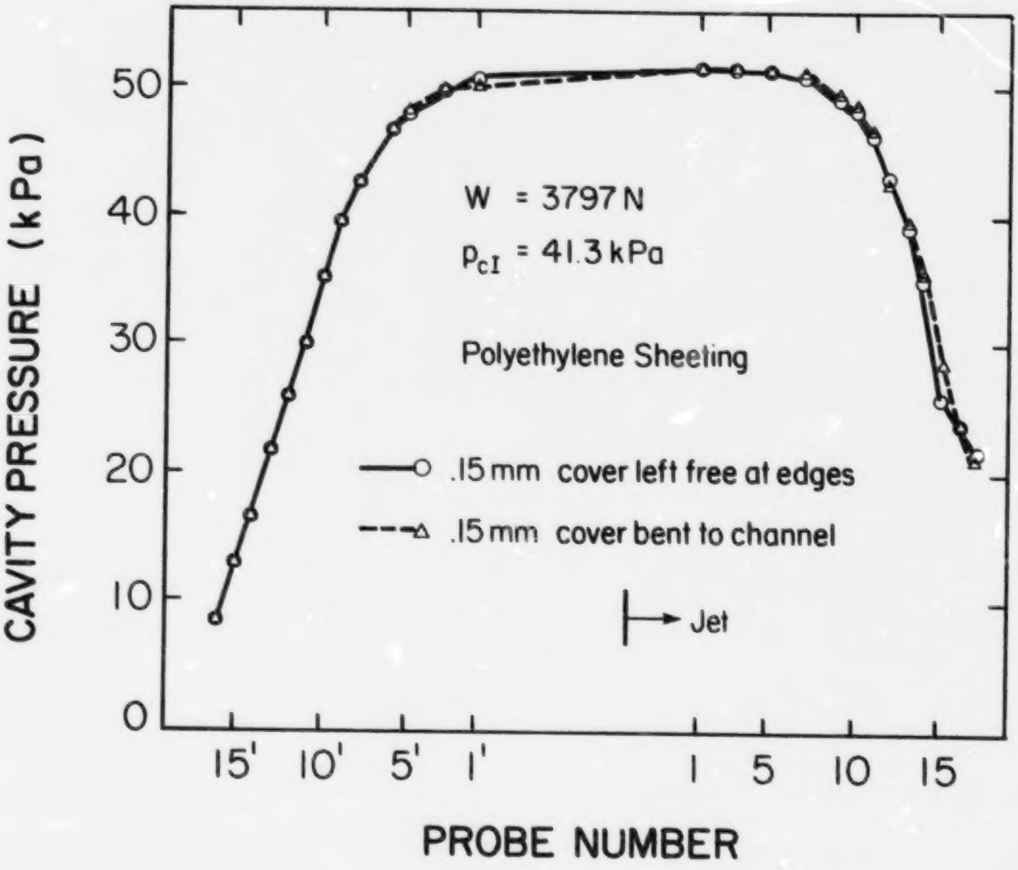

Figure D9. Effect of bending 0.15mm polyethylene cover on pressure distribution between shoe and rail.

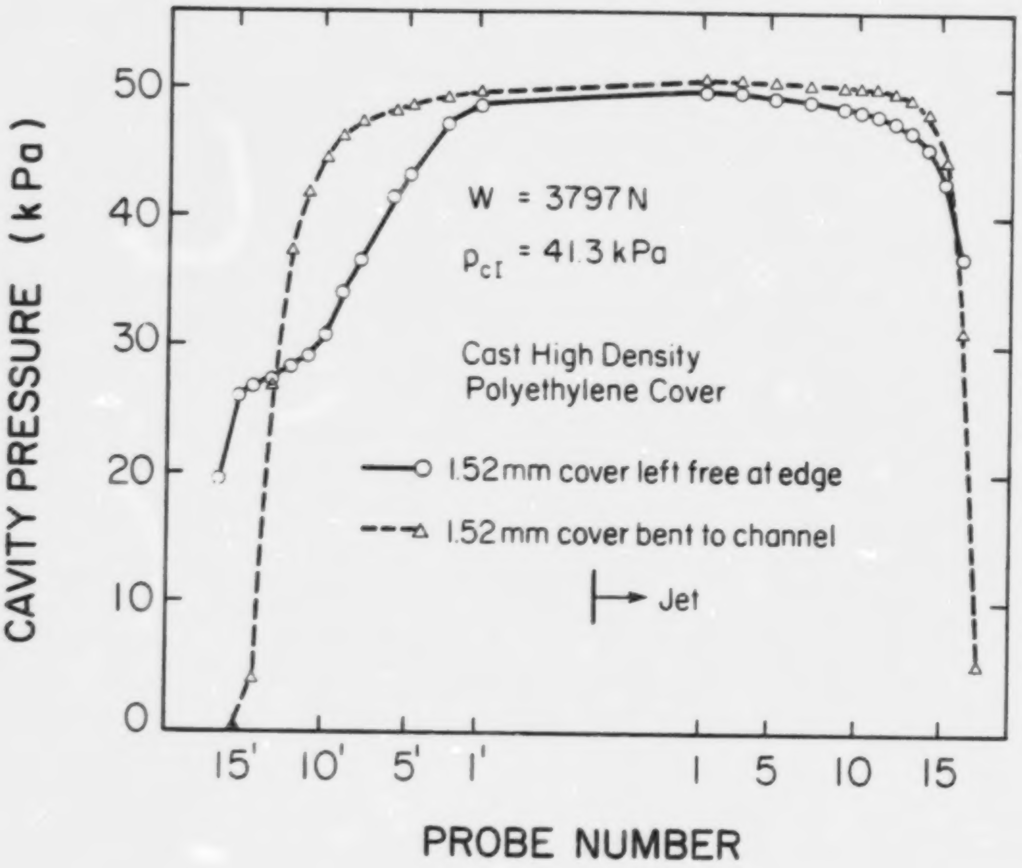

Figure D10. Effect of bending 1.52 mm high density polyethylene cover on pressure distribution between shoe and rail.

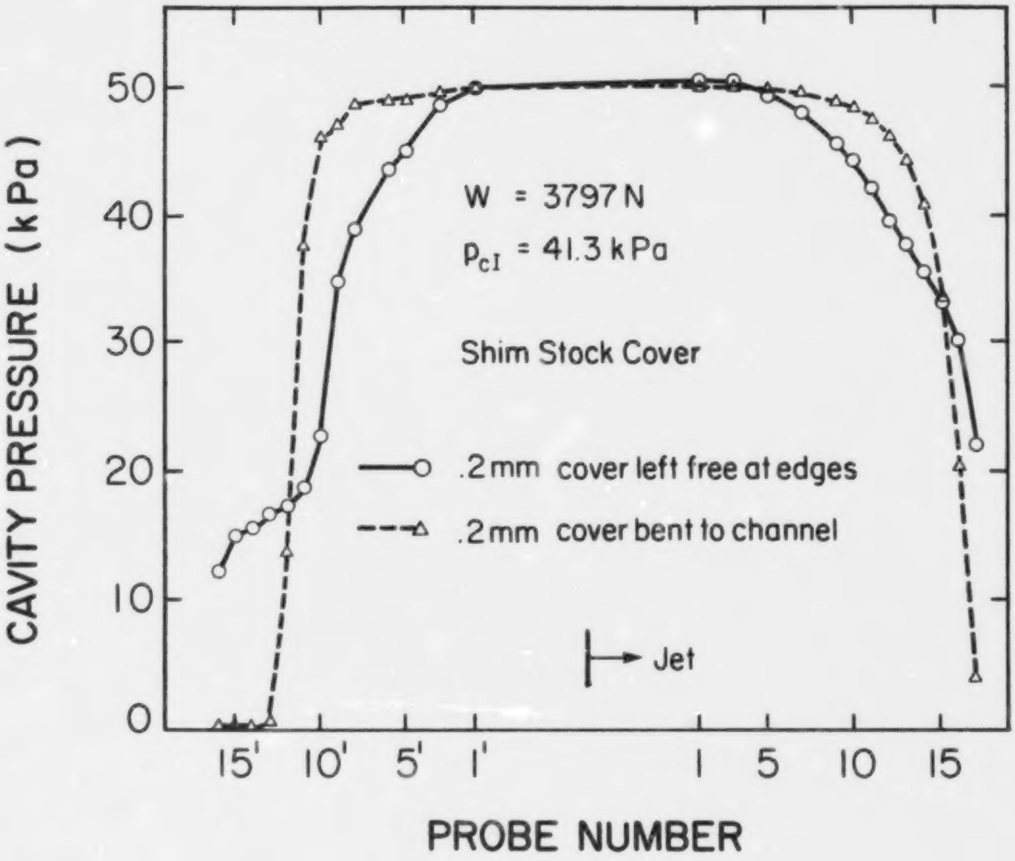

Figure D11. Effect of bending 0.20 mm steel shim stock cover on pressure distribution between shoe and rail.

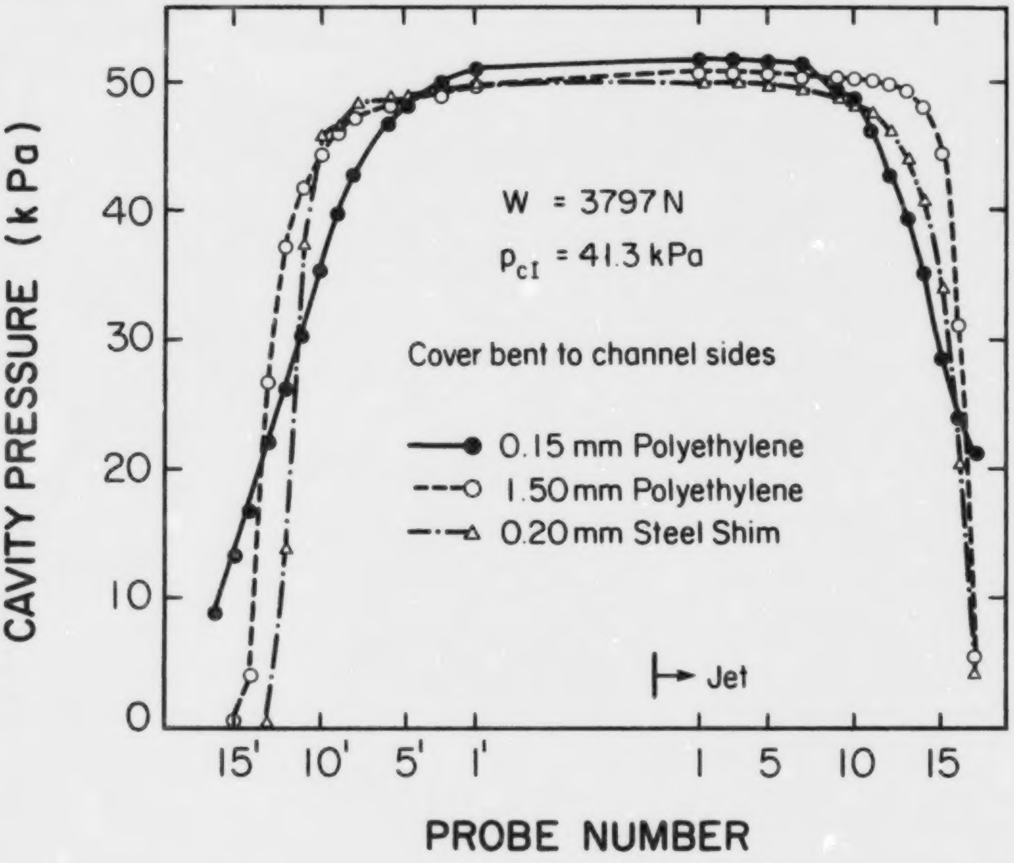

Figure D12a. Comparison of pressure distributions as obtained for three covers and with covers bent to channel.

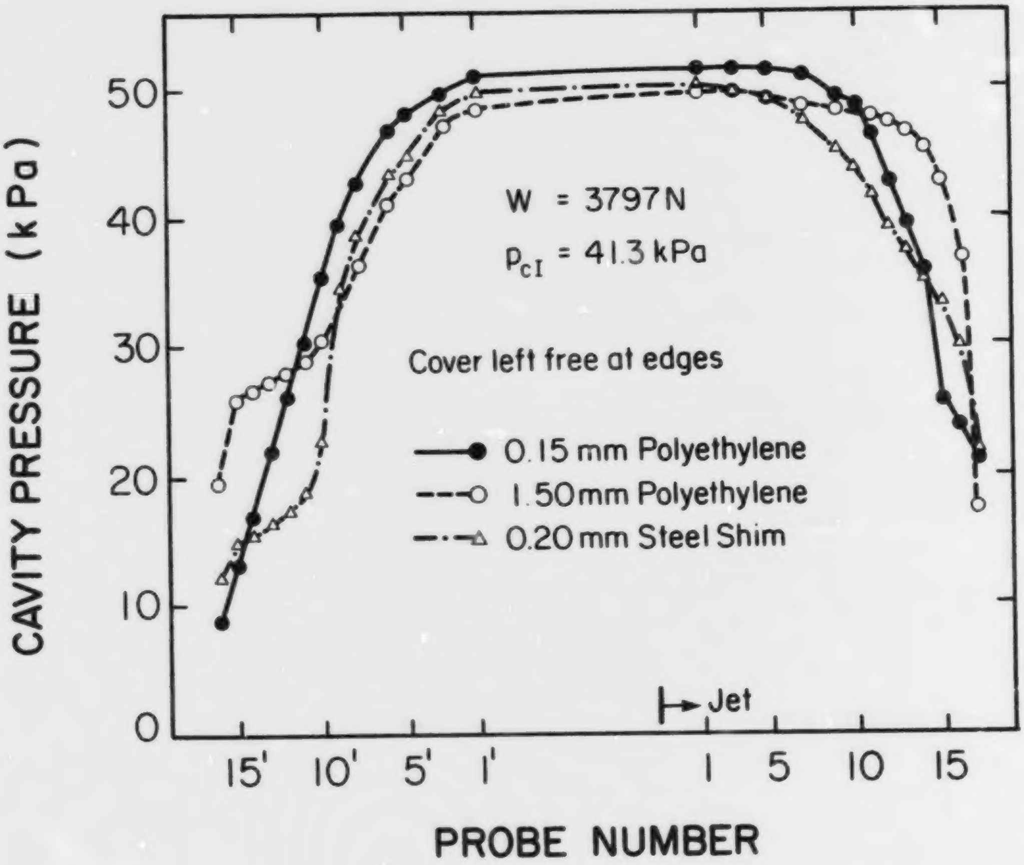

Figure D12b. Comparison of pressure distributions obtained for three covers left free at the edges.

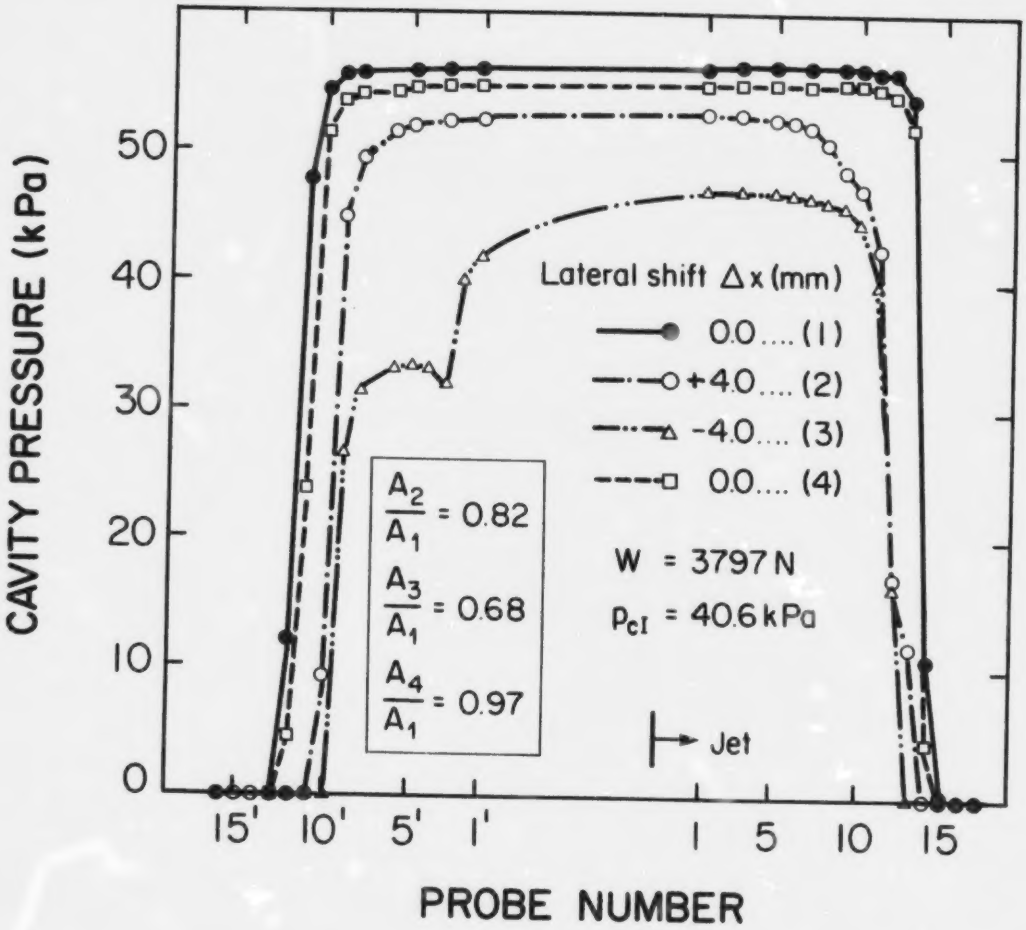

Figure D13. Effect of a lateral misalignment on pressure distributions.

In Figure D13, curve (1) is the pressure distribution obtained with the shoe centrally aligned and conditioned for 25 hours. Curve (2) was obtained when the shoe was moved laterally +4 mm (0.16 in) towards the air feed holes, while (3) is that corresponding to a shift 4 mm (0.16 in) from the centre in the opposite direction, and finally, curve (4) is that obtained when the shoe was realigned centrally. In each case the pressure distributions were taken after 24 hours conditioning. These measurements show the sensitivity of the results to shoe alignment; for case (2) the load carrying capacity is reduced to 82% of the aligned value, and in case (3) the reduction is to 68%. These results also provide part of the explanation of the difficulties in obtaining repeatable data from the prototype test bed (Appendix C). Furthermore, it is significant that the degradation is much more serious when the shoe is shifted away from the feed holes, and this indicates the importance of feed hole location or orientation or both. Unfortunately, the data does not distinguish between these two since orientation and location are in the same direction, but if the feed holes are well inside the cavity region, as is the case for the data here, then it is expected that orientation effects should be small. If these results are related to transit time as described in Appendix F, and the area under curve (1) is assumed to give the frictionless time, the transit time predicted from curve (4) would be 20% greater than inertial time and, in the other two cases no movement would be expected, since the friction force exceeds that of the 1.1% driving weight.

A series of tests was performed to determine the effect on the pressure profile of inserting various sizes of rod between the shoe and the supporting surface of the underside. It was intended to provide information on how large a disturbance would be required to cause a serious degradation of pressure profile by isolating the nozzle on one side of the centreline and limiting air entry to that side only. The results, shown in Figure D14, indicate that for rods as large as 12.7 mm (0.5 in) in diameter this does not occur. For a 25.4 mm (1.0 in) rod a distinct shift in the pressure profile was noted in which the side of the shoe which contained the nozzle experienced almost 50% higher pressure than the side which did not. The profiles shown are incomplete at the outer edges; this was done since only gross changes were of interest.

D.7 Measurements of Gap in Seal Region

In general, vertical displacement of the load W associated with changes in track pressure p_t include both effects of shoe deformation and change of height of the bottom of the shoe relative to the rail surface. Consequently, measurement of changes in the height of the load does not give direct information on the dependence of effective seal height h_s on the air flow rates. However, whereas at low values of p_t the load is supported partly by air pressure and partly by direct shoe-rail contact, as p_t is increased, at a certain critical value the load should be supported entirely by the air pressure, and the shoe can then be said to have achieved "lift-off". Since W is fixed, further increases of p_t should not alter

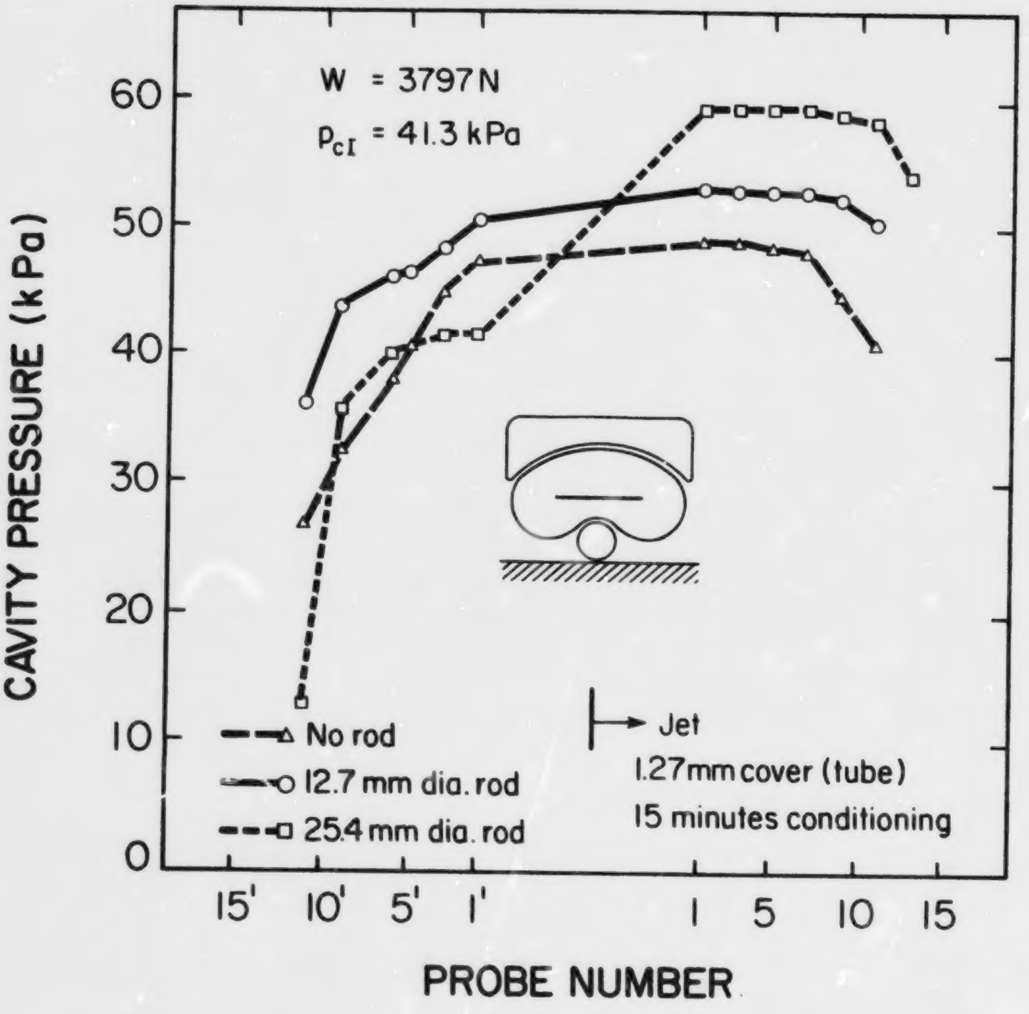

Figure D14. Effect of disturbance placed between shoe and load on pressure distributions.

significantly the pressure distribution acting on the shoe. Hence, if this is the case, once lift-off has occurred, any further vertical motion of the load W is associated with increases in h_s and not shoe deformation. This should therefore enable an estimate of h_s to be obtained from measurements of the movement of the load under the action of increasing p_t.

One problem with this approach to obtaining data on h_s is ascertaining when lift-off occurs. The data obtained from the prototype test bed (Appendix C) suggests that there is no readily detectable transition, and that shoe deformation under the action of increasing flows and rising cavity pressures makes the process of reduction of the fraction of the load carried by direct shoe-rail contact relatively gradual. Consequently, for the present purposes, "lift-off" is arbitrarily said to have occurred when the air pressure is supporting 95% of W. Typical transit time data obtained from the prototype test bed and measurements of sliding friction (Appendix F) can be used to estimate when the 95% W condition has been reached. For a well conditioned shoe and W = 9800 N, lift-off occurs at about p_t = 75 kPa.

Figure D15 gives pressure profles for p_t higher than 75 kPa; it shows that, once lift-off occurs, as p_t increases to 267 kPa the cavity pressure increases by only 2.8%. Now if the shoe was constructed from linear elastic materials, then the associated deformation would be about the same order of magnitude. However, since the deformation properties of the shoe are expected to be determined largely by those of the tissue, and since the data in Appendix H shows that the tissue stiffens considerably as it is compressed, the deformation of the shoe caused by an increase in cavity pressure of 2.8% should be much less. Hence one can conclude that, for $p_t >$ 75 kPa, vertical motion of the load is associated with increasing h_s.

A dial gauge was installed on the pressure measurement apparatus as shown in Figure D2 to measure vertical displacement of the track supporting structure as a function of track pressure and flow. Typical results are given in Figures D16 and D17. The data in Figure D16 shows a very rapid increase in displacement before lift-off followed by a transition to a much slower rate of increase thereafter. The asymmetry in the initial motion of the load is believed to be caused by a slight misalignment of either the load or linear ball bushing assembly. Since the shoe is supporting the load prior to supplying air, the relatively large displacement that occurs even at the 1-end in Figure D16 suggests that the shoe expands prior to lift off. Presumably this occurs because the air pressure provides a more evenly distributed loading of the shoe than does direct shoe-rail contact. Note that after lift-off, the displacements at either end are nearly equal. Figure D17 gives the measured vertical displacement as a function of air flow rate, and compares this with the theory developed in Appendix A. Considering the preliminary nature of the theory, and the experimental problems reasonable agreement has been obtained.

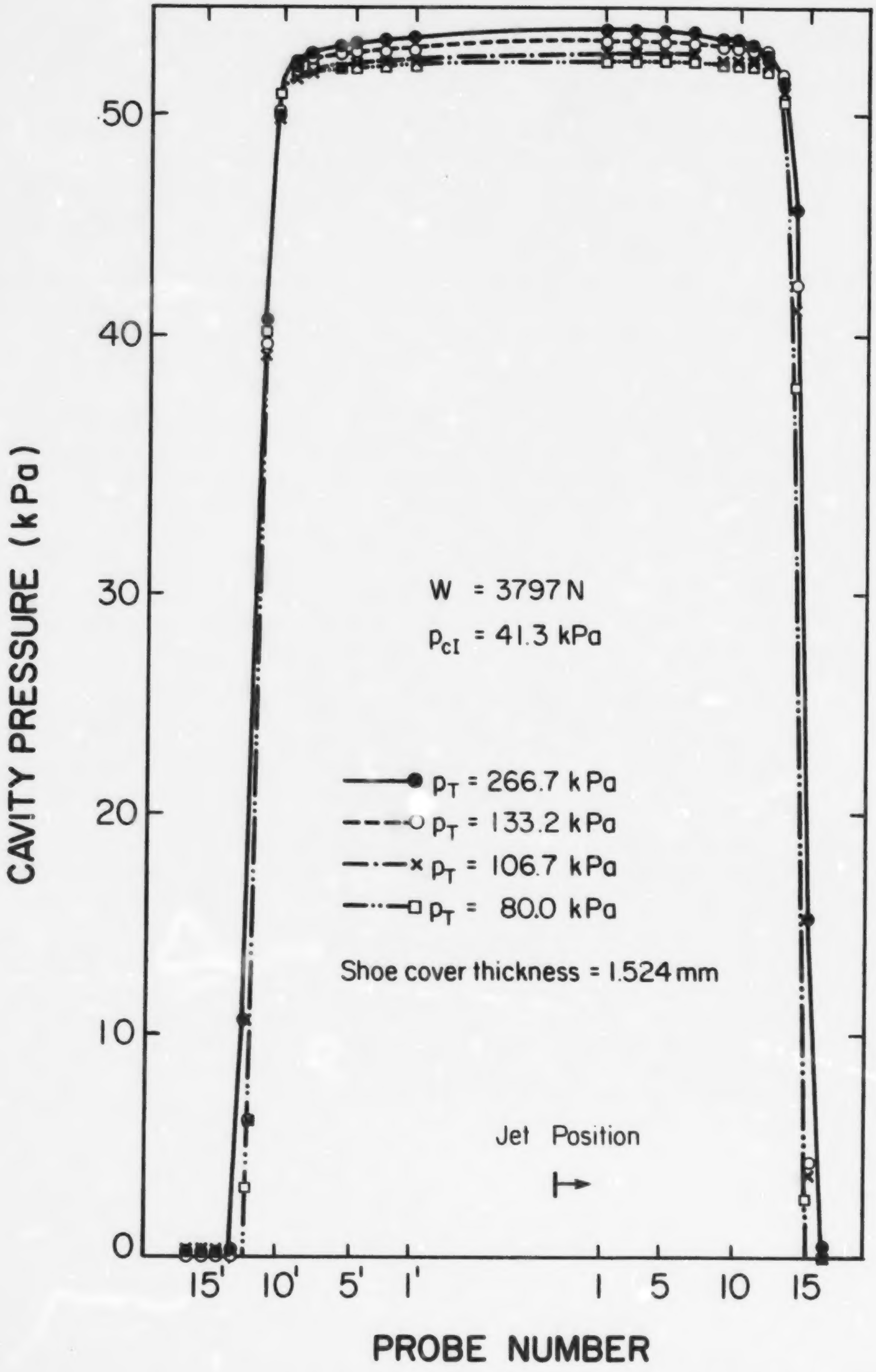

Figure D15. Effect of track pressure on pressure distributions after lift-off has occurred.

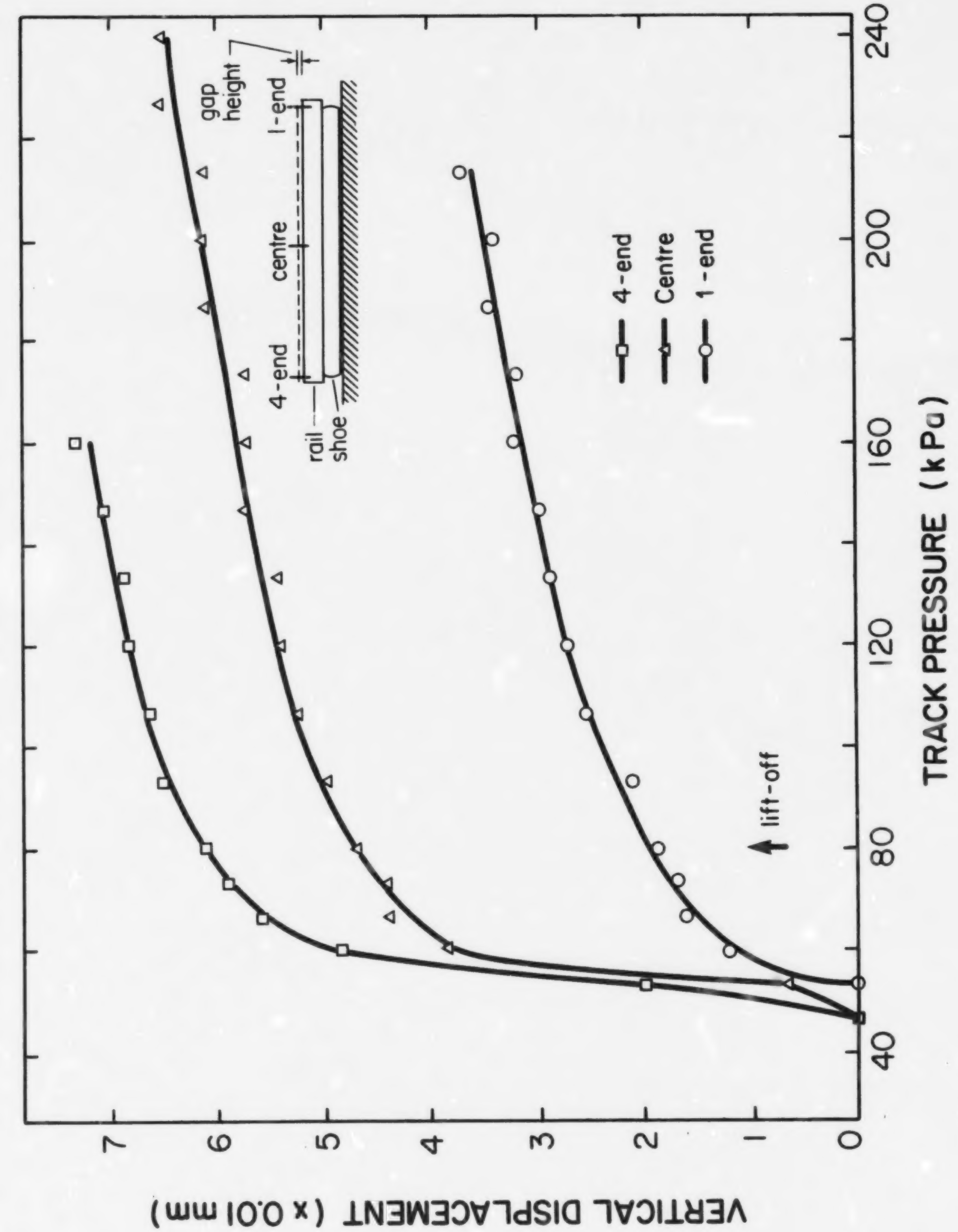

Figure D16. Effect of track pressure on vertical displacement of load.

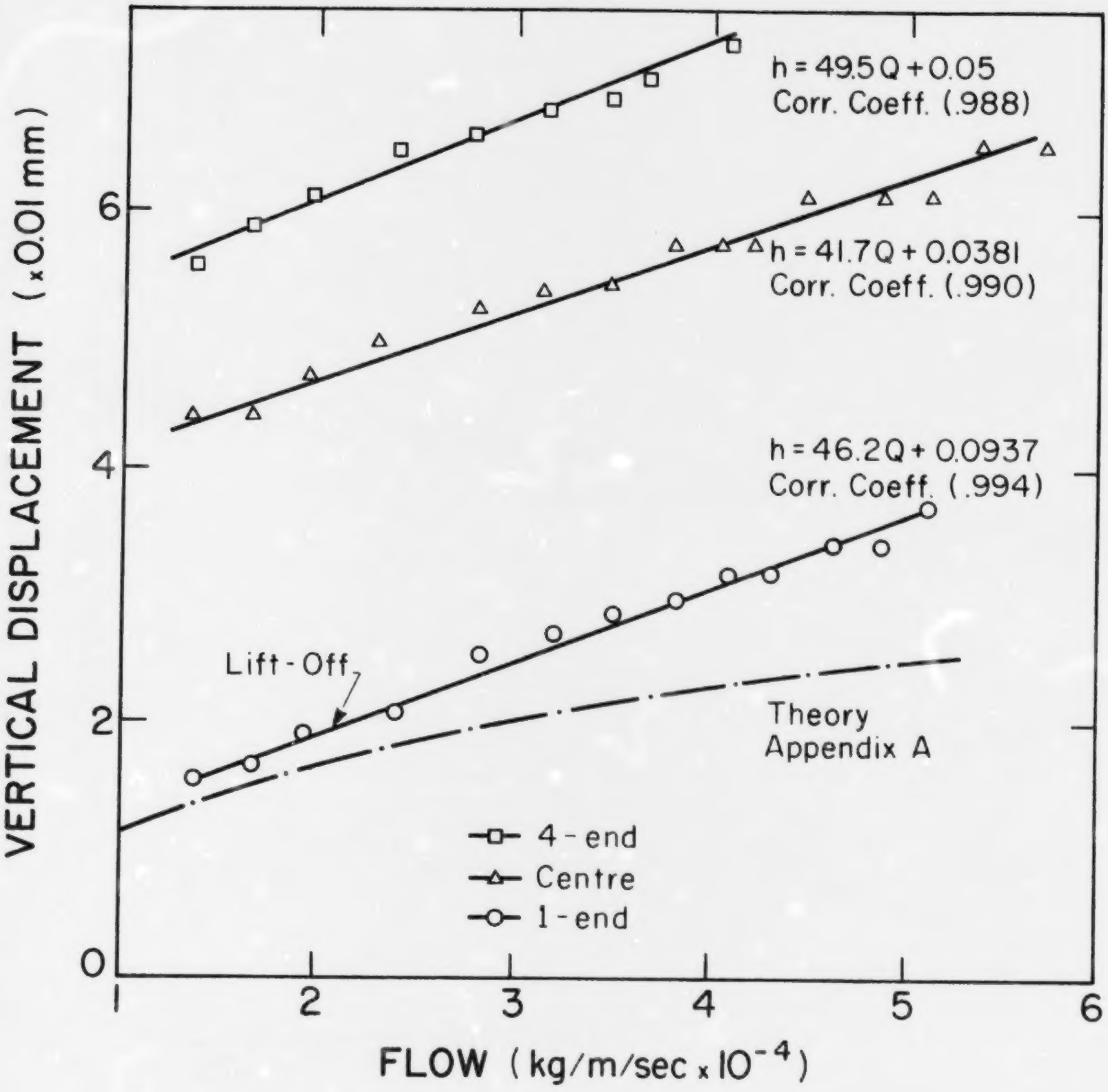

Figure D17. Vertical displacement of the shoe as a function of air flow rate. The mass flow is quoted for a unit length of seal region. For the 0.8m shoe used in the tests, an allowance of 0.1 metre for the seal at each end is included to give a total equivalent seal length of 1.8m.

No attempt was made to eliminate the loading or alignment asymmetry in the displacement tests, because at the time we had decided to continue the work in different apparatus.

D.8 A Concluding Note

Although, as noted in the Introduction to this Appendix, pressure data provides basic information on the air bearing aspects of SailRail, determination of the fraction of the load carried directly by air pressure, is very time consuming. Owing to the low air flow rates involved, individual pressure tap readings can take many minutes to stabilize. Also, recent measurements indicate that pressure profiles taken at four stations along the shoe may be required to determine the lift force to a reasonable accuracy. If the coefficient of sliding friction for a particular rail-shoe combination is known then the transit time data obtained on the test bed can be used to compute the lift due to air pressure. The initial experiments in measuring friction coefficients described in Appendix F suggest that if the test bed could be modified to allow routine measurements of this quantity just prior to measuring transit times, the lift due to air pressure can be computed with acceptable accuracy.

APPENDIX E. REVIEW OF POLYMER FRICTION (M. Simard and P. A. Sullivan)

E.1 Introduction

The test bed data described in Appendix C shows that, at the values of track pressure p_t used in current applications, some fraction of the load is being supported by direct contact between shoe and rail. Also in applications such as warehouse storage and retrieval systems, to provide retarding forces, reliance is placed on sliding friction. Hence both effective interpretation of test data and design of commercial applications requires a knowledge of the sliding friction properties of shoe and rail. In current practice the shoe cover is made from high density polyethylene and the surface of the aluminium rail is anodized for hardness and then impregnated with Teflon for low friction. This Appendix is a brief review of the available literature on polymer friction with special emphasis on the materials of interest here. A bibliography of selected papers on the friction and wear of polymers is included in this report after the main references. Some of these are references for this Appendix.

E.2 The Molecular Nature of Polymers

The literature describing the frictional properties of polymers suggests that the materials be classified into three groups [E2]:

(a) Smooth Molecular Profile Polymers such as:

   (i) high density polyethylene (HDPE),
   (ii) polytetrafluoroethylene (PTFE),
   (iii) Teflon.

(b) Normal Polymers such as:

   (i) low density polyethylene (LDPE),
   (ii) polypropylene (PP).

(c) Amorphous Polymers such as:

   (i) polymethyl methacrylate (PMMA),
   (ii) polyvinyl chloride (PVC),
   (iii) polystyrene (PS).

We are concerned mainly with the properties of polymers in class (a) since they have very low sliding friction coefficients.

Polymers consist of long molecular chains of covalently bonded atoms. One of the simplest polymers is polyethylene; Figure E1 shows its planar structure; it is made of CH_2 groups. Important differences between the mechanical behaviour of LDPE and HDPE is due to chain-branching where a secondary chain initiates from a point on the main chain as in Figure E2. LDPE has about 340 side groups for every 1000 carbon atoms compared to 3 side groups for every 1000 carbon atoms for HDPE. For PTFE the planar zigzag structure is twisted into a gentle helix to accommodate the side groups, which are made of fluorine atoms [E15]. For commercial Teflon, a perfluoromethyl (CF_3) group replaces a fluorine atom along the carbon chain.

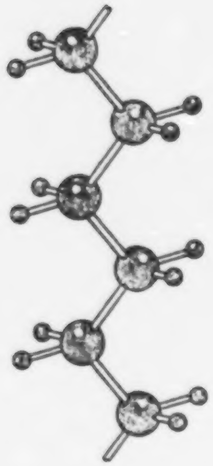

Figure E1 Polyethylene chain.

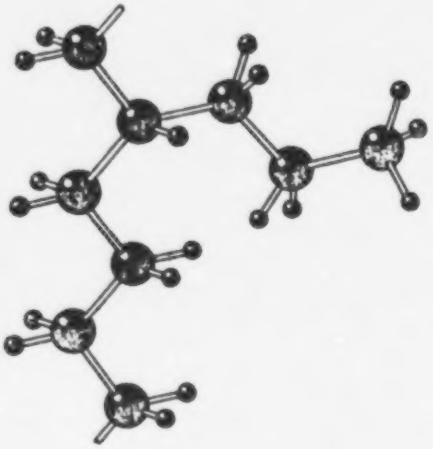

Figure E2 Chain branch in polyethylene.

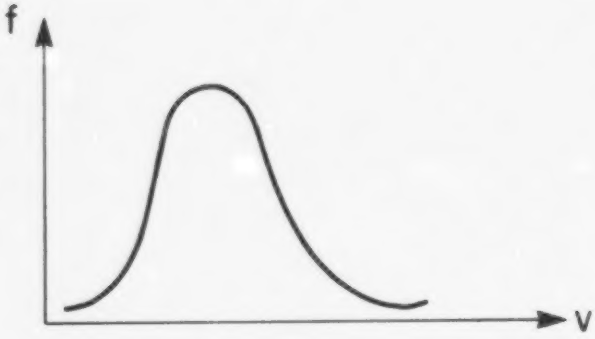

Figure E3 Effect of sliding speed on friction of polymers.

The molecules have the same helical structure but the CF_3 group destroys the smooth profile.

E.3 Friction Mechanisms

It is now generally thought that forces caused by sliding friction arise from two main sources [E12]:

(i) adhesion, or the rupture of bonds caused by intermolecular forces at regions of true contact,

(ii) for dissimilar materials, ploughing or penetration of surface irregularities of the harder material into the softer material, causing deformation and flow of the latter as sliding occurs.

With metal pairs the first of these mechanisms is usually the main source of frictional forces, but for polymers sliding on each other or on metal the second mechanism can be very significant [E12]. Hence the frictional properties of polymers can be complex, so that for this and other reasons polymer friction usually does not obey the classic laws, which are that the frictional force is proportional to the load W and independent of the apparent area of contact A.

Now consider the first mechanism in more detail. The frictional force F is proportional to the shear strength S of the junctions produced by adhesion, and to the true area of contact A_r, $F = A_r S$. The value of A_r depends on the topography of the surfaces and on the deformation processes that occur at the localized areas of contact when the surfaces are loaded. If the elastic moduli are high, as is the case for metals, and there are relatively few regions of contact, then the deformation tends to be plastic, in which case $A_r = W/p_m$, where p_m is the flow pressure of the softer material. In this case, the coefficient of friction $\mu = S/p_m$ and is independent of W. If the deformation is elastic, as is likely to be the case if one of the materials has a much lower elastic modulus, then $A_r \propto W^{+n}$ where $0 < n < 1$ usually, in this case $\mu \propto W^{n-1}$ and decreases as W increases. For similar surface topographies then, polymers are much more likely to undergo elastic deformation, so μ can depend on W [E12]. At some point, as the roughness of the surfaces decreases and the number of contacts increases, the deformation becomes elastic; however μ becomes independent of W for both elastic and plastic deformation [E12, E20].

For the ploughing mechanism, since polymers can respond viscoelastically to applied stresses, the speed of sliding can play an important role. Figure E3 shows a typical speed effect; there can be a peak in μ at some intermediate speed. One explanation of this is as follows [E12]. Consider a symmetric asperity of a hard material pressed into a plane of viscoelastic material. At zero sliding speed the symmetrical pressure distribution creates no side force at the interface between the two materials, so that the contribution to the frictional force is zero. This is shown in Figure E4a. When relative motion occurs, pressure at the leading face of the asperity causes viscoelastic material to accumulate in this region whereas at the trailing face, the viscoelastic material does not instantaneously return to its original shape. Hence, the arc of contact moves from a-b to c-d, thus creating an unsymmetrical pressure distribution as shown in Figure E4b. At higher speeds, the delayed recovery of the viscoelastic material on

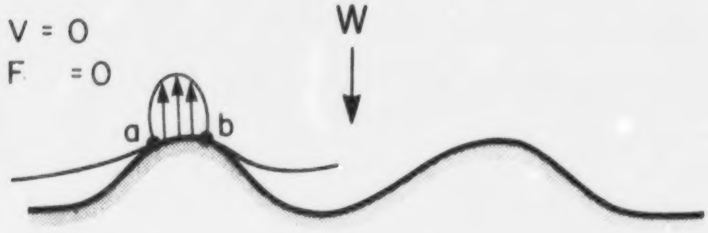

a) Zero sliding speed.

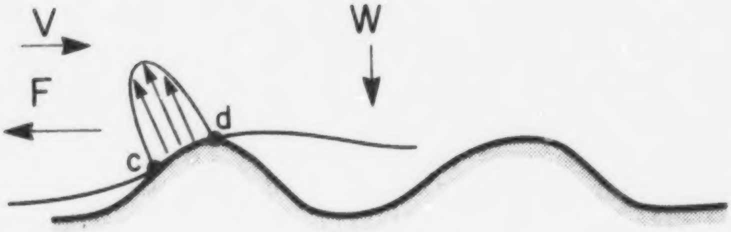

b) Low sliding speed.

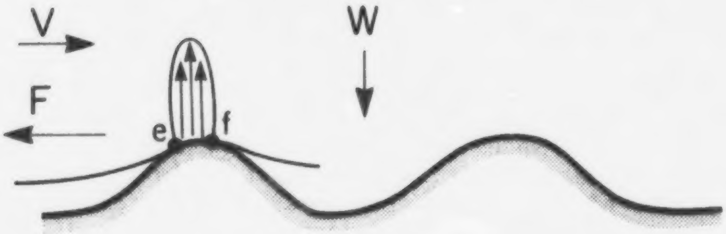

c) High sliding speed.

Figure E4 Mechanism of friction caused by deformation or ploughing, for a regular hard asperity pressed into a viscoelastic material.

the downward slope of one asperity will decrease the accumulation on the upward slope of the succeeding asperity. Hence "c" and "d" approach each other and the contact arc at very high slidings is not only reduced but becomes more nearly symmetrical. This is shown in Figure E4c.

Of the possible effects of environmental conditions on friction, temperature appears to be the most important parameter. For example, Ref. E12 notes that linear crystalline thermoplastics such as polyethylene show only small differences in friction when tested in air, inert gases or the environment. Temperature affects the adhesion mechanism because the shear strength of the junctions and the hardness or elastic modulus decrease with increase in ambient temperature. But the rates of decrease can be different for both properties, so the resultant effect can be either an increase or a decrease. Also temperature can have a strong effect on the ploughing mechanism since in certain temperature ranges, the viscoelastic properties of polymers can vary rapidly with temperature. The overall effect of increased temperature is usually to move the curve in Figure E3 to the right [E17].

E.4 Properties of PTFE and HDPE

Of the smooth molecular profile polymers, PTFE is preferred for bearing applications because of its low μ and high thermal stability. The lowest values of μ are obtained when PTFE is in the form of a thin film on a harder substrate, and for heavy loads at low speeds (less than 10 cm/sec), in which case values of $\mu = 0.05$ and less have been obtained [E12]. This appears to be related to its ability to transfer thin oriented films onto a hard, smooth counterface to a much greater extent than HDPE. However when PTFE is used in bulk to slide against itself or metals, the ploughing mechanism becomes important and μ can be in the range $0.05 < \mu < 0.15$ [E12]. Owing to the film transfer mechanism, sliding experiments using PTFE often show a decrease in μ after repeated runs [E15]. However at high speeds, the film is stripped away and has to be renewed for every run of the slider [E12].

In contrast to most polymers, μ for PTFE has been shown to be affected by humidity; Ref. E17 measured a higher μ in dry air than in air with 50% relative humidity.

Very little data on HDPE was found. However the main point to note is that, in addition to its reduced ability to transfer thin oriented films, it has a low softening temperature, about 120°C in contrast to PTFE, which is about 325°C.

E.5 Implications for the Present Work

The main conclusion to be drawn from the above discussion is that for polymers sliding on themselves or on metals a unique coefficient of friction does not exist. Also because so many variables are involved, the only feasible approach is to routinely make measurements as required.

In the case of the experiments described in Appendix C the data seems to suggest that frictional forces are directly proportional to load (see Figure C20), a result which, in view of the above discussion, seems surprising. It was also observed that, in a sequence of measurements of transit time taken with track pressure p_t increasing and then decreasing, slightly longer times were observed when p_t was decreasing (see Figure C2). No clear explanation of this trend was obtained, however Ref. E18 observed a similar trend for PTFE sliding on itself when, in repeated tests, the speed of sliding was increased and then decreased.

Finally, the preliminary sliding friction measurements described in Appendix F seem to indicate that PTFE film deposition does not occur, since repeated traversals by the slider did not show a reduction in friction [see Figure F2]. No literature on HDPE sliding on Teflon was found, so the present results suggest that, for this combination, film deposition does not occur.

APPENDIX F. SLIDING FRICTION MEASUREMENTS AND THEIR RELATION TO PROTOTYPE TEST BED RESULTS (T. A. Graham)

F.1 Introduction

Since the transit times obtained in the prototype test bed results of Appendix C are significantly greater than those corresponding to frictionless acceleration, there is always partial contact between the shoe and the rail at the air supply pressures used in practice. Presumably this occurs because the minimum effective gap between shoe and rail is very small, and because both shoe and rail have surface irregularities. It implies that a fraction of the load is carried by this direct contact. If the coefficient of sliding friction between the shoe cover and rail is known, then the transit time data can be used to estimate the fraction of the load carried by direct contact. This Appendix describes sliding friction measurements on several combinations of rail and cover and their application of the results to the interpretation of test bed data.

F.2 Analysis

The motion of the pallet is described by the equation

$$(m_D + m_p)\chi + \mu\dot{\chi} = m_D g - k_f N \tag{F1}$$

where

χ = pallet position

m_p = mass of the pallet

m_D = mass of the driving weight

g = gravitational acceleration

μ = viscous fluid resistance coefficient

k_f = coefficient of sliding friction

N = weight supported by shoe-track contact

In equation (F1) the term $\mu\dot{\chi}$ accounts for the effect of the shear of the air between shoe and rail; it was estimated to be about two orders of magnitude smaller than the other terms in the equation, and has been neglected. The weight N supported by shoe-rail contact may be expressed as

$$N = cm_p g \tag{F2}$$

where the coefficient c is the fraction of pallet weight supported by direct contact.

Equation F1 then becomes

$$(m_p + m_D)\ddot{\chi} = (m_D - k_f c m_p)g \tag{F3}$$

and this may be integrated to give

$$\chi(t) = (m_D - k_f c m_p) g t^2 / [2(m_D + m_p)] \qquad \text{(F4)}$$

where the boundary conditions $\chi(0) = \dot{\chi}(0) = 0$ have been used. If χ_1 and χ_2 are the locations of the timing switches on the test bed, then the transit time Δt is given by

$$\Delta t = \left\{\frac{2}{g} \frac{(m_D + m_p)}{(m_D - k_f c m_p)}\right\}^{1/2} (\chi_2^{1/2} - \chi_1^{1/2}) \qquad \text{(F5)}$$

F.3 Sliding Friction Measurements

The coefficient k_f was determined for several combinations of cover and rail surface using data obtained on the apparatus depicted in Figure F1. Friction forces were measured using a spring balance inserted in the cable as shown and the flat lower surface of the rail was used for the tests to eliminate horizontal alignment problems. Figures F2 to F5 give the static, $\dot{\chi} = 0$, friction coefficient k_{fs} and values for k_f at a low constant speed. As noted in Appendix E, k_f for the material combinations used here may depend on speed and contact stress σ_c. Owing to the limitations of the apparatus, the effect of speed was not explored in detail, however it was found that for the small speed range attainable little variation in k_f occurred.

The effect of variation of σ_c on test-bed results can be difficult to assess, since although the pressure measurements in Appendix D can in principle be used to ascertain the fraction of the load being carried by direct contact, at any given track pressure p_t the actual contact area is not known. However, it is possible to ascertain the range of σ_c that can occur in a typical test bed experiment, and if it can be established that k_f remains constant in this range, interpretation of test bed data is straightforward. It seems reasonable to assume that, when there is no air flow between shoe and rail σ_c is at a maximum, and that it decreases monotonically to near zero as p_t increases to its maximum value. Hence, if the width w_c of the region of contact between shoe and rail for no air flow is known, the maximum value of σ_c can be estimated. The value of w_c is difficult to measure directly, but since as p_t increases from zero, the deformation of the shoe associated with the formation of the cavity is very small, it can be safely assumed that w_c is about the same as the width of the pressure footprints described in Appendix D. From Figure D15 a representative value of w_c = 90 mm so that for a load of 1000 kg on a 1.22m long pallet, the maximum value σ_c is about 45 kPa. In the tests described in this Appendix the effect of variation of σ_c was examined by taking some measurements at two stress levels, 37.2 kPa and 18.7 kPa. The resultant values of k_f were found to differ by less than 3% of the measured value. Hence it was assumed that k_f was independent of σ_c in the test bed results.

Figures F2 and F3 show that k_f and k_{fs} for the Teflon treated hard anodized surface and the polished aluminum surface are about 18% lower than the corresponding values for the plain hard anodized surface. The results in Figure F3 for the 0.762 mm (0.030 in) cover are about 12% lower than those of the 1.22 mm (0.048 in) cover in Figure F2, although the samples are

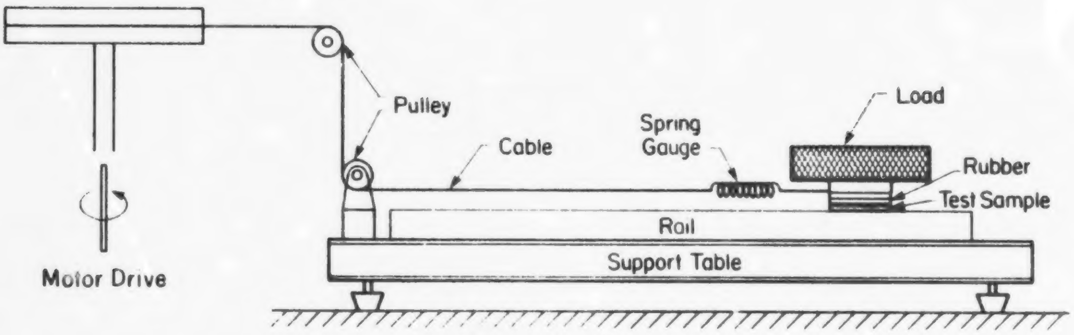
Pulley
Load
Spring
Gauge
Cable
Rubber
Test Sample
Rail
Support Table
Motor Drive

Figure F1 Apparatus used to measure coefficients of friction.

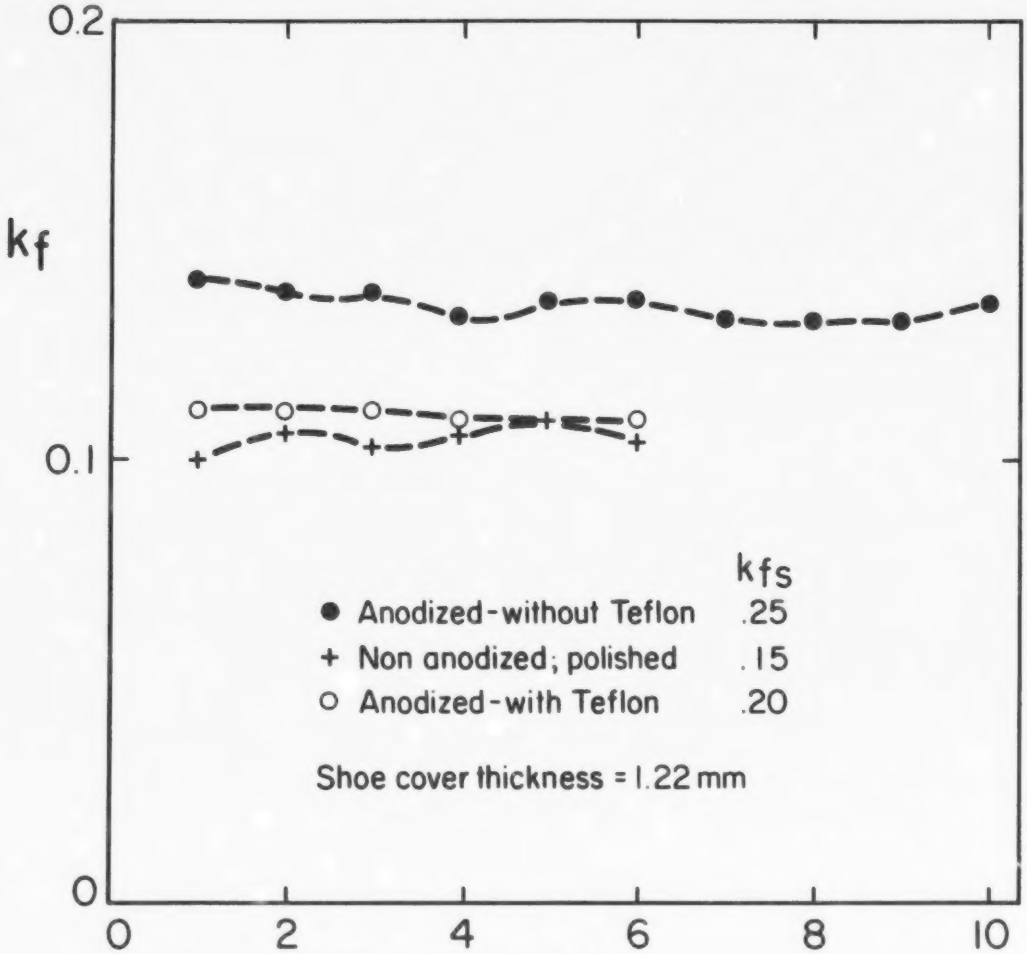

Figure F2 Friction coefficient K_f for 1.27mm extruded polyethylene sheet sliding on various surfaces. The static value, K_{fs} is also given.

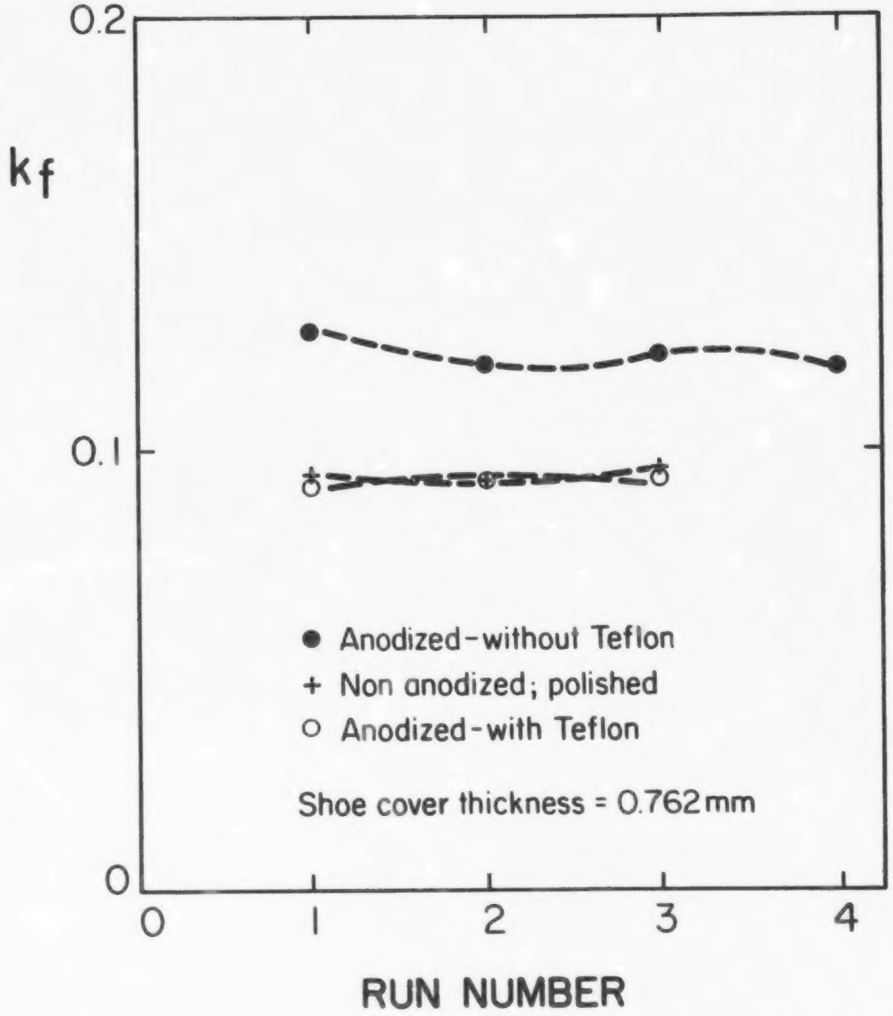

Figure F3 Friction coefficient for 0.762mm extruded polyethylene sheet sliding on various surfaces.

from nominally the same material. The difference could be attributed to variations in material molecular structure (since the samples are from different producion runs), to differences in surface quality, or to the effects of prior use of the 0.762 mm sample in the prototype test bed. Figures F4 compare typical plastic results with those obtained for steel shim-stock; it shows that the shim-stock friction coefficient steadily increased with run number. This was thought to be caused by removal of oil or other anticorrosion surface coatings in successive runs. Cleaning the shim-stock with chlorothene prior to testing did not eliminate this problem, so that the testing was discontinued.

Tests to determine the effect of relative humidity on k_f were performed since the developer had indicated that pallet motion was more sluggish during hot humid weather. The results presented in Figure F5 show that the relative humidity of the air has little effect on the coefficient of friction.

F.4 Relationship to Test Bed Results

The friction data was used to predict the effect of track pressure on transit time. Transverse pressure profiles in the cavity and seal regions were obtained at various track pressures, see Figure D15. The profile obtained at a track pressure of 267 kPa was assumed to provide 100% support for the shoe load. The profiles at all pressures were integrated, and the reduction in the pressure forces at lower track pressures was assumed to be caused by increased shoe-track contact, so that a fixed total lift force was provided. These shoe-track contact forces and the coefficient of friction were then used to produce the transit curves shown in Figure F6. These curves show the influence of coefficient of friction on the shape of the curve. A typical data curve is also presented for comparison.

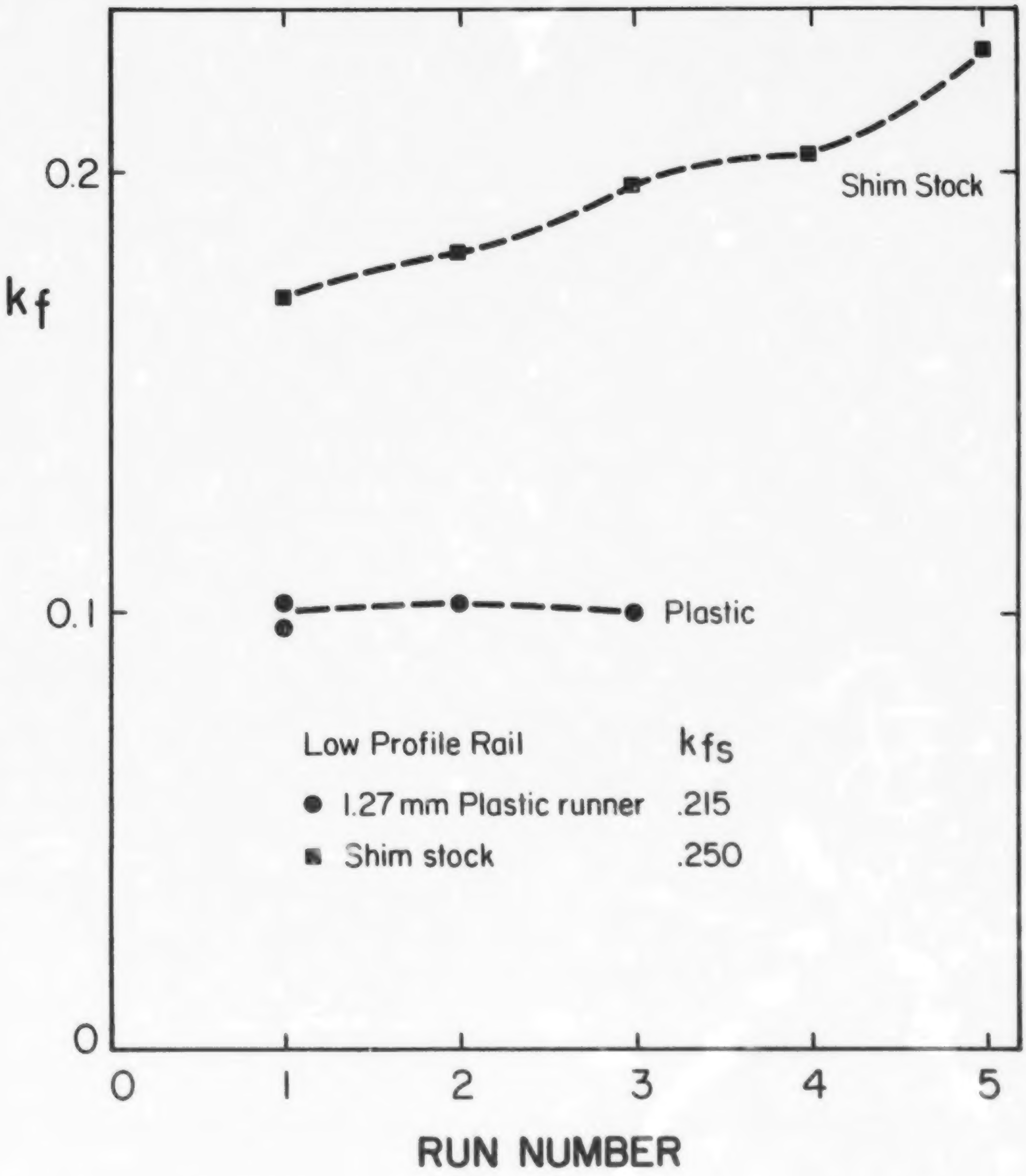

Figure F4 Sliding friction coefficient for steel shim stock compared with that for 1.27mm extruded polyethylene.

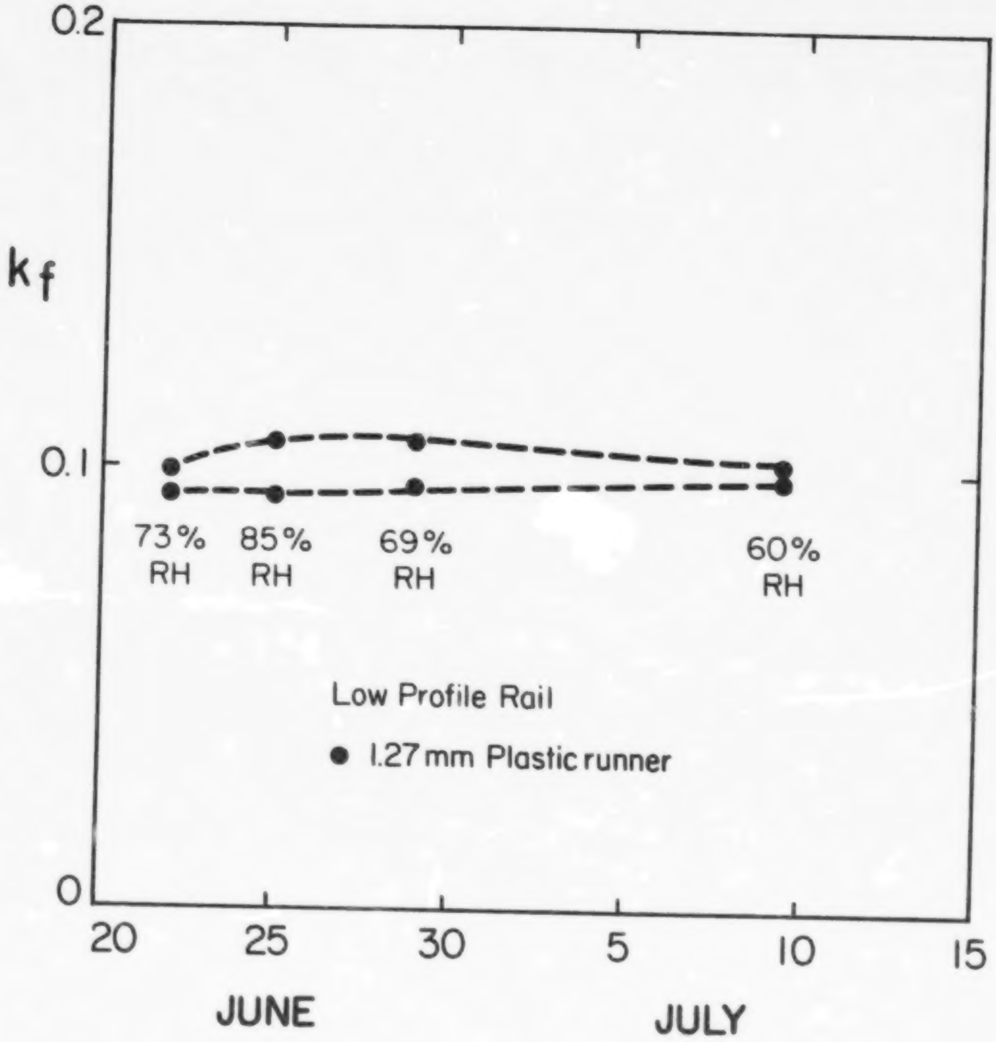

Figure F5 Measurements of sliding friction over an extended period of time.

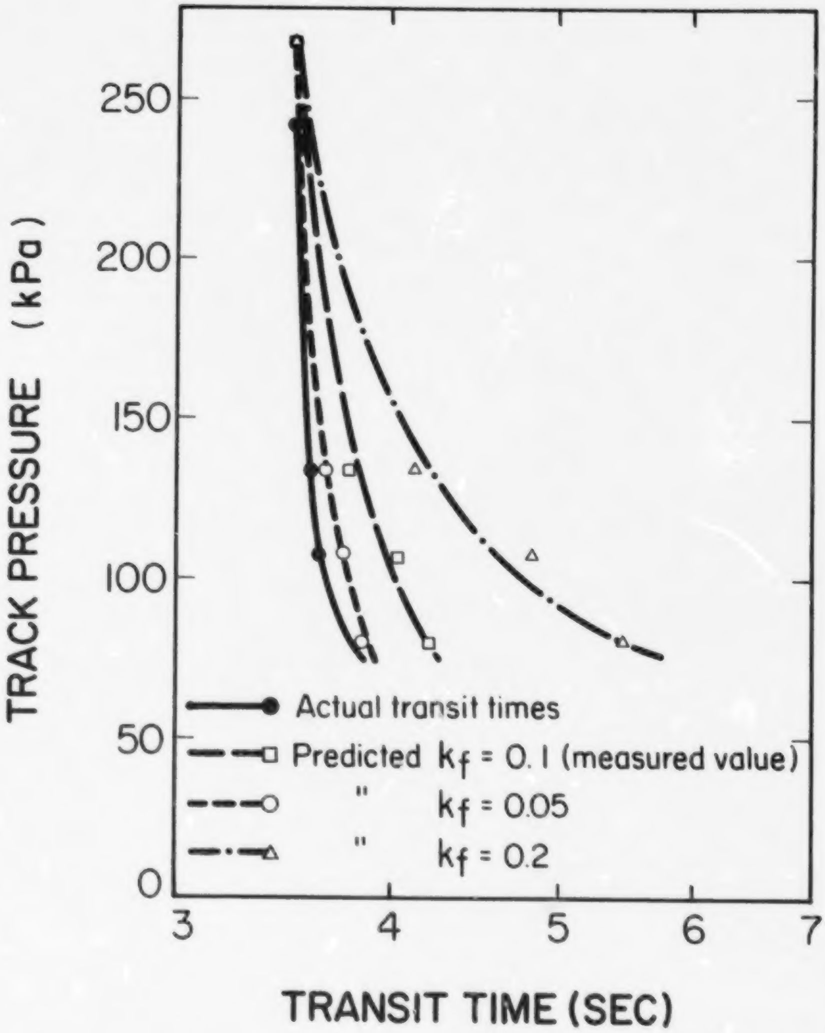

Figure F6 Comparison of measured transit time data with values computed by assuming various values of k_f.

APPENDIX G. PRELIMINARY RESULTS OF A DYNAMIC STABILITY INVESTIGATION (M. J. Hinchey and P. A. Sullivan)

G.1 Introduction

A problem that has been encountered in the development of rigid and compliant air bearings is pneumatic hammer [4]. This is a self-excited oscillation of the load-carrying part of the bearing resulting from a dynamic instability induced by the compressibility of the air in the bearing gap. The compressibility acts like a spring and introduces a phase lag between the bearing pressure force oscillations and any motion. When the pneumatic spring stiffness falls below a certain value, in an oscillation caused by a small disturbance, the net work done by the pressure force is positive and the oscillation grows with time until nonlinearities limit its amplitude. The effective stiffness can be decreased by increasing the size of any volumes in the bearing and by introducing compliant elements, so that both adversely affect dynamic stability. Indeed the increased susceptibility to pneumatic hammer caused by the introduction of compliant elements has been cited as a major impediment to their widespread use [21]. Fortunately, the SailRail design has proved to be remarkably free of this problem. This Appendix describes preliminary results of an analytical investigation intended to determine the factors in the design which give it excellent stability.

G.2 Simplified Model Assumptions

The major assumptions used in the analysis are:

(i) the air escape process in the seal region is isothermal, inertialess and quasisteady so that the analysis in Appendix A can be used;

(ii) the compression-expansion process in the cavity region can be modelled as an isothermal pneumatic capacitance [5,6];

(iii) the air flow through the nozzles is choked in the gasdynamic sense, and modulated only by changes in the local gap;

(iv) the viscoelastic properties of the shoe can be modelled as a spring-dashpot secondary suspension separating the load mass M and the shoe mass m.

Figure G1 depicts the major features of the model.

G.3 Governing Equations

From Appendix A, the mass flux per unit length through the seal region is given by

$$\dot{m}_o = \frac{1}{12\mu RT}\left(p\,\frac{dp}{dy}\,h^3\right) \qquad \text{(G1)}$$

where p(y) is the absolute pressure and h = h(y). The quasisteady assumption implies that this formula can be used at each instant in time. For the present analysis this formula is applied by estimating p and dp/dy at the point y_s of minmum gap h_s. The data in Figure A4 suggests that we

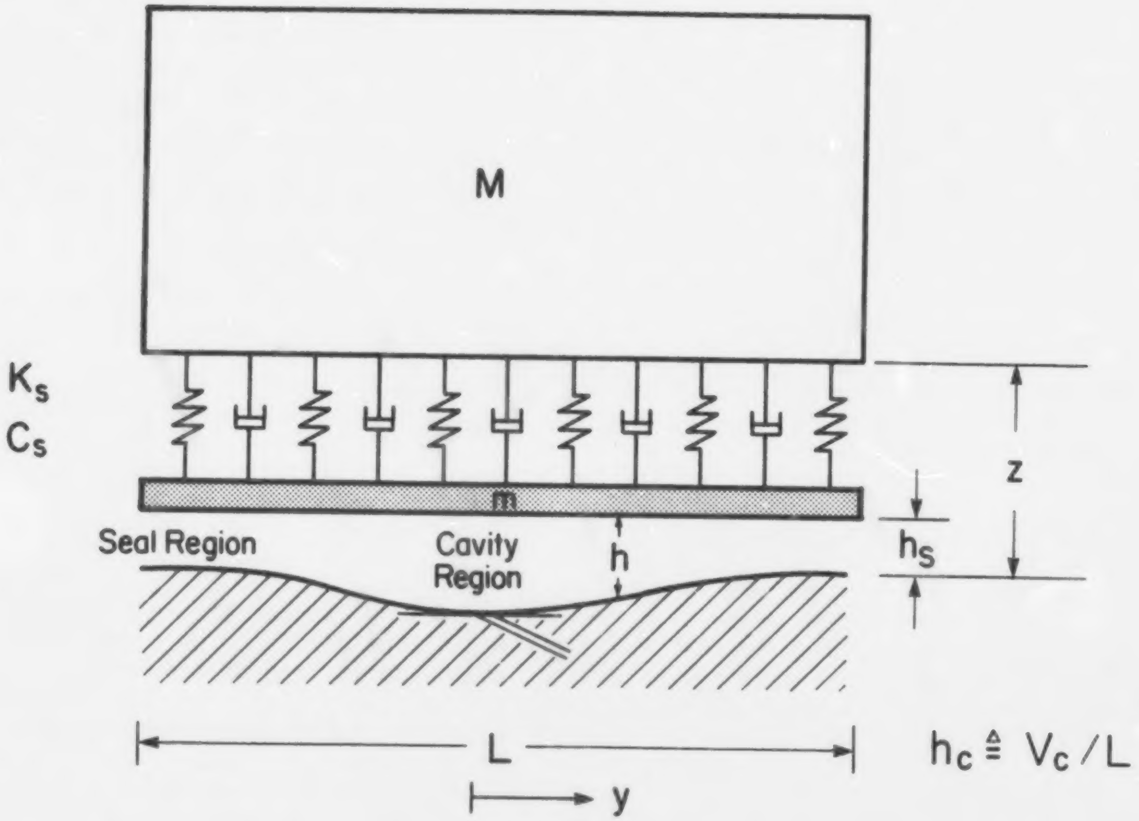
M
K_s
C_s
m
z
h_s
h
Seal Region
Cavity Region
L
$h_c \triangleq V_c / L$
y

Figure G1 Conceptual model used in dynamic stability investigation.

can take

$$p(s) \simeq \frac{1}{2}(p_c + p_a), \qquad \frac{dp}{dy}\bigg|_{y_s} \simeq -(p_c - p_a)/L_s \tag{G2}$$

where p_c is the absolute pressure in the cavity, p_a is atmospheric pressure, and L_s is an equivalent seal width.

Combining equations (G1) and (G2) gives

$$\dot{m} = \frac{1}{12\mu RT}\,\frac{(p_c{}^2 - p_a{}^2)}{2L_s}\,h_s{}^3 \tag{G3}$$

or

$$\dot{m} = K_o(p_c{}^2 - p_a{}^2)h_s{}^3 \tag{G4}$$

where K_o is a constant which can be determined from steady state flow measurements.

The linearized or small disturbance approximation to equation (G4) is obtained by letting $m_o = m_e$, $h_s = h_{se} + \Delta h$, and $p_c = p_{ce} + \Delta p_c$, where the subscript "e" denotes equilibrium values. Equation G4 becomes, on retaining only first order terms

$$\Delta\dot{m}_o = \dot{m}_e[\{2p_{ce}/(p_{ce}^2 - p_a{}^2)\}\Delta p_c + 3h_{se}^{-1}\,\Delta h_s] \tag{G5}$$

where K_o has been eliminated by noting that

$$\dot{m}_e = K_o(p_{ce}^2 - p_a{}^2)h_{se}^3 \tag{G6}$$

In general, for a given shoe and rail geometry at equilibrium, the mass flux into the cavity m_i is a function of track pressure p_t, the cavity height h_c at the nozzles, and the cavity pressure p_c;

$$\dot{m}_i = f(p_t, h_c, p_c) \tag{G7}$$

since the cross-sectional area of the air supply manifold in the rail is very much greater than that of the nozzles, it is reasonable to assume that during an oscillation p_t remains fixed, in which case, with the assumption of quasisteady flow, the linearized approximation to equation G7 would be

$$\Delta\dot{m}_i = \dot{m}_e[K_{ih}\Delta h + K_{ip}\Delta p] \tag{G8}$$

where K_{ih} and K_{ip} are determined from steady flow data. If p_t is high enough to choke the flow through the nozzles, then equation G8 becomes independent of Δp. When the nozzles are not covered by a shoe, the transition from subsonic to supersonic fluid speeds characteristic of choked flow will occur in the nozzle entry region [point (1) of figure B.1], but when they are covered by the shoe, the computed flow fields for the radial nozzles in Appendix B and the experimental data in Appendix 0 suggest that choking might occur just downstream of the nozzle exit. In the former case $\dot{m}_i$ would be independent of h . For now it is assumed that choking occurs in the second location, since the effect of choking in the first can be examined by setting $K_{ih} = 0$. Hence for the present analysis

$$\Delta m_i = j\dot{m}_e K_{ih} \Delta h \qquad \text{(G9)}$$

where j = 1 for choking downstream of the nozzle exit and j = 0 for choking inside the nozzle. If $h_c/d \ll 1$, then, as discussed in Appendix B, $\dot{m}_c \propto h_c$, and

$$\Delta\dot{m}_i = \frac{\dot{m}_e}{h_{ce}} \Delta h, \qquad K_{ih} = \frac{1}{h_{ce}} \qquad \text{(G9a)}$$

The three equations describing the heave dynamics are:

(i) Newton's law for the load mass,
(ii) Newton's law for the shoe mass,
(iii) The mass conservation law for the air in the cavity region.

The first of these equations is

$$M\Delta y + C_s(\Delta\dot{z} - \Delta\dot{h}) + K_s(\Delta z - \Delta h) = 0 \qquad \text{(G10)}$$

where M is the load mass, Δz is the vertical displacement of the load mass from its equilibrium position, Δh is the shoe mass displacement from its equilibrium position, C_s is the viscous damping coefficient for the shoe, K_s is the shoe spring stiffness coefficient, and L is the effective cavity width. Newton's second law for the shoe mass is

$$m\Delta h + C_s(\Delta\dot{h} - \Delta\dot{z}) + K_s(\Delta h - \Delta z) = L\Delta p_c \qquad \text{(G11)}$$

The mass conservation law for the cavity region is simply

$$\frac{d}{dt}(\rho_c V_c) = \Delta\dot{m}_i - \Delta\dot{m}_o \qquad \text{(G12)}$$

where ρ_c is the air density in the cavity. For an isothermal [illegible] process and for small perturbations, equation G12 becomes to first or[illegible]

$$\frac{V_{ce}}{RT_c}\Delta\dot{p}_c + \frac{p_{ce}}{RT_c}\Delta\dot{V}_c = \Delta\dot{m}_i - \Delta\dot{m}_o \qquad \text{(G13)}$$

Now introduce an average cavity height h_c such that $V_c = Lh_c$, then on introducing equations G5 and G9 for $\Delta\dot{m}_i$ and $\Delta\dot{m}_o$ respectively

$$\frac{V_{ce}}{RT_c}\,\Delta\dot{p}_c + \frac{p_{ce}}{RT_c}\,L\Delta\dot{h} = \dot{m}_e\left[\left(jK_{ih} - \frac{3}{h_{se}}\right)\Delta h - K_{op}\Delta p\right] \tag{G14}$$

where

$$K_{op} = \frac{2p_{ce}}{p_{ce}^2 - p_a{}^2} \tag{G15}$$

Upon introducing the isothermal capacitance

$$C_{ci} = \frac{V_{ce}}{p_{ce}RT_{ce}} \tag{G16}$$

and the volume flow at p_{ce}, $Q_e = \dot{m}_e/p_{ce}$ equation G14 becomes

$$C_{ci}\Delta\dot{p}_c + L\Delta\dot{h} = Q_e\left[\left(jK_{ih} - \frac{3}{h_{se}}\right)\Delta h - K_{op}\Delta p\right] \tag{G17}$$

Equations G10, G11 and G17 describe the dynamics of the system, and the conditions for dynamic stability can be ascertained by standard techniques. Some preliminary results for a simplified case is described below.

G.4 Stability for the Rigid Shoe Approximation

If the shoe is assumed to be attached rigidly to the load a particularly simple stability criterion can be derived. In this case $\Delta z = \Delta h$ and equations G10 and G11 are replaced by

$$(M + m)\Delta h = L\Delta p_c \tag{G18}$$

On combining equations G17 and G18 one obtains

$$\frac{(M + m)C_{ci}}{L}\,\dddot{\Delta h} + Q_eK_{op}\frac{(M + m)}{L}\,\ddot{\Delta h} + L\Delta\dot{h} + Q_e\left[\frac{3}{h_{se}} - jK_{ih}\right]\Delta h = 0 \tag{G19}$$

Following the usual Laplace technique, seek solutions of the form

$$\Delta h = \Delta He^{st} \tag{G20}$$

with the Laplace variable $s = \sigma + i\omega$, $i = \sqrt{-1}$. Hence equation G19 becomes

$$As^3 + Bs^2 + Cs + D = 0 \tag{G21}$$

where

$$A = \frac{(M + m)V_{ce}}{p_{ce}RT_cL}; \qquad B = \frac{2Q_e p_{ce}(M + m)}{L(p_{ce}^2 - p_a{}^2)}$$

$$C = L; \qquad D = Q_e[3/h_{se} - jK_{ih}] \qquad \text{(G22)}$$

The onset of dynamic stability corresponds to σ becoming positive, so that the stability criterion is found by setting $\sigma = 0$ in G21 to obtain

$$-Ai\omega^3 - B\omega^2 + Ci\omega + D = 0 \qquad \text{(G23)}$$

Since A, B, C and D are real we must have, on equating real and imaginary parts of G23,

$$\omega^2 = \frac{D}{B}, \qquad A\omega^2 = C \qquad \text{(G24)}$$

This result is interpreted as follows. When the flow is incompressible, $C_{ci} = 0$ and the equation reduces to that for a second order system with positive damping, so that it is always stable. When $C_c \neq 0$ the first term in equation G21 acts like a negative damping so that when $A\omega^2 > C$ oscillations grow in amplitude. Hence the stability criterion reduces to

$$\frac{AD}{BC} > 1 \qquad \text{(G25)}$$

or

$$C_{ci}[3/h_{se} - jK_{ih}](p_{ce}^2 - p_a{}^2)/(2p_{ce}L) > 1 \qquad \text{(G26)}$$

To obtain a simple interpretation of this result, proceed as follows. Assume that, as suggested by the data in Figure 0.3, $\dot{m}_i \propto h_c$ so that $K_{ih} = 1/h_{ce}$; then define an average h_{ce} such that $V_{ce} = Lh_{ce}$. The inequality G26 then becomes

$$\frac{[3h_{ce}/h_{se} - j](p_{ce}^2 - p_a{}^2)}{2p_{ce}^2} > 1 \qquad \text{(G27)}$$

Put $p_{ce} = (1 + \xi)p_a$, so that ξ is the ratio of the cavity gauge pressure p_{cg} to atmospheric pressure, and the inequality becomes

$$(1 + \xi)^2 - 1 > 2(1 + \xi^2)\Gamma_h \qquad \text{(G28)}$$

where

$$\Gamma_h \triangleq [3h_{ce}/h_{se} - j]^{-1} \qquad \text{(G29)}$$

Solving G28 for ξ one obtains finally

$$\xi = \frac{p_{cg}}{p_a} > (1 - 2\Gamma_h)^{-1/2} - 1 \qquad \text{(G30)}$$

Now usually $\Gamma_h \ll 1$; a representative value of h_{ce} is 0.2 mm and h_{se} = 0.017 mm so that Γ_h = 0.02916 if choking occurs at the nozzle exit. Hence with little loss in accuracy the stability criterion reduces to

$$\frac{p_{cg}}{p_a} > \Gamma_h = \left(\frac{3h_{ce}}{h_{se}} - j\right)^{-1} \qquad (G31)$$

Also note that if choking occurs in the nozzle entry region, j = 0, and Γ_h = 0.02833 for the above example, so that this has little effect on stability and, to acceptable accuracy, the condition for the onset of instability becomes simply

$$\frac{p_{cg}}{p_a} > \frac{h_{se}}{3h_{ce}} \qquad (G32)$$

G.5 Discussion and Conclusions

Equation G32 implies that for h_{ce} = 0.2 mm and h_{se} = 0.017 mm, the system becomes dynamically unstable when p_c is larger than 2.8% of atmospheric pressure, or about 2.8 kPa. This contrasts with the typical cavity pressures up to 50 kPa, and implies that factors such as the damping properties of the tissue play a crucial role in preventing dynamic instability and the associated pneumatic hammer. The next stage of the analysis is to examine the effects of the stiffness and damping properties of the tissue described in Appendix H. A complication is that, owing to the hysteretic nature of the damping, the problem is inherently nonlinear. However, as a first step, if the oscillation frequencies are known, one can proceed using the linear analysis formulated here by choosing an appropriate value of C_s. This should at least establish the basic effect of damping. Experimental verification of the analysis by using suitably simplified configurations is also needed. In view of the very large difference between the rigid shoe prediction and the observed behaviour, a model of the rigid shoe should also be tested.

APPENDIX H. STRUCTURAL PROPERTIES OF THE SHOE TISSUE (T. A. Graham)

H.1 Introduction

The SailRail shoe consists of three components, a cardboard tube core of about 42 mm diameter and 0.75 mm thickness which is enclosed by a 39 mm thick body of wound creped cellulose fibre tissue providing the bulk of the structure, and an outer plastic cover which is usually about 1 mm thick. Its structure becomes oval when flattened under load. Although the test data given in Appendices C and D show that the bending stiffness of the cover affects system performance, and although it has been speculated that the core plays a structural role [1], it seems that the overall structural properties of the shoe should be determined largely by those of the tissue. Paper, and in particular the cellulose tissue used in the SailRail shoe, is known to have complicated properties. It exhibits damping when subjected to vibration [7,8,9]. In compression, its stiffness is highly nonlinear and hysteretic, often with a rate dependent loading curve but a rate independent unloading curve [8]. Vibration tests on SailRail shoes performed by the Department of National Defence showed strong absorption at vibration frequencies in the range 15 Hz to 55 Hz and a weak resonance between the 8 and 12 Hz [9]. If the damping is assumed to be of the linear dashpot type these results correspond to a second order system with damping about 25% of critical.

These nonlinear and viscoelastic properties suggest that simple static tests are inadequate for characterizing shoe structure. This appendix describes a series of tests undertaken to assess the nonlinear and rate dependent aspects of the shoe structure when subjected to compression. Samples of tissue of various composition used by the developer were tested in an attempt to relate structural properties to reported performance differences.

H.2 Test Programme and Results

The first tests were compressive loading and unloading of layers of one sample of tissue laid flat to about 10 mm thick and placed between two circular metal disks of 381 mm diameter. The plates and tissue were compressed in a Tinius Olsen stress test machine to which a linear variable displacement transducer (LVDT) had been attached for deflection measurement. The tissue was loaded and unloaded a total of 5 times, at rates of 1.27, 0.64 and 2.54 mm/min, corresponding to strain rates based on initial thickness of 0.2, 0.1 and 0.4%/sec respectively. For each loading cycle the outputs of the force and displacement transducers were recorded by an X-Y plotter, and discrete readings were also taken at regular intervals for subsequent analysis. The output curves presented in Figure H1 have several important features; first, the initial compression shows much larger hysteresis than any of the subsequent ones, and a significant amount of permanent deformation takes place; second, subsequent compression tests, repeated up to 5 times at the same strain rate in some cases, fall on the same curve; and third, compression at double and half the initial rates of strain of 0.2%/sec are nearly identical to the original rates. The vibration tests on SailRail shoes described in Ref. 9 indicated significant damping for frequencies in the range 5 Hz to 55 Hz. The smallest strain rate

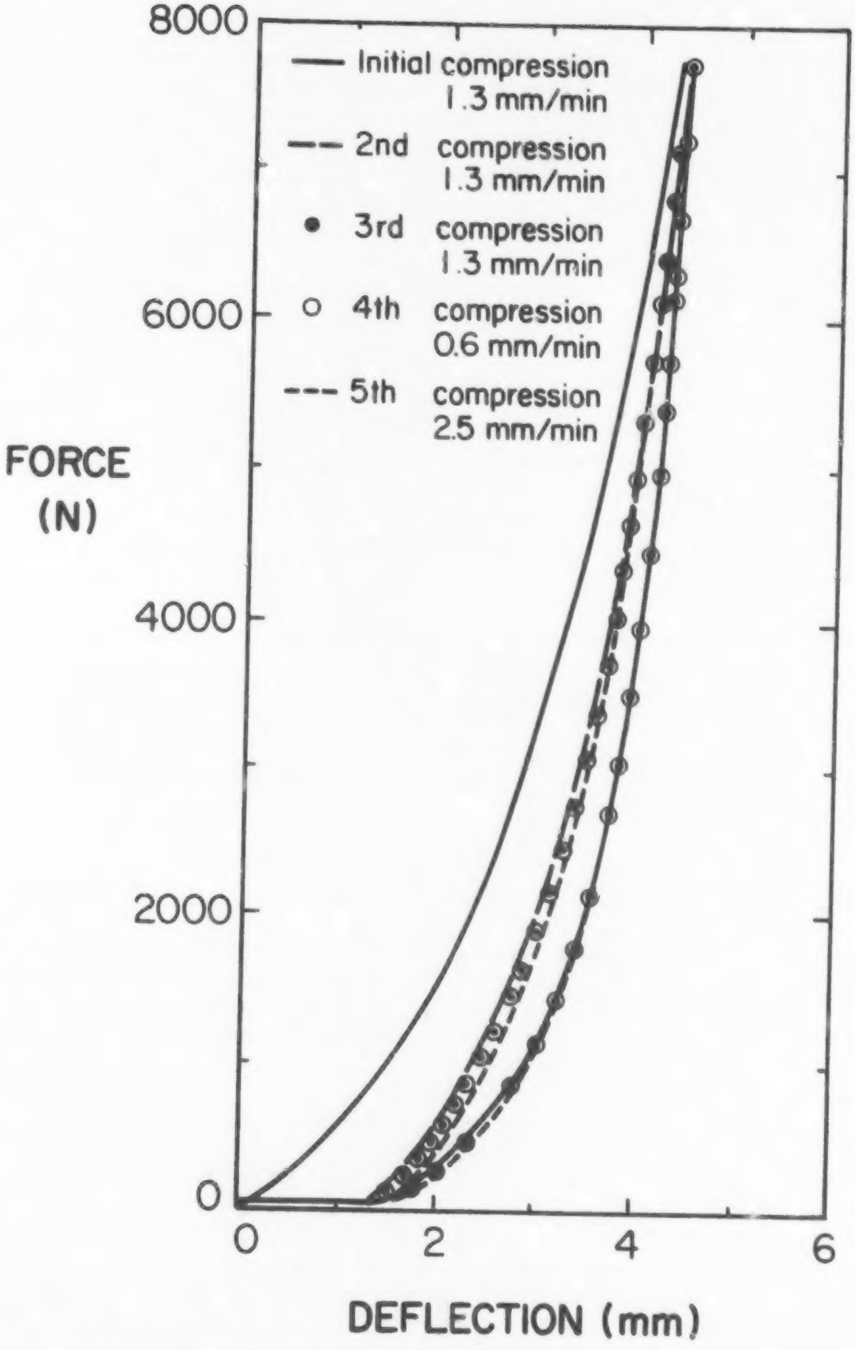

Figure H1 Load-deflection characteristics of a sample of tissue 100mm thick and having a cross-sectional area of 0.114m^2.

used here corresponds to a frequency of about 0.01 Hz, thus indicating that the damping capability is still present even at such a low frequency. It implies that the damping cannot be modelled by a simple linear dashpot type. The manually recorded readings were fitted with a third order least squares regression polynomial to produce a mean value curve for use in deflection prediction. The resulting polynomials are

$$\varepsilon = 0.02313 + 0.01320\sigma - 0.0002510\sigma^2 + 0.0000017\sigma^3 \qquad \text{(H1)}$$

and

$$\sigma = -1.393 + 171.5\varepsilon - 1287\varepsilon^2 + 4820\varepsilon^3 \qquad \text{(H2)}$$

where σ is the stress in kPa and ε is the strain, which here is positive for compression.

The sample was then subjected to stress relaxation tests using the same apparatus. The resulting curves, shown in Figure H2, indicate significant stress relaxation in the first five minutes following load.

A similar set of tests was then performed on a 580 mm long section of SailRail log.[1] The log used was selected from among ones which were known to give good performance in the pallet-moving application. Figures H3, H4 and H5 show the results of repeated loading, partial loading and stress relaxation tests, respectively. As with the flat tissue tests, there was some permanent deformation following the initial compression, the load-deflection curve is nonlinear, and subsequent tests at different strain rates fall on essentially the same curve for strain rates up to about 0.6%/sec. This strain rate would be the maximum achieved under a sinusoidal test of the same amplitude at about 0.01 Hz. The stress-relaxation tests again show significant stress decay in the first five minutes. The general character of the tissue under compression thus remains the same whether it is laid flat or wound upon the core prior to testing.

The developer supplied logs having a range of tissue composition, and provided qualitative opinions about their field performance and structure. The samples are described in Table H1, which lists composition as determined by E. B. Eddy Forest Products. 120 mm long samples of several of these materials were subjected to compression tests, and the results are given in Figures H6-H8, with the results for sample 6 used as a reference. As noted in Table H1, samples 4, 6 and 11 were identified as having "acceptable" performance, while that of sample 5 was deemed "poor". Of the samples described as having adequate performance, that of sample 11 was described as "best". Figure H6 compares the stiffness characteristics for these four samples. This data suggests that there is no simple correlation between system performance and shoe stiffness. Figure H7 compares the stiffness characteristics of logs used early in the system development period with that of the reference sample 6. Figure H8 gives stiffness data for the so-called "Clark log"; this had been subjected to a load of about twice the design value for an extended period and was, as a result, highly flattened and presumably very "hard". When tested in the prototype test bed at a driving weight of 1.1% of pallet weight this shoe would not move. The data for sample 8, which was designated as "hard" by the manufacturer is also included in Figure 8 to illustrate the subjective nature of opinions expressed about the structural characteristics of logs.

---

[1] "Log" is a term used for the shoe without the plastic cover.

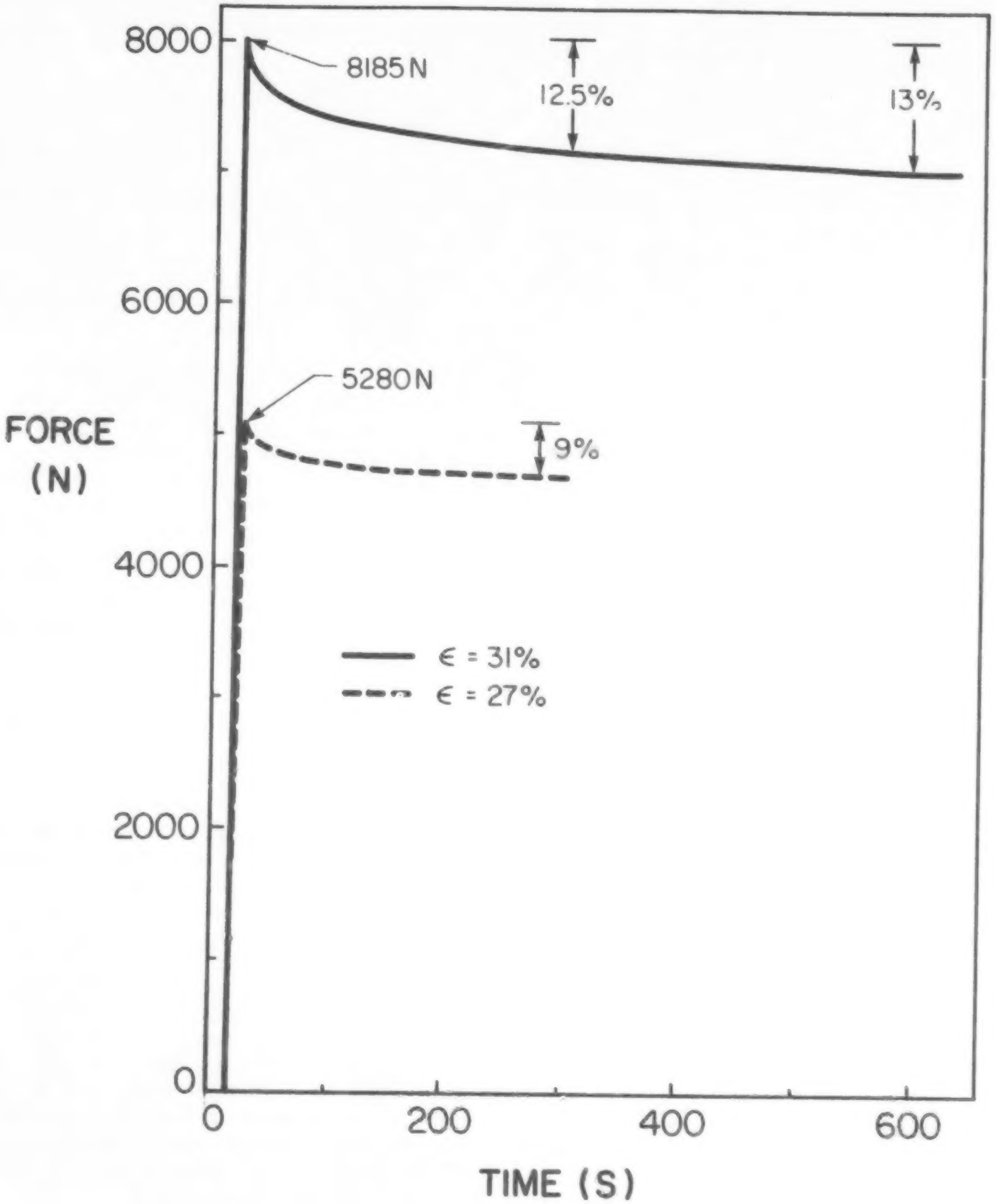

Figure H2 Stress relaxation results for tissue sample of Figure H1.

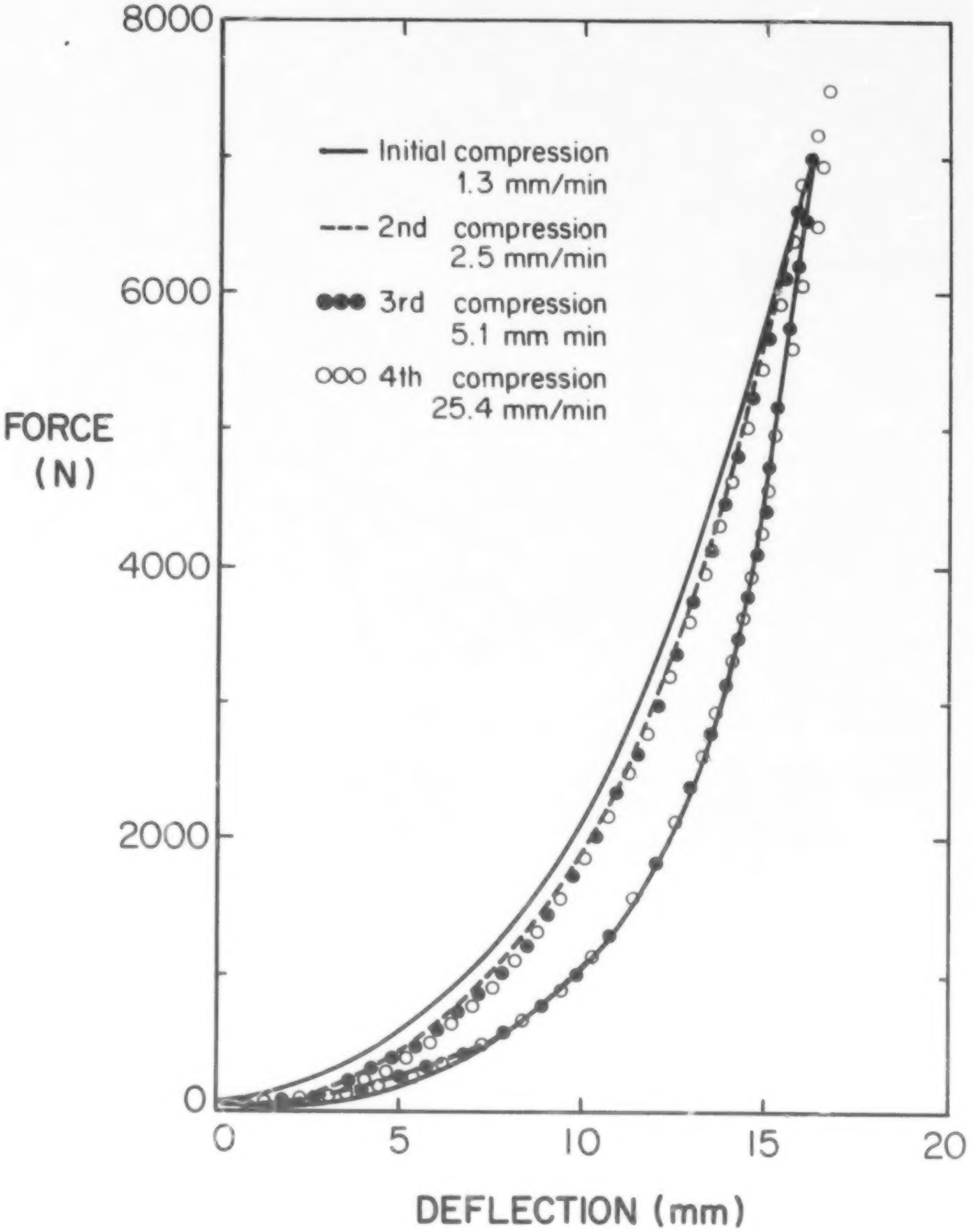

Figure H3 Load-deflection characteristics of a 580mm long sample of SailRail log (shoe without cover).

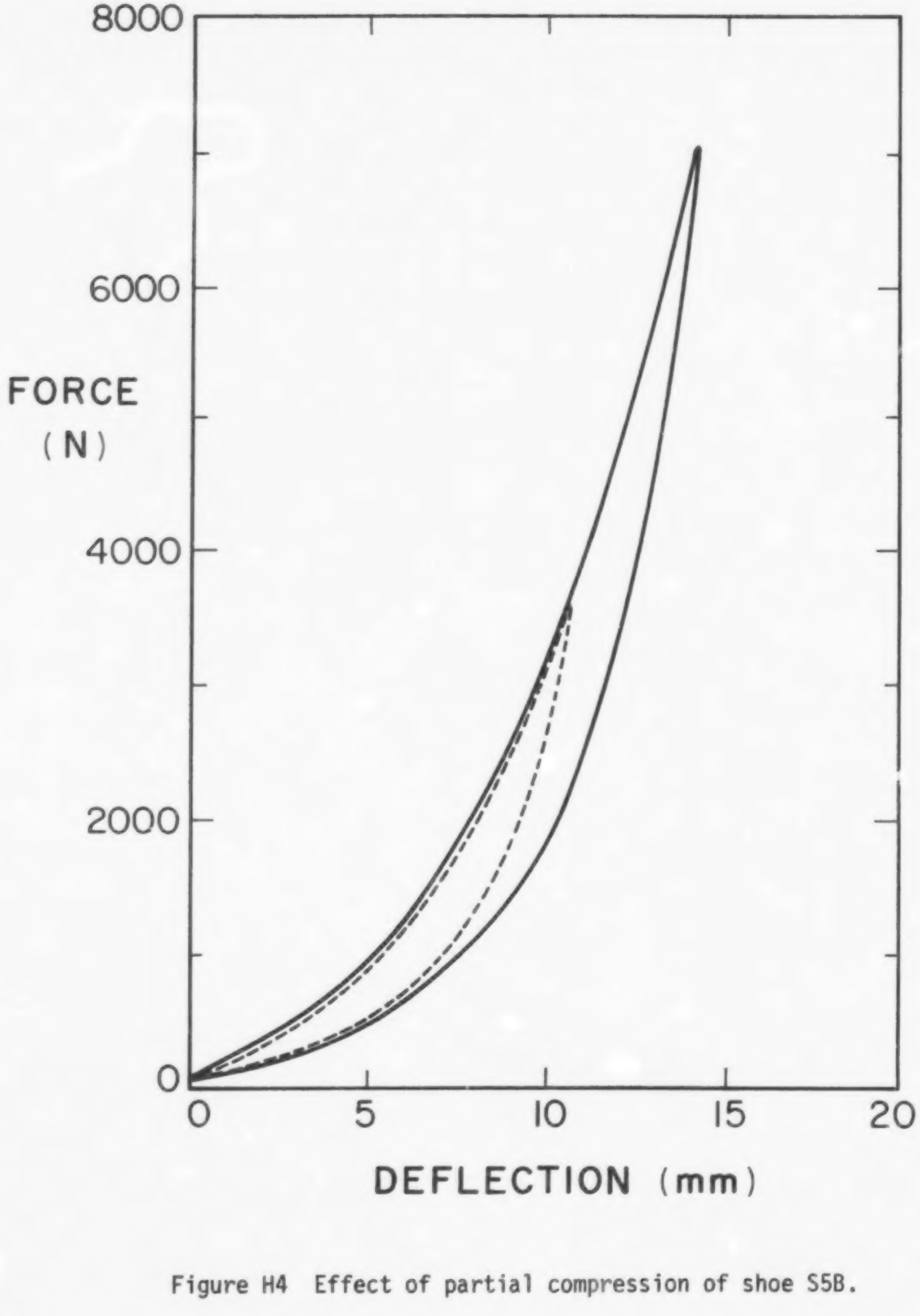

Figure H4 Effect of partial compression of shoe S5B.

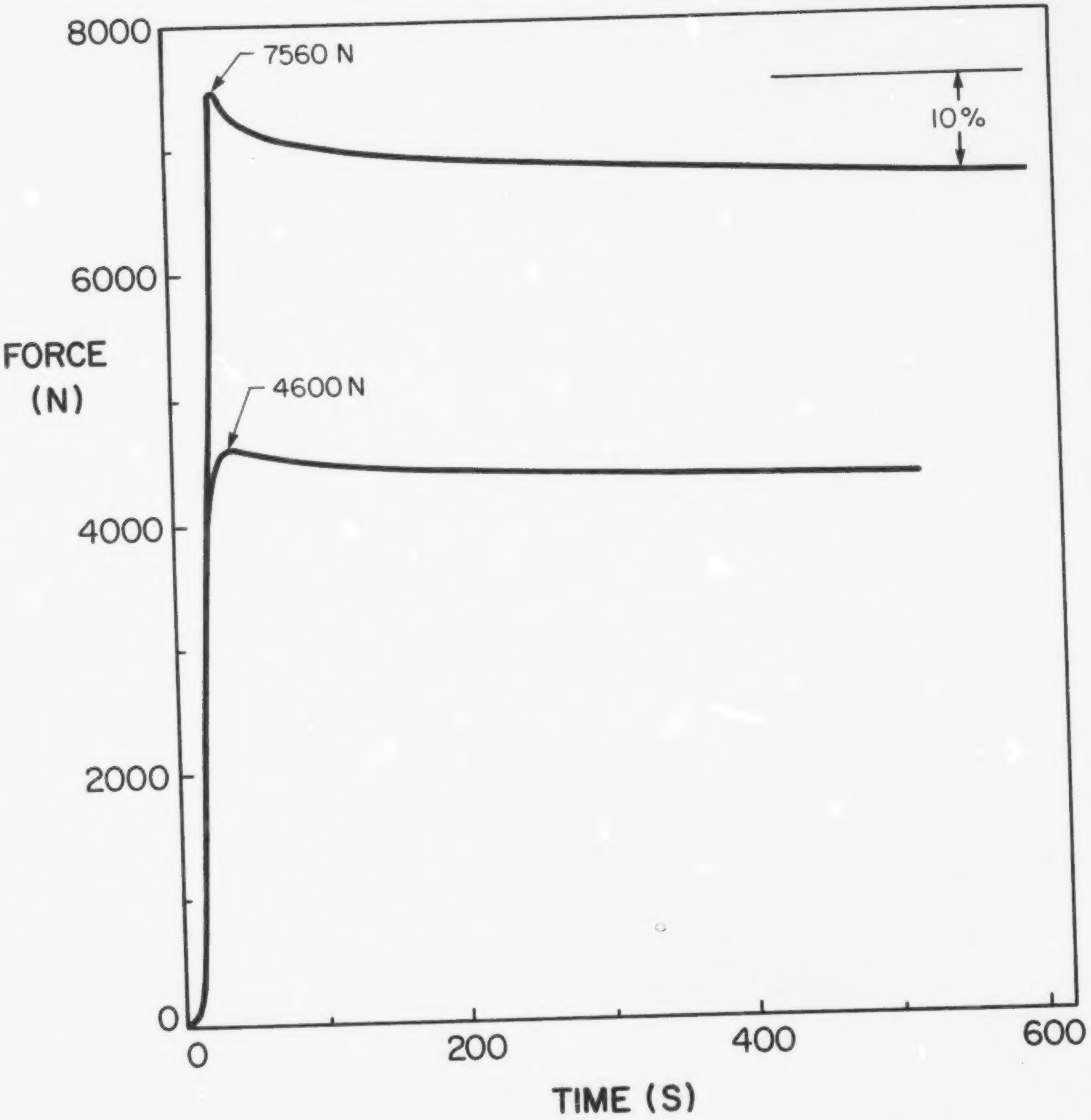

Figure H5 Stress relaxation results for log sample of Figure H3.

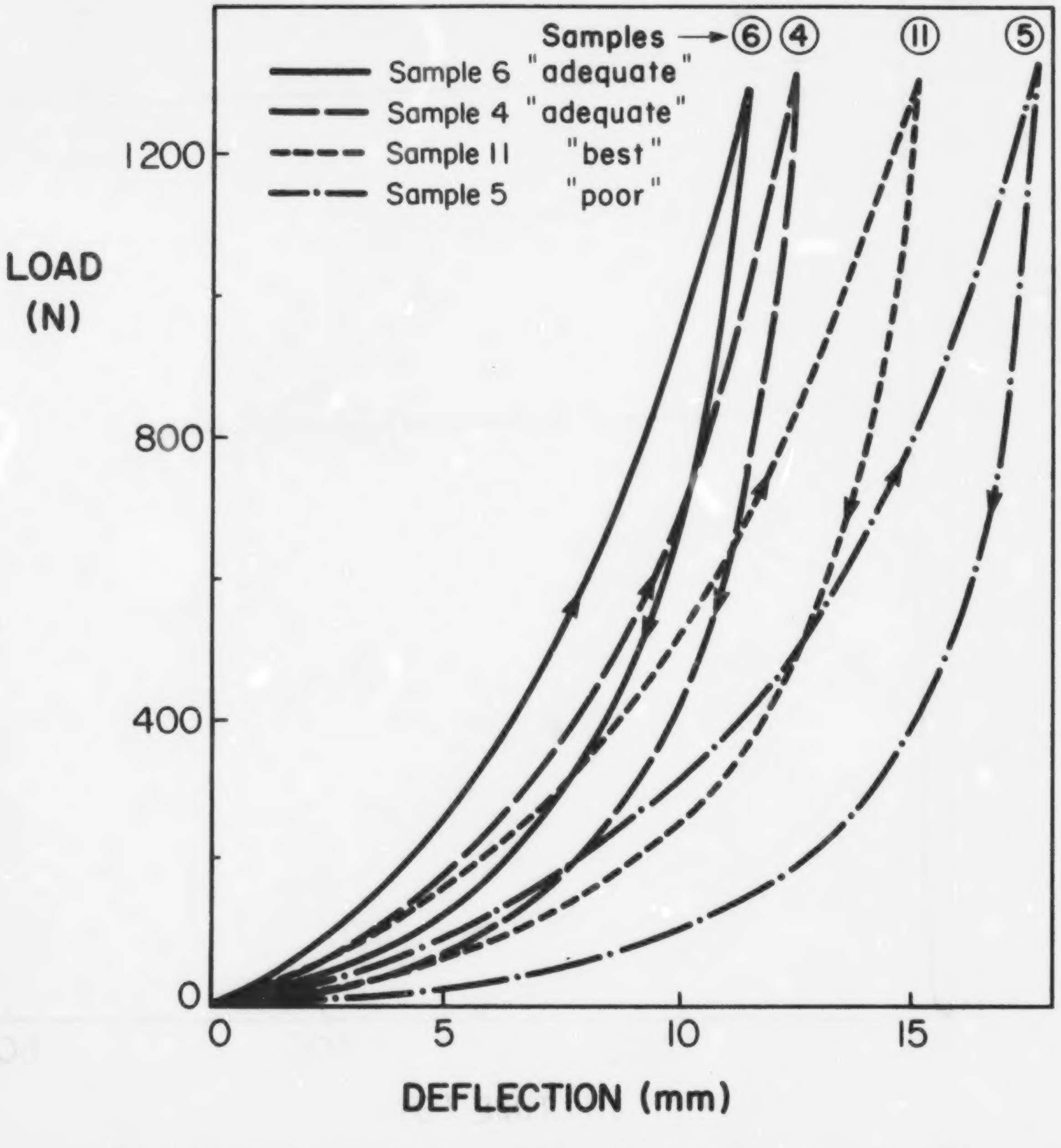

Figure H6 Load-deflection characteristics of various logs supplied by the manufacturer, along with qualitative descriptions of performance. Note that the sample described as having the "best" performance has a stiffness intermediate between that of samples described as "poor" and "adequate".

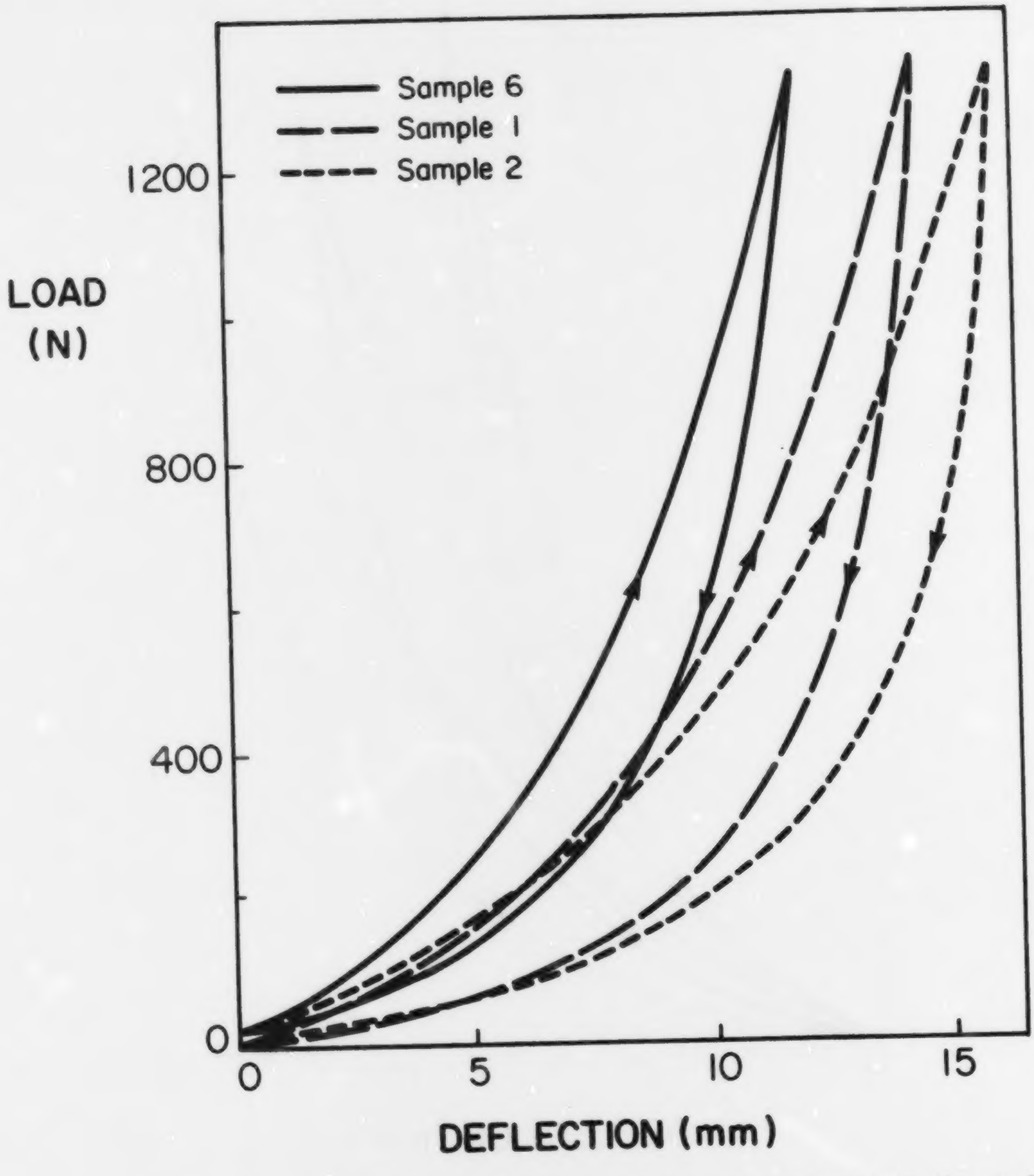

Figure H7 Load-deflection characteristics of logs used in the early stages of development compared with that of sample 6.

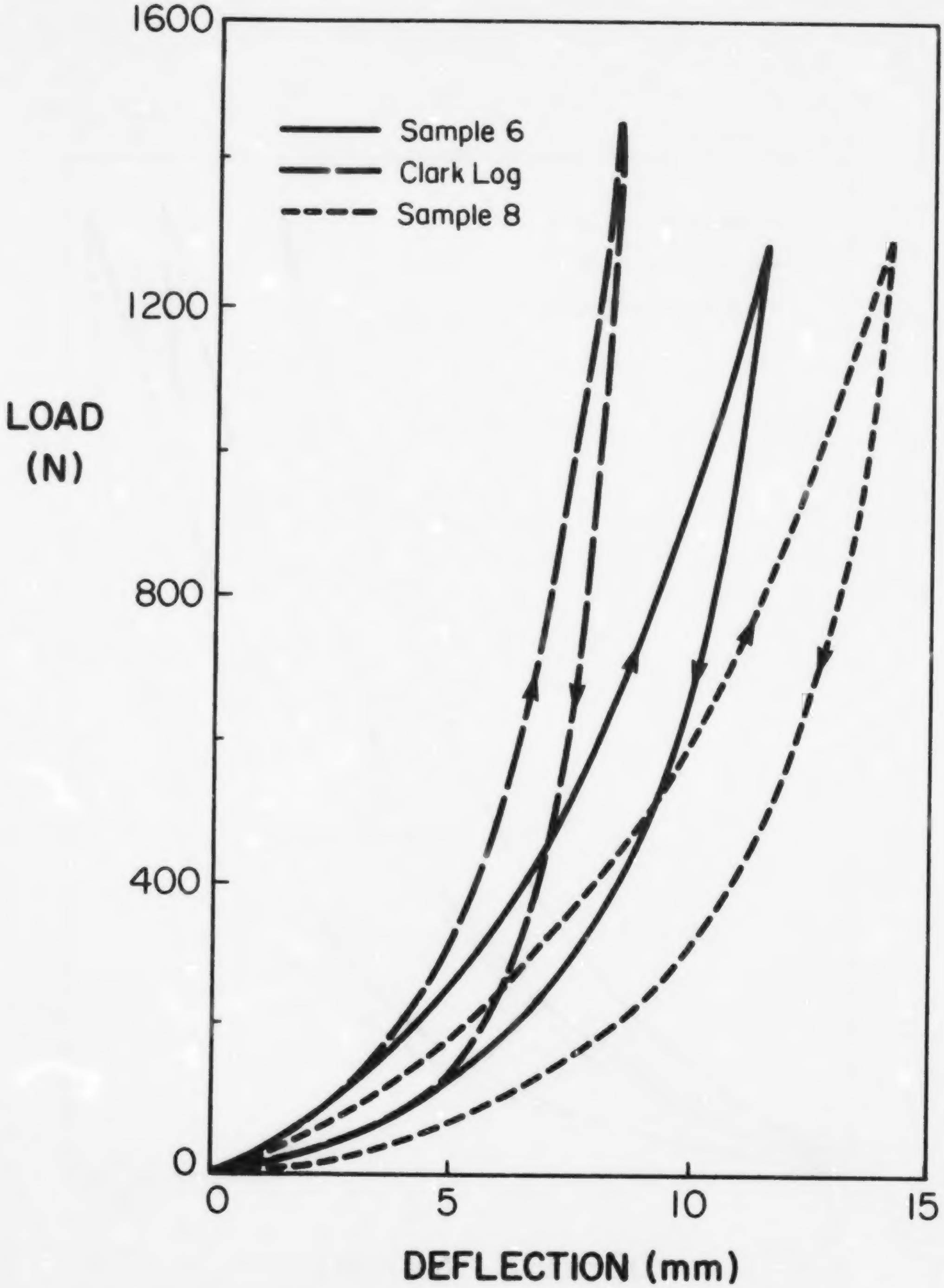

Figure H8 Comparison of load-deflection characteristics of a highly flattened log, the "Clark shoe", with that of a sample designated as "hard" by the manufacturer.

SAMPLE		Composition Analysis						
		Bleached Kraft		Bleached Sulphite		Unbleached Sulphite Softwood	Groundwood	Rag
#	Description	Softwood	Hardwood	Softwood	Hardwood			
		%	%	%	%	%	%	%
1	Perkins	45	55	-	-	trace	trace	-
2	Perkins Elegant	40	60	-	-	trace	trace	-
3	Charmin	25	30	-	45	-	-	-
4	Old Thick Core White Swan Material - the Original Log Material	15	35	-	-	-	50	-
5	Swan's Down	35	65	-	-	-	-	-
6	UTIAS Test Shoe S5B - from same Eddy production run as standard test shoe	35	25	10	-	trace	30	-
7	White Swan-marked as Original best with thin core	35	35	-	-	trace	30	-
8	Industrial 1000 - indicated as being"hard"	40	30	-	-	-	30	-
9	Old shoe material received marked only " ? ? "	25	30	-	-	-	trace	-
10	Swan's Down Delux	40	60	-	-	-	trace	-
11	Old White Swan "best"	30	30	-	-	trace	40	trace
12	UTIAS Test Shoe 60B	50	30	-	-	-	20	-
13	5PB	60	20	-	-	-	20	-
14	59B	55	45	-	-	-	trace	-
15	"Nov 4/81" run	65	35	-	-	-	trace	-
16	62B	70	30	-	-	-	trace	-
17	63A	50	30	-	-	trace	20	-
18	62A	60	40	-	-	-	trace	-
19	"Nov 4/81" special dry shoe	65	35	-	-	trace	trace	-
20	S5A	40	25	10	-	-	25	-
21	63B	50	30	-	-	trace	20	-

Notes 1) Samples #6 and #20 are from the same cellulose production run.

2) Samples #12, 13, 14, 16 and 18, are from the same production run. All shoes from this run gave non repeatable performance when tested in the prototype test bed and by the developer in the field.

3) Samples #17 and #21 are from the same production run.

TABLE H1 COMPOSITION ANALYSIS OF VARIOUS TISSUES USED IN PROTOTYPE TEST BED. ANALYSIS PERFORMED AND SUPPLIED BY E. B. EDDY FOREST PRODUCTS.

H.3 Discussion

The hysteretic and creep properties of the tissue observed in the present test results provide the most likely explanation of the conditioning effect encountered in the prototype testing described in Appendix C. Tests by E. B. Eddy have shown that significant creep can continue for periods as long as several weeks [10]. But apart from this, no significant correlation between log composition and overall shoe stiffness has been observed. In fact the data suggests that factors not controlled in the present tests might be more important. The literature on the structural properties of wound paper rolls indicates that winding tension may be the most important of these factors [8,11,12]. It is known that this tension plays an important part in determining overall structural properties of a roll; for example, it provides compressive radial stresses which, owing to the highly nonlinear material, can cause large changes in effective radial stiffness. The behaviour is expected to be complicated by the flattening of the originally circular core in the manufacture of the shoe, since this should cause a redistribution of internal stresses.

An indication of the importance of the uncontrolled effects may be obtained by estimating the cavity height from the shoe stiffness data. In Appendix D the concept of ideal bearing cavity pressure is introduced; it is based on the load, and on a reference area determined by the track width and shoe length. This pressure is the average compressive stress that occurs when the shoe rests loaded on the track with no air supplied. For the load used in the pressure test rig this average stress is σ_{av} of about 41.3 kPa, whereas the corresponding measured cavity pressure gives σ_c of about 53 kPa. The loads resulting from these stresses acting over the reference area for the 120 mm samples were calculated as 575N and 740N respectively, which gives an incremental deflection of about 0.7 mm if the data for sample 6 is used. Similarly the incremental deflection may be calculated from equation H1 by inserting the two values of stress, σ_{ave} and σ_c, and using a typical undeformed log thickness of 75 mm to get a value of about 0.8 mm for the deflection. These predicted deflections are approximately 2.4 to 4. times the 0.2 mm to 0.3 mm maximum gaps measured previously [1], and they illustrate the inadequacy of using this compression data without a knowledge of the winding tension and the effects of flattening the shoe.

APPENDIX I. ANALYSIS OF SHOE COVER FLUTTER (M. J. Hinchey)

I.1 Introduction

It has been observed by the developer that on occasion the shoes could emit discrete acoustical tones having a fundamental frequency of about 1 kHz. He also suggested that, when such sounds could be heard, system performance was improved. One possible way in which such an effect could occur is the presence of aeroelastic flutter of the shoe cover, which causes vibrations of those parts of the shoe in contact with the rail and an associated reduction of sliding friction forces. A well-known phenomenon of this type is the oscillation of the panels in the skin of an aircraft induced by an interaction of the elastic and inertial properties of the plate with an adjacent fluid flow [14]. Also the injection of high frequency oscillations into mechanisms is a standard technique for the elimination of sliding friction forces [15].

Because the gauge pressures associated with hydrostatic lubrication never go negative, one would not expect any static instability problem such as cover suck-down in regions where lubrication theory holds. However, as discussed in Appendix B, close to a nozzle inertia forces dominate and suck-down is a possibility. If longitudinal bending and tension forces in the shoe cover are ignored, then suck-down would occur when the magnitude of the negative stiffness associated with the high speed air flow became greater than the positive stiffness of the shoe. This argument gives, for a specific shoe stiffness, the critical flow speed for onset of instability [16]

$$U_s = \sqrt{\frac{h}{\rho}\frac{dp}{dh}} \quad \text{(one dimensional air flow)} \tag{I1}$$

where h is the gap, ρ is the air density and dp/dh is the shoe stiffness. This critical speed is identical to the speed at which long waves would travel in the shoe cover.

Using the stiffness data presented in Appendix H, U_s was estimated for one of the logs tested (S5B). A typical load on a 122 cm shoe is 454 Kg. This means that for the 10.2 cm long test section used in Appendix H, a scaled load would be about 38.6 Kg. The slope of the return stiffness curve at this load is approximately 12365 Kg/m (Figure I.1). Assuming a shoe footprint width of 7.62 cm, the total area over which this force acts is about 77.4 cm^2. This gives

$$\frac{dp}{dh} = 15250 \text{ kPa/m} \tag{I2}$$

Assuming a gap of 0.127 mm and an air density corresponding to the average of ρ_{ce} and ρ_a, that is, $\rho \cong 1.2\ \rho_a$, one finally obtains

$$U_s = 38.7 \text{ m/sec} \tag{I3}$$

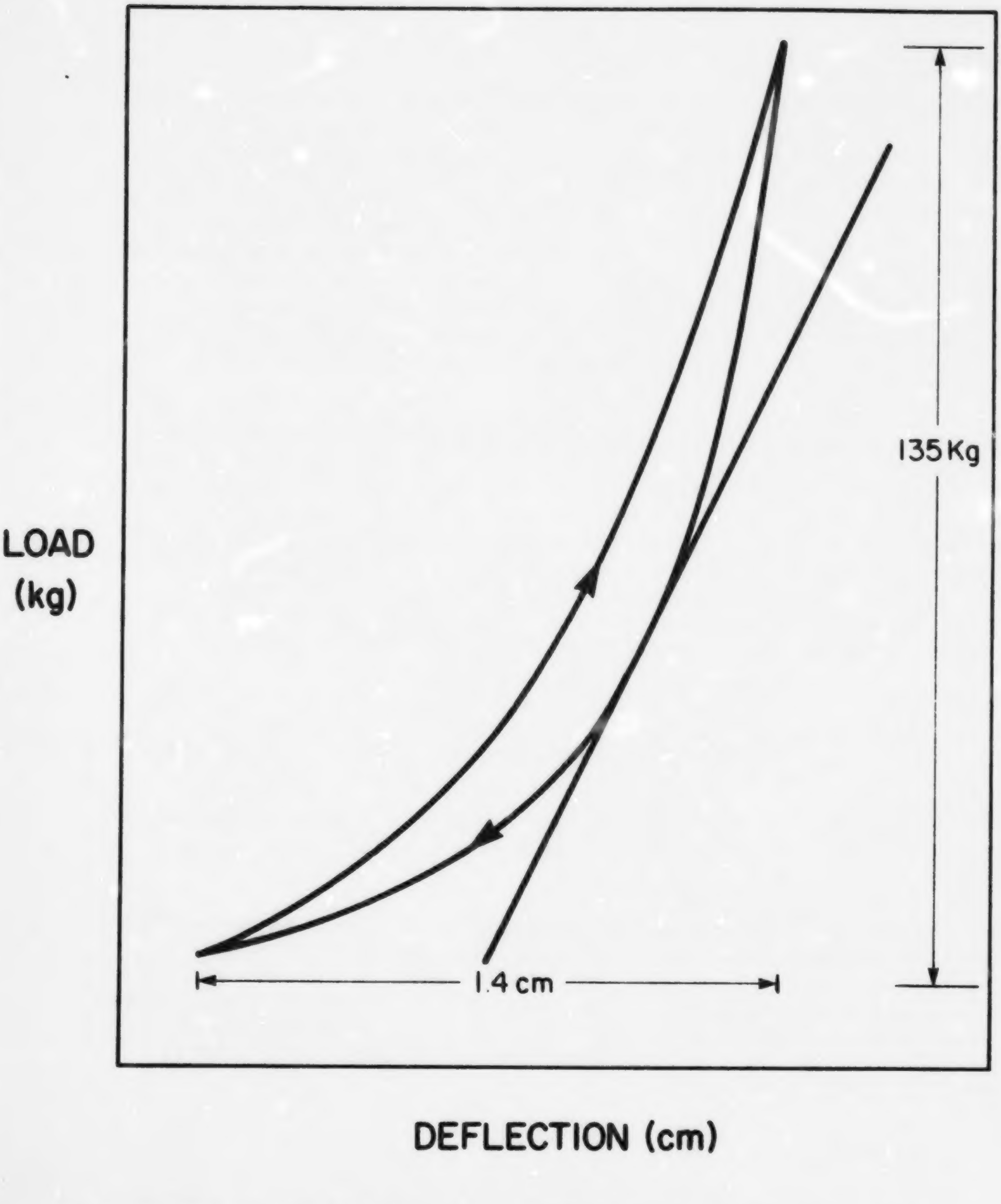

Figure I.1 Load-deflection characteristics of shoe used to obtain data for flutter analysis.

which is about an order of magnitude lower than the acoustic wave speed. Gap and pressure measurements made during the previous contract period [1] indicate that the Appendix H estimate of dp/dh might be an order of magnitude too small. In fact, the previous measurements indicate that U_s may be as high as 200 m/sec.

I.2 Cover Flutter Analysis

If the wavelength of the actual instability is short, then the above argument would not be valid. For short wavelengths, one finds that tension forces in the cover, and bending forces if the cover is thick enough, cannot be ignored. Also, the flow cannot be assumed one dimensional. A linear stability analysis for the variable wavelength situation has been developed for flow-structure interaction problems such as aircraft panel flutter [14], flutter of flexible tubes carrying fluid [17, 18] and flutter in air cushion landing gear [19]. Because of the insights this analysis yields, it is outlined below for the simplified geometry shown in Figure I.2.

The airflow between the cover and the rail is assumed to be two-dimensional, incompressible, unsteady and irrotational. This implies that it is governed by Laplace's equation,

$$\nabla^2 \phi = \frac{\partial^2 \phi}{\partial x^2} + \frac{\partial^2 \phi}{\partial y^2} = 0 \qquad \text{(I4)}$$

where ϕ = velocity potential. The boundary conditions imposed on this flow by the cover motion are:

(1) Unsteady Bernoulli Condition:

$$\frac{\partial \phi}{\partial t} + U \frac{\partial \phi}{\partial x} + \frac{p}{\rho_a} = 0; \qquad y = 0 \qquad \text{(I5)}$$

(2) Kinematic Condition:

$$\frac{\partial \eta}{\partial t} + U \frac{\partial \eta}{\partial x} = \frac{\partial \phi}{\partial y}, \qquad y = 0 \qquad \text{(I6)}$$

where η is the heave displacement of the cover from its reference position ($y = 0$), U is the mean or steady state air flow speed, p is the air static pressure at the cover, and ρ_a is the air density. The equation governing the cover motion is

$$\rho_c \frac{\partial^2 \eta}{\partial t^2} = p + T \frac{\partial^2 \eta}{\partial x^2} - D \frac{\partial^4 \eta}{\partial x^4} - K_s \eta - C_s \frac{\partial \eta}{\partial t} \qquad \text{(I7)}$$

where T is the cover tension, D is the bending rigidity, K_s is the shoe spring stiffness, C_s accounts for its damping properties, and ρ_c is the surface density of the cover.

Consider a wave travelling in the positive x-direction away from the slot with the general form

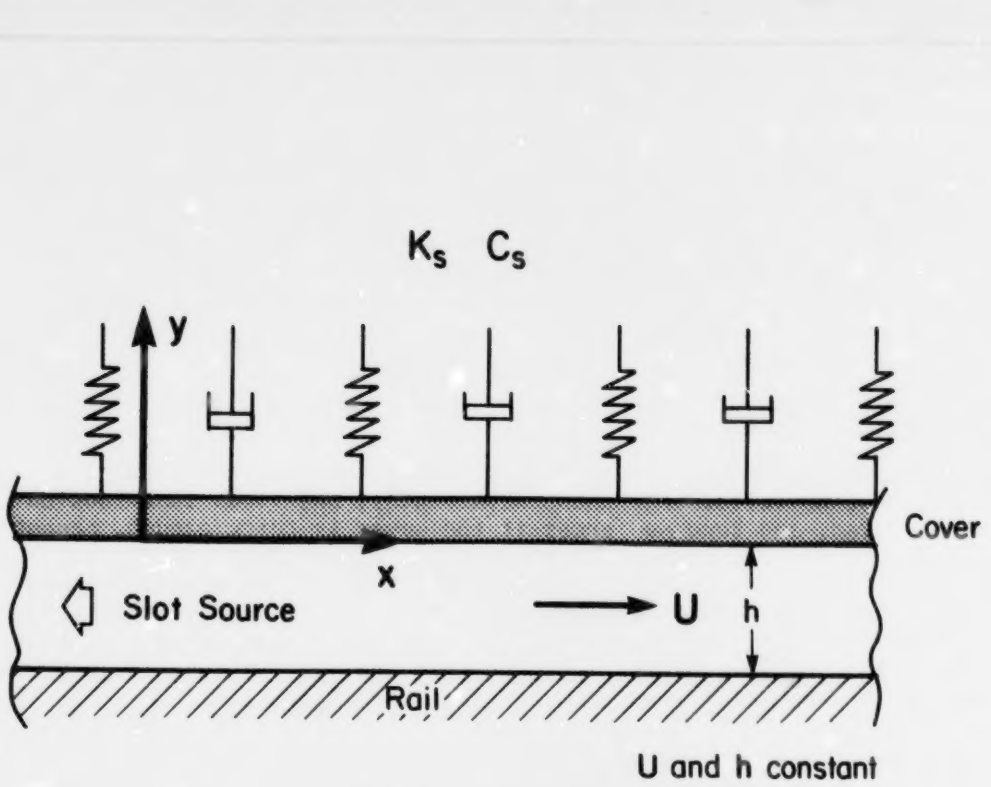
K_s C_s
y
Cover
x
Slot Source
U
h
Rail
U and h constant

END VIEW

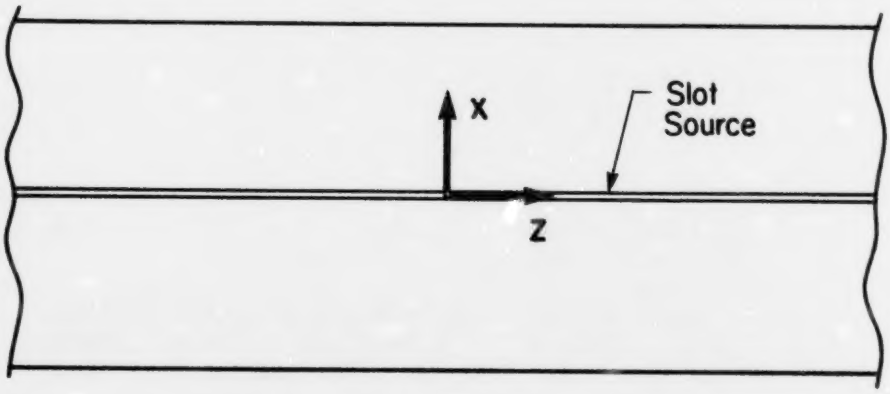
x
Slot Source
z

TOP VIEW

Figure I.2 Simplified geometry used in cover flutter analysis.

$$\eta = \eta_0 e^{i(kx-\omega t)}, \qquad \phi = \phi_0 \cosh[k(h+y)]e^{i(kx-\omega t)} \tag{I8}$$

where ω is the wave angular frequency, k is the wave number, and η_0 and ϕ_0 are wave amplitudes (the wavelength λ is $2\pi/k$). Substitution shows that these forms automatically satisfy Laplace's equation and the zero normal flow condition at the rail surface. Substitution into the cover condition gives

$$p = -\rho_c\omega^2\eta + Tk^2\eta + Dk^4\eta + K_s\eta - i\omega C_s\eta \tag{I9}$$

Substitution of this into the unsteady Bernoulli condition gives

$$-i\omega\phi_0\cosh[kh] + Uik\phi_0\cosh[kh] - \frac{\rho_c}{\rho_a}\omega^2\eta_0 + \frac{(Tk^2+Dk^4+K_s)}{\rho_a}\eta_0 - \frac{i\omega C_s}{\rho_a}\eta_0 = 0 \tag{I10}$$

The kinematic condition reduces to

$$-i\omega\eta_0 + Uik\eta_0 = k\sinh[kh]\phi_0 \tag{I11}$$

Solving this for ϕ_0 in terms of η_0 and substituting into the unsteady Bernoulli condition gives the following characteristic equation for the frequency

$$A\omega^2 + B\omega + C = 0 \tag{I12}$$

where

$$A = 1 + (\rho_c/\rho_a)k\tanh[kh], \qquad B = -2Uk + i(C_s/\rho_a)k\tanh[kh]$$
$$C = -[(Tk^2 + Dk^4 + K_s)/\rho_a]k\tanh[kh] + U^2k^2 \tag{I13}$$

Solving the quadratic yields the dispersion relationship

$$\omega = -\frac{B \pm \sqrt{B^2 - 4AC}}{2A} \tag{I14}$$

Thus, for a given flow speed there are two characteristic frequencies. For zero flow speed, they are equal in magnitude but opposite in sign. The negative ω corresponds to waves travelling towards the nozzle while the positive ω is for waves travelling away from it. For now, assume C_s equal to zero. In this case, $B^2 - 4AC = 0$ represents a stability boundary because $B^2 = 4AC < 0$ implies that one frequency root would have a positive imaginary part. Equation (I8) shows that in this case there would be wave growth. The $B^2 - 4AC = 0$ condition yields the following equation for critical flow speed U_f as a function of wave number k:

$$U_f = \sqrt{\left(\frac{Tk^2 + Dk^4 + K_s}{\rho_a k^2}\right)\left(\frac{\rho_a}{\rho_c} + k\tanh[kh]\right)} \tag{I15}$$

Plots of U_f versus k are shown schematically in Figure I.3. The minimum in

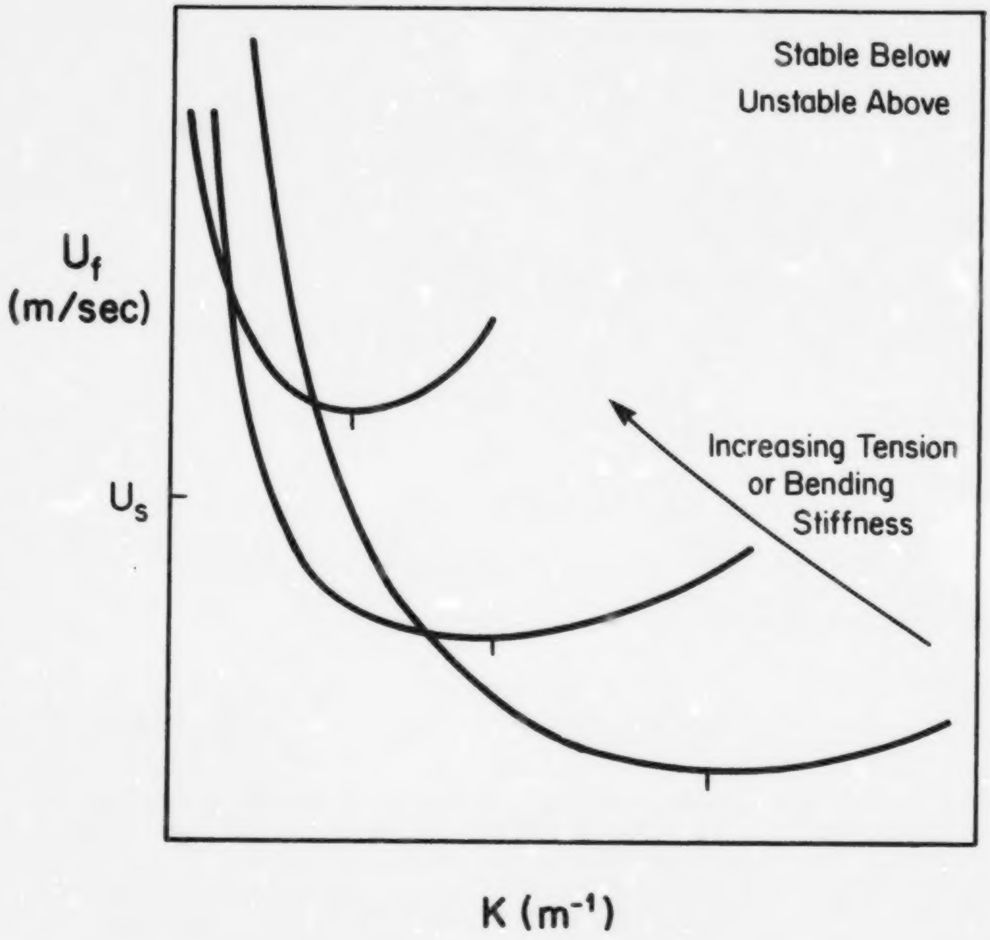

Figure I.3 Typical flutter stability boundaries.

each curve identifies the critical wave number at the onset of instability.

Note that when $C > 0$ [equation (I13)], information in the form of waves would not be able to propagate upstream against the flow. In other words, all waves wuld be swept downstream and the flow would become insensitive to downstream conditions. The $C = 0$ condition gives a flow limitation speed U_D where

$$U_D = \sqrt{\left(\frac{Tk^2 + Dk^4 + K_s}{\rho_a k^2}\right) k\tanh[kh]} \qquad (I16)$$

Note that for very long waves ($k = 0$) this reduces to

$$U_D = \sqrt{\frac{K_s h}{\rho_a}} = U_s \qquad (I17)$$

which is the long wavelength static instability condition given in equation (I1). One should also note that when C_s is nonzero a divergence or static instability can be shown to occur at U_D. In other words, damping would make a critically stable situation unstable. Plots of U_D versus k are shown schematically in Figure I4.

I.3 Results and Discussion

One would expect that, in practice, shoe-rail contact in the seal region would not allow wavelengths greater than about twice the distance between the tips of the crushed cardboard tube in the shoe. Also, the above theory requires that the wavelength be much geater than the cover thickness. This allows one to define a range of allowable wavelengths. Plots of U_f, U_D and f as a function of wavelength are shown in Figures I.5 to I.8. Figures I.5 and I.6 give the data for a 1.27 mm thick cover, and Figures I.7 and I.8 correspond to a cover 0.125 mm thick. The cover material in both cases is high density polyethylene. Cover tension effects are ignored but bending stiffness effects are allowed for. The bending stiffness is given by

$$D = \frac{E^* t^3}{12}, \qquad E^* = E/(1-\nu^2) \qquad (I18)$$

where E is the Young's modulus for polyethylene (8.6×10^5 kPa), ν is the Poisson's ratio (0.35), and t is the cover thickness. The calculations make use of the spring stiffness of the tissue backing ($K_s = 15250$ kPa/m) and the shoe-rail gap ($h = 0.127$ mm) given earlier for log S5B. The minimum in each U_f versus λ curve defines a critical wavelength. The frequency associated with this wavelength is 565 Hz for the thick cover and 1410 Hz for the thin cover.

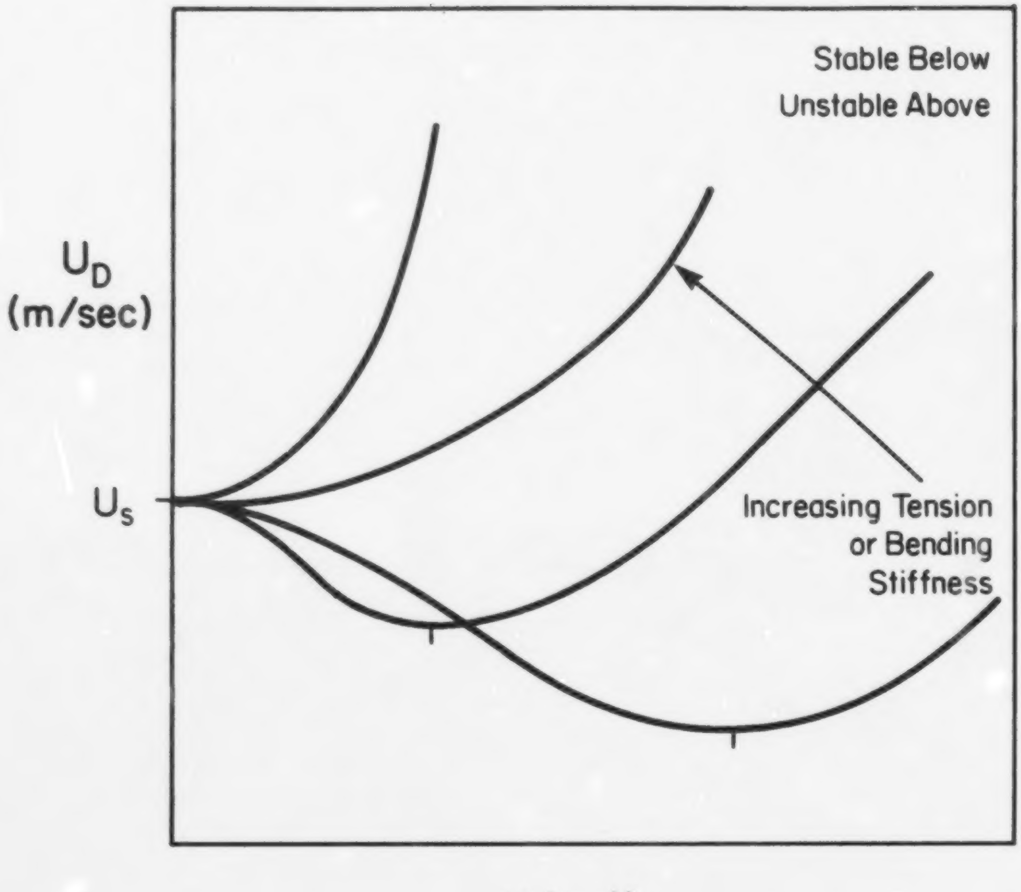

Figure I.4 Typical divergence stability boundaries.

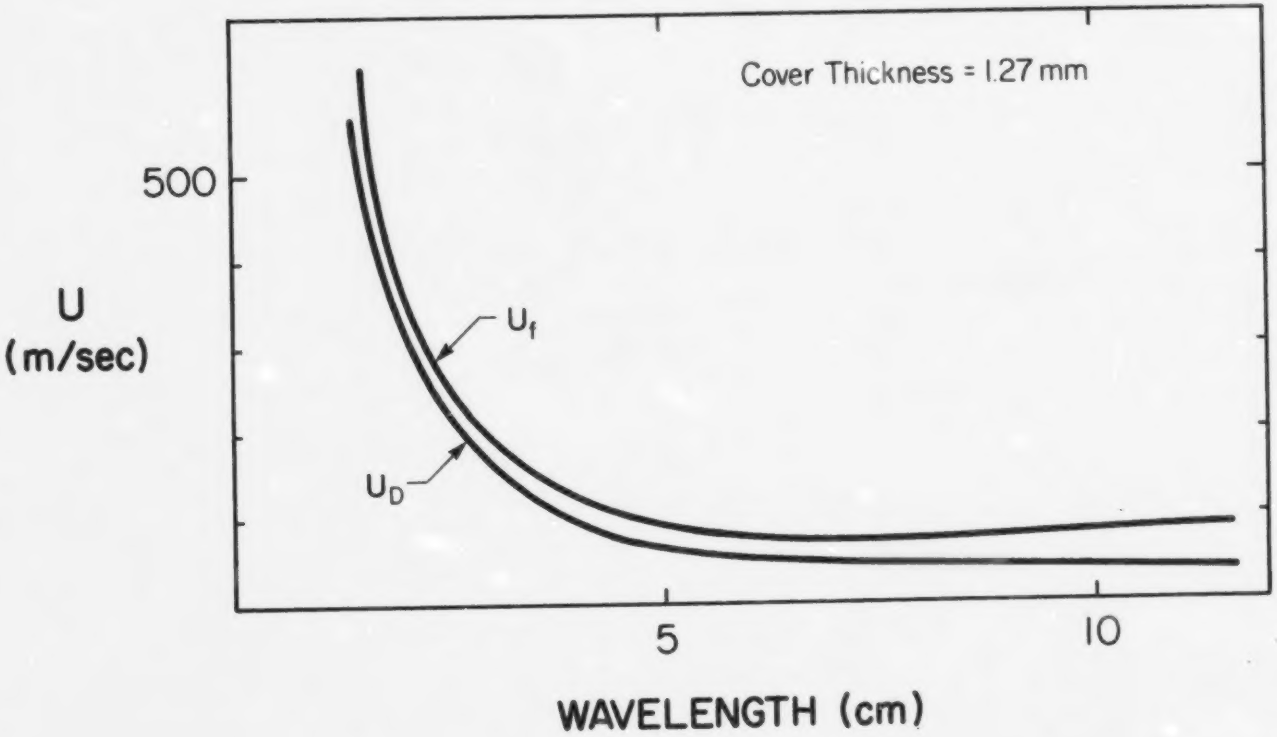

Figure I.5 Flutter and divergence stability boundary for 1.27mm shoe cover.

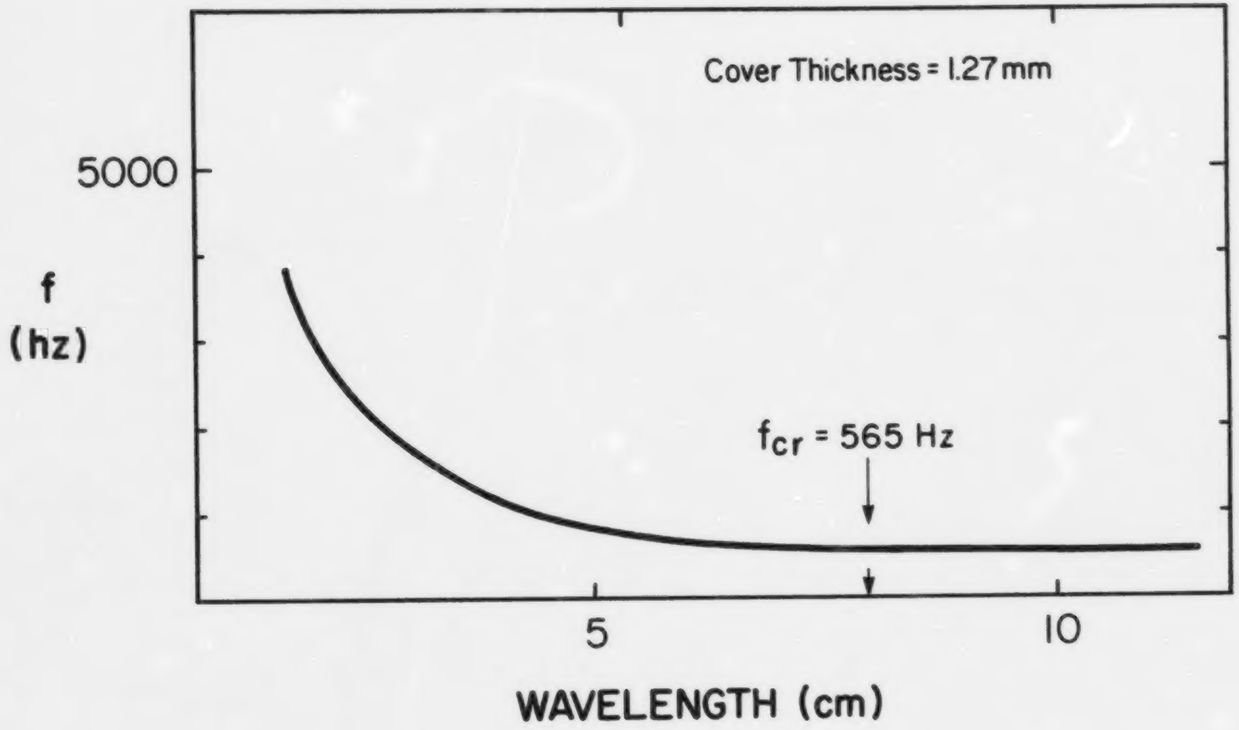

Figure I.6 Frequency at flutter stability boundary as a function of wavelength. The frequency at the wavelength corresponding to the lowest U_f at which flutter occurs is 565 Hz.

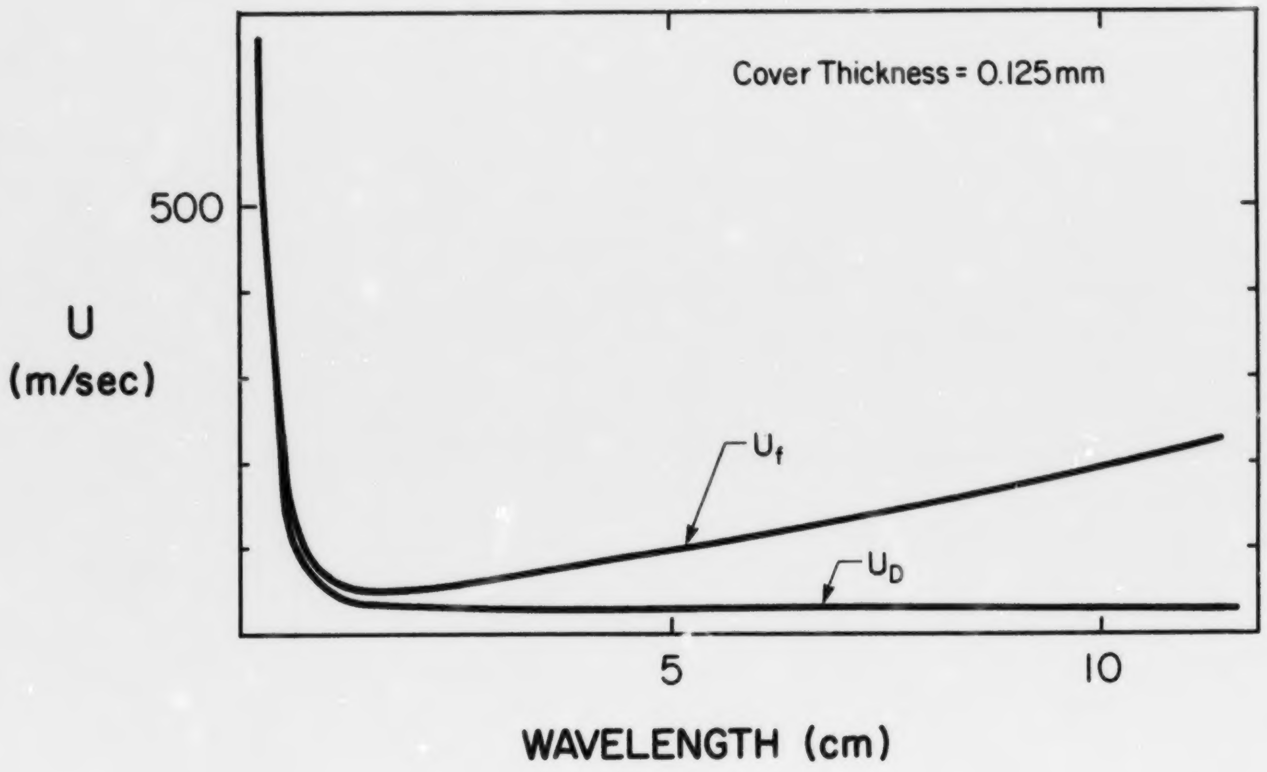

Figure I.7 Flutter and divergence stability boundary for 0.125mm shoe cover.

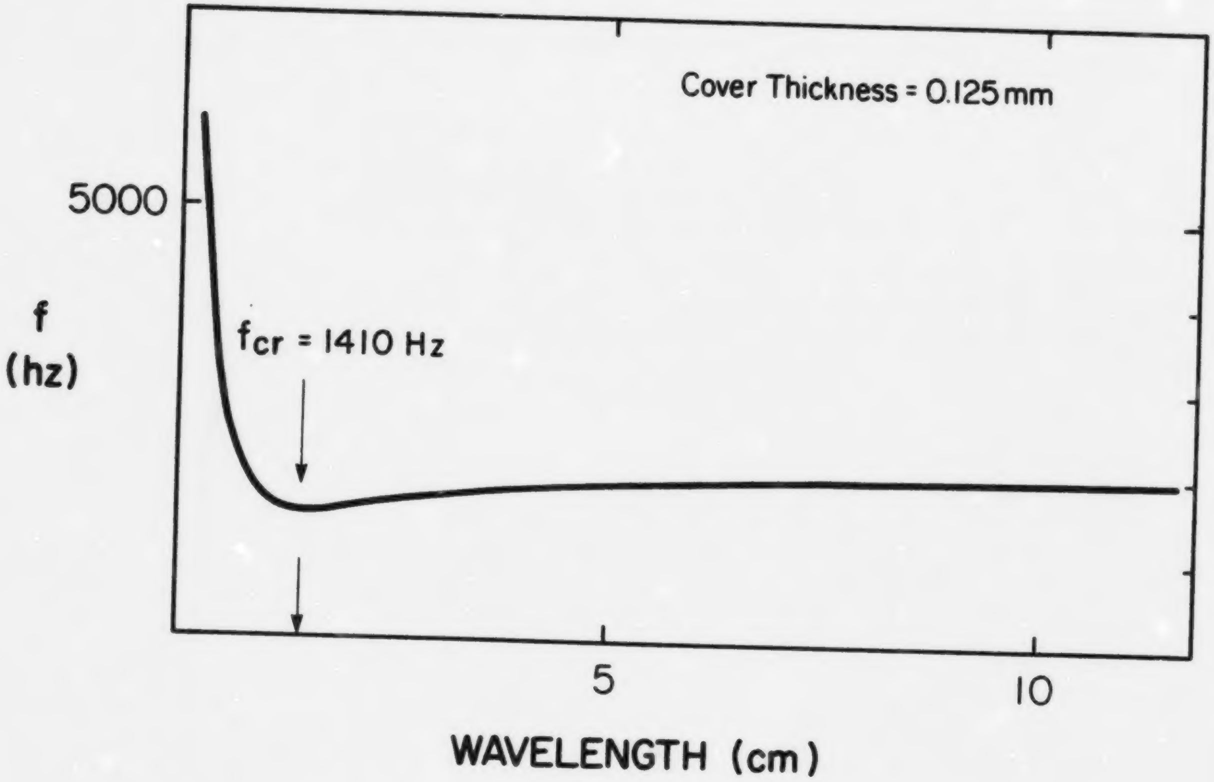

Figure I.8 Frequency at the flutter stability boundary as a function of wavelength. The frequency corresponding to the lowest U_f at which flutter occurs is 1410 Hz.

I.4 Conclusion

During the experiments described in Appendix D, some cover vibrations were encountered. The vibration frequencies were measured using a microphone and were typically of the order of 750 Hz. Also the writers of this report have observed an incident at the developer's facility in which the emission of an acoustical tone is clearly associated with a reduction in sliding friction. However the practical significance of the phenomenon needs to be clarified before further work on it could be recommended.

APPENDIX J. VISUALIZATION OF THE FLOW BETWEEN TRACK AND SHOE (M. J. Hinchey)

J.1 Introduction

During the previous contract period [1], a number of techniques were developed for visualization of the gap flow. The most promising of these used ammonia-sensitive sheets such as blueprint paper attached to the shoe cover. When ammonia was introduced into the air supply line and thus into the shoe-rail gap, it caused the sheets to change colour locally. During the present contract period, this flow visualization technique was refined slightly and used to help interpret our experimental results. Its use by the developer, also during this period, has resulted in major design changes to the rail and in the nozzle layout. UTIAS was directly involved in this development work.

J.2 Flow Visualization Refinement

Initially, ammonia was introduced into the air supply line by passing the air through the upper part of a container partially filled with liquid ammonia. The exact amount of ammonia entering the shoe-rail gap region was unknown. In the refined method a measured amount of ammonia was injected by hypodermic needle directly into the flexible supply line at a point immediately upstream of the rail.

J.3 Effect of Changes in Nozzle Layout

A visualization obtained during the previous contract period using the original method is shown in Figure J.1; the nozzle pattern is the original standard. This shows that the 15° nozzle vents locally to atmosphere in spite of its orientation towards the centre of the rail. This implies that the air used to generate lift was being supplied almost entirely by the 5° row of nozzles, and is the main result that led the manufacturer to remove the 15° row to obtain the "new standard" of Figure C.3.

Typical results obtained by the refined method are shown in Figures J.2 and J.3. Figure J.2 gives the results for two nozzle patterns, the new standard and a variant in which the nozzle locations remain the same, but the orientation has been changed to point to alternate sides of the rail. The main feature to note is the well-defined cellular structure, in which the cells have a length very close to the nozzle spacing. Also the alteration of the nozzle orientation shown in Figure J.2 does not change the global structure of the flow pattern. Figure J.3 is an enlargement of one of the cells in Figure J.2; it clearly shows the streamline pattern. Note that the flow at the edges is always at right angles to the shoe, as is assumed in the analysis of Appendix A.

These results strongly support the conclusion that, of the two aspects of nozzle pattern, namely location and orientation, the former is the principal factor affecting performance, with the latter playing at most a minor role.

Figure J1 Visualization of the flow between rail and shoe for original standard nozzle pattern, nozzles at -15° and +5° with 12 inch spacing.

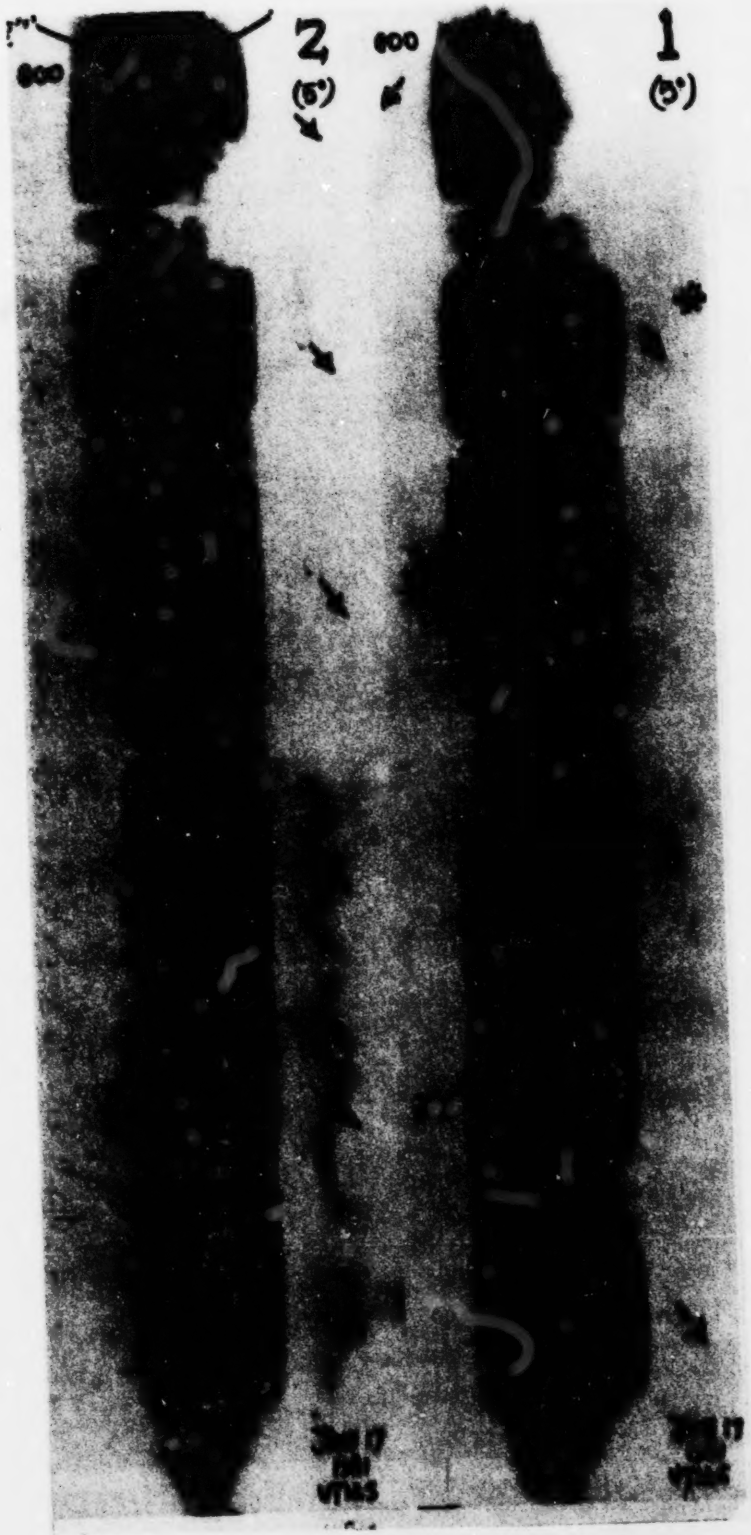

Figure J2 Visualization of the flow between rail and shoe obtained by the metered ammonia method for a single row of nozzles at the $+5^0$ location and 6 in. spacing for two nozzle orientations as indicated by the marked arrows. The left hand visualization corresponds to the new standard nozzle geometry, and in the right hand visualization the nozzles point to alternate sides of the rail.

Figure J3 Details of flow in one of the cells of Figure J2 showing streamlines.

APPENDIX K. FINITE ELEMENT ANALYSIS OF FLOW BETWEEN SHOE AND RAIL (M. J. Hinchey)

K.1 Introduction

The finite element hydrostatic lubrication analysis of SailRail developed during the previous contract period was based on the Reynolds equation for isothermal compressible flow [1]:

$$\nabla \cdot (p h^3 \nabla p) = 0 \qquad \text{(K1)}$$

where p is the absolute pressure and h is the gap between shoe and rail (see Figure A2). The nozzles were modelled as pressure sources and the gap distribution was assumed known. During the present contract period, an orifice flow model for the nozzles was developed. The local shoe pressure in the immediate vicinity of a nozzle is now taken to be the track pressure minus a loss which is dependent on the local gap. Also, instead of an assumed gap distribution, the local spring stiffness distribution of the shoe is now assumed and the gap is a function of the local pressure. This Appendix describes these two new features, and some preliminary results. The modified computer programme is listed in Appendix P.

K.2 A Property of Flows Obeying the Reynolds Equation

Equation K1 is derived by a generalization of the analysis in Appendix A1. Using the coordinate system of Figure A1, in which the general velocity vector is

$$\vec{q} = u\hat{e}_x + v\hat{e}_y + w\hat{e}_z \qquad \text{(K2)}$$

and with the following assumptions:

(i) the flow is isothermal and inertialess,

(ii) the velocity component and the pressure gradient in the z direction are both negligibly small,

(iii) viscous shear stresses caused by velocity gradients in the x and y directions are negligible,

the Navier Stokes equations for compressible flow reduce to

Continuity: $$\frac{\partial}{\partial x}(\rho u) + \frac{\partial}{\partial y}(\rho v) = 0 \qquad \text{(K3)}$$

x-momentum: $$\frac{\partial p}{\partial x} = \mu \frac{\partial^2 u}{\partial z^2} \qquad \text{(K4)}$$

y-momentum: $$\frac{\partial p}{\partial y} = \mu \frac{\partial^2 v}{\partial z^2} \qquad \text{(K5)}$$

Here, whereas u and v are functions of x, y, and z, p is a function of x and y only, so that Equations (K4) and (K5) can be integrated in the z direction as in Appendix A. The resultant expressions are

$$u = \frac{1}{2\mu} \frac{\partial p}{\partial y} z(h - z) \tag{K6}$$

$$v = \frac{1}{2\mu} \frac{\partial p}{\partial y} z(h - z) \tag{K7}$$

where $0 < z < h(x, y)$ and the no-slip condition on velocity has been applied at $z = 0$ and $z = h$.

Equations (K6) and (K7) can be expressed in a single vector equation

$$\vec{q} = u\hat{e}_x + v\hat{e}_y = \frac{z(h-z)}{2\mu} \left[\frac{\partial p}{\partial x} e_x + \frac{\partial p}{\partial y} e_y\right] \tag{K8}$$

or, more compactly

$$\vec{q} = \frac{z(h-z)}{2\mu} \nabla p \tag{K9}$$

This states that, at any particular location in the x-y plane, the velocity vectors for all z between $z = 0$ and $z = h$ point in the same direction, and this direction is the same as that of the local pressure gradient. This result explains why well defined streamlines can be observed in the flow visualization shown in Figure J4.

Equation (K1) is derived from equation (K9) by applying continuity and using the fact that for isothermal flows $\rho \propto p$. Also it is possible to define average velocities in the x and y direction; by a straightforward integration these are

$$v_x = -\frac{h^2}{12\mu} \frac{\partial p}{\partial x}, \qquad v_y = -\frac{h^2}{12\mu} \frac{\partial p}{\partial y} \tag{K10}$$

K.3 Local Spring Shoe Model

The local spring model of the shoe assumes that at any point (x, y) the deflection of the shoe depends only on the air pressure at that point, that is

$$h = h_0 + (p - p_a)/[k(x,y)] \tag{K11}$$

where $k(x,y)$ is the distribution of local stiffness. Hence this model ignores any bending stiffness contributed by the shoe cover. For the present calculations three distributions were assumed; they are shown in Figure K1.

K.4 Orifice Flow Model of Nozzles

In the calculations undertaken for the first contract the nozzles were modelled as sources of a specified constant pressure, and the air flow rates required to maintain this pressure were determined as part of the solution. In practice the rail manifold pressure is maintained at a constant value. A first step towards including the pressure losses through the entry region was made as follows. The transition from inertia dominated flow to viscous flow in the cavity was assumed to occur at a specified radial distance r_s

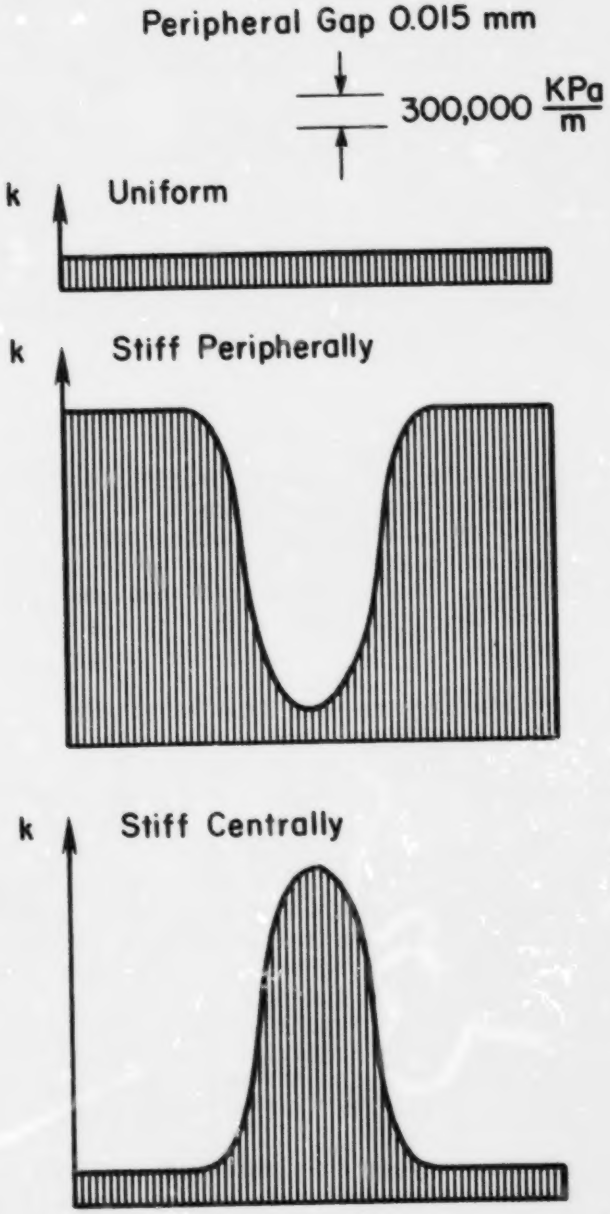
Peripheral Gap 0.015 mm
300,000 $\frac{KPa}{m}$
k
Uniform
k
Stiff Peripherally
k
Stiff Centrally

Figure K1 Shoe stiffness distributions assumed for finite element lubrication analysis.

from a nozzle. The pressure p_s at this radius was called the source pressure, and the pressure drop $p_t - p_s$ from rail manifold to the edge of the source was assumed to obey an orifice law

$$p_t - p_s = \frac{1}{2} C_d(h)\rho_s v_s{}^2 \qquad \text{(K12)}$$

where C_d is a discharge coefficient, ρ_s is the air density at the source edge, and v_s is the mean radial velocity at r_s, given by

$$v_s = \frac{\dot{m}}{\pi \rho_s r_s h} \qquad \text{(K13)}$$

Here $\dot{m}$ is the mass flow through the nozzle and h is the local gap. The discharge coefficient C_d was assumed to be a function of h.

K.5 Results

Figures K2, K3 and K4 give gap and pressure profiles obtained using the three shoe stiffness distributions shown schematically in Figure K1. These results show that a shoe which is soft centrally but stiff peripherally gives pressure profiles which are qualitatively similar to the measured profiles described in Appendix D. The uniform stiffness shoe gives the next best profiles whereas the shoe which is stiff centrally but soft peripherally gives the poorest.

Figure K5 gives some preliminary results from an attempt to include the nozzle head loss feature. The results are for a shoe with a uniform stiffness distribution. For reasons to be given shortly, the nozzle discharge coefficient was assumed to be constant and independent of gap. Also, an average head loss for the four nozzles was estimated and applied to each node instead of the individually calculated node head loss given earlier. The height of the small cylinder at each nozzle in the pressure plot indicates the magnitude of the predicted pressure drop. Even with the simplifications noted above, numerical instabilities were encountered when this feature was added to the computer program. To circumvent these, the head loss had to be gradually introduced during the iteration process. This is unsatisfactory because it is accompanied by a significant increase in the number of iterations required to obtain a converged solution. It might be better to experiment with the nozzle model in a one-dimensional slot source geometry before continuing to work with it in the finite element program.

Figure K6 gives typical velocity vectors obtained from the numerical solutions by using equation K10. The similarity to the flow visualization given in Figure J3 provides additional evidence that, except near the nozzles, equation K1 describes the flow processes involved.

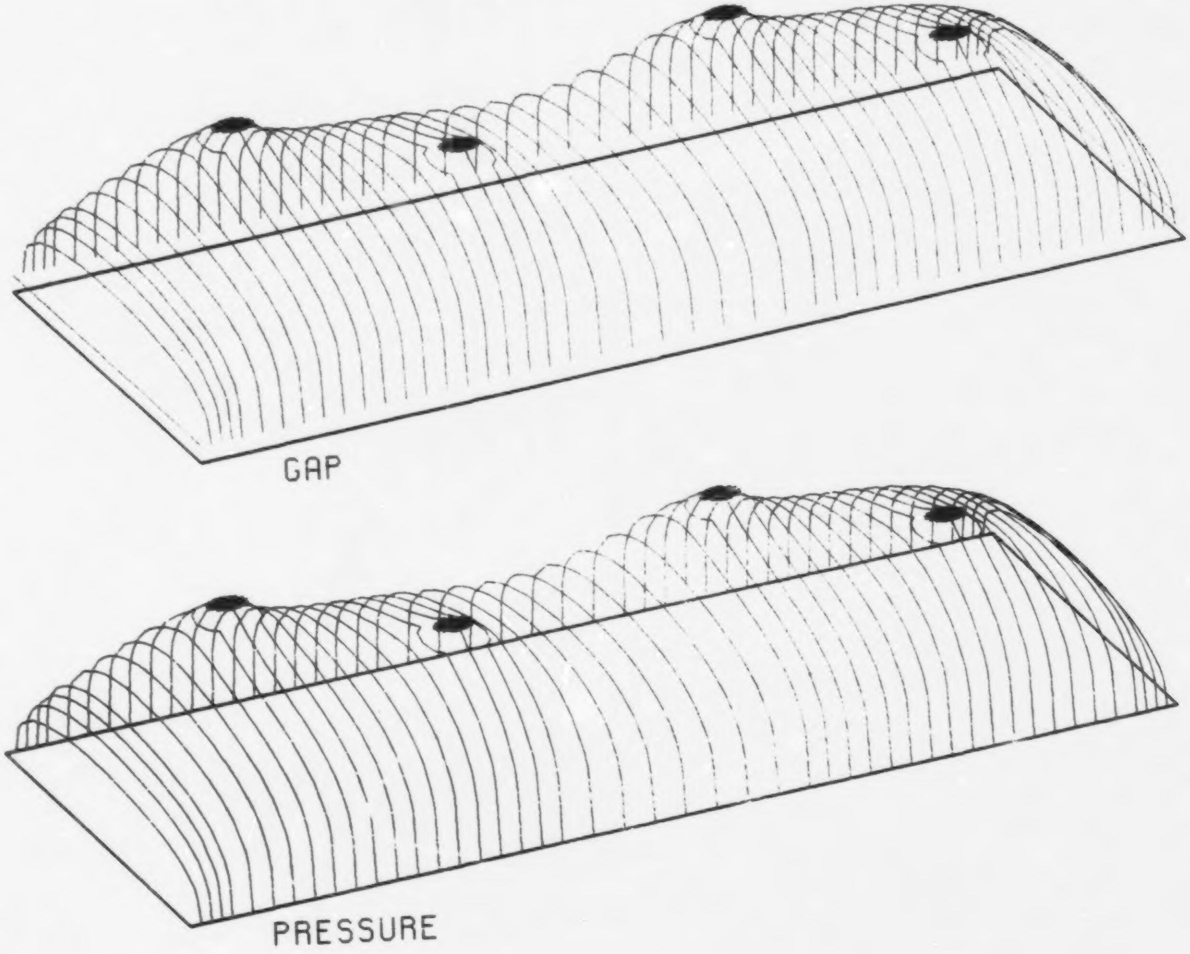

Figure K2 Computed pressure and gap distributions for a shoe having uniform stiffness. The nozzle locations are marked by the cross-hatched circles.

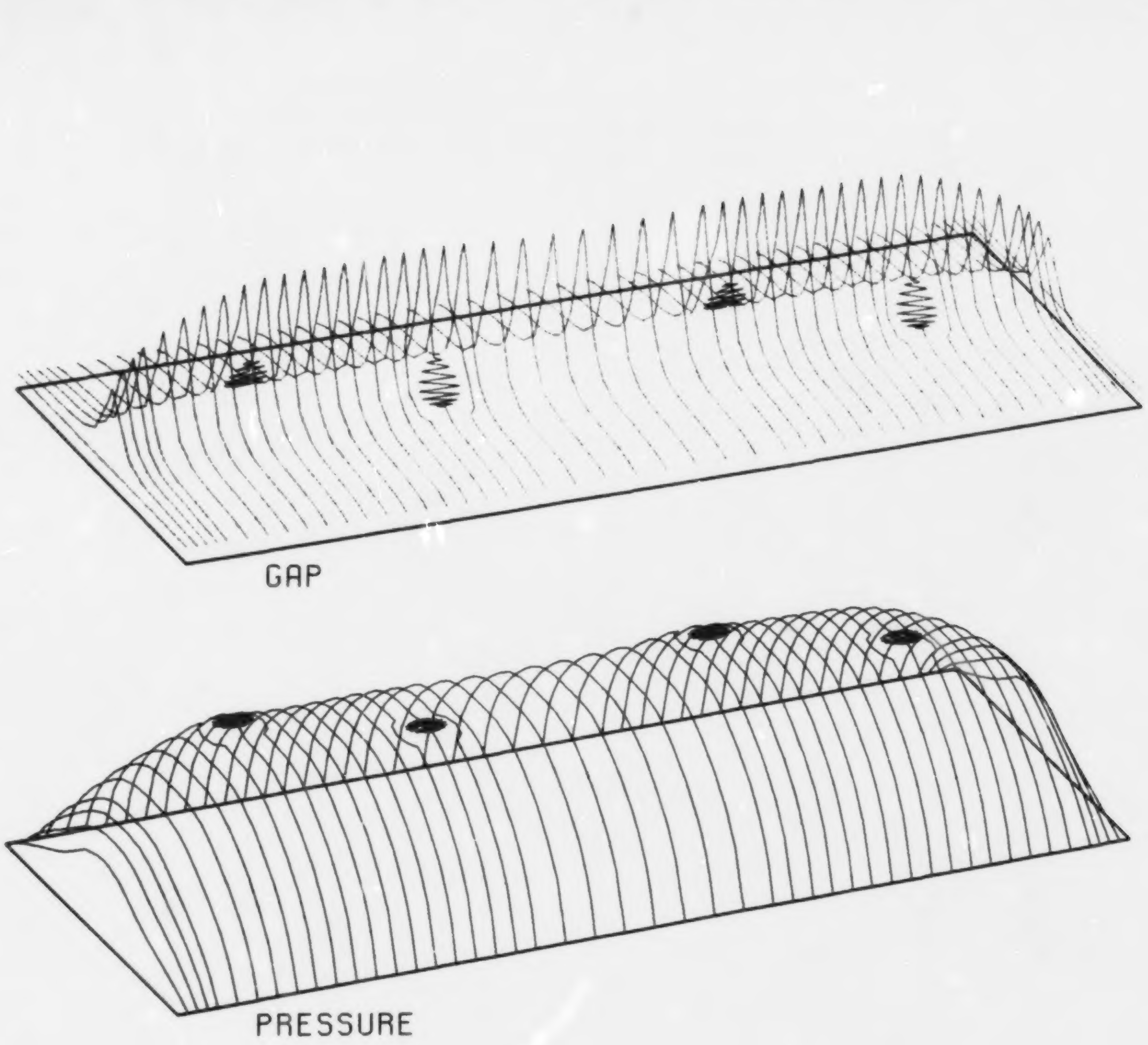

Figure K3 Computed pressure and gap distributions for a shoe which is soft in the centre and stiff on the periphery.

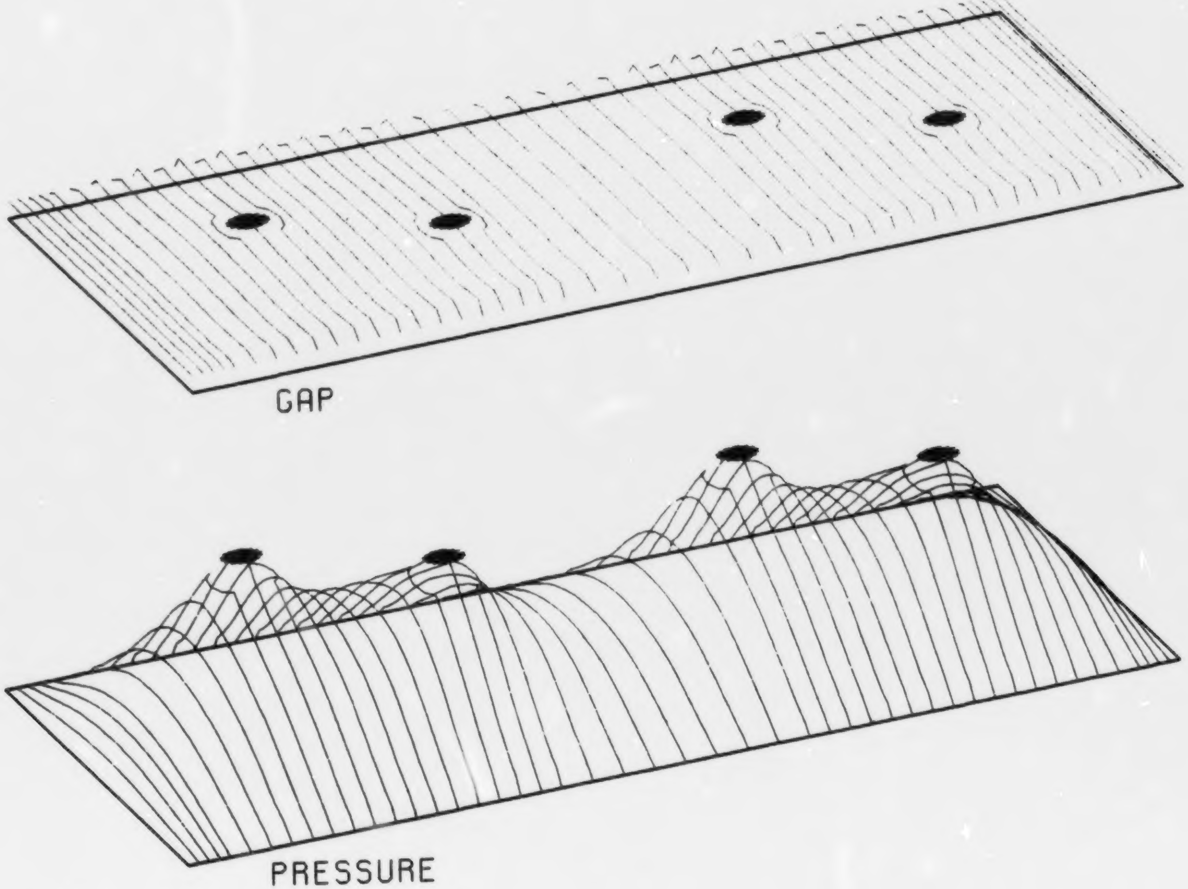

Figure K4 Computed pressure and gap distributions for a shoe which is stiff in the centre and soft on the periphery.

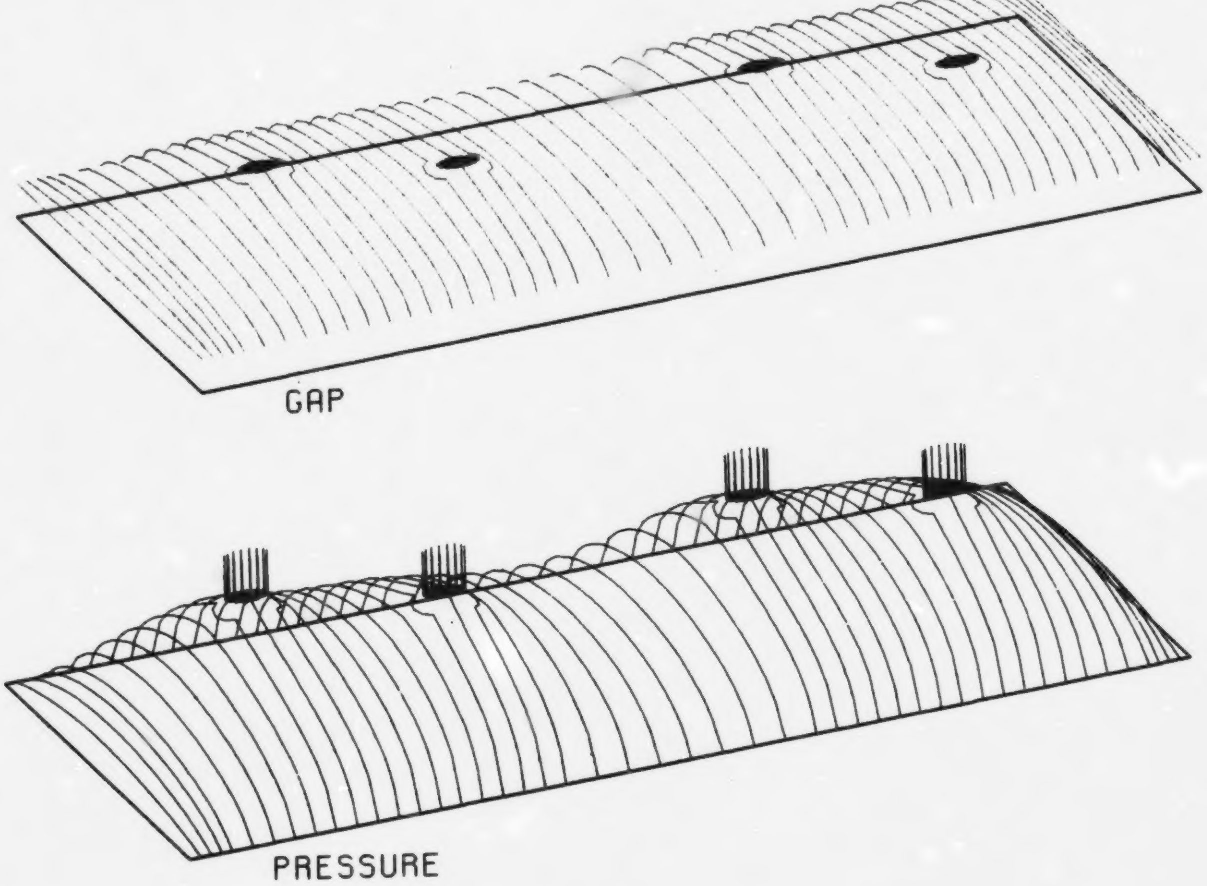

Figure K5 Computed pressure and gap distributions for analysis including nozzle head losses.

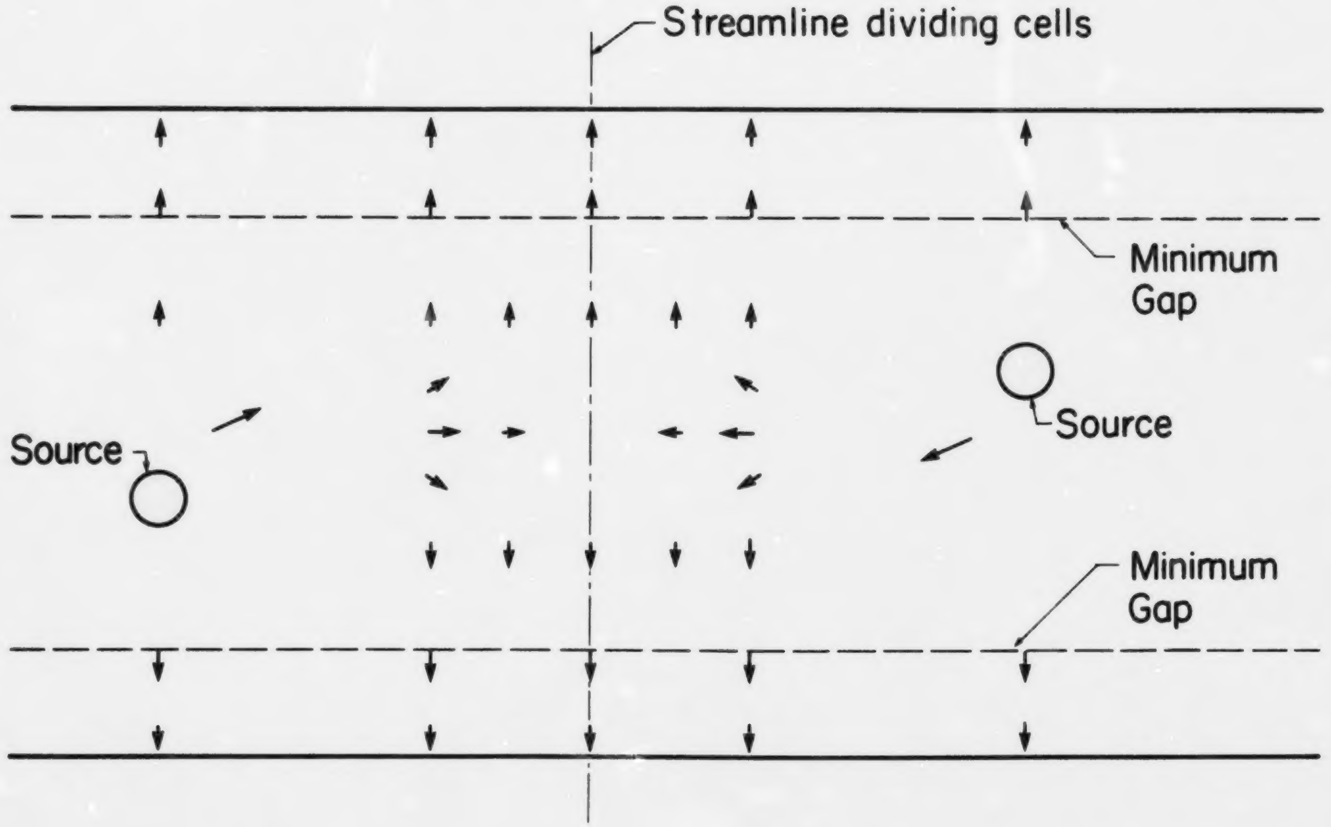
Streamline dividing cells
Minimum Gap
Source
Source
Minimum Gap

Figure K6 Typical velocity vectors for flow between shoe and rail determined using equation K9.

APPENDIX L. FINITE DIFFERENCE SIMULATION OF RADIAL NOZZLE FLOW (L. Z. Yong and M. J. Hinchey)

L.1 Introduction

To aid in the interpretation of our experimental work on the resistance characteristics of the radial nozzle, the pressure and flow patterns within its immediate vicinity were calculated using the finite difference technique developed by Gosman and Ideriah [20] for turbulent recirculating flow. This appendix describes briefly the details of the numerical simulation.

L.2 Governing Equations

The turbulence model developed by Gosman and Ideriah [20] does not deal directly with the small-scale structure of turbulence but only with its time averaged effects. Their model is based on the Reynolds equation which is obtained by time-averaging the Navier Stokes equations. This introduces the Reynolds stresses by way of the convective terms. It is these stresses which give turbulence its diffusive character. Gosman and Ideriah [20] modelled this behaviour using a k-ε eddy viscosity turbulence model. The details of the derivation of this model are quite involved and will not be given here. The governing equations in their final form are (see Figure L1)

Continuity:

$$\frac{\partial}{\partial x}(r\rho u) + \frac{\partial}{\partial r}(r\rho v) = 0 \qquad \text{(L1)}$$

x-Momentum:

$$\frac{1}{r}\left\{\frac{\partial}{\partial x}(r\rho u^2) + \frac{\partial}{\partial r}(r\rho uv)\right\} = -\frac{\partial p}{\partial x} + \frac{1}{r}\left[\frac{\partial}{\partial x}\left(\mu_{eff} r \frac{\partial u}{\partial x}\right) + \frac{\partial}{\partial r}\left(\mu_{eff} r \frac{\partial u}{\partial r}\right)\right] + S_u \qquad \text{(L2)}$$

where

$$S_u = \frac{\partial}{\partial x}\left(\mu_t \frac{\partial u}{\partial x}\right) + \frac{1}{r}\frac{\partial}{\partial r}\left(\mu_t r \frac{\partial v}{\partial x}\right)$$

r-Momentum:

$$\frac{1}{r}\left\{\frac{\partial}{\partial x}(r\rho uv) + \frac{\partial}{\partial r}(r\rho v^2)\right\} = -\frac{\partial p}{\partial r} + \frac{1}{r}\left[\frac{\partial}{\partial x}\left(\mu_{eff} r \frac{\partial v}{\partial x}\right) + \frac{\partial}{\partial r}\left(\mu_{eff} r \frac{\partial v}{\partial r}\right)\right] - \frac{\mu_{eff}}{r^2} v + S_v \qquad \text{(L3)}$$

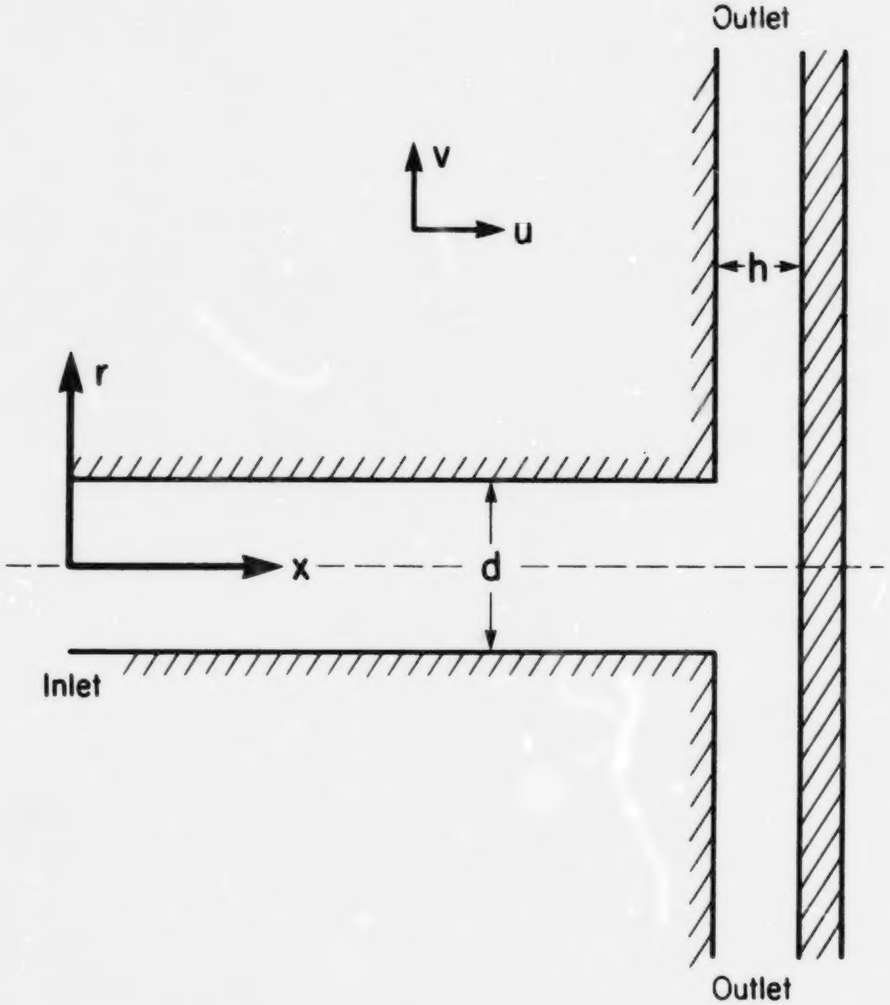
Outlet
v
u
h
r
x
d
Inlet
Outlet

Figure L1 Geometry used in turbulent flow calculations for sharp edged radial nozzle.

where

$$S_v = \frac{\partial}{\partial x}\left(\mu_t \frac{\partial u}{\partial r}\right) + \frac{1}{r}\frac{\partial}{\partial r}\left(\mu_t r \frac{\partial v}{\partial r}\right) - \frac{\mu_t}{r^2} v$$

Kinetic Energy of Turbulence:

$$\frac{1}{r}\left[\frac{\partial}{\partial x}(r\rho u k) + \frac{\partial}{\partial r}(r\rho v k)\right] = \frac{1}{r}\frac{\partial}{\partial x}\left(\frac{\mu_{eff}}{\sigma_k} r \frac{\partial k}{\partial x}\right)$$

$$+ \frac{1}{r}\frac{\partial}{\partial r}\left(\frac{\mu_{eff}}{\sigma_k} r \frac{\partial k}{\partial r}\right) + G - C_D \rho \varepsilon \qquad \text{(L4)}$$

where

$$G = 2\mu_t\left[\left(\frac{\partial u}{\partial x}\right)^2 + \left(\frac{\partial v}{\partial r}\right)^2 + \left(\frac{v}{r}\right)^2\right] + \mu_t\left(\frac{\partial u}{\partial r} + \frac{\partial v}{\partial x}\right)^2 \qquad \text{(L5)}$$

Dissipation Rate of Turbulence:

$$\frac{1}{r}\left[\frac{\partial}{\partial x}(r\rho u \varepsilon) + \frac{\partial}{\partial r}(r\rho v \varepsilon)\right] = \frac{1}{r}\frac{\partial}{\partial x}\left(\frac{\mu_{eff}}{\sigma_\varepsilon} r \frac{\partial \varepsilon}{\partial x}\right)$$

$$+ \frac{1}{r}\frac{\partial}{\partial r}\left(\frac{\mu_{eff}}{\sigma_\varepsilon} r \frac{\partial \varepsilon}{\partial r}\right) + C_1 \frac{\varepsilon}{k} G - C_2 \rho \frac{\varepsilon^2}{k} \qquad \text{(L6)}$$

where

k = kinetic energy of turbulence

ε = dissipation rate of turbulence

and the turbulence viscosity μ_t is given by

$\mu_t = C_\mu \frac{k^2}{\varepsilon}$ turbulence viscos (L7)

$\mu_{eff} = \mu_t + \mu_\ell$ effective viscosity

Numerical values for the so-called universal constants, as determined from a combination of dimensional arguments and geometrically simple experiments are [20]

$$\sigma_k = 1.0 \quad C_1 = 1.44 \quad C_D = 1.0$$
$$\sigma_\varepsilon = 1.3 \quad C_2 = 1.92 \quad C_\mu = 0.9 \qquad \text{(L8)}$$

L.3 Finite Difference Code

The finite difference procedure developed by Gosman and Ideriah [20] reduces each partial differential equation given above to a system of algebraic equations with values of u, v, p, k or ε at specific grid oints as unknowns. Its distinguishing feature is a volume integration of each equation over an Eulerian subdomain or cell. It uses the staggered grid arrangement shown in Figure L2, where the scalars p, k and ε are the unknowns at the intersections of the grid lines and the velocities are the unknowns at the staggered positions shown.

A segregated approach is used whereby the finite difference equations for a particular governing equation are assembled into their own global matrix. For the nozzle problem, u is associated with the x-momentum equation and v, p, k and ε are associated with the r-momentum, continuity, kinetic energy of turbulence and dissipation rate of turbulence, respectively. Where v, p, k and ε appear in the x-momentum finite difference equations, values from the previous iteration step are inserted and the resulting equations are then solved for u. Each governing equation is dealt with separately, one after the other. This is in cotrast to a coupled approach where all finite difference equations are considered together.

The Semi-Implicit Method for Pressure Linked Equations or SIMPLE procedure is used to obtain pressure from the continuity equation. To start the calculations, a distribution of pressure is assumed and the momentum equation finite difference approximations are solved in sequence using the segregated approach. The resulting velocity field approximately satifies momentum, but not continuity, and therefore must be corrected. For this, a Taylor series expansion is used to obtain for each staggered grid point

$$\begin{aligned} u_{pu} &= \hat{u}_{pu} + \frac{\partial u_{pu}}{\partial(p_S - p_N)} (\delta p_S - \delta p_N) \\ v_{pv} &= \hat{v}_{pv} + \frac{\partial v_{pv}}{\partial(p_W - p_E)} (\delta p_W - \delta p_E) \end{aligned} \tag{L9}$$

where the symbol $(\hat{\ })$ indicates the old velocity field, the subscripts pu and pv indicate u and v staggered velocity positions, respectively, the subscripts N, S, E, W refer respectively to pressure grid points north, south, east or west of either the staggered point pu or the point pv, and δp indicates a pressure correction. Estimates of the slopes

$$\frac{\partial u_{pu}}{\delta(p_S - p_N)} \quad \text{and} \quad \frac{\partial v_{pv}}{\delta(p_W - p_E)} \tag{L10}$$

are obtained from the momentum equation finite difference approximations. When the resulting expressions for u_{pu} and v_{pv} are substituted into the finite difference analog of the continuity equation, a system of equations

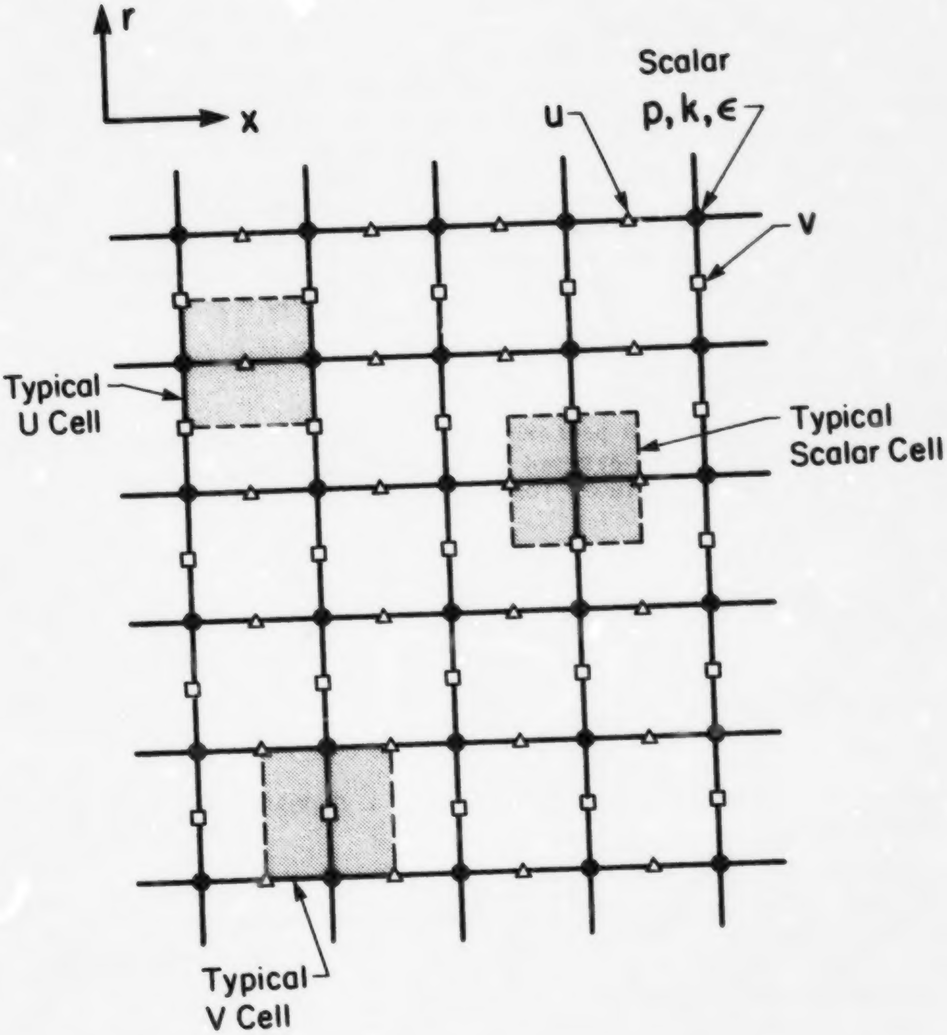
r
x
Scalar
u
p, k, ϵ
v
Typical U Cell
Typical Scalar Cell
Typical V Cell

Figure L2 Staggered grid used in finite difference computations.

for the pressure corrections is obtained. By solving these, the pressure and velocity fields can be updated. The whole process is repeated until the pressure corrections tend to zero.

The convection, diffusion and pressure terms appearing in the various transport equation volume integrals are converted to surface integrals by means of an integration by parts. An upwind scheme is used for the resulting convective fluxes. This ensures that the global matrices will be diagonally dominant, which is essential for the numerical stability of the tridiagonal matrix line-by-line iterative solution procedure used. The upwind representation is said to be physically realistic in that it states that a grid point will receive convective information only from points upstream and will transmit information only to points downstream. To evaluate the source term volume integrals, it is assumed that the values of a source term at the centre of a particular cell is a good average for the cell. This is also important for numerical stability.

L.4 Boundary Conditions

To obtain a nozzle flow pattern, the following inlet conditions were specified: typically u was assumed to be uniform with $u = u_{in}$, v was assumed to be zro, k was assumed to be given by

$$k = iu_{in}^2 \qquad (L11)$$

where i, the intensity factor, was typically i = 0.01 and ε was assumed to be given by

$$\varepsilon = \frac{k^{3/2}}{\ell_m} \qquad (L12)$$

where ℓ_m, the mixing length, was typically $\ell_m = 0.0025d$, and d is the nozzle diameter.

Because of the convective nature of the flow at the outlet, u, p, k and ε did not have to be specified there. However, v, the normal outflow velocity, was forced to satisfy overall continuity (flow in-flow out). The value of v at each point on the outlet plane was set equal to the value at the corresponding point immediately upstream but modified to account for the radial nature of the flow and corrected by an amount Δv which was the same for each point on the outlet plane and which ensured that the flow into the nozzle balanced with the flow out at the gap outlet plane.

Next to a wall, the flow is usually boundary layer-like and gradients normal to the wall are very steep. If boundary conditions were applied at the wall, many grid points or cells would have to be used to accurately model the near-wall behaviour. To avoid this, wall funtions, derived from an approximate analysis, were used to relate values at a wall to values in either the laminar sublayer or the buffer layer, where the laminar sublayer is a region next to the wall in which laminar viscosity dominates while the buffer layer is a region which separates the laminar sublayer from the fully turbulent region outside.

The pressure p was specified at one point on the solution domain boundary. At that point, δp was set equal to zero. For the other boundary points, where the normal velocities were specified, equation (L9) showed that the appropriate condition on δp was the vanishing normal gradient condition.

L.5 Computer Program Outline

A flow chart for the computer program is given in Figure L3. Immediately following this is a program listing. The program consists of the following subprograms:

HOLE	Generates geometric data and controls the itertion.
INIT	Manipulates geometric data and sets variables to their initial state. It is called by HOLE.
PROPS	Calculates effective viscosity. It is called by HOLE.
CALCU, CALCV, CALCP, CALCTE, CALCED	These are called by HOLE during each step of the iteration. CALCU is called first then followed by CALCV and so on. CALCU applies the finite difference code to the x-momentum eqution. The unknowns in the resulting algebraic equation system are the values of u at u cell staggered grid points. CALCV, CALCP, CALCTE and CALCED do the same for the r-momentum, continuity, turbulence kinetic energy and turbulence dissipation, respectively.
LISOLV	Solves the algebraic equation systems. It is called by CALCU, CALCV, CALCP, CALCTE and CALCED. A line-by-line tridiagonal matrix Gaussian elimination procedure is used to solve each equation system.
PROMOD	Applied boundary conditions. It is called by CALCU, CALCV, CALCP, CALCTE and CALCED.

For more program details, see References 20 and 6. For results, see Appendix B.

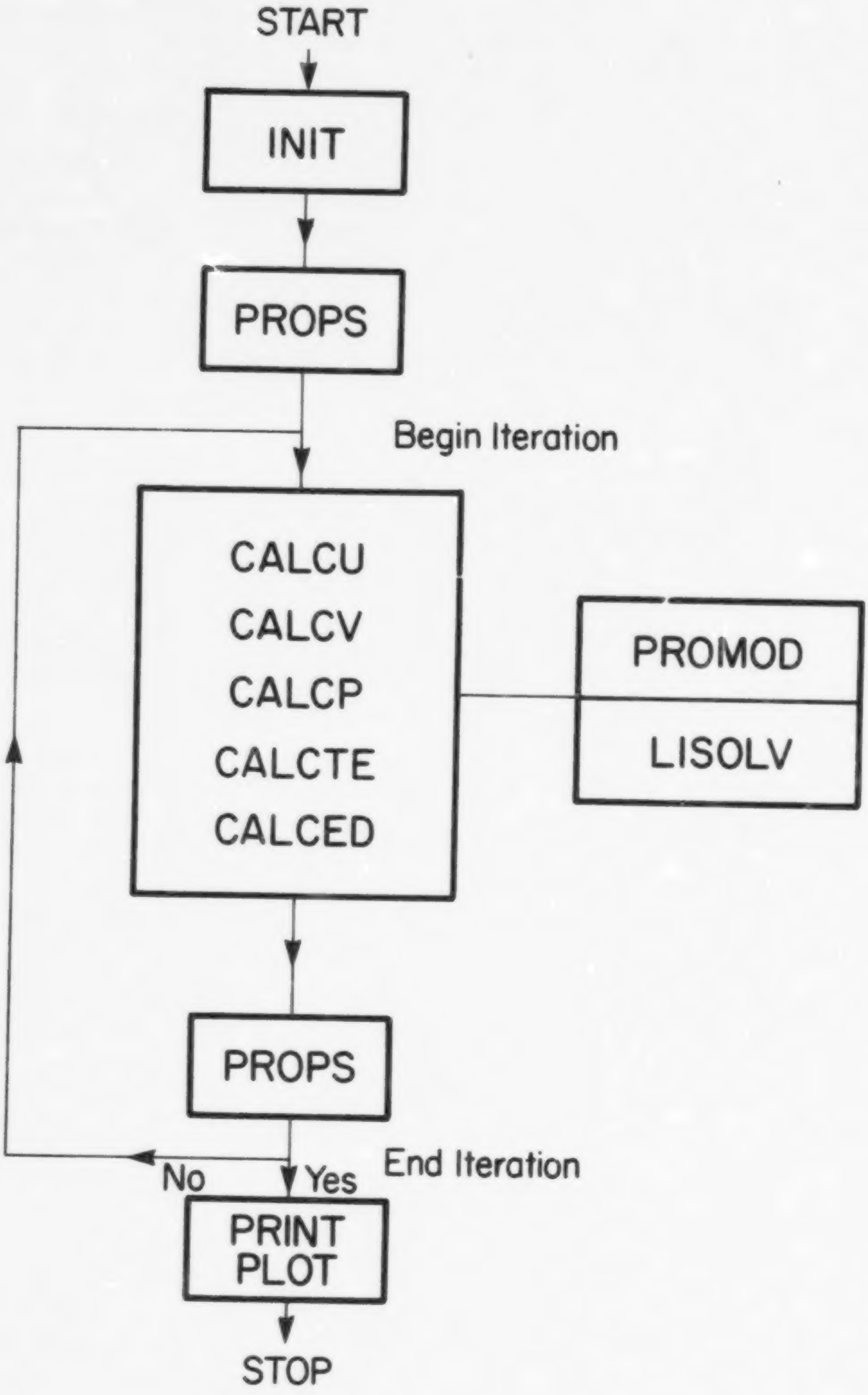
START
INIT
PROPS
Begin Iteration
CALCU
CALCV
CALCP
CALCTE
CALCED
PROMOD
LISOLV
PROPS
No
Yes
End Iteration
PRINT
PLOT
STOP

Figure L3 Flow chart for computer program.

APPENDIX M. DEVELOPMENT OF RAIL SECTION PROFILE (P. A. Sullivan)

The cross section of the rail first used in the experimental stage is shown in Figure M1 (Section I). It consisted of a 6in × 2 in aluminium channel onto which a rolled aluminium plate was welded. The radius of the bearing surface was 6 ins and this has not been changed in any subsequent developments. The original standard nozzle pattern was used [see Figure C3] and the nozzle diameter was nominally 0.026 ins (0.660 mm). The nozzle axis was at 20° to the tangent to the rail surface and at 45° to the plane of the rail section.

The first development prototype section is shown in Figure M2 (Section II). Known as the "plastic" rail, it was extruded from polyvinyl chloride. The nozzles were again located according to the original standard nozzle pattern but the nozzle positions moved to +6° and -11° relative to the rail centre in order to clear the webs shown in Figure M2. It was produced in two versions, "high lug" and "low lug"; the former is shown in Figure M2. Owing to its low longitudinal bending stiffness it was continuously supported by a steel trough.

The first extruded aluminium rail section is shown in Figure M3 (Section III). Since the curved bearing part of this section was about half as thick as that of Section I, in order to keep the length of the nozzle passage the same, the section was thickened locally as shown in Figure M3. Known as the "single web" rail, its increased bending stiffness eliminated the need for continuous support. The original standard nozzle pattern was used, with the nozzle rows relocated to the +5° and -15° position. As the name implies, it incorporated only a single interior web in order to simplify the supply of air to the two rows of nozzles, but it was subject to the performance degradation described in Appendix C. This problem was solved by introducing an additional web as shown in Figure M4 (Section IV). This "double web" rail was used in the test programme described in Appendix C.

The test programme at UTIAS showed that, for this section, the width of the air support cavity formed between the shoe and the rail was only a small fraction of the rail width, and that the 15° row of nozzles was contributing very little to the lift. Consequently, the manufacturer cut the width of the rail to 5 ins (127 mm) and changed the nozzle pattern to the "new standard" shown in Figure C3. The new section, known as the "single port" rail is shown in Figure M5 (Section V); to obtain a higher bending stiffness for the same rail weight as Section IV the profile was deepened considerably. Figure M6 shows the modified double web rail used to demonstrate the feasibility of cutting the rail width. Also the nozzle length was reduced by eliminating the thickened regions shown in Figure M4. To further increase the bending stiffness for certain applications an extended single port rail was also manufactured; this is shown in Figure M7 (Section VI).

The section in current use (Section VII) is shown in Figure M8. It is known as the "four port" rail. The two outer passages are used for long distance transmission of air. To activate short lengths of track, valves spaced at suitable intervals are used to transmit air to the inner passages and thus to the nozzles. The two inner ports are used in warehouse storage

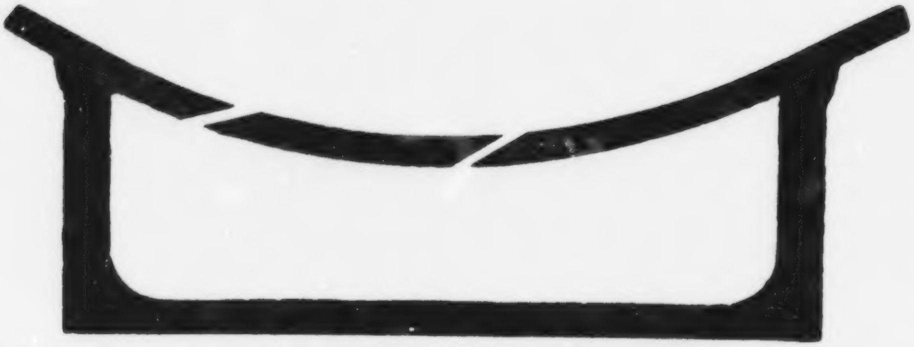

Figure M1 Rail section I, used in early experiments.

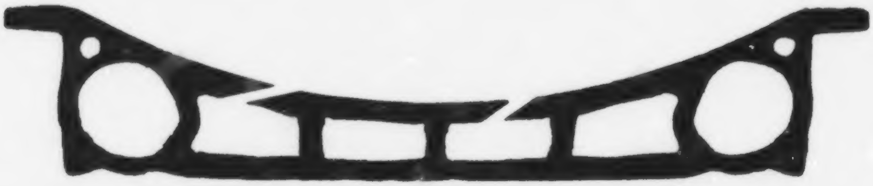

Figure M2 Rail section II, used in first pre-production prototypes. This was the only rail extruded from a plastic.

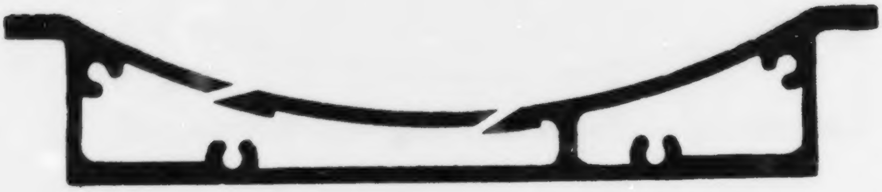

Figure M3 First extruded aluminium rail section, (III), known as the single web rail.

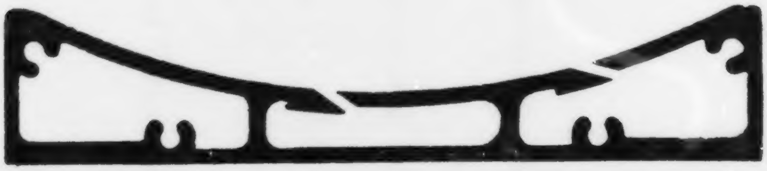

Figure M4 Rail section IV, "double web" rail, used in the trailer loading and unloading demonstration system at E. B. Eddy Forest Products, Hull.

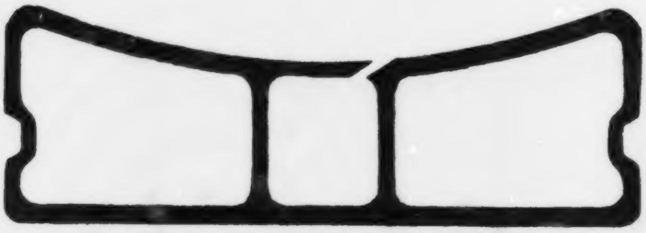

Figure M5 Rail section V, "single port" rail, used in first commercial application.

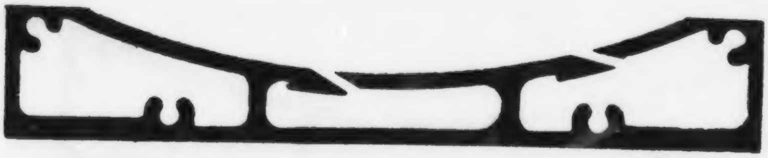

Figure M6 Modified double web rail used to explore the feasibility of reducing the rail width.

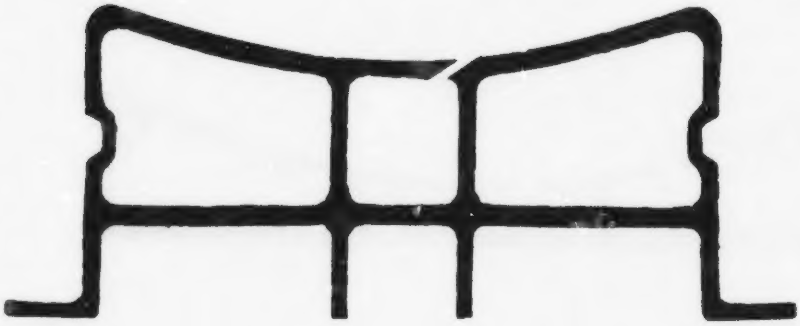

Figure M7 Extended single port rail, section VI.

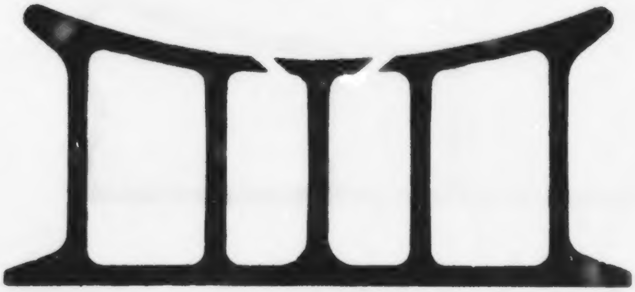

Figure M8 Section VII, "four port" rail used in current production.

and retrieval systems to provide an important safety feature. The first commercial applications used Section IV. However in a system in which a large number of pallets could be stored in one inclined row, there was always a danger of an uncontrolled slide of the entire row after one had been moved at the retrieval end. In systems using section VII, at any given time only alternate pallets are moved, so that, for any given moving pallet, the one ahead acts as an emergency stop. This is achieved by drilling sections of nozzles alternately in the right and left inner ports, and by supplying air to these ports alternately.

APPENDIX N: HEAD LOSSES IN SHARP EDGED RADIAL NOZZLES (P. A. Sullivan)

N.1 Introduction

For the sharp-edged radial nozzles, and with the assumption that the gap h between shoe and rail is a small fraction of the hole diameter d, it is possible to derive a simple estimate of the head losses. The idea is an adaptation of the analysis used in basic texts on fluid mechanics to calculate the effect of an abrupt contraction in a pipe on the head loss [q.v. e.g., Ref. 3, p. 185].

N.2 Simplified Model

The simplified model is depicted in Figure N.1. The speed of the fluid inside the separation bubble shown in Figure B16 is small compared with that of the flow passing through the throat. Consequently, it is assumed to be effectively at rest, in which case the pressure throughout the bubble should be constant. Furthermore, at the throat and beyond the velocity component in the z-direction is a very small fraction of the maximum radial component. This suggests that the pressure at each r is constant along the local z direction, and in particular across the faces "t" and "a" of the control volume in Figure N1. Since the streamline that divides the recirculating flow from the main flow is effectively a free surface, it assumed that the flow up to the throat is similar to that out of a slot orifice, so that it is effectively inviscid with a vena contracta having the usual value C_t = 0.611. Hence Bernoulli's law can be used to find the mean velocity of the fluid q_t at the throat in terms of the pressure p there:

$$\frac{p_2}{\rho} + \frac{1}{2}\bar{U}^2 = \frac{p_t}{\rho} + \frac{1}{2} q_t^2 \tag{N1}$$

Because the fluid decelerates rapidly in passing through the control volume it cannot be assumed inviscid, however, the momentum integral applies. Also because the distance the fluid passing through the throat takes to reattach to the top plate is relatively short, viscous shear forces on the top and bottom plate can be assumed very small compared with the pressure forces acting on the ends of the control volume. Finally, if h is very small, the flow in the control volume is two-dimensional, and the usual momentum integral argument gives

$$(p_t - p_a)h = \rho q_a^2 h - \rho q_t^2 C_t h \tag{N2}$$

where q_a is the mean fluid velocity at location "a".

Finally, conservation of mass yields two more equations:

$$Q = \frac{\pi}{4} d^2 \bar{U} = C_t \pi d h q_t \tag{N3}$$

$$Q = \pi d h q_e \tag{N4}$$

where again the two-dimensional assumption is used for the flow through the control volume.

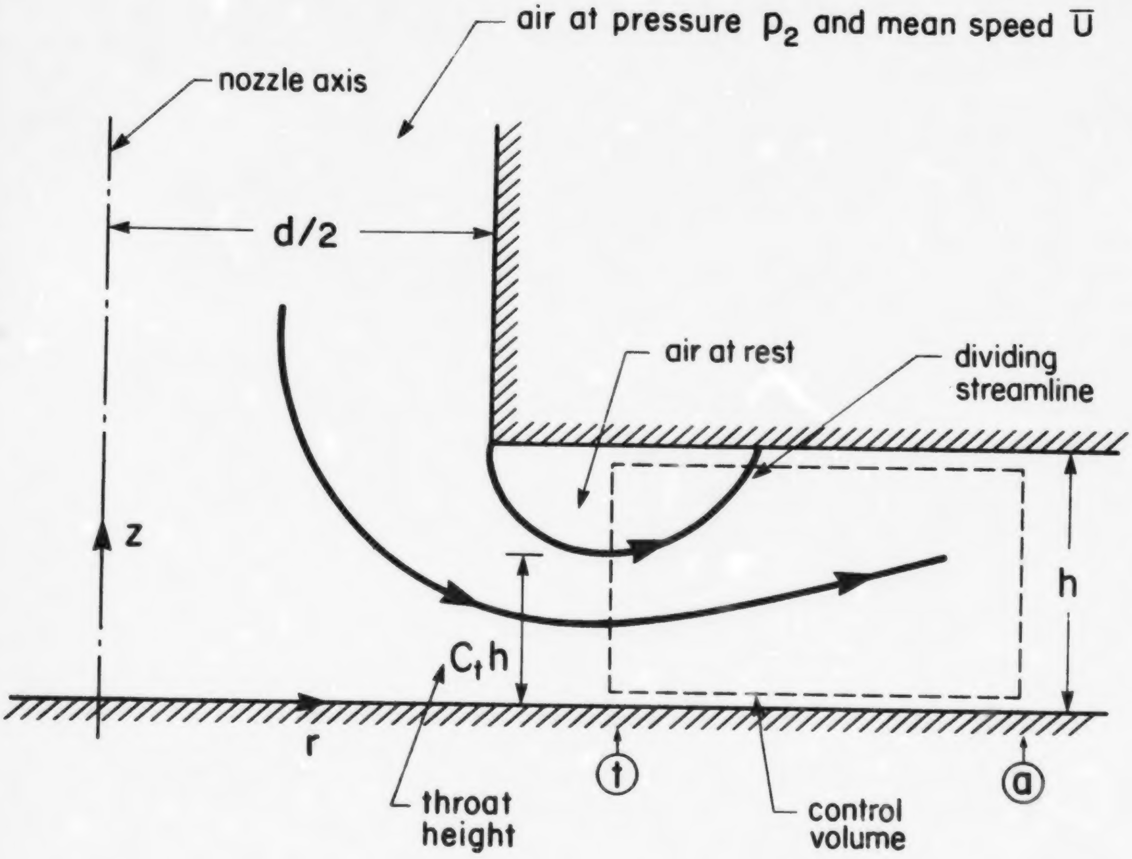
air at pressure p_2 and mean speed $\overline{U}$
nozzle axis
d/2
air at rest
dividing streamline
z
h
$C_t h$
r
throat height
ⓣ
control volume
ⓐ

Figure N1 Conceptual model used to calculate head losses for sharp-edged radial nozzle.

From equations N1 and N2 the pressure drop from nozzle to station "a" is

$$(p_2 - p_a) = \rho[q_a{}^2 + q_t{}^2(0.5 - C_t) - \frac{1}{2}\,\overline{U}^2] \qquad \text{(N5)}$$

Now assume that for the model in Appendix B, p_a = atmospheric pressure so that it can be set to zero, and apply continuity to eliminate velocities in favour of Q:

$$p_2 = \rho Q^2 \left[\frac{1}{(\pi dh)^2} + \frac{1}{(C_t \pi dh)^2}\left(\frac{1}{2} - C_t\right) - \frac{8}{\pi^2 d^4}\right] \qquad \text{(N6)}$$

Introduce the reference area $A_{r_2} = \pi dh$ and rearrange to give

$$p_2 = \frac{\rho Q^2}{2A_{r_2}^2}\left[\frac{2C_t{}^2 - 2C_t + 1}{C_t{}^2} - 16\,\frac{h^2}{d^2}\right] \qquad \text{(N7)}$$

From the definition of C_{Q2} and the reference velocity V_{ref} in equation B4, after a straightforward manipulation,

$$p_2 = \frac{\rho Q^2}{2A_{r_2}^2}\left[\frac{1}{C_{Q2}^2} - 16\,\frac{h^2}{d^2}\right] \qquad \text{(N8)}$$

Eliminating p_2 from equations N7 and N8 gives

$$C_{Q2} = C_t/[2C_t{}^2 - 2C_t + 1]^{1/2} \qquad \text{(N9)}$$

and $C_{Q1} = (4h/d)C_{Q2}$.

Upon using the value $C_t = 0.611$ for a slot orifice, one obtains

$$C_{Q2} = 0.843 \quad \text{and} \quad C_{Q1} = 3.37\ h/d \qquad \text{(N10)}$$

Note that this result is consistent with that of the dimensional analysis in Appendix B (equations B6 and B7). Note also that C_{Q2} is, by the definitions in Equations B3 and B4, the usual discharge coefficient C_m for flow through a slot orifice of height h and length πd from a reservoir at stagnation pressure $p_t = p_2 + 1/2\ \rho\overline{U}^2$. For the usual slot orifice $C_m = C_t$, but here owing to the pressure rise that occurs downstream of the throat, $C_m > C_t$ by 38%.

APPENDIX O. COMPRESSIBILITY EFFECTS IN THE NOZZLE REGION (P. A. Sullivan and T. A. Graham)

O.1 Introduction

The investigation of the fluid mechanics of the nozzle region described in Appendix B is limited to consideration of incompressible flow phenomena. The compressible flow effect that is potentially the most important for SailRail is the limitation or choking of flow through a nozzle. The essential features of the phenomenon as it applies to SailRail are depicted in Figure O.1. Air is supplied to a nozzle at pressure p_t in the rail reservoir or supply manifold. With the valve in Figure O.1 shut there is no flow and the pressure p_c at the nozzle exit equals p_t, and at first as p_c is lowered by opening the valve, the mass flow $\dot{m}$ increases. However, the rate of flow increase, $d\dot{m}/dp_c$, decreases and, when the air speed at the nozzle throat reaches the local sound speed, any further reduction of p_c does not increase $\dot{m}$. This occurs because the flow disturbances created downstream of the throat by lowering p_c cannot propagate upstream to adjust the flow there.

According to ideal fluid theory, for a calorically perfect gas such as air at room temperature, the absolute pressure ratio p_c/p_t at the onset of choking is given by

$$\frac{p_c}{p_t} = [2/(\gamma+1)]^{\gamma/(\gamma-1)} \tag{O.1}$$

and the mass flow is given by

$$\dot{m} = \frac{Kp_t}{\sqrt{T_t}} A_t; \qquad K = \left(\frac{\gamma}{R}\right)^{1/2}\left(\frac{2}{\gamma+1}\right)^{\frac{(\gamma+1)}{2(\gamma-1)}} \tag{O.2}$$

Here γ is the ratio of specific heats, A_t is the nozzle throat area, T_t is the absolute temperature of the gas in the supply manifold and R is the gas constant. For air $\gamma = 1.40$ and $R = 286.8$ J/kg°K, so that $p_c/p_t|_{cr} = 0.5283$ and $K = 4.043\times10^{-2}$. Note that $\dot{m}$ through a choked nozzle can be increased by raising p_t. However, the volume flux at track pressure p_t is given by $Q_t = \dot{m}/\rho_t$, or since $\rho_t = p_t/RT_t$

$$Q_t = KR\sqrt{T_t}\, A_t \tag{O.3}$$

Hence to observe choking effects in cases where p_c is fixed and p_t varies, which is the case for the present work, it is only necessary to use Q_t. To repeat, the essential feature of choking is not that the mass flow in through a nozzle cannot be further increased but that for p_c/p_t below a certain critical value, variation of p_c has no influence on $\dot{m}$.

For the SailRail system, representative maximum downstream or cavity gauge pressures p_{cg} are about 40 kPa, so that if the flow process from

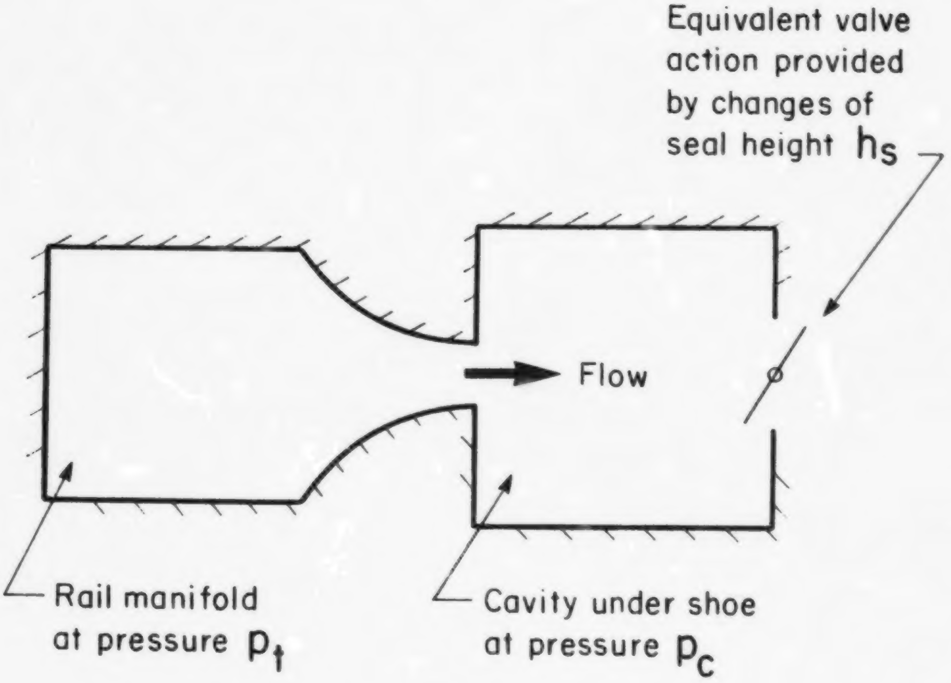
Equivalent valve action provided by changes of seal height h_s
Flow
Rail manifold at pressure p_t
Cavity under shoe at pressure p_c

Figure 0.1 Concept of gasdynamic choking as applied to SailRail nozzles.

rail manifold to cavity is inviscid, then choking would occur if the track gauge p_{tg} is greater than about 170 kPa = 25 psi). Since this is typical of track pressures used in practice, choking effects are likely to occur and have significant practical consequences. An important point in this connection is the location of the point of sonic flow, or the effective nozzle throat. One possibility is the vena contracta formed at the nozzle entrance, or point 1 in Figure B1. However, the flow field computations for radial nozzles described in Appendix B show that a vena contracta can also occur at the nozzle exit, or point 3 in Figure B.1, which implies that, for the radial nozzles at least, choking could occur at that location. This has an important practical implication for the following reason. If choking occurs at the nozzle entrance when a nozzle is covered by a shoe then, when it is uncovered as a result of movement of the load, there is no increased consumption of air. In contrast, if choking occurs at the nozzle exit, when it is uncovered Q_t will increase until choking occurs at the nozzle entrance, thus increasing air consumption.

This Appendix describes measurements of air flow rates for radial and inclined nozzles for values of p_t ranging up to levels sufficient to cause choking when the nozzles are covered and compares them with the corresponding measurements for uncovered nozzles.

0.2 Measurements of Air Flow for Covered and Uncovered Nozzles

Figure 0.2 compares computed and measured volume flows through an 0.660 mm (0.026 in) inclined nozzle for both covered and uncovered cases. The predicted values were obtained from the ideal theory [3, p.386] and do not include a discharge coefficient C_m. Qualitative agreement between theory and experiment is very good. For the choked flow, $C_m = 0.81$ when the nozzles are covered by a shoe and 0.850 when uncovered, thus indicating the presence of relatively small hydrodynamic losses through the cavity entry region, or between points 2 and 4 in Figure B1. However, the most striking feature of the results is that for $p_{tg} > 100$ kPa, which is the lower limit of that used in practice, uncovering the holes increases the air flow by a relatively small amount. This implies that the flow chokes at the nozzle entrance.

The value of C_m for the uncovered case is higher than expected. The only other relevant data readily available was empirical measurements quoted by Dudgeon and Lowe [22] for a sharp edged orifice plate, which gives

$$C_m = 0.85 - 0.15 \left(\frac{p_a}{p_t}\right) - 0.1 \left(\frac{p_a}{p_t}\right)^2 \qquad (0.4)$$

or, for $p_{tg} = 100$ kPa, $C_m = 0.75$. However C_m is very sensitive to the details of the geometry of the nozzle entrance which, for the present measurements were uncontrolled and differed considerably from that of a sharp-edged orifice plate. Also it is possible that the average nozzle diameter, was larger than the nominal 0.026 ins (0.660 mm). An increase of only 0.001 ins (0.025 mm) would cause an apparent increase in C_m by 7.8%.

Figure 0.3 shows the effect of p_{tg} on Q_t for covered radial nozzles of three diameters, 0.508, 0.711 and 1.016 mm (0.020, 0.028 and 0.040 in), with the corresponding inclined nozzle data included for

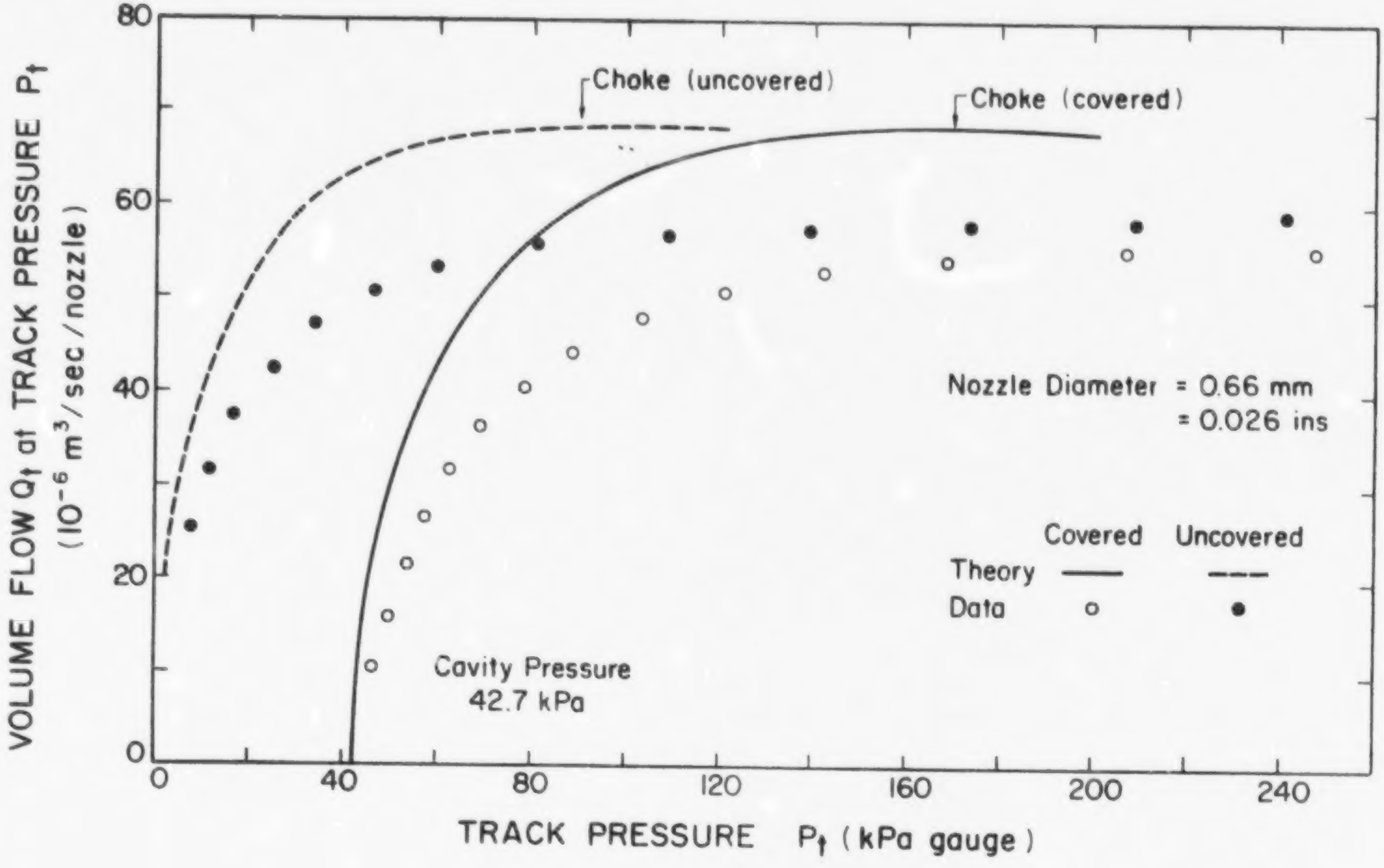

Figure 0.2 Effect of track pressure on air flow through a standard 0.66 mm inclined nozzle when uncovered and when covered by a shoe.

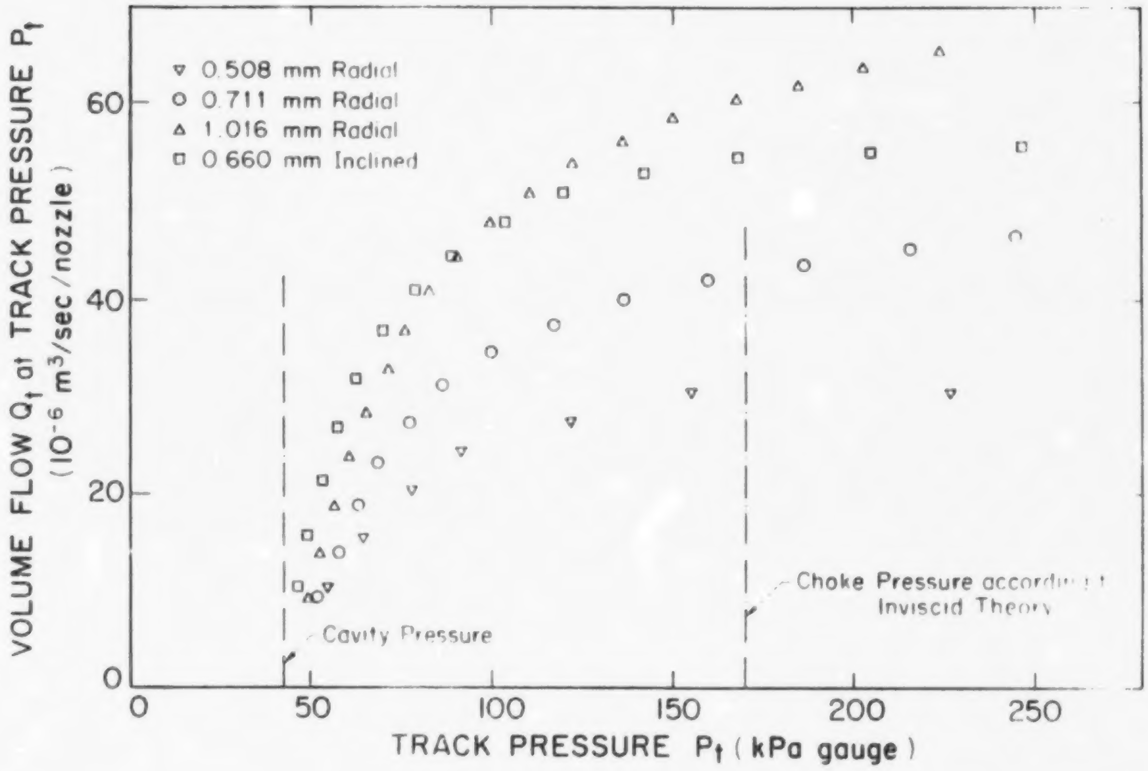

Figure 0.3 Effect of track pressure on air flow through radial nozzles when covered by a shoe, and comparison with inclined nozzle data.

comparison. Consider first the data for the 1.016 mm nozzle, two features occur. The first is that for p_{tg} below 80 kPa the inclined nozzle Q_c is higher than that for the 0.016 mm radial nozzle, but above 80 kPa the reverse is true. This implies that below 80 kPa the inclined nozzle has lower hydrodynamic losses; this is consistent with the data for incompressible flow described in Appendix B, since the peripheral reference area $A_{r2} = 3.19h$ mm^2 for the 1.016 mm nozzle and 4.32h mm^2 for the inclined nozzle. For p_{tg} above 80 kPa, the 1.016 mm nozzle Q_t becomes substantially higher than that for the inclined nozzle. Furthermore, when p_{tg} rises above the critical value, in contrast with the inclined nozzle data, Q_t continues to increase linearly. This continued increase suggests that the 1.016 mm radial nozzle is choking at the nozzle exit for the following reasons. First, as noted above, when the system is choked, $\dot{m}$ continues to increase as p_{tg} increases. As shown in Appendix D (see Figure D15) no further increase in cavity pressure p_{cg} occurs when p_{tg} is increased beyond 80 kPa.The analysis in Appendix A (equation A10 or G3) shows that with p_{cg} fixed any increase in $\dot{m}$ has to be accommodated by a vertical motion of the shoe in order to increase the seal height h_s. Therefore the throat area A_t of a nozzle choking at the exit will increase as $\dot{m}$ increases, whereas a nozzle choking at the inlet has a constant A_t. Also Q_t for the 0.711 mm nozzle increases with p_{tg} beyond the choking value, indicating that this nozzle also chokes at the exit.

Insufficient data was obtained to ascertain on the basis of Figure 0.3 alone the location of the choke point for the 0.508 mm nozzle. However an indication that it choked at the exit has been obtained as follows. According to equation 0.2, $\dot{m}$ at choking is proportional to the area at the choke point. This implies that if d is the nozzle diameter, $\dot{m} \propto d^2$ if choking occurs at the nozzle entrance, and $\dot{m} \propto d$ if it occurs at the exit. To check this, the data in Figure 0.2 has been used to calculate reduced mass flow rates

$$Q_{r1} = \frac{Q_t(d)d_r}{d}, \qquad m_{r2} = \frac{Q_t(d)d_r{}^2}{d^2} \tag{0.5}$$

where d_r is reference diameter. The reduced data is given in Figure 0.4, where d_r has been set equal to that of the 0.711 mm nozzle. The very close correlation of Q_{r1} for all three nozzle diameters supports the idea that choking of all three occurs at the exit.

Confirmation that this is the case is obtained by comparing the flow for the covered and uncovered nozzles, and this is given in Figure 0.5. For the 1.016 mm nozzle the flow increase when uncovered is very large, for example at the representative p_{tg} = 140 kPa it is higher by a factor of about 2.4. The data for the 0.711 mm nozzle also shows a substantial increase when uncovered, whereas the 0.508 mm nozzle does not, thus suggesting that the smallest nozzle is a borderline case. Note that at p_{tg} = 140 kPa C_m for the uncovered 1.016 mm nozzle is 0.842, and for the 0.711 mm and 0.508 mm nozzles it is 0.847 and 0.829 respectively.

0.3 Discussion and Conclusions

In all current SailRail applications, of the track into which air is being pumped at any given time, a fraction is unoccupied by the load being

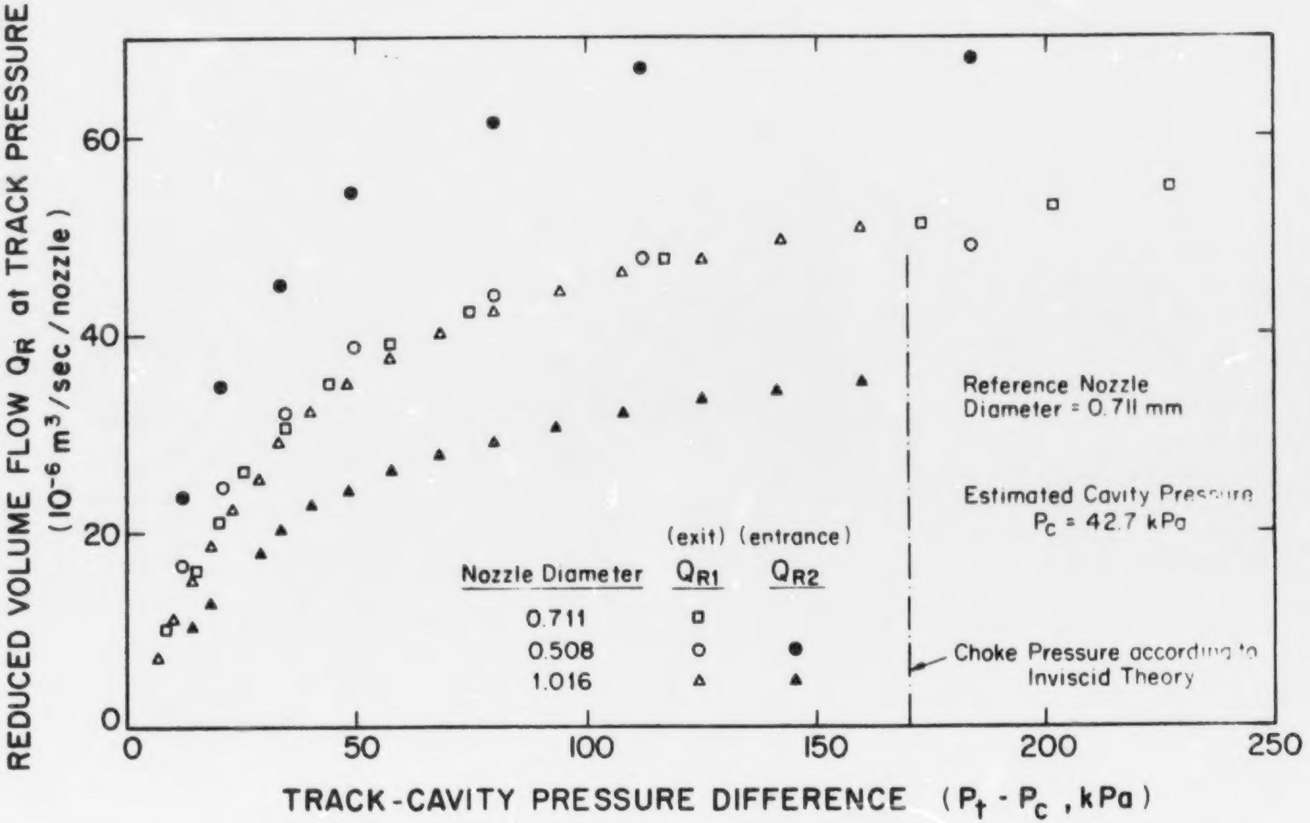

Figure 0.4 Effect of track pressure on reduced volume flows for radial nozzles covered by a shoe.

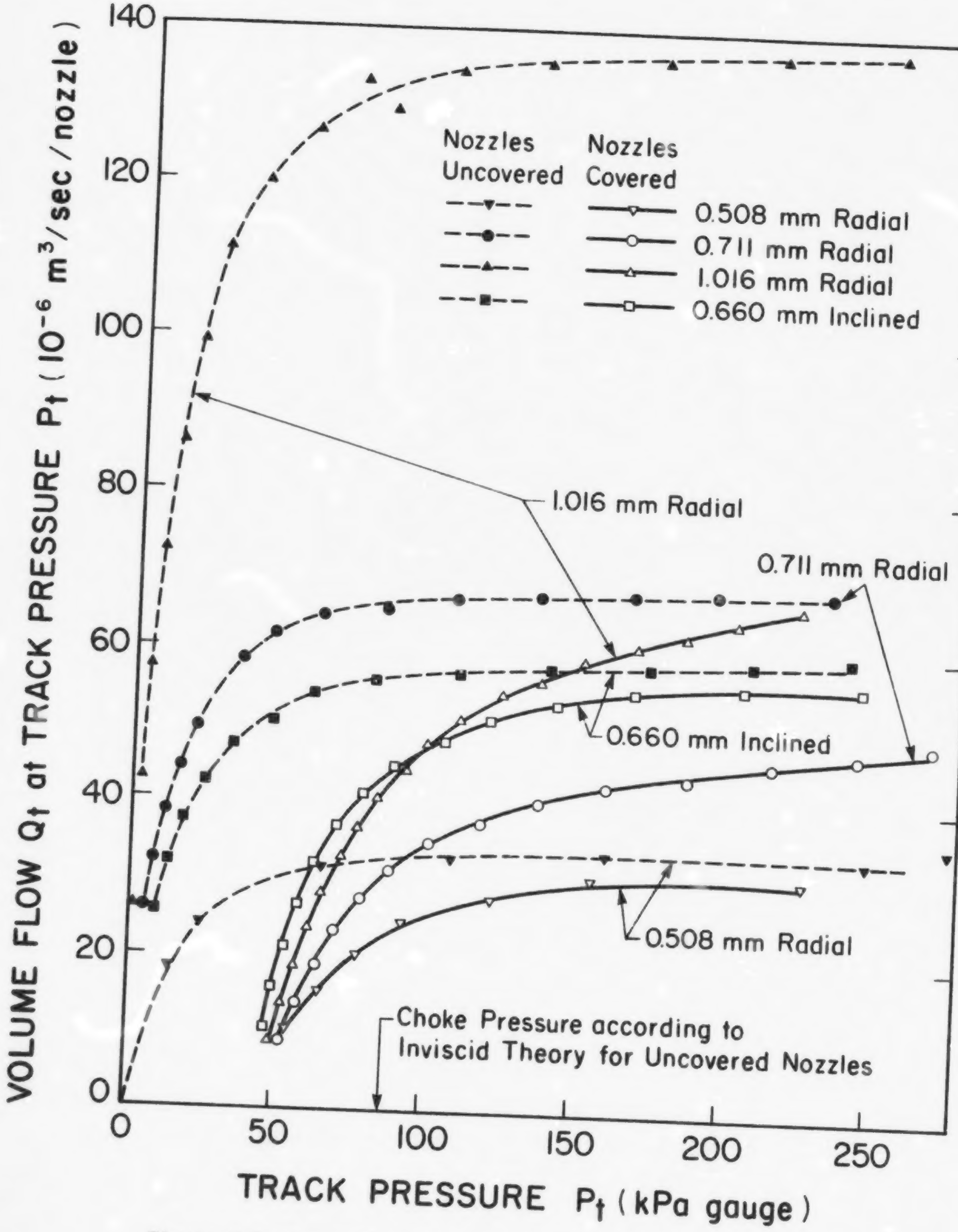

Figure 0.5 Comparison of covered and uncovered flow rates for radial nozzles, and with inclined nozzle data of Figure 0.2.

moved. This fraction depends on the application and may vary from a low of about 50% for warehouse storage and retrieval systems to perhaps 95% and more for passenger transporters. Hence the choking of the inclined nozzles at the entrance has considerable practical significance. For example the data in Figure 0.5 shows that at a typical operating p_{tg} = 140 kPa (20.3 psig) the 0.66 mm inclined nozzle delivers about 53 μm^3/sec, or 1.50×10^{-4} kg/sec at a room temperature of 22°C. To obtain equivalent performance by using either the 1.016 mm or 0.711 mm nozzles, the same mass flow has to be delivered. The data in Figure 05 shows that the 1.016 mm nozzle delivers the required mass flow at a slightly lower p_{tg} (130 kPa). However its uncovered $\dot{m}$ at this pressure is 3.67×10^{-4} kg/sec. This corresponds to a 65% increase in air consumption for 50% track occupancy, and to a 113% increase for a 10% occupancy.

This penalty is reduced but not eliminated by using the 0.711 mm radial nozzles because, in addition to unchoking when not covered by the shoe, they must operate at a subtantially higher p_{tg} to obtain the requisite mass flow for levitation. The data in Figure 0.5 shows that, since $\dot{m}_t = p_t Q_t/(RT_t)$, the 0.711 mm nozzles require p_t = 190 kPa and Q_t = 44.0 μm^3/sec to produce the same mass flow. Also, in making comparisons of performance at different p_{tg}, since air delivered at higher p_{tg} requires more work to compress it before delivery, the appropriate comparison index is the power consumption. That is, to the flow power $P_f = (p_t - p_a)Q_t$ one must add the power P_c required to raise its pressure from p_a to p_t. The actual value of P_c depends on the details of the compression process, but for insight purposes, here we assume a single stage compression following the law p/ρ^n = const with $n = 1.2$. It can readily be shown that

$$\frac{P_c}{P_f} = \frac{[\xi + n - 1 - n\xi^{1/n}]}{(n-1)(\xi-1)} \tag{0.6}$$

where ξ is the ratio of absolute pressures; $\xi = (p_{tg} + p_a)/p_a$. For an 0.66 mm inclined nozzle, when operating at p_{tg} = 140 kPa, P_c/P_f = 0.396 and the power is 10.4 Watts/nozzle covered and 11.2 Watts/nozzle uncovered. For the 0.711 mm radial nozzle operating at p_{tg} = 188 kPa, P_c/P_f = 0.486 so that the power for the covered case is 12.3 Watts/nozzle, and rises to 18.7 Watts/nozzle when uncovered. Hence the power penalty is 44% at 50% track coverage and 62% at 10% coverage.

It is interesting to speculate on the consequences of making radial nozzles choke at the entrance. Presumably this can be achieved by reducing their diameter while increasing the number so that the total cross sectional area is maintained, or by contouring as suggested in Appendix B. However contrary to the inferences to be made from Appendix B, because the flow inside the nozzle then becomes supersonic, substantial hydrodynamic losses might be incurred. A stagnation region has to form at the nozzle exit as part of the process of turning the flow into the cavity region and this must therefore be accompanied by strong shock waves as shown in Figure 0.6. It is also possible that the hydrodynamic losses associated with supersonic flow in the inclined nozzles could be much less because the fluid has only to turn through a very shallow angle, and could therefore involve much weaker inclined shock waves. This speculation about an additional unenvisaged benefit of using inclined nozzles underscores the need for a detailed investigation of compressibility effects in any future work.

Finally, note that owing to the work required to compress air, current designs incur a substantial power penalty by delivering the air to the nozzles at a pressure which is much higher than that needed to lift the load. To illustrate this, assume that the maximum cavity pressure p_{cg} = 50 kPa and that the nozzle diameter is increased sufficiently to incur only a 1 kPa pressure drop from rail to shoe cavity, that is, with $(p_{tg} - p_{cg})$ = 1 kPa. For the standard SailRail nozzle $\dot{m} \simeq 1.50\times10^{-4}$ kg/sec. At $p_{tg} = 51$ kPa the air density is $\rho_t = 1.78$ kg/m^3 at 22°C so $Q_t = \dot{m}/\rho_t = 84.2$ µm^3/sec, and the compression work is $P_c/P_w = 0.179$. Hence the power is 5.02 W/nozzle, or about half that at $p_{tg} = 140$ kPa. The nozzle diameter required to achieve this can be determineed directly from the data in Appendix B, since the flow process from track to cavity will be effectively incompressible. From equations B3 and B4,

$$d = [(4Q_t)/(\pi V_{ref} C_{Q1})]^{1/2} \qquad (0.7)$$

where

$$V_{ref} = [2(p_t - p_c)/\rho_t]^{1/2}$$

The data in Figure B.7 can be used to choose C_{Q1}, however this is dependent on the local cavity height h_c through the ratio h/d, which is initially unknown. A trial and error process assuming h_c = 0.25 mm gives C_{Q1} = 0.61 and d = 2.30 mm.

For SailRail applications in which the lift air is not generated on board the moving element, the air power requirements are already so low that the economics of compressing the air at one station and distributing it to its points of application may dictate the use of a relatively high p_{tg}. But even if this was not the case, at low p_{tg} the inclined nozzles will not be choked, and will incur a power penalty when uncovered. Because their diameter is large the penalty can be substantial. Using the data in Figure 0.2 for the 0.66 mm nozzle at p_{tg} = 51 kPa, and scaling in proportion to nozzle area, Q_t = 632 µm^3/sec. The corresponding power for an uncovered 2.30 mm nozzle will be 38 W/nozzle, an increase by a factor of 3.4. This result is, however, very sensitive to the value of $p_t - p_c$. If $p_t - p_c$ = 10 kPa and p_{cg} = 50 kPa, the above calculation gives d = 1.23 mm (0.048"), and a covered and uncovered power of 5.75 and 11.9 W/nozzle respectively. The latter power is about the same as that for the uncovered 0.66 mm nozzle.

From this discussion and the results of Appendix B one can draw the following conclusions about the relative merits of inclined and radial nozzles. When the lift air is to be compressed onboard the moving element, nozzles will normally be covered so that p_t should be kept as low as possible and contoured radial nozzles should be used to minimize power. For applications which involve significant amounts of air flow through uncovered nozzles, if the economics of the air supply system and the range of loads to be transported do not dictate otherwise, $p_t - p_c$ should be kept at a minimum of about 10 kPa, and contoured radial nozzles should also be used. However if p_t is to be kept at the levels currently used in practice, the use of inclined nozzles should continue.

APPENDIX P. COMPUTER LISTING FOR PROGRAMME USED IN APPENDIX K

```
FORTRAN IV G1  RELEASE 2.0             MAIN                DATE = 82217          19/42/03              PAGE 0001
                 C
                 C
                 C     HYDROSTATIC LUBRICATION ANALYSIS OF THE 'SAILRAIL'
                 C     COMPLIANT SURFACE AIR BEARING.
                 C
                 C
                 C     GOVERNING DIFFERENTIAL EQUATION:
                 C     REYNOLDS EQUATION FOR PRESSURE.
                 C     COLUMN MODEL FOR SHOE.
                 C     ORIFICE MODEL FOR NOZZLE.
                 C
                 C
                 C     A FINITE ELEMENT METHOD IS USED TO REDUCE THE GOVERNING EQUATION
                 C     TO A SYSTEM OF ALGEBRAIC EQUATIONS.
                 C
                 C     ALGEBRAIC EQUATION SYSTEM SOLVED USING GAUSS SEIDEL ITERATION.
                 C
                 C
 0001                  COMMON/NUM/NP,NE,NBAND,NODE,NIP
 0002                  COMMON/CYCLE/NPRINT,ICYCLE,JCYCLE
 0003                  COMMON/NODE/COORD(1500,2),NFIX(1500)
 0004                  COMMON/SQUARE/ALPHA(6),WF(6),NCP(500,9)
 0005                  COMMON/GAP/H(1500),SK(1500),HSET,SKSET
 0006                  COMMON/PARM/VISL,POW,PATM,PTRACK,PLAST
 0007                  COMMON/JET/FJET,CDO,CDH
 0008                  COMMON/RESULT/P(1500)
 0009                  COMMON/MATRIX/GM(1500,27),EM(8,8),R(1500),EP(8),ISP(1500,27)
 0010                  COMMON/SHAPE/EF(8,6,6),DEFA(8,6,6),DEFB(8,6,6)
 0011                  COMMON/SAIL/NFLD,NELA,NELB,NELC,NELD,NI,NJ
 0012                  COMMON/RAIL/X(10),Y(13),DX(9),DY(12)
 0013                  COMMON/ZER/XZERO(21),YZERO(21),NCPZ(8,8),NZERO(5),MZERO(5)
 0014                  COMMON/ON/XONE(40),YONE(40),NCPO(8,8),NONE(5),MONE(5)
 0015                  COMMON/FLOW/DEFASQ(8,8),DEFBSQ(8,8)
 0016                  COMMON/SOURCE/XS(4),YS(4)
                 C
                 C
                 C     DATA.
 0017                  CALL INFO
                 C
                 C     STARTING VALUES FOR ITERATION.
 0018                  CALL GUESS
                 C
 0019                  I=0
 0020                  J=0
 0021                  NLIM=10
 0022                  NPRINT=5
 0023                  NLIM=12
 0024                  NPRINT=4
                 C
 0025                  PLAST=PTRACK
                 C
                 C     ITERATION.
 0026               10 CONTINUE
 0027                  I=I+1
 0028                  J=J+1
 0029                  ICYCLE=I
 0030                  JCYCLE=J
                 C
```

```
FORTRAN IV G1  RELEASE 2.0             MAIN                DATE = 82217          19/42/03              PAGE 0002
                 C     FORMATION OF GLOBAL MATRIX.
 0031                  CALL GLOBAL
                 C
                 C     ALGEBRAIC EQUATION SYSTEM SOLUTION BY GAUSS SEIDEL ITERATION.
 0032                  CALL SEIDEL
                 C
                 C     GAP.
 0033                  DO 1 K=1,NP
 0034                  H(K)=(P(K)-PATM)/SK(K)+HSET
 0035                1 CONTINUE
                 C
 0036                  IF(J.EQ.NPRINT) CALL PRINT
 0037                  IF(J.EQ.NPRINT) J=0
 0038                  IF(I.LT.NLIM) GO TO 10
                 C
 0039                  CALL GRAPH
                 C
                 C
 0040                  STOP
 0041                  END
```

```
FORTRAN IV G1  RELEASE 2.0          INFO             DATE = 82217        19/42/03              PAGE 0001
                  SUBROUTINE INFO
            C
            C     DATA.
            C
            C
                  COMMON/NUM/NP,NE,NBAND,NODE,NIP
                  COMMON/NODE/COPD(1500,2),NFIX(1500)
                  COMMON/SQUARE/ALPHA(6),WF(6),NOP(500,9)
                  COMMON/SHAPE/FF(8,6,6),DEFA(8,6,6),DEFB(8,6,6)
                  COMMON/GAP/H(1500),SK(1500),HSET,SKSET
                  COMMON/PARM/VISL,ROW,PATM,PTFACK,PLAST
                  COMMON/JET/RJET,CDO,CDH
                  COMMON/SAIL/NELD,NELA,NELB,NELC,NELD,NI,NJ
                  COMMON/RAIL/X(10),Y(13),DX(9),DY(12)
                  COMMON/ZER/XZERO(21),YZERO(21),NOPZ(4,8),NZERO(5),MZERO(5)
                  COMMON/ON/XONE(40),YONE(40),NOPO(8,8),NONE(5),MONE(5)
                  COMMON/FLOW/DEFASO(8,8),DEFBSO(8,8)
                  COMMON/SOURCE/XS(4),YS(4)
                  DIMENSION NOPG(9,12),NOA(12),NOB(12),NOC(12),NIJ(4,2)
                  DIMENSION AA(8),BB(8)
            C
            C
                  PI=3.14159
            C
                  WRITE(6,50000)
            C
            C     CONTROL DATA.
                  READ(5,100) NP,NE,NBAND,NODE,NIP
                  WRITE(6,100) NP,NE,NBAND,NODE,NIP
            C
            C     PARAMETERS.
                  READ(5,200) VISL,PATM,PTFACK,HSET,SKSET,ROW
                  WRITE(6,200) VISL,PATM,PTFACK,HSET,SKSET,ROW
                  ROW=PTFACK/PATM*ROW
                  READ(5,222) RJET,CDO,CDH
                  WRITE(6,222) RJET,CDO,CDH
            C
            C     DATA FOR NUMERICAL INTEGRATION.
                  READ(5,300)  (WF(I),I=1,NIP)
                  WRITE(6,300) (WF(I),I=1,NIP)
                  READ(5,300)  (ALPHA(I),I=1,NIP)
                  WRITE(6,300) (ALPHA(I),I=1,NIP)
                  READ(5,444)  (AA(I),I=1,NODE)
                  WRITE(6,444)  (AA(I),I=1,NODE)
                  READ(5,444)  (BB(I),I=1,NODE)
                  WRITE(6,444)  (BB(I),I=1,NODE)
            C
            C
            C     MACRO-ELEMENT DATA.
            C
                  WRITE(6,10000)
                  READ(5,100) NI,NJ,NHOLE
                  WRITE(6,100) NI,NJ,NHOLE
                  READ(5,300)  (DX(I),I=1,NI)
                  WRITE(6,300) (DX(I),I=1,NI)
                  READ(5,300)  (DY(J),J=1,NJ)
                  WRITE(6,300) (DY(J),J=1,NJ)
```

```
FORTRAN IV G1  RELEASE 2.0          INFO             DATE = 82217        19/42/03              PAGE 0002
                  READ(5,300)  (XZERO(I),I=1,21)
                  WRITE(6,300) (XZERO(I),I=1,21)
                  READ(5,300)  (YZERO(I),I=1,21)
                  WRITE(6,300) (YZERO(I),I=1,21)
                  READ(5,300)  (XONE(I),I=1,40)
                  WRITE(6,300) (XONE(I),I=1,40)
                  READ(5,300)  (YONE(I),I=1,40)
                  WRITE(6,300) (YONE(I),I=1,40)
                  READ(5,100)  (NZERO(I),I=1,5)
                  WRITE(6,100) (NZERO(I),I=1,5)
                  READ(5,100)  (MZERO(I),I=1,5)
                  WRITE(6,100) (MZERO(I),I=1,5)
                  READ(5,100)  (NONE(I),I=1,5)
                  WRITE(6,100) (NONE(I),I=1,5)
                  READ(5,100)  (MONE(I),I=1,5)
                  WRITE(6,100) (MONE(I),I=1,5)
                  READ(5,400)  ((NIJ(K,L),L=1,2),K=1,NHOLE)
                  WRITE(6,400) ((NIJ(K,L),L=1,2),K=1,NHOLE)
                  READ(5,400)  ((NOPZ(N,K),K=1,8),N=1,4)
                  WRITE(6,400) ((NOPZ(N,K),K=1,8),N=1,4)
                  READ(5,400)  ((NOPO(N,K),K=1,8),N=1,8)
                  WRITE(6,400) ((NOPO(N,K),K=1,8),N=1,8)
              100 FORMAT(10X,5I5)
              200 FORMAT(10X,6E10.3)
              222 FORMAT(10X,3E10.3)
              300 FORMAT(10X,6F10.5)
              400 FORMAT(10X,8I5)
              444 FORMAT(10X,8F5.2)
            10000 FORMAT(1X,/,20X,'MACRO-ELEMENT DATA')
            50000 FORMAT(1X,/,20X,'GENERAL DATA')
            C
            C
            C
            C     GENERATED DATA.
            C
                  DO 5 I=1,NI
                  DO 5 J=1,NJ
                  NOPG(I,J)=0
                5 CONTINUE
                  DO 10 K=1,NHOLE
                  I=NIJ(K,1)
                  J=NIJ(K,2)
                  NOPG(I,J)=1
               10 CONTINUE
                  NIPO=NI+1
                  NJPO=NJ+1
                  X(1)=0.0
                  Y(1)=0.0
                  DO 25 I=2,NIPO
                  X(I)=X(I-1)+DX(I-1)
               25 CONTINUE
                  DO 50 J=2,NJPO
                  Y(J)=Y(J-1)+DY(J-1)
               50 CONTINUE
                  DO 1 J=1,NJ
                  NU=0
                  DO 7 I=1,NI
                  NU=NU+NOPG(I,J)
                7 CONTINUE
               NUC=NI-NB
               NOA(J)=NB*4+1
               NOB(J)=NB*4+NUC*2+1
               NOC(J)=NB*19+NUC*4+1
             1 CONTINUE
               NE=0
               KOP=1
               NFLD=1
               DO 4 J=1,NJ
               NELA=NFLD+NOA(J)
               NELB=NELA+NOB(J)
               NELC=NELB+NOC(J)
               NELD=NELC+NOB(J)
               DO 3 I=1,NI
               IF(NOPG(I,J).EQ.0) CALL ZERO(I,J)
               IF(NOPG(I,J).EQ.1) CALL ONE(I,J,KOP)
               IF(NOPG(I,J).EQ.1) GO TO 2
               NFLD=NFLD+4
               NELA=NELA+2
               NELB=NELB+4
               NELC=NELC+2
               NELD=NELD+4
               GO TO 3
             2 CONTINUE
               NFLD=NFLD+4
               NELA=NELA+4
               NELB=NELB+10
               NELC=NELC+4
               NELD=NELD+4
             3 CONTINUE
               NFLD=NELC+1
             4 CONTINUE
               NP=NELD
         C
               DO 15 I=1,NIP
               A=ALPHA(I)
               DO 15 J=1,NIP
               B=ALPHA(J)
               FP(1,I,J)=1./4.*(1.-A)*(1.-B)*(-A-B-1.)
               FP(3,I,J)=1./4.*(1.-A)*(1.+B)*(-A+B-1.)
               FP(6,I,J)=1./4.*(1.+A)*(1.-B)*(A-B-1.)
               FP(8,I,J)=1./4.*(1.+A)*(1.+B)*(A+B-1.)
               FP(4,I,J)=1./2.*(1.-A*A)*(1.-B)
               FP(5,I,J)=1./2.*(1.-A*A)*(1.+B)
               FP(2,I,J)=1./2.*(1.-A)*(1.-B*B)
               FP(7,I,J)=1./2.*(1.+A)*(1.-B*B)
               DEFA(1,I,J)=-1./4.*(1.-B)*((-A-B-1.)+(1.-A))
               DEFB(1,I,J)=-1./4.*(1.-A)*((-A-B-1.)+(1.-B))
               DEFA(3,I,J)=-1./4.*(1.+B)*((-A+B-1.)+(1.-A))
               DEFB(3,I,J)=1./4.*(1.-A)*((-A+B-1.)+(1.+B))
               DEFA(6,I,J)=1./4.*(1.-B)*((A-B-1.)+(1.+A))
               DEFB(6,I,J)=-1./4.*(1.+A)*((A-B-1.)+(1.-B))
               DEFA(8,I,J)=1./4.*(1.+B)*((A+B-1.)+(1.+A))
               DEFB(8,I,J)=1./4.*(1.+A)*((A+B-1.)+(1.+B))
               DEFA(4,I,J)=-A*(1.-B)
               DEFB(4,I,J)=-1./2.*(1.-A*A)
               DEFA(5,I,J)=-A*(1.+B)
               DEFB(5,I,J)=1./2.*(1.-A*A)
```

```
               DEFA(2,I,J)=-1./2.*(1.-B*B)
               DEFB(2,I,J)=-B*(1.-A)
               DEFA(7,I,J)=1./2.*(1.-B*B)
               DEFB(7,I,J)=-B*(1.+A)
            15 CONTINUE
               DO 555 I=1,NODE
               A=AA(I)
               B=BB(I)
               DEFASC(1,I)=-1./4.*(1.-B)*((-A-B-1.)+(1.-A))
               DEFBSC(1,I)=-1./4.*(1.-A)*((-A-B-1.)+(1.-B))
               DEFASC(3,I)=-1./4.*(1.+B)*((-A+B-1.)+(1.-A))
               DEFBSC(3,I)=1./4.*(1.-A)*((-A+B-1.)+(1.+B))
               DEFASC(6,I)=1./4.*(1.-B)*((A-B-1.)+(1.+A))
               DEFBSC(6,I)=-1./4.*(1.+A)*((A-B-1.)+(1.-B))
               DEFASC(8,I)=1./4.*(1.+B)*((A+B-1.)+(1.+A))
               DEFBSC(8,I)=1./4.*(1.+A)*((A+B-1.)+(1.+B))
               DEFASC(4,I)=-A*(1.-B)
               DEFBSC(4,I)=-1./2.*(1.-A*A)
               DEFASC(5,I)=-A*(1.+B)
               DEFBSC(5,I)=1./2.*(1.-A*A)
               DEFASC(2,I)=-1./2.*(1.-B*B)
               DEFBSC(2,I)=-B*(1.-A)
               DEFASC(7,I)=1./2.*(1.-B*B)
               DEFBSC(7,I)=-B*(1.+A)
           555 CONTINUE
         C
               DO 1000 I=1,NP
               SK(I)=SKSET
          1000 CONTINUE
         C
               WRITE(6,500)
           500 FORMAT(1X,/,20X,'GENERATED DATA')
               DO 2000 I=1,NP
               WRITE(6,747) I,NFIX(I),SK(I),CORD(I,1),CORD(I,2)
          2000 CONTINUE
           747 FORMAT(10X,2I5,10X,3(E12.5,5X))
               DO 5000 I=1,NE
               WRITE(6,707) I,(NOP(I,K),K=1,9)
          5000 CONTINUE
           707 FORMAT(10X,10I5)
         C
         C
               RETURN
               END
```

```
FORTRAN IV G1  RELEASE 2.0           ZERO            DATE = 82217          19/42/03          PAGE 0001

            SUBROUTINE ZERO(I,J)
C
C
C           MACRO-ELEMENT WITHOUT SOURCES.
C
C
            COMMON/NUM/NP,NE,NBAND,NODE,NIP
            COMMON/NODE/CORD(1500,2),NFIX(1500)
            COMMON/SQUARE/ALPHA(6),WF(6),NOP(500,9)
            COMMON/SAIL/NFLD,NELA,NELB,NELC,NELD,NI,NJ
            COMMON/RAIL/X(10),Y(13),DX(9),DY(12)
            COMMON/ZER/XZERO(21),YZERO(21),NOPZ(4,8),NZERO(5),MZERO(5)
            DIMENSION NHL(21)
C
C
            DO 10 K=1,21
            IF(K.LE.5)
           *NHL(K)=NFLD+K-1
            IF(K.GT.5.AND.K.LE.8)
           *NHL(K)=NELA+K-6
            IF(K.GT.8.AND.K.LE.13)
           *NHL(K)=NELB+K-9
            IF(K.GT.13.AND.K.LE.16)
           *NHL(K)=NELC+K-14
            IF(K.GT.16)
           *NHL(K)=NELD+K-17
         10 CONTINUE
            DO 50 N=1,4
            NOP(NE+N,9)=0
            DO 50 M=1,8
            NOP(NE+N,M)=NHL(NOPZ(N,M))
         50 CONTINUE
            NE=NE+4
            KKO=4
            IF(J.EQ.NJ) KKO=5
            DO 100 KK=1,KKO
            KO=MZERO(KK)-1
            IF(I.EQ.NI) KO=MZERO(KK)
            KS=NZERO(KK)
            DO 100 K=KS,KO
            NIT=NHL(K)
            CORD(NIT,1)=X(I)+XZERO(K)*DX(I)
            CORD(NIT,2)=Y(J)+YZERO(K)*DY(J)
            NFIX(NIT)=0
            IF(J.EQ.1.AND.K.LT.5) NFIX(NIT)=2
            IF(J.EQ.1.AND.K.LT.5) GO TO 100
            IF(J.EQ.NJ.AND.K.LT.21.AND.K.GE.17) NFIX(NIT)=2
            IF(J.EQ.NJ.AND.K.LT.21.AND.K.GE.17) GO TO 100
            IF(I.EQ.1.AND.K.EQ.KS) NFIX(NIT)=2
            IF(I.EQ.1.AND.K.EQ.KS) GO TO 100
            IF(I.EQ.NI.AND.K.EQ.KO) NFIX(NIT)=2
        100 CONTINUE
C
C
            RETURN
            END
```

```
FORTRAN IV G1  RELEASE 2.0           ONE             DATE = 82217          19/42/03          PAGE 0001

            SUBROUTINE ONE(I,J,KOP)
C
C
C           MACRO-ELEMENT WITH ONE PRESSURE SOURCE.
C
C
            COMMON/NUM/NP,NE,NBAND,NODE,NIP
            COMMON/NODE/CORD(1500,2),NFIX(1500)
            COMMON/SQUARE/ALPHA(6),WF(6),NOP(500,9)
            COMMON/SAIL/NFLD,NELA,NELB,NELC,NELD,NI,NJ
            COMMON/RAIL/X(10),Y(13),DX(9),DY(12)
            COMMON/ON/XONE(40),YONE(40),NOPO(8,8),NONE(5),MONE(5)
            COMMON/SOURCE/XS(4),YS(4)
            DIMENSION NHL(40)
C
C
            DO 10 K=1,40
            IF(K.LE.5)
           *NHL(K)=NFLD+K-1
            IF(K.GT.5.AND.K.LE.10)
           *NHL(K)=NELA+K-6
            IF(K.GT.10.AND.K.LE.30)
           *NHL(K)=NELB+K-11
            IF(K.GT.30.AND.K.LE.35)
           *NHL(K)=NELC+K-31
            IF(K.GT.35)
           *NHL(K)=NELD+K-36
         10 CONTINUE
            DO 50 N=1,8
            NOP(NE+N,9)=KOP
            DO 50 M=1,8
            NOP(NE+N,M)=NHL(NOPO(N,M))
         50 CONTINUE
            NE=NE+8
            KKO=4
            DO 100 KK=1,KKO
            KO=MONE(KK)-1
            KS=NONE(KK)
            DO 100 K=KS,KO
            NIT=NHL(K)
            CORD(NIT,1)=X(I)+XONE(K)*DX(I)
            CORD(NIT,2)=Y(J)+YONE(K)*DY(J)
            NFIX(NIT)=0
            IF(K.GT.13.AND.K.LE.28) NFIX(NIT)=1
        100 CONTINUE
            XS(KOP)=X(I)+DX(I)/2.0
            YS(KOP)=Y(J)+DY(J)/2.0
            KOP=KOP+1
C
C
            RETURN
            END
```

```
FORTRAN IV G1  RELEASE 2.0          GUESS            DATE = 82217          19/42/03              PAGE 0001
                           SUBROUTINE GUESS
                 C
                 C
                 C         STARTING VALUES FOR ITERATION.
                 C
                 C
                           COMMON/NUM/NP,NE,NBAND,NODE,NIP
                           COMMON/PARM/VISL,POW,PATM,PTBACK,PLAST
                           COMMON/GAP/H(1500),SK(1500),HSET,SKSET
                           COMMON/RESULT/P(1500)
                 C
                 C
                           DO 10 I=1,NP
                           P(I)=PATM
                           P(I)=PTBACK
                           H(I)=(P(I)-PATM)/SK(I)+HSET
                        10 CONTINUE
                 C
                 C
                           RETURN
                           END
```

```
FORTRAN IV G1  RELEASE 2.0          PRINT            DATE = 82217          19/42/03              PAGE 0001
                           SUBROUTINE PRINT
                 C
                 C
                 C         OUTPUT.
                 C
                 C
                           COMMON/NUM/NP,NE,NBAND,NODE,NIP
                           COMMON/MODE/CORD(1500,2),NFIX(1500)
                           COMMON/GAP/H(1500),SK(1500),HSET,SKSET
                           COMMON/RESULT/P(1500)
                 C
                 C
                           WRITE(6,10)
                        10 FORMAT('1',/,10X,'PRESSURE PROFILES')
                           DO 1000 I=1,NP
                           WRITE(6,100) I,NFIX(I),P(I),H(I),CORD(I,1),CORD(I,2)
                      1000 CONTINUE
                       100 FORMAT(10X,2I5,10X,4(E12.5,5X))
                 C
                 C
                           RETURN
                           END
```

```
FORTRAN IV G1  RELEASE 2.0          GLOBAL             DATE = 82217          19/42/03              PAGE 0001
 0001                      SUBROUTINE GLOBAL
                   C
                   C
                   C       FORMATION OF GLOBAL MATRIX.
                   C
                   C
 0002                      COMMON/NUM/NP,NE,NBAND,NODE,NIP
 0003                      COMMON/CYCLE/NPRINT,ICYCLE,JCYCLE
 0004                      COMMON/NODE/CORD(1500,2),NFIX(1500)
 0005                      COMMON/SQUARE/ALPHA(6),WF(6),NOP(500,9)
 0006                      COMMON/GAP/H(1500),SR(1500),HSET,SKSET
 0007                      COMMON/PARM/VISL,ROW,PATM,PTRACK,PLAST
 0008                      COMMON/JET/FJET,CDO,CDH
 0009                      COMMON/RESULT/P(1500)
 0010                      COMMON/MATRIX/GM(1500,27),EM(8,8),R(1500),ER(8),ISP(1500,27)
 0011                      COMMON/SHAPE/EF(8,6,6),DEFA(8,6,6),DEFB(8,6,6)
 0012                      COMMON/FLOW/DEFASO(6,8),DEFBSO(6,8)
 0013                      COMMON/SOURCE/IS(4),YS(4)
 0014                      DIMENSION SF(1500)
                   C
                   C
 0015                      DO 1 I=1,NP
 0016                      DO 2 J=1,NBAND
 0017                      GM(I,J)=0.0
 0018                      ISP(I,J)=0
 0019                    2 CONTINUE
 0020                      ISP(I,1)=I
 0021                      R(I)=0.0
 0022                      SF(I)=0.0
 0023                    1 CONTINUE
                   C
 0024                      DO 10 N=1,NE
 0025                      CALL LOCAL(N)
 0026                      DO 10 I=1,NODE
 0027                      NROW=NOP(N,I)
 0028                      DO 20 J=1,NODE
 0029                      NCOL=NOP(N,J)
 0030                      DO 5 M=1,NBAND
 0031                      IF(ISP(NROW,M)-NCOL) 6,7,6
 0032                    6 IF(ISP(NROW,M)) 8,8,5
 0033                    5 CONTINUE
 0034                    8 CONTINUE
 0035                      ISP(NROW,M)=NCOL
 0036                    7 CONTINUE
 0037                      GM(NROW,M)=GM(NROW,M)+EM(I,J)
 0038                   20 CONTINUE
 0039                      SR(NROW)=SR(NROW)+ER(I)
 0040                   10 CONTINUE
                   C
 0041                      CD=CDO
 0042                      ROP=0.0
 0043                      DO 50 I=1,NP
 0044                      IF(NFIX(I).EQ.0) GO TO 50
 0045                      RO=PLAST
 0046                      IF(NFIX(I).EQ.1.AND.JCYCLE.EQ.NPRINT)
                          *RO=PTRACK-CD*0.5*ROW*SR(I)*ABS(SR(I))
 0047                      IF(NFIX(I).EQ.1) ROP=ROP+RO
 0048                      IF(NFIX(I).EQ.2) RO=PATM
```

```
FORTRAN IV G1  RELEASE 2.0          GLOBAL             DATE = 82217          19/42/03              PAGE 0002
 0049                      DO 25 J=2,NBAND
 0050                      GM(I,J)=0.0
 0051                   25 CONTINUE
 0052                      GM(I,1)=1.0
 0053                      R(I)=RO
 0054                   50 CONTINUE
                   C
 0055                      PAVG=ROP/16./4.
 0056                      PAVG=(PAVG+PLAST)/2.
 0057                      SCALE=(PAVG-PATM)/(PLAST-PATM)
 0058                      DO 500 I=1,NP
 0059                      P(I)=PATM+(P(I)-PATM)*SCALE
 0060                      IF(NFIX(I).EQ.1) P(I)=PAVG
 0061                  500 CONTINUE
 0062                      PLAST=PAVG
                   C
                   C
 0063                      RETURN
 0064                      END
```

```
FORTRAN IV G1  RELEASE 2.0          SEIDEL         DATE = 82217        19/42/03            PAGE 0001
 0001                SUBROUTINE SEIDEL
               C
               C
               C     ALGEBRAIC EQUATION SYSTEM SOLUTION BY GAUSS SEIDEL ITERATION.
               C
 0002                COMMON/NUM/NP,NE,NBAND,NODE,NIP
 0003                COMMON/RESULT/P(1500)
 0004                COMMON/MATRIX/GM(1500,27),EM(8,8),R(1500),ER(8),ISP(1500,27)
 0005                DIMENSION POLD(1500)
               C
               C
               C     RELAXATION COEFFICIENT.
 0006                RELAX=1.0
               C
               C     NUMBER OF OFF-DIAGONAL TERMS.
 0007                DO 1 N=1,NP
 0008                DO 2 M=1,NBAND
 0009                IF(ISP(N,M).NE.0) GO TO 2
 0010                ISP(N,1)=M-1
 0011                GO TO 1
 0012              2 CONTINUE
 0013              1 CONTINUE
               C
               C     NUMBER OF CYCLES.
 0014                NMAX=250
               C
               C     STORING ESTIMATE OF PRESSURE.
 0015                DO 10 N=1,NP
 0016                POLD(N)=P(N)
 0017             10 CONTINUE
               C
               C     LOOP ON CYCLES.
 0018                DO 500 NLOOP=1,NMAX
               C     LOOP ON EQUATIONS.
 0019                DO 700 N=1,NP
 0020                PX=P(N)
 0021                NCM=ISP(N,1)
 0022                DO 707 M=2,NCM
 0023                L=ISP(N,M)
 0024                PX=PX-GM(N,M)*P(L)
 0025            707 CONTINUE
 0026                DOG=PX/GM(N,1)
 0027                P(N)=POLD(N)*(1.-RELAX)+RELAX*DOG
 0028            700 CONTINUE
 0029            500 CONTINUE
               C
               C
 0030                RETURN
 0031                END
```

```
FORTRAN IV G1  RELEASE 2.0          LOCAL          DATE = 82217        19/42/03            PAGE 0001
 0001                SUBROUTINE LOCAL(N)
               C
               C
               C     ELEMENT CONTRIBUTIONS TO GLOBAL MATRIX.
               C
               C
 0002                COMMON/NUM/NP,NE,NBAND,NODE,NIP
 0003                COMMON/NODE/CORD(1500,2),NFIX(1500)
 0004                COMMON/SQUARE/ALPHA(6),WF(6),NOP(500,9)
 0005                COMMON/GAP/H(1500),SK(1500),HSET,SKSET
 0006                COMMON/PARM/VISL,ROW,PATM,PTRACK,PLAST
 0007                COMMON/JET/PJET,CDO,CDH
 0008                COMMON/RESULT/P(1500)
 0009                COMMON/MATRIX/GM(1500,27),EM(8,8),R(1500),ER(8),ISP(1500,27)
 0010                COMMON/SHAPE/FP(8,6,6),DEPA(8,6,6),DEPB(8,6,6)
 0011                COMMON/FLOW/DEPASO(8,8),DEPBSO(8,8)
 0012                COMMON/SOURCE/XS(4),YS(4)
 0013                DIMENSION DXDA(6,6),DXDB(6,6),DYDA(6,6),DYDB(6,6)
 0014                DIMENSION DETJ(6,6),DJII(6,6),DJIJ(6,6),DJJI(6,6),DJJJ(6,6)
 0015                DIMENSION DXDAN(8),DXDBN(8),DYDAN(8),DYDBN(8)
 0016                DIMENSION DETN(8),DNII(8),DNIJ(8),DNJI(8),DNJJ(8)
               C
               C
 0017                DO 1 I=1,NODE
 0018                DO 2 J=1,NODE
 0019                EM(I,J)=0.0
 0020              2 CONTINUE
 0021                ER(I)=0.0
 0022              1 CONTINUE
               C
 0023                DO 100 I=1,NIP
 0024                DO 100 J=1,NIP
 0025                DXDA(I,J)=0.0
 0026                DXDB(I,J)=0.0
 0027                DYDA(I,J)=0.0
 0028                DYDB(I,J)=0.0
 0029            100 CONTINUE
 0030                DO 500 I=1,NIP
 0031                DO 500 J=1,NIP
 0032                DO 500 K=1,NODE
 0033                M=NOP(N,K)
 0034                DXDA(I,J)=DXDA(I,J)+DEPA(K,I,J)*CORD(M,1)
 0035                DXDB(I,J)=DXDB(I,J)+DEPB(K,I,J)*CORD(M,1)
 0036                DYDA(I,J)=DYDA(I,J)+DEPA(K,I,J)*CORD(M,2)
 0037                DYDB(I,J)=DYDB(I,J)+DEPB(K,I,J)*CORD(M,2)
 0038            500 CONTINUE
 0039                DO 1000 I=1,NIP
 0040                DO 1000 J=1,NIP
 0041                DETJ(I,J)=DYDA(I,J)*DXDB(I,J)-DXDA(I,J)*DYDB(I,J)
 0042                DJII(I,J)=DXDB(I,J)/DETJ(I,J)
 0043                DJIJ(I,J)=-DXDA(I,J)/DETJ(I,J)
 0044                DJJI(I,J)=-DYDB(I,J)/DETJ(I,J)
 0045                DJJJ(I,J)=DYDA(I,J)/DETJ(I,J)
 0046           1000 CONTINUE
 0047                IF(NOP(N,9).EQ.0) GO TO 1500
 0048                DO 2000 IP=1,NODE
 0049                DXDAN(IP)=0.0
 0050                DXDBN(IP)=0.0
```

```
FORTRAN IV G1  RELEASE 2.0            LOCAL              DATE = 82217          19/42/03             PAGE 0002
                    DYDAN(IP)=0.0
                    DYDBN(IP)=0.0
               2000 CONTINUE
                    DO 2500 KP=1,NODE
                    DO 2500 IP=1,NODE
                    MP=NCP(N,IP)
                    DXDAN(KP)=DXDAN(KP)+DEFASO(IP,KP)*COPD(MP,1)
                    DXDBN(KP)=DXDBN(KP)+DEFBSO(IP,KP)*COPD(MP,1)
                    DYDAN(KP)=DYDAN(KP)+DEFASO(IP,KP)*COPD(MP,2)
                    DYDBN(KP)=DYDBN(KP)+DEFBSO(IP,KP)*COPD(MP,2)
               2500 CONTINUE
                    DO 5000 IP=1,NODE
                    DETN(IP)=DYDAN(IP)*DXDBN(IP)-DXDAN(IP)*DYDBN(IP)
                    DNII(IP)=DXDBN(IP)/DETN(IP)
                    DNIJ(IP)=-DXDAN(IP)/DETN(IP)
                    DNJI(IP)=-DYDBN(IP)/DETN(IP)
                    DNJJ(IP)=DYDAN(IP)/DETN(IP)
               5000 CONTINUE
                    DO 6000 IP=1,NODE
                    NOD=NCP(N,IP)
                    IPIX=NPIX(NOD)
                    IF(IPIX.EQ.0) GO TO 6000
                    KOP=NOP(N,9)
                    DPX=0.0
                    DPY=0.0
                    DO 6666 JP=1,NODE
                    NOW=NOP(N,JP)
                    DPX=DPX+(DEFASO(JP,IP)*DNJI(IP)+DEFBSO(JP,IP)*DNJJ(IP))*P(NOW)
                    DPY=DPY+(DEFASO(JP,IP)*DNII(IP)+DEFBSO(JP,IP)*DNIJ(IP))*P(NOW)
               6666 CONTINUE
                    XNOD=COPD(NOD,1)-XS(KOP)
                    YNOD=COPD(NOD,2)-YS(KOP)
                    RNOD=SQRT(XNOD*XNOD+YNOD*YNOD)
                    ANGP=0.
                    ANGP=0.
                    IF(XNOD.NE.0..OR.YNOD.NE.0.)
                   *ANGP=ATAN2(XNOD,YNOD)
                    IF(DPX.NE.0..OR.DPY.NE.0.)
                   *ANGP=ATAN2(DPX,DPY)
                    IF(ANGP.LE.0.) ANGP=2.*3.14159+ANGP
                    IF(ANGP.LE.0.) ANGP=2.*3.14159+ANGP
                    DPN=SQRT(DPX*DPX+DPY*DPY)
                    DPR=DPN*COS(ANGP-ANGP)
                    VR=-DPR*H(NOD)*H(NOD)/12./VISL
                    VJET=VR*RNOD/RJET
                    ER(IP)=VJET
                    IF(IP.EQ.1) ER(IP)=ER(IP)/2.0
                    IF(IP.EQ.3) ER(IP)=ER(IP)/2.0
                    IF(IP.EQ.6) ER(IP)=ER(IP)/2.0
                    IF(IP.EQ.8) ER(IP)=ER(IP)/2.0
               6000 CONTINUE
               1500 CONTINUE
                    DO 20 M=1,NODE
                    MOC=NCP(N,M)
                    IOO=NPIX(MOC)
                    IF(IOO.NE.0) GO TO 22
                    DO 20 I=1,NIP
                    DO 20 J=1,NIP

FORTRAN IV G1  RELEASE 2.0            LOCAL              DATE = 82217          19/42/03             PAGE 0003
                    WFO=WF(I)*WF(J)
                    DWX=DEFA(M,I,J)*DJJI(I,J)+DEFB(M,I,J)*DJJJ(I,J)
                    DWY=DEFA(M,I,J)*DJII(I,J)+DEFB(M,I,J)*DJIJ(I,J)
                    HO=0.0
                    PO=0.0
                    DO 25 K=1,NODE
                    MM=NOP(N,K)
                    HO=HO+EF(K,I,J)*H(MM)
                    PO=PO+EF(K,I,J)*P(MM)
                 25 CONTINUE
                    PO=PO*HO*HO*HO*DETJ(I,J)*WFO
                    DO 50 K=1,NODE
                    DPX=DEFA(K,I,J)*DJJI(I,J)+DEFB(K,I,J)*DJJJ(I,J)
                    DPY=DEFA(K,I,J)*DJII(I,J)+DEFB(K,I,J)*DJIJ(I,J)
                    EM(M,K)=EM(M,K)+(DWX*DPX+DWY*DPY)*PO
                 50 CONTINUE
                 22 CONTINUE
                 20 CONTINUE
              C
              C
                    RETURN
                    END
```

```
      SUBROUTINE GRAPH
C
C     PRESSURE 3-D PLOT.
C
      COMMON/NUM/NP,NE,NBAND,NCDE,NIP
      COMMON/MODE/CORD(1500,2),NFIX(1500)
      COMMON/GAP/H(1500),SK(1500),HSET,SKSET
      COMMON/PARM/VISL,ROW,PATM,PTRACK,PLAST
      COMMON/RESULT/P(1500)
      DIMENSION XOC(5),YOC(5)
      DIMENSION PX(1500),PY(1500),HX(1500),HY(1500)
      DIMENSION NT(100)
C
C
      PI=3.14159
      DELX=.15
      DELY=.025
      CON=40.
C
      CALL PLOTST('//AEROT/MJH/',12)
      CALL FACTOR(0.3333)
      CALL PLOT(1.,1.,-3)
      CALL LINEWT(-1)
      CALL SYMBOL(8.0,.50,0.50,8HPRESSURE,0.0,8)
      XOC(1)=DELX
      YOC(1)=DELY
      XOC(2)=XOC(1)-0.15*COS(PI/4.)
      YOC(2)=YOC(1)+0.15*SIN(PI/4.)
      XOC(3)=XOC(2)+0.6*COS(PI/18.)
      YOC(3)=YOC(2)+0.6*SIN(PI/18.)
      XOC(4)=XOC(3)+0.15*SIN(PI/4.)
      YOC(4)=YOC(3)-0.15*COS(PI/4.)
      XOC(5)=XOC(1)
      YOC(5)=YOC(1)
      DO 1 I=1,5
      XOC(I)=CON*XOC(I)
      YOC(I)=CON*YOC(I)
    1 CONTINUE
      CALL PLOT(XOC(1),YOC(1),3)
      CALL LINEWT(-2)
      DO 2 I=2,5
      CALL PLOT(XOC(I),YOC(I),2)
    2 CONTINUE
      CALL LINEWT(0)
      DO 10 I=1,NP
      XP=CORD(I,2)*COS(PI/18.)-CORD(I,1)*SIN(PI/4.)+DELX
      YP=CORD(I,2)*SIN(PI/18.)+CORD(I,1)*COS(PI/4.)+DELY
      PX(I)=XP*CON
      PY(I)=((P(I)-PATM)/PATM/5.0+YP)*CON
   10 CONTINUE
      SMOLD=0.0001
      J=0
      DO 20 I=1,NP
      YP=ABS(CORD(I,1))
      IF(YP.LE.SMOLD) J=J+1
      IF(YP.LE.SMOLD) NT(J)=I
```

```
   20 CONTINUE
      KKK=0
      NT(J+1)=NP+1
      DO 50 K=1,J
      NPOINT=NT(K+1)-NT(K)
      DO 25 KK=1,NPOINT
      KKK=KKK+1
      PXL=PX(KKK)
      PYL=PY(KKK)
      CALL PLOT(PXL,PYL,2)
      IFIX=NFIX(KKK)
      IF(IFIX.EQ.1) POP=PYL+(PTRACK-P(KKK))/PATM/5.0*CON
      IF(IFIX.EQ.1) CALL PLOT(PXL,POP,3)
      IF(IFIX.EQ.1) CALL PLOT(PXL,PYL,2)
   25 CONTINUE
      KO=KKK+1
      IF(KKK.EQ.NP) GO TO 50
      CALL PLOT(PX(KO),PY(KO),3)
   50 CONTINUE
      CALL PLOT(30.0,0.0,-3)
      CALL LINEWT(-1)
      CALL SYMBOL(8.0,.50,0.50,3HGAP,0.0,3)
      CALL PLOT(XOC(1),YOC(1),3)
      CALL LINEWT(-2)
      DO 3 I=2,5
      CALL PLOT(XOC(I),YOC(I),2)
    3 CONTINUE
      CALL LINEWT(1)
      DO 60 I=1,NP
      XP=CORD(I,2)*COS(PI/18.)-CORD(I,1)*SIN(PI/4.)+DELX
      YP=CORD(I,2)*SIN(PI/18.)+CORD(I,1)*COS(PI/4.)+DELY
      HX(I)=XP*CON
      HSOT=HSET
      HSOT=HSET/2.
      HY(I)=(H(I)/HSOT/100.+YP)*CON
   60 CONTINUE
      CALL PLOT(HX(1),HY(1),3)
      KKK=0
      DO 75 K=1,J
      NPOINT=NT(K+1)-NT(K)
      DO 70 KK=1,NPOINT
      KKK=KKK+1
      HXL=HX(KKK)
      HYL=HY(KKK)
      CALL PLOT(HXL,HYL,2)
   70 CONTINUE
      KO=KKK+1
      IF(KKK.EQ.NP) GO TO 75
      CALL PLOT(HX(KO),HY(KO),3)
   75 CONTINUE
      CALL LINEWT(0)
      CALL PLOTND
C
C
      RETURN
      END
```

REFERENCES

1. Hinchey, M. J., Sullivan, P. A., and Graham, T. A., "Research on the SailRail Compliant Surface Air Bearing", Transportation Development Centre, Transport Canada, Montreal, Contract Report TP2817, Jan. 1981.

2. Schlichting, H., Boundary-Layer Theory, 6th Edition, McGraw-Hill, New York, 1968.

3. Massey, B. S., Mechanics of Fluids, 6th Edition, Van Nostrand Reinhold, London, 1970.

4. Lowe, I. R. G., "Characteristics of Externally Pressurized Thrust Bearings with One Compliant Surface", Proceedings of the Sixth International Gas Bearing Symposium, University of Southampton, Southampton, England, Mar. 1974.

5. Ribich, W. A., and Richardson, H. H., "Dynamic Analysis of Heave Motion for a Transport Vehicle Fluid Suspension", Dept. of Mechanical Engineering, Massachusetts Institute of Technology, Boston, Mass., DSR-76110-3, Jan. 1967.

6. Hinchey, M. J., "Heave Instabilities of Amphibious Air Cushion Suspension Systems", Institute for Aerospace Studies, University of Toronto, Toronto, Canada, Report 246, Nov. 1980.

7. Roylance, D., Mcelroy, P, and McGarry, F., "Viscoelastic Properties of Paper", Journal of Fibre Science and Technology, Vol. 13, 1980, pp. 411-421.

8. Pfeiffer, J. D., "Internal Pressures in a Wound Roll of Paper", Technical Association of the Pulp and Paper Industry, Vol. 49, No. 8, 1966, pp. 342-347.

9. Davidge, R. O. C., "Evaluation of the Vibration Isolation Characteristics of SailRail Air Cushion Pads", Department. of National Defence, Canada, Quality Engineering Test Establishment Project No. E00479, March 1980.

10. Gladish, H. E., Private Communication.

11. Altmann, H. C., "Formulas for Computing the Stresses in Centre-Wound Rolls", Technical Association of the Pulp and Paper Industry, Vol. 15, No. 4, 1968, pp. 176-179.

12. Yagoda, H. P., "Resolution of a Core Problem in Wound Rolls", Journal of Applied Mechanics, Vol. 47, No. 4, Dec. 1980, pp. 847-854.

13. Graham, W. B., "Material Damping and Its Role in Linear Dynamic Equations", Institute for Aerospace Studies, University of Toronto, Review No. 36, 1973.

14. Dugundji, J., Dowell, E., and Perkin, B., "Subsonic Flutter of Panels on Continuous Elastic Foundatons", AIAA Journal, Vol. 1, No. 5, 1963, pp. 1146-1154.

15. Gelb, A., and Vander Velde, W. E., Multiple-Input Describing Functions and Nonlinear System Design, McGraw-Hill, New york, 1968, p. 350.

16. Shapiro, A. H., "Steady Flow in Collapsible Tubes", Journal of Biomechanical Engineering, Vol. 99, Aug. 1977, pp. 126-147.

17. Paidoussis, M. P., and Denise, J. P., "Flutter of Thin Cylindrical Shells Conveying Fluid", Journal of Sound and Vibration, Vol. 20, No. 1, 1972, pp. 9-26.

18. Leblanc, R., "Study of Flow in an Artificial Trachea", Institute for Aerospace Studies, University of Toronto, Toronto, Canada, M.A.Sc. Thesis, 1982.

19. Hinchey, M. J., and Sullivan, P. A., "Kelvin-Helmholtz Stability Analysis of Air Cushion Landing Gear Trunk Flutter", Journal of Aircraft, Vol. 19, No. 1, 1982, pp. 94-96.

20. Gosman, A., and Ideriah, F., "Teach-T: A General Computer Program for Two-Dimensional Turbulent Recirculating Flow", Department of Mechanical Engineering, Imperial College of Science and Technology, London, England, 1976.

21. Lowe, I. R. G., "Some Experimental Results from Compliant Air Lubricated Thrust Bearings", Journal of Lubrication Technology, Vol. 96, No. 4, 1974, pp. 547-560. See Discussion.

22. Dudgeon, E. H. and Lowe, I. R. G., "A Theoretical Analysis of Hydrostatic Gas Journal Bearings", National Research Council of Canada, Division of Mechanical Engineering, Report MT-54, Aug. 1965.

BIBLIOGRAPHY OF PAPERS AND BOOKS ON FRICTION AND WEAR OF POLYMERS CAUSED BY SLIDING

E1 Amuzu, J. K. A., Briscoe, B. J., and Tabor, D., "Polymers as Bearings and Lubricants: Aspects of Fundamental Research", Advances in Tribiology, Institute of Mechanical Engineers, London, 1978.

E2 Belyi, V. A., et al, "Adhesive Wear of Polymers", Journal of Lubrication Technology, Vol. 99, No. 4, Oct. 1977, pp. 396-400.

E3 Bowers, R. C., Clinton, W. C., and Zizman, W. A., "Frictional Behaviour of Polyethylene, Polytetrafluoroethylene and Halogenated Derivatives", Lubrication Engineering, Vol. 55, Aug. 1953, pp. 204-208, 218-219.

E4 Briscoe, B. J., Pogosian, A. K., and Tabor, D., "Friction and Wear of High Density Polythene: The Action of Lead Oxide and Copper Oxide Fillers", Wear, Vol. 27, 1974, pp. 19-34.

E5 Briscoe, B. J., and Tabor, D., "Friction and Wear of Polymers: The Role of Mechanical Properties", The British Polymer Journal, Vol. 10, No. 1, Mar. 1978, pp. 74-78.

E6 Briscoe, B. J., and Tabor, D., "The Sliding Wear of Polymers: A Brief Review", Proceedings of the International Conference on the Fundamentals of Tribology, Massachusetts Institute of Technology, Cambridge, Massachusetts, June 1978, pp. 733-758.

E7 Clerico, M., "Sliding Wear Mechanisms of Polyers", Proceedings of the International Conference on the Fundamentals of Tribology, Massachusetts Institute of Technology, Cambridge, Massachusetts, June 1978, pp. 769-785.

E8 Fuchsluger, J. H., and Taber, R. D., "The Effect of Atmospheric Environment on the Wear Properties of Filled TFE Materials", Journal of Lubrication Technology, Vol. 93, No. 3, July 1971, pp. 423-429.

E9 Jahanmir, "On the Wear Mechanisms and The Wear Equations", Proceedings of the International Conference on the Fundamentals of Tribology, Massachusetts Institute of Technology, Cambridge, Massachusetts, June 1978, pp. 455-467.

E10 Kar, M. K., and Bahadur, S., "Mechanism of Film Formation in Polymer-Metal Sliding", Proceedings of the International Conference on the Fundamentals of Tribology, Massachusetts Institute of Technology, Cambridge, Massachusetts, June 1978, pp. 759-768.

E11 King, R. F., and Tabor, D., "The Effect of Temperature on the Mechanical Properties and Friction of Plastics", Proceedings of the Physical Society of London, Series B, Vol. 6, 1953, pp. 728-736.

E12 Lancaster, J. K., "Basic Mechanisms of Friction and Wear of Polyumers", presented at Conference on Plastics in Bearings (Plastics Institute, London), Feb. 1973.

E13 Makinson, K. R., and Tabor, D., "Friction and Transfer of Polyethylene", Proceedings of the Royal Society of London, Series A, Vol. 281, 1964, pp. 49-61.

E14 Milz, W. C., Sargent, L. B., "Frictional Characteristics of Plastics", Lubrication Engineering, Sept.-Oct., 1955, pp. 313-318.

E15 Pooley, C. M., and Tabor, D., "Friction and Molecular Structure: The Behaviour of Some Thermoplastics", Proceedings of the Royal Society of London, Series A, Vol. 329, Aug. 1972, pp. 251-274.

E16 Schubert, R., "The Influence of a Gas Atmosphere and Its Moisture on Sliding Wear in PTFE Compositions", Journal of Lubrication Technology, Apr. 1971, pp. 216-223.

E17 Steijn, R. P., "The Effect of Time, Temperature and Environment on the Sliding Behaviour of Polytetrafluoroethylene", American Society of Lubrication Engineers Transactions, Vol. 9, 1966, pp. 149-159.

E18 Steijn, R. P., "Sliding Experiments with Polytetrafluoroethylene", American Society of Lubrication Engineers Transactions, Vol. 11, 1968, pp. 235-247.

E19 Suh, N. P., "Wear Mechanisms: An Assessment of the State of Knowledge", Proceedings of the International Conference on the Fundamentals of Tribology, Massachusetts Institute of Technology, Cambridge, Massachusetts, June 1978, pp. 443-453.

E20 Tabor, D., "Friction - The Present State of Our Understanding", Journal of Lubrication Technology, Vol. 103, Apr. 1981, pp. 169-179.